School of Electrical Engineering, Computing and
Mathematical Sciences

International Centre for Radio Astronomy Research

Exploring the Lensing of Cosmological Transients on Nanosecond Timescales

Mawson William Sammons

0000-0002-4623-5329

This thesis is presented for the Degree of
Doctor of Philosophy
of
Curtin University of Technology

June 2023

To the best of my knowledge and belief this thesis contains no material previously published by any other person except where due acknowledgement has been made. This thesis contains no material which has been accepted for the award of any other degree or diploma in any university.

Mawson William Sammons

"*Now just crank the mathematical handle...*"

— Jean-Pierre Macquart.

Acknowledgements

I would like to acknowledge the Wadjuck people, past, present and future, as Australia's first astronomers, and the original custodians of the land on which this work was done.

As with any scientific endeavour, the growth of my understanding throughout this Ph.D. reflects the environment which fostered its growth. I am deeply grateful to all staff and students at both nodes of the International Centre for Radio Astronomy Research and members of the CRAFT team, who have created such a delightful environment in which I could develop as a researcher. Specifically, I would like to thank the late J-P. Macquart, for introducing me to the field of fast radio burst science, and for inspiring me to try my hand at some of its more difficult theoretical concepts. I am also immeasurably grateful to my supervisory team: Cathryn Trott, Clancy James, and Mark Walker, who generously took up my supervision in J-P.'s absence. You provided me with the freedom to discover the research I found most engaging, and equipped me with the tools to pursue it. I believe J-P. would have been proud of the supervision you've delivered, and the research we have accomplished together.

To my family, thank you for your love and support, and for providing the perfect Perth Hills retreat throughout the years. To the denizens of Bone Street, thank you for being the company I always want to come home to.

Abstract

Cosmological transients such as fast radio bursts (FRBs) are the most angularly compact sources observed to date. As a result, they are potentially sensitive to propagation effects from matter distributed on scales that are otherwise inaccessible. By understanding the propagation effects caused by these matter distributions, cosmological transients can be used to probe unexplored regimes of the Universe's fine-scale structure, over cosmological volumes.

In this thesis, I primarily explore how the nature of dark matter can be investigated by observing signatures of gravitational lensing in FRBs. A fundamental question within the study of dark matter is whether its distribution is similar to that of a gas of microscopic particles, or an ensemble of macroscopic clumps, such as primordial black holes (PBHs). I investigate two potential ways in which future FRB surveys will be able to form constraints on the parameter space of PBHs. First, I discuss searching for images of strongly gravitationally lensed FRBs in the temporal domain of individual bursts, and update previous forecasts with limits informed by improved FRB data quality. I conclude that based on existing constraints approximately 130 FRBs would need to be observed before a lensing signal could be expected. Second, I derive the effect of gravitational lensing on the expected ensemble rate of observed FRBs, and introduce a novel method for simultaneously constraining the entire range of PBHs capable of lensing FRBs. Both investigations conclude that the large FRB samples expected from future surveys will be sufficient to form constraints that will dominate over existing limits.

In addition to exploring FRB gravitational lensing, I consider how observations of plasma scattering in FRBs can be used to constrain their progenitor scenarios and check the validity of Galactic electron distribution models. To do so I develop existing models for two-screen scattering in FRBs and apply them to localise scattering media in a sample of Commensal Real-time ASKAP Fast Transient survey (CRAFT) FRBs observed using the Australian Square Kilometre Array Pathfinder (ASKAP). The results suggest that the dominant contribution to extragalactic scattering in FRBs comes from within each FRB's host galaxy and that Galactic scattering models may over-predict observed scattering times.

Statement of Originality

The content of chapter 5 is my own work, except for the following. A/Prof. Jean-Pierre Macquart motivated the original idea. Initial calibration and pre-processing of data, including PFB inversion and de-dispersion, was performed by Prof. Adam Deller, Dr Cherie Day and Ms. Hyerin Cho. I performed all analyses of the processed data, making use of code written by Prof. J. Xavier Prochaska to evaluate Galactic intersection probabilities. Prof. Ron Ekers and A/Prof. Ryan Shannon motivated sections on clumpy dark matter. Apart from Figure 3, which was generated for publication by Ms. Hyerin Cho, the draft manuscript was written by me and distributed to co-authors for critique. All co-authors provided input over several iterations of feedback until the manuscript was complete.

The content of chapter 6 is my own work, except for the following. Prof. Cathryn Trott, Dr. Clancy James and Dr. Mark Walker suggested the functional forms used for modelling the lensing probabilities and aided in the implementation of numerical integration routines. I wrote the draft of the paper and distributed copies to all co-authors for critique. All co-authors provided input over several iterations of feedback until the manuscript was complete.

The content of chapter 7 is my own work, except for the following. A/Prof. Ryan Shannon contributed to the initial discovery of the FRBs used in the analysis. Initial calibration and pre-processing of data was performed by Ms. Danica R. Scott, Prof. Adam Deller, Dr Kelly Gourdji and Dr Marcin Glowacki. I performed all analyses of the processed data, making use of code written by Dr Hao Qiu to characterise burst morphology. Prof. J. Xavier Prochaska motivated additional extragalactic scattering constraints. The draft manuscript was written by me and distributed to co-authors for critique. All co-authors provided input over several iterations of feedback until the manuscript was complete.

(Signature of Candidate)

(Signature of Supervisor)

Contents

List of Figures

Chapter 1

Introduction

From gentle beach waves to violent gamma-ray bursts (GRBs), all transient signals are shaped by the environments through which they propagate. By understanding how these environments affect the signals we observe, not only can we correct for them, improving our understanding of a signals' source, but we can use them to measure properties of an environment without the need for direct observation. Such a technique is invaluable to astronomers, who often have little recourse in the face of observational barriers. This thesis aims to add to our understanding of how matter in our Universe influences the propagation of cosmological transients, and in doing so contribute to our understanding of both their emission and the structure of our Universe.

1.1 Our Universe

Within the bounds of the Milky Way the Universe is well described by a Euclidean geometry. Prior to the 20th century the dominant picture of our Universe extended this simple geometry to infinity in all directions, describing a static Universe. Early spectroscopic studies showed, however, that almost all distant galaxies (termed nebulae at the time) are receding away from the observer (Slipher, 1917)— behaviour that is difficult to reconcile with a static model. To resolve this

apparent tension, Lemaître (1927) derived an alternate model for the Universe's geometry known as the Friedmann-Lemaitre-Robertson-Walker metric (FLRW; termed to include earlier and subsequent contributions to its development). The FLRW metric is an exact solution to the field equations of Einstein's theory of general relativity (Einstein, 1916), found by assuming the Universe is homogeneous and isotropic. These assumptions follow from the Copernican principle, that we as observers do not occupy a special vantage point in the Universe. The FLRW metric describes a Universe that is not only homogeneous and isotropic, but also expanding uniformly, such that every point in the Universe is receding from every other point. Furthermore, Lemaître (1931) proposed that tracing this behaviour backward in time implies that the Universe expanded out from an infinitely dense singularity which we term the Big Bang and mark as the origin of our Universe.

The expansion of the Universe proposed by Lemaitre was subsequently confirmed by Hubble (1929), providing a natural explanation for the observed recession of extragalactic objects. Moreover, the distance to an object is proportional to its recessional velocity following Hubble's law $v = H_0 d$ where v and d are proper velocity and distance (i.e. they are quantities measured between points at constant cosmic time) and H_0 is Hubble's constant describing the rate of the Universe's expansion in the current epoch. At cosmological distances the observed motion of a galaxy is dominated by its recession due to expansion, allowing its distance to be estimated from the redshift of its spectrum. Physically, this cosmological redshift is caused by the expansion of the Universe. The finite speed of light means that observations of distant sources were emitted at earlier times when the scale factor of the Universe was smaller (i.e. the Universe was contracted relative to the present). As this light propagates its wavelength expands with the Universe. As shown in Eq. 1.1 the ratio of the observed to emitted wavelength of light corresponds to $(1+z)$, where z denotes cosmological redshift. The factor $(1+z)$ is also equivalent to the ratio of the scale factor at the time of observation,

$a(t_{\rm obs})$, to the time of emission, $a(t_{\rm emit})$ i.e.

$$\frac{\lambda_{\rm obs}}{\lambda_{\rm emit}} = (1+z) = \frac{a(t_{\rm obs})}{a(t_{\rm emit})}. \tag{1.1}$$

Therefore, both distance and the timeline of the Universe's evolution can be expressed as a function of redshift, with $z = 0$ being the local Universe at the present time and $z = \infty$ being the distant Universe at the time of the Big Bang.

From the singularity of the Big Bang the Universe is thought to have gone through a period of rapid inflation, where the scale factor of the Universe grew exponentially. This expansion causes the Universe to cool adiabatically from its initial hot and dense state (Peebles, 1993). Once the Universe cools sufficiently such that high energy collisions no longer disrupt the strong force bonds between quarks and gluons, matter and antimatter form. The subsequent annihilation between the matter and anti-matter results in most of the formed particles being destroyed. However, small excesses of leptons and quarks over anti-leptons and anti-quarks leaves a remainder of matter that dominates over anti-matter in the Universe today.

Further cooling leads to the formation of the light nuclei, namely hydrogen, helium and trace amounts lithium and beryllium in a process known as big bang nucleosynthesis (Alpher et al., 1948). All heavier elements are formed through the fusion of these light nuclei in other processes such as stellar nucleosynthesis. The relative abundances of each nuclear species depend sensitively on the conditions of the early Universe, including the total density in baryons. As the early Universe is relatively homogeneous we expect these relative abundances to be consistent across the Universe at the time of their formation. Therefore, by measuring the ratios of light elements in environments uncontaminated by stellar evolution the total density of baryons in the Universe can be measured (Cooke et al., 2018).

Following this first three minutes of the evolution the Universe exists as a hot plasma. Due to the plasma's large density of free charges light can only travel a short distance through the plasma before it is Thompson scattered by an ion.

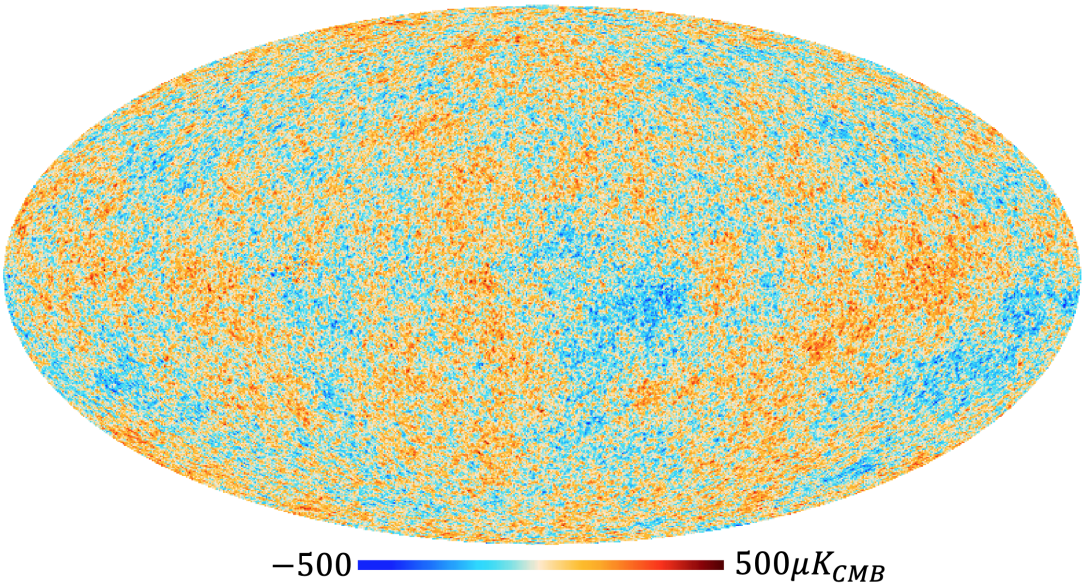

Figure 1.1: Sky map of CMB temperature anisotropies compared to mean temperature of $\sim 2.73\,\mathrm{K}$. Adapted from (Ade et al., 2014).

As a result of this the plasma is opaque and the ions and photons are in thermal equilibrium. The high energy black-body spectrum of the photons, corresponding to the high temperatures prevents the synthesised nuclei from becoming neutral atoms and keeps the photons and ions thermally coupled. As expansion cools the Universe the photon spectrum decreases in energy and nuclei begin to capture electrons and form neutral atoms in a process known as recombination. The heavier nuclei with their deeper coulomb potentials capture electrons first, with hydrogen recombination being the last to occur at around $\sim 400\,000$ years after the big bang (Peebles & Yu, 1970). After recombination the Universe is effectively neutral causing photons to decouple from matter and propagate through the Universe unimpeded. These photons which peaked in the visible and infrared spectrum at the time of recombination constitute the Cosmic Microwave Background (CMB) radiation, which today has been cosmologically redshifted by a factor of $z \sim 1000$ to microwave frequencies.

Often referred to as the afterglow of the Big Bang, the CMB provides strong evidence that the Universe existed in the extreme state predicted by the Big Bang

model. Furthermore, the observed spectrum of the CMB can be used to calculate the temperature of the surface of last scattering and in doing so reveal properties of the Universe at the time of recombination. Fig. 1.1 shows this temperature calculated from the latest Planck data (Ade et al., 2014). It shows that the temperature of the pre-recombination plasma was exceptionally uniform across the sky, with a root-mean-square (RMS) variation of approximately $17\mu K$(Ade et al., 2014). The observed homogeneity across the CMB is difficult to explain as regions separated by more than approximately 2° in Fig. 1.1 cannot be causally connected at the time of recombination. This horizon problem (Rindler, 1956) is a primary motivation for the theorised inflationary epoch described earlier, as rapid expansion of the Universe can cause regions in thermal equilibrium to appear causally disconnected at later times.

In the time since recombination the Universe has continued to expand and cool. The anisotropies seen in the CMB become the seeds of large scale structure formation and within these structures the pressure of gravitational collapse births stars from the neutral gas (Peebles, 1980). High energy radiation emitted by these stars and other compact objects such as active galactic nuclei ionises most of the remaining neutral gas in the Universe during the epoch of reionisation (Kogut et al., 2003). This is the last major evolution of the Universe, leaving it in the familiar, transparent state we observe today.

Throughout all the above epochs, the evolution of the Universe is driven primarily by its expansion. The rate at which the Universe expands depends on the densities of each component of the Universe at a given redshift, as given by (Hogg, 2000)

$$\begin{aligned} H(z) &= H_0 E(z) \\ E(z) &= \sqrt{\Omega_M(z) + \Omega_R(z) + \Omega_k(z) + \Omega_\Lambda} \end{aligned} \tag{1.2}$$

where $H(z)$ is the value of Hubble's constant at redshift z and each Ω_X represents the average density in the Universe of matter, radiation, curvature and dark

energy respectively, at redshift z with respect to the critical density of the FLRW universe. The critical density, given by

$$\rho_{\rm crit} = \frac{3H_0^2}{8\pi G}, \tag{1.3}$$

is the density required for a Universe to be completely flat, i.e. have $\Omega_k = 0$. This leads to the curvature often being expressed separately from the other density paramaters in the following general relation

$$\Omega(z) = \Omega_M(z) + \Omega_R(z) + \Omega_\Lambda = 1 - \Omega_k(z). \tag{1.4}$$

Because a universe described by the FLRW metric must be everywhere isotropic and homogeneous there are only three possible curvatures it may have; positive ($k = +1$), negative ($k = -1$) and flat ($k = 0$). In each case the curvature contributes a density given in units of the critical density by

$$\Omega_k(z) = \frac{-kc^2}{a^2(z)H(z)^2}, \tag{1.5}$$

which evolves with redshift as $(1+z)^2$. These curvatures dictate the ultimate fate of our Universe with positively curved Universes eventually recollapsing, whereas negatively curved and flat Universes continue to expand indefinitely.

The remaining density parameters each evolve with redshift at their own rate. The energy density of matter ($\Omega_M(z)$) decreases as the volume of space increases and hence evolves with redshift as $(1 + z)^3$. Whereas, the energy density of radiation ($\Omega_R(z)$) will decrease more quickly as its wavelength is also dilated by expansion resulting in a $(1+z)^4$ redshift evolution. Finally the dark energy, which drives the expansion of the Universe is most commonly modelled as a cosmological constant Λ, the density of which (Ω_Λ) does not evolve with redshift. Using these evolutionary behaviours the density parameters can be expressed in terms of their

density in the present epoch ($\Omega_{X,0}$) yielding

$$E(z) = \frac{H(z)}{H_0} = \sqrt{\Omega_{M,0}(1+z)^3 + \Omega_{R,0}(1+z)^4 + \Omega_{k,0}(1+z)^2 + \Omega_\Lambda} \qquad (1.6)$$

Observations of the CMB also provide a way to measure these densities in our Universe. As seen in Fig. 1.1 the near perfect black body of the CMB at ≈ 2.73 K shows small intrinsic temperature fluctuations on the scale of 1 part in 100000 (Smoot et al., 1992; Fixsen et al., 1996). These temperature anisotropies come from two processes associated with matter-energy density inhomogeneities in the Universe prior to recombination. The first is the Sachs-Wolfe effect; a result of the gravitational redshift predicted by Einstein's theory of general relativity (Sachs & Wolfe, 1967). Gravitational redshift causes photons escaping a gravitational potential well to be shifted to lower frequencies, and therefore energies. At the time of recombination the matter-density inhomogeneities in the Universe setup inhomogeneous gravitational potentials. Therefore, as the CMB photons are deflected off the surface of last scattering towards the observer, they undergo a non-uniform amount of gravitational redshift across the sky, manifesting as CMB temperature fluctuations.

The second effect comes from the dynamics of the photo-baryon fluid that permeates the Universe prior to recombination. During this epoch the ionised baryons are drawn by gravity into the inhomogeneous potential wells, compressing the fluid. The increased pressure pushes back against gravity, causing the fluid to expand. The decreased pressure from expansion then allows gravity to dominate once more and the cycle continues, leading to an acoustic oscillation in the plasma (Peebles & Yu, 1970; Sunyaev & Zeldovich, 1970). Similar to an image of rain over the surface of a pond, many oscillations, at various phases were frozen-in to the CMB signal after recombination when matter became neutral and photons decoupled from baryons. These are the smaller scale temperature fluctuations observed in the CMB. They can also be seen in the modern Universe's large scale structure in the excess probability for galaxies to be separated at the

characteristic oscillation length (Eisenstein et al., 2005). This confirms that the density fluctuations in the Universe's pre-recombination plasma responsible for temperature anisotropies in the CMB seeded the formation of structure in our Universe today. However, it also presents a significant issue, as insufficient time has elapsed in the Universe since recombination for those small amplitude density fluctuations to have evolved into the structures of the present day Universe (Smoot et al., 1992). A proposed solution to this issue is the presence of non-baryonic matter that does not interact strongly with the electromagnetic field (Davis et al., 1985). Without the pressure of electromagnetic forces opposing gravity this matter can form the necessary structures before recombination, giving today's structures the necessary time to form. Through the use of simulations a forward model can be built which takes in fundamental properties of the Universe such as the total matter density and the baryon density and calculates the resulting CMB signal. By matching these simulated expectations to the observed CMB the density parameters for our Universe can be calculated. The most recent Planck results estimate that matter comprises roughly a third of the Universe's energy budget, with $\Omega_{M,0} = 0.31$. Conversely, radiation contributes negligibly to the Universe's total density and therefore is often set $\Omega_{R,0} = 0$ for calculations restricted to the present epoch. The curvature as measured from the CMB is consistent with a flat Universe ($\Omega_k = k = 0$), these results are consistent with independent estimates from observations of type 1a SNe. Assuming zero curvature and therefore $\Omega(z) = 1$ as per Eq. 1.4, the remaining energy density is attributed to dark energy giving $\Omega_\Lambda = 0.69$.

Within the matter density the CMB also constrains the baryonic density to be $\Omega_{b,0} = 0.049$, consistent with estimates of baryonic matter abundance from Big Bang Nucleosynthesis analysis (Planck Collaboration et al., 2018). The remaining 84% of the matter density is attributed to the structure forming non-baryonic matter. This theoretical substance is termed dark matter due to the expectation that it does not interact strongly with the electromagnetic field, and evidence for

its existence was discovered long before the CMB was observed.

1.1.1 Dark Matter

Dark matter refers to theoretical matter in our Universe which is non-luminous and therefore undetectable by direct observation. Typically, it is hypothesised to be matter that does not interact electromagnetically and therefore does not emit, reflect or absorb any light. The existence of dark matter was theorised to explain discrepancies between the expected and observed behaviours of luminous matter distributions in our Universe. The first evidence for dark matter came from the velocity dispersion of stars in gravitationally bound structures such as the Milky Way (Zwicky, 1933). On galactic scales stars are point-like, and their great number allows them to be treated like the particles of a gravitationally bound gas. If a system of stars is pressure/velocity dispersion supported such as a galaxy cluster, elliptical galaxy or the central region of a spiral galaxy (i.e. it is not rotationally supported like a galactic disk), then the system's mass can be determined using the virial theorem (Zwicky, 1933). Velocity dispersion measurements from the broadening of spectral line emission can be used to determine a system's average total kinetic energy, which then through the virial theorem yields the system's total gravitational potential energy and therefore its mass. Efforts dating back over a century have used similar techniques to measure the mass of the Milky Way (Kelvin, 1904; Battaglia et al., 2005) and on an even greater scale, the mass of extragalactic galaxy clusters (Zwicky, 1933). In each case the results suggest that the mass of the system inferred from its dynamics was far greater than that expected from its luminosity, i.e. each contains a significant amount of non-luminous or dark matter.

Later studies of the rotation curves of galaxies similarly revealed that the rotational velocities of almost all galaxies continue to increase up to the edge of their optical disks, contrary to the Keplerian expectation (Rubin et al., 1980; Rubin, 1983; Bosma, 1981). A natural conclusion of these observations is that

galaxies contain a substantial amount of dark matter beyond the extent of their optical disks. Today we term this the dark matter halo of a galaxy. Early simulations of dark matter halos suggested their density profiles had a common shape for all galaxies, given by the Navarro Frenk and White (NFW) profile (Navarro et al., 1996). While this model survives today as a simple description of halo shapes (especially at large galactic radii), more recent, higher resolution simulations have shown that the more complicated, mass dependent Einasto profile provides a better fit for the inner-most regions of dark matter halos (Navarro et al., 2010; Klypin et al., 2016).

Perhaps the most convincing piece of evidence for dark matter comes from the interacting cluster 1E 0657–558. The Bullet cluster, as it is known, is so-called because the smaller of the two colliding galaxy clusters has passed through the larger causing a prominent bow-shock to be seen in the x-ray (Clowe et al., 2004). The shock front is caused by the fluid-like electromagnetic interaction between the hot gas which dominates the baryonic content of each cluster. Conversely, the cluster galaxies are relatively collisionless and so pass through each other unimpeded. Measurements of gravitational lensing of sources background to the cluster indicate that each cluster's centre of mass is coincident with the position of its galaxies, rather than the interacting gas which dominates its visible mass. Again, this indicates the presence of non-luminous matter causing the lensing that has a small electromagnetic interaction cross section (i.e. a small probability of interacting) (Markevitch et al., 2004) allowing it to follow the collisionless path of the galaxies. Furthermore, recent simulations of dark matter and baryonic gas interactions in Bullet-cluster-like mergers indicate that the observed shapes of their bow shocks cannot occur from baryonic gas alone (Keshet et al., 2021). Instead, these properties correspond precisely to our expectation of dark matter, providing strong evidence for its existence.

Despite knowing its abundance throughout the Universe, the identity and precise nature of dark matter remains one of the largest unsolved problems in

astrophysics and cosmology. Theories of dark matter are broadly categorised as hot, warm or cold based on the speed at which the dark matter particles are theorised to travel (see Bertone et al., 2005, for a review). Cold dark matter forms structure in our Universe from the bottom up, with small perturbations accreting matter and merging over time to yield the galaxies and clusters we observe today. Conversely, hot dark matter forms structure from the top down, with large structures being the first to fragment from the uniformity of the early Universe. Finally, warm dark matter labels theories which combine behaviours from both hot and cold types. The top down structure formation scenario intrinsic to a hot dark matter dominated universe is disfavoured by studies which show that super-clusters (combinations of galaxy clusters) would have to form after $z = 2$ (Dekel, 1983; Frenk et al., 1983; Kaiser, 1983; Dekel et al., 1984), in conflict with observations of galaxies as early as $z = 11.5$ (Adams et al., 2023). Data informed simulations of structure formation instead dictate that the matter component of the Universe is comprised mostly of non-relativistic or "cold" dark matter (Navarro et al., 1996; Springel et al., 2005). Furthermore, observations of Type Ia supernovae show that the Universe's energy budget is dominated by dark energy which drives universal expansion, labelled as the cosmological constant Λ (Riess et al., 1998; Perlmutter et al., 1999; Abbott et al., 2019). Together these components form the standard cosmological model, known as ΛCDM (see Springel et al., 2006, for a review).

ΛCDM has been very successful at reproducing the evolution of large scale structure in the Universe, however, on scales below 1 Mpc several problems have been identified (Bullock & Boylan-Kolchin, 2017). Foremost among these have been the missing satellite and core-cusp problems. The missing satellite problem refers to the over-prediction of galactic satellites by ΛCDM N-body simulations compared to observations (Moore et al., 1999; Klypin et al., 1999). This problem can be considered solved, as more recent simulations including baryonic physics in their galaxy evolution show a number of satellites consistent with observa-

tions (Sawala et al., 2016). The core-cusp problem, which persists today, is the discrepancy in the predicted density profile of dark matter halos compared with observations, with the simulated profiles having systematically denser and cuspier cores than observations imply (Flores & Primack, 1994).

Amongst others (see Del Popolo & Le Delliou, 2021, for a review), a proposed solution to these small scale problems is to modify cold dark matter to smooth over structures below some critical scale (Bullock & Boylan-Kolchin, 2017). Warm dark matter achieves this by increasing the characteristic temperature of its particles. As the temperature of the particles increases so does their average kinetic energy, and therefore minimum mass required to keep a dark matter structure gravitationally bound is greater. This minimum mass is known as the free streaming mass, as below it all structures are smoothed by the free streaming of the warm dark matter particles. Therefore, on large scales, warm dark matter behaves identically to cold dark matter, but on small scales structures are suppressed, resolving the aforementioned small scale discrepancies (Bode et al., 2001). Observations indicate that dark matter may only be warm enough to smooth very small scales and cannot resolve the tension between theoretical predictions and observations (Viel et al., 2013) but a consensus in this field is yet to be reached (see Perivolaropoulos & Skara, 2022, for a review).

On smaller scales still the behaviour of dark matter is an almost complete mystery, however differences between macroscopic and microscopic dark matter candidates begin to emerge below stellar mass scales. Microscopic refers to dark matter candidates that take the form of exotic particles such as weakly interacting massive particles (WIMPs) or axions which are the currently favoured candidates for cold dark matter. Conversely, macroscopic dark matter candidates are non-luminous celestial bodies such as rogue planets. One of the few remaining macroscopic dark matter matter candidates that could constitute the majority of dark matter is primordial black holes (PBHs).

There are several theories for how PBHs form, from the nucleation of vac-

uum bubbles (Garriga et al., 2016) to the collapse of cosmic strings (Hawking, 1989). The most natural channel stems from the gravitational collapse of large overdensities in the Universe shortly after inflation (Zel'dovich & Novikov, 1966; Hawking, 1971). Regardless of the precise nature of their formation, PBHs evolve separately to stellar evolution channels. As a result of this PBHs can have a much greater range in mass, from 10^{-5}g to comparable with the mass of our Universe (Carr & Hawking, 1974). Several decades of theoretical consideration and observational searches for PBHs has led to tight constraints on the fraction of dark matter which may be comprised of PBHs over a wide range of masses. I'll briefly review some of these constraints now, but for a more complete discussion see Carr et al. (2016); Carr & Kühnel (2020).

All black holes, primordial or otherwise are expected to emit Hawking radiation, due to quantum effects in the relativistic region of a black hole's event horizon (Hawking, 1974). The black hole will emit Hawking radiation as a black body, with a characteristic temperature inversely proportional to the black hole's mass (Hawking, 1974). To fuel the emission the mass of the black hole itself is lost causing it to shrink over time. This evaporation has a negligible impact on the mass of large black holes, with the timescale for complete evaporation of a stellar mass black hole being greater than the Universe's age. For small, higher temperature black holes however, the evaporation can be dramatic, accelerating until the object vanishes completely in a γ-ray explosion (Hawking, 1974). Therefore, low mass PBHs are expected to emit an observable flux of x-rays and γ-rays. Fig. 1.2's INTEGRAL constraint corresponds to limits on the x-ray flux from evaporation of PBHs in the centre of the Milky Way as observed by the INTEGRAL satellite observatory (Laha et al., 2020). The EGRB constraint corresponds to the extragalactic γ-ray background that PBH evaporation would emit and the dissociative effect it would have on light element formation during big-bang nucleosynthesis (Carr et al., 2010). Finally, the Voyager limits in Fig. 1.2 come from constraints on the electron and positron flux expected from PBH

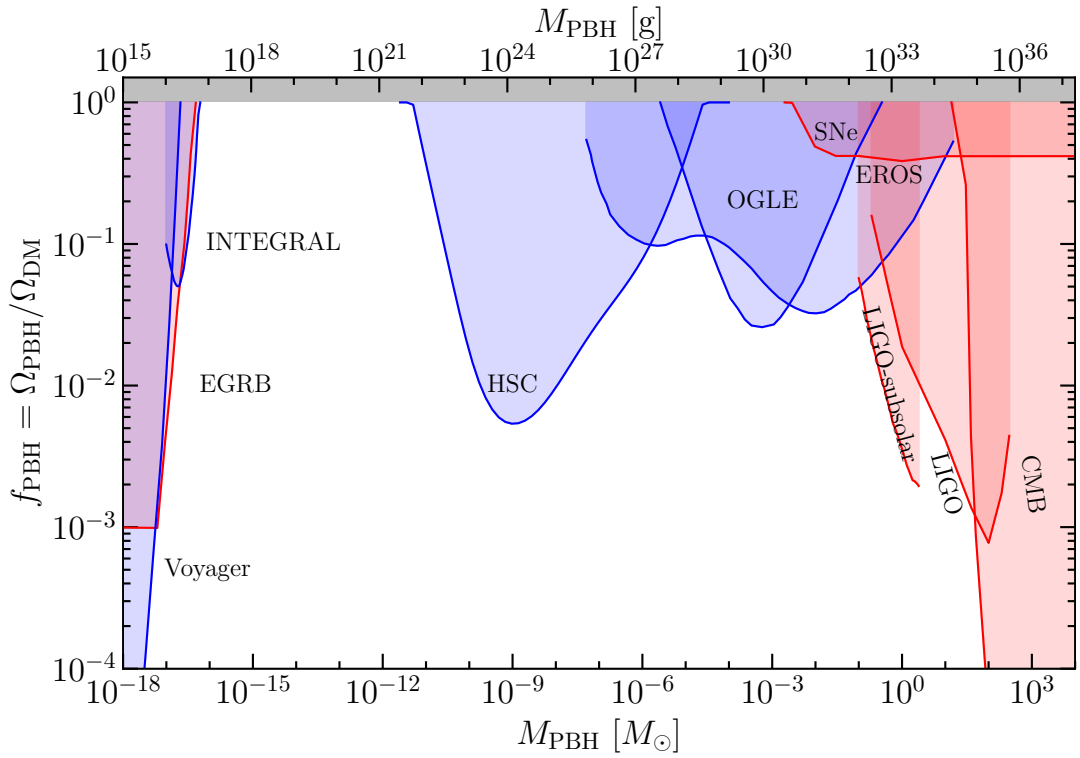

Figure 1.2: PBH mass constraint diagram. The fraction of dark matter comprised of monochromatic mass distribution of PBHs of mass $M_{\rm PBH}$. Shaded regions represent areas of the parameter space currently ruled out by observations. Blue shaded regions are excluded by observations in or local to the Milky Way. Conversely, red shaded regions are excluded by observations which sample a cosmological volume of our Universe. INTEGRAL, EGRB and Voyager are related to the evaporation of low mass PBHs; HSC, OGLE EROS and SNe are derived from gravitational lensing phenomena; LIGO constraints come from observations of gravitational waves and CMB from the expected effect of PBH accretion on the CMB signal. This plot was made using code from the github repo https://github.com/bradkav/PBHbounds (Kavanagh, 2019, and references therein). For an extended version of this plot see Carr & Kühnel (2020)

.

evaporation in the Milky Way that can only be observed now that the Voyager 1 probe is no longer shielded by the Sun's magnetic field (Boudaud & Cirelli, 2019). The probes I consider within this thesis primarily constrain the range of stellar mass black holes $0.1\,M_\odot \lesssim M_L \lesssim 100\,M_\odot$, however in §6 we also consider novel methods that may allow much smaller and larger scales to be investigated simultaneously.

As we shall detail further in §2 gravitational fields can cause the deflection of incident light in a phenomenon known as gravitational lensing. This lensing can result in the magnification of background sources through the focusing caused by the lens. Stronger gravitational fields cause greater deflections and therefore compact objects such as PBHs can effect large magnifications. If a significant fraction of dark matter in our Galaxy is comprised of PBHs then we expect to observe background stars undergoing short periods of increased brightness due to magnification from intervening PBHs passing through the line of sight. The MACHO, EROS, OGLE and HSC constraints are derived from long term observational projects to monitor the variability of millions of stars to look for magnification from compact dark matter such as PBHs. The mass range constrained by each experiment corresponds to the variability time scales which it was sensitive to, with larger mass lenses causing longer timescale lensing variability (Tisserand et al., 2007). MACHO and EROS limits come from observations of the Magellanic clouds (Bennett, 1993; Tisserand et al., 2007), OGLE also observes stars in the Galactic bulge (Niikura et al., 2019), and lastly HSC observes the stars of our nearest neighbour, the Andromeda galaxy (Croon et al., 2020). While thousands of magnification events have been observed, Fig. 1.2 shows that together these experiments place tight constraints on the fraction of nearby dark matter that can be comprised of PBHs in the lunar to stellar mass range. The abundance of stellar mass PBHs is also constrained over cosmological volumes by observations of type 1a supernovae (Zumalacárregui & Seljak, 2018). Dark matter concentrated in clumps such as PBHs on stellar mass scales would result in a distribution of

magnifications and therefore inferred energies that is not observed in the narrow, standard candle distribution of SNe Ia energies, resulting in the limits on PBH abundance seen in Fig. 1.2.

Constraints on larger mass PBHs on the right hand side of Fig. 1.2 come from signals associated with the accretion and merging of PBHs. During the early Universe, shortly after their formation PBHs would begin to accrete matter from the surrounding Universe. This process generates high energy radiation which, after recombination, would ionise matter in the Universe which had cooled to neutrality. As detailed by Ricotti et al. (2008) this would have a measurable effect on the anisotropies and polarisation of the CMB, which are not observed, allowing limits to be placed on the abundance of high mass PBHs (Serpico et al., 2020).

In the Universe today we would expect the mutual gravitational attraction between PBHs to cause merger events. The changing quadrupole moment associated with the non-circularly symmetric mass distribution of the merging system causes the emission of gravitational waves (Thorne, 1980) as observed by LIGO (LIGO Scientific Collaboration and Virgo Collaboration et al., 2016). The observation of several merger events in the stellar mass regime initially caused significant interest in the possibility of PBHs in this mass range, however the rate of merger events restricts any associated PBH distribution from comprising a majority of dark matter as seen in Fig. 1.2 (Kavanagh et al., 2018; Nitz & Wang, 2022).

As seen in Fig. 1.2 there are broad areas of the PBH parameter space that remain either completely unconstrained or only probed in the nearby Universe. This thesis aims to contribute to constraints on sub-stellar mass PBHs by making use of the lensing effect they would introduce into observations of extragalactic transients such as FRBs and GRBs. These would sample a cosmological volume and so would be complementary to current lensing constraints. In the following section we will introduce these extragalactic fast transients.

Chapter 2

Propagation Effects

As light propagates through the Universe its speed and direction are affected by the matter it travels through. To understand these effects there are two important properties of light to consider, namely, group and phase velocities. The group velocity (v_G) denotes the speed of the light, which will be less than c in a non-vacuum environment. The group velocity is given by the partial derivative of the wave's angular frequency (ω) with respect to its angular wavenumber (k)

$$v_G = \frac{\partial \omega}{\partial k}. \tag{2.1}$$

Whereas, the phase velocity v_p denotes the speed with which a crest or trough propagates within the envelope of the light. Generally, v_p may be greater than, less than or even in the reverse direction to the light's group velocity and is defined as

$$v_p = \frac{\omega}{k}. \tag{2.2}$$

The phase velocity is crucial to understanding the direction of light propagation as all waves propagate perpendicular to their surface of constant phase. The refractive index of light may therefore be defined as

$$n = \frac{c}{v_p}. \tag{2.3}$$

In the following sections we shall use the above properties of light to introduce various propagation effects likely to be encountered by astrophysical sources.

2.1 Dispersion

Cold plasma is a typical form of matter encountered by light propagating through the Universe. A characteristic property of any plasma is its plasma frequency

$$\frac{\omega_p}{2\pi} = \nu_p = \sqrt{\frac{n_e e^2}{4\pi^2 m_e \varepsilon_0}}, \tag{2.4}$$

where n_e is the density of free electrons within the plasma, e is the charge of an electron, m_e is the rest mass of an electron and ε_0 is the permittivity of free space. From the plasma frequency the refractive index of a cold plasma can be calculated as (Bellan, 2006)

$$n(\omega) = \sqrt{1 - \left(\frac{\omega_p}{\omega}\right)^2}, \tag{2.5}$$

If a plane wave of light is normally incident upon a homogeneous cold plasma the change in refractive index will not deflect the incident wave. However, because the refractive index also changes as a function of the incident light's frequency (i.e. cold plasma is dispersive) it will have an effect on the group velocity. By expressing the wavenumber in terms of the refractive index and partially differentiating by the angular frequency, the group velocity may be generally expressed in terms of the refractive index as

$$v_G = \frac{\partial \omega}{\partial k} = \frac{c}{n(\omega) + \omega \frac{\partial n(\omega)}{\partial \omega}}. \tag{2.6}$$

Substituting Eq. 2.5 and evaluating the group velocity reveals that for a cold plasma Eq. 2.3 holds in terms of the group velocity as well with $v_G = cn$. Using

this relation, and assuming that $\omega_p \ll \omega$[1] the time delay at frequency ω due to cold plasma dispersion, with respect to propagation in a vacuum, can be calculated as

$$t_d = \frac{e^2}{2c\varepsilon_0 m_e \omega^2} \mathrm{DM}, \tag{2.7}$$

where DM is the dispersion measure, representing the integrated column density of free electrons along the length of the bursts path of propagation (ℓ) (Lorimer, 2005)

$$\mathrm{DM} \equiv \int_0^\ell n_e d\ell. \tag{2.8}$$

For a delta function pulse this time delay manifests as a quadratic sweep in arrival time with frequency, with lower frequencies of the signal arriving later than high frequencies as seen in Fig. 2.1 which shows the recorded spectrum as a function of time (dynamic spectrum) of the Lorimer burst (Lorimer et al., 2007).

The absolute time delays calculated by Eq. 2.7 are of little use to interpretting observations such as Fig. 2.1, as they are relative to the arrival time of the same signal in a vacuum, which cannot be observed. The quantity which can be measured is the difference in time delay between two observed frequencies (ν_{Lo} and ν_{Hi}) given by

$$\left(\frac{\Delta t_d}{\mathrm{ms}}\right) \approx 4.149 \left(\frac{\mathrm{DM}}{\mathrm{pc\,cm^{-3}}}\right) \left[\left(\frac{\nu_{\mathrm{Lo}}}{\mathrm{GHz}}\right)^{-2} - \left(\frac{\nu_{\mathrm{Hi}}}{\mathrm{GHz}}\right)^{-2}\right], \tag{2.9}$$

where the constants have been simplified for convenience. High frequencies such as optical and X-ray have negligible delays due to dispersion, whereas at radio frequencies the time delay becomes large enough to be observed. Short pulse radio signals such as pulsars and FRBs always show obvious dispersion due to the width of their intrinsic pulses being much shorter than the typical dispersion time delays. By measuring the time delay between two observed frequencies the

[1]Mean electron density in the Milky Way Galactic is $\langle n_e \rangle = 0.03\mathrm{cm}^{-3}$ (Davidson & Terzian, 1969), yielding $\omega_p/2\pi = \nu_p \approx 1.5$kHz, much less than typical radio observing frequencies $\omega/2\pi = \nu \sim$GHz.

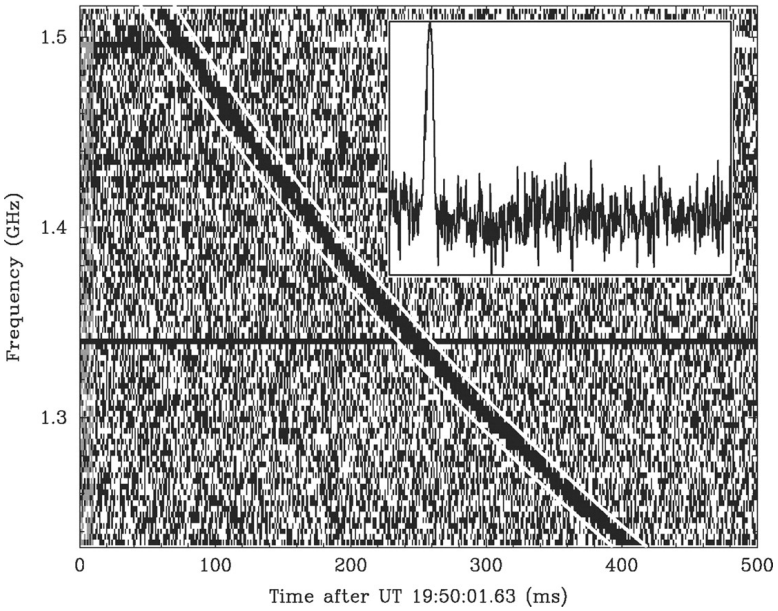

Figure 2.1: Taken from Lorimer et al. (2007): Dynamic spectrum of the first detected FRB, known as the Lorimer burst. The burst shows a quadratic sweep in arrival time characteristic of cold plasma dispersion.The measured DM= $375 \pm 1\,\mathrm{pc\,cm^{-3}}$. Accounting for the dispersion the burst has an approximately 15ms width with intensity concentrated in a single peak as shown in the inset plot.

DM of a burst and therefore the integrated column density of electrons along that line of sight can be determined. For the case of pulsars, which have been observed across the Galactic plane, their dispersion measures can be used to reconstruct an electron density profile for the Milky Way. This has been done by Cordes & Lazio (2003) and more recently Yao et al. (2017) to develop the NE2001 and YMW16 Galactic electron density models respectively. The NE2001 distribution depicted in Fig. 2.2 shows that the Galactic distribution of electrons is concentrated at low latitudes in the disk of the Milky Way with a slightly elevated density in the spiral arms as expected. These general results are consistent with YMW16.

2.2 Multi-path Propagation

A more realistic scenario for light propagation will be that of a plane wave incident upon an inhomogeneous medium with a refractive index that changes across its

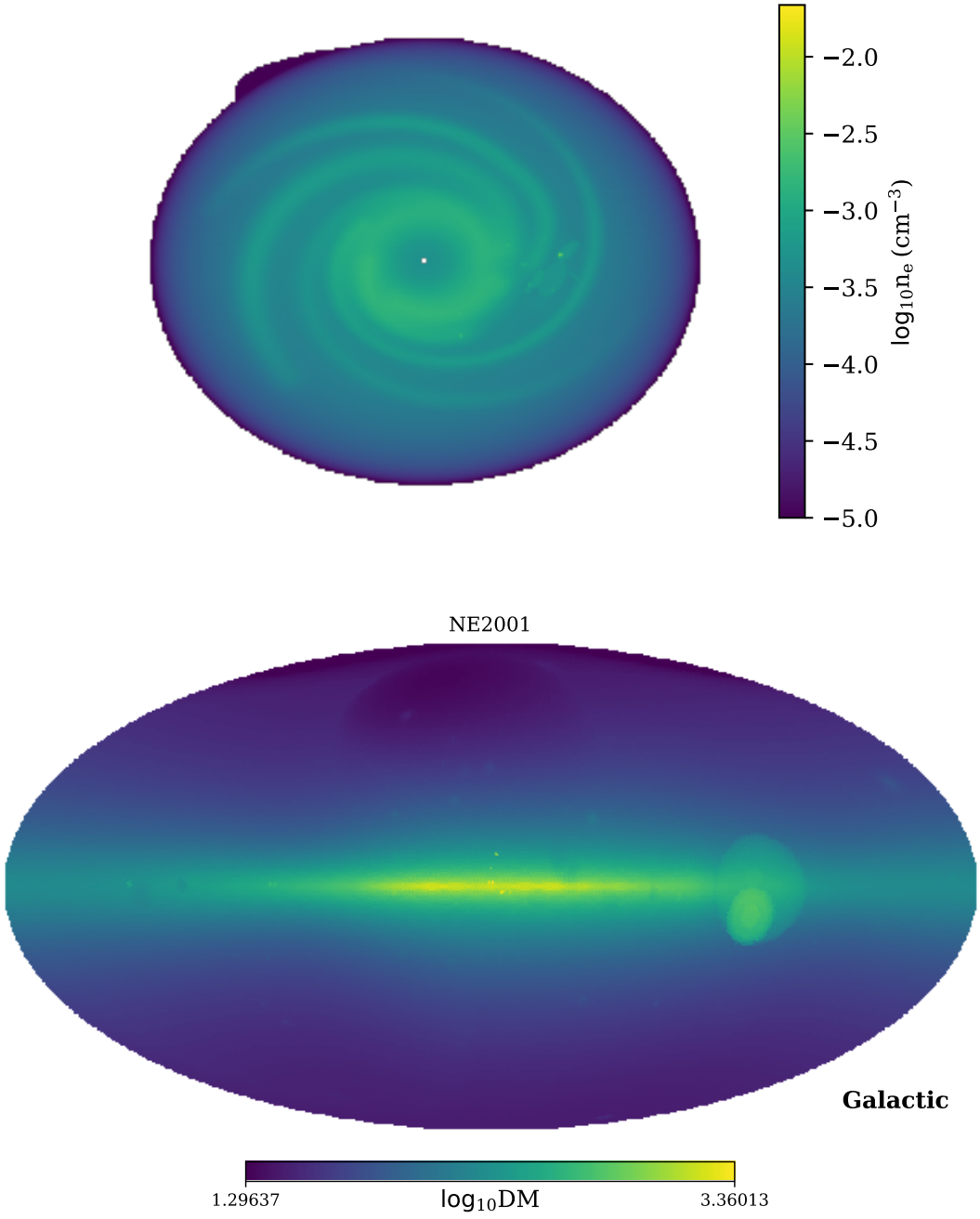

Figure 2.2: *Top:* NE2001 Galactic electron distribution modelled by Cordes & Lazio (2003) from pulsar dispersion measures plotted across the spatial extent of the Galaxy. *Bottom:* Associated DM of the NE2001 distribution integrated over the complete extent of the Galaxy as observed from Earth, plotted across a mollwide projection of Galactic coordinates.

volume. However, modelling light propagation through an extended, inhomogeneous three dimensional medium is difficult. To make the problem more tractable extended media are often approximated as a thin screen with changes in phase velocity integrated over the line of sight to yield a total phase contribution from the medium at each point across the screen. This predicts the true propagation behaviour well when the thickness of the extended medium is much less than the distance between the source and the observer, e.g. nebulae intervening an interstellar source or a galaxy intervening an extragalactic source.

For plane waves from a point source incident upon a thin phase changing screen with amplitude described by $u(D_d; \vec{x})$, the resulting amplitude in the plane of the observer $u(\vec{X})$ can be calculated from the Fresnel-Kirchhoff integral as (Born & Wolf, 2013)

$$u(\vec{X}) = \frac{-i}{2\pi r_F^2} \int\int d^2\vec{x}\, u(D_d; \vec{x}) \exp\left[\frac{i(\vec{x}-\vec{X})^2}{2r_F^2} + i\phi(\vec{x})\right], \tag{2.10}$$

where $\phi(\vec{x})$ is the phase change caused by the screen at point $\vec{x}$ on the screen and $\vec{X}$ is the coordinate vector of the observer in the observers plane separated by D_d from the screen as shown in Fig. 2.3. r_F is the Fresnel scale given by

$$r_F = \sqrt{\frac{\lambda D_d D_{ds}}{2\pi D_s}} = \sqrt{\frac{D_{\text{eff}}}{k}}, \tag{2.11}$$

where λ is the wavelength of the incident light, D_s is the distance to the source from the observer, and D_{ds} is the distance to the source from the screen. For convenience the ratio of these distances is labelled the effective distance (D_{eff}). Formally the source must be at $D_s = \infty$ for the incident wave to be truly planar, however given the large distances of interstellar and intergalactic sources we assume that wave incident upon the screen is approximated well by a plane wave.

The integrand of Eq. 2.10 oscillates rapidly making analytical evaluation difficult[2]. The stationary phase approximation however indicates that the integral

[2]The recent application of Picard-Lefschetz theory to the Fresnel-Kirchhoff integral has made

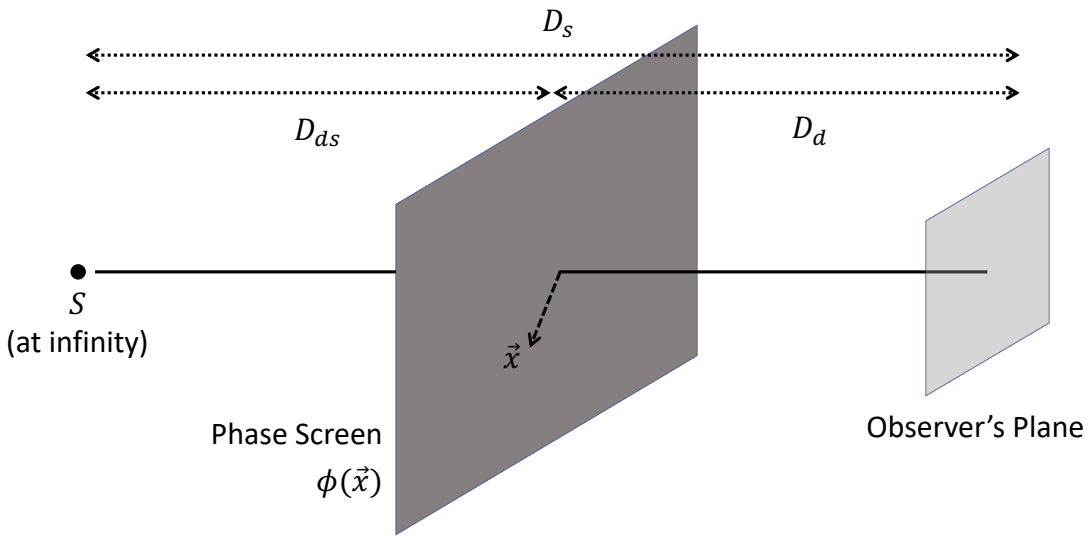

Figure 2.3: Geometry of the thin screen approximation.

will be dominated by points satisfying (Courant et al., 1924)

$$0 = \nabla_{\vec{x}} \left[\frac{(\vec{x} - \vec{X})^2}{2r_F^2} + \phi(\vec{x}) \right]. \tag{2.12}$$

At each of these points an image of the source will be observed. In the limit of geometric optics, where the interference between waves is not considered, these points of stationary phase are rays of light contributing to the total observed intensity. This is analogous to Fermat's principle that the path taken by a ray between two points must be a local extremum in traversal time. In wave optics each point of stationary phase contributes coherently to the incident wavefront, with all other points oscillating in phase rapidly enough to cancel out their contribution to the integral in Eq. 2.10.

By plotting the surface of constant phase of the incident plane wave we can visualise the effect the screen has on the light's propagation. We can do this simply by plotting the geometric and screen phase contributions within the square brackets of Eq. 2.12. The simple case of a homogeneous medium, i.e. $\phi(\vec{x}) = \phi_0$

progress in this area (Feldbrugge et al., 2019).

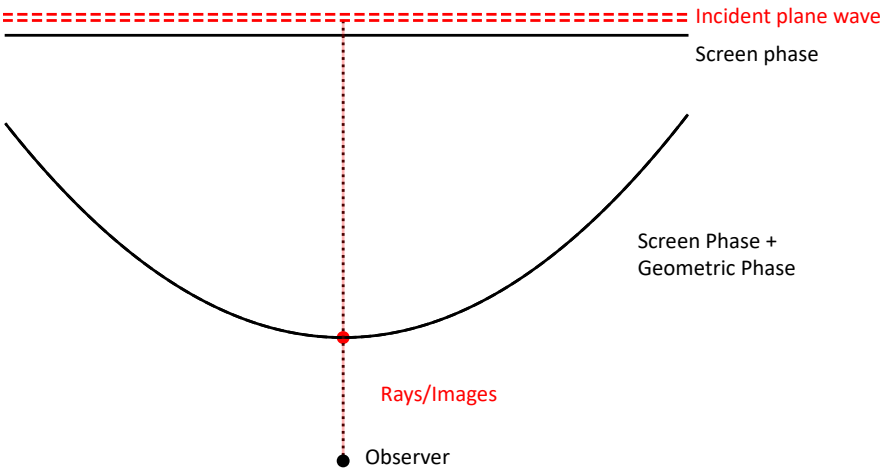

Figure 2.4: Propagation of light through a thin phase changing screen with a constant phase contribution ϕ_0. The red dotted line depicts a plane wave from a point source incident upon the thin screen marked in black. The solid black lines depict phase contributions from the screen and the surface of constant phase containing both the geometric and screen phase contributions. Following Eq. 2.12 images of the source (shown as a red ray) are observed along lines of sight where the surface of constant phase has a gradient of zero (shown as red dots).

is plotted in Fig. 2.4. In this case the solution to Eq. 2.12 occurs at $\vec{x} = \vec{X}$, i.e. the observer sees one image of the source along the optic axis as shown in Fig. 2.4.

If we neglect the phase contributions from the screen entirely we can see that as $|\vec{x} - \vec{X}|$ becomes comparable to the Fresnel scale the exponential term in Eq. 2.10 will begin to vary quickly and suppress the value of the integral. An observation of the source in vacuo is therefore dominated by light from within r_F of the optic axis, known as the first Fresnel zone. Physically the first Fresnel zone defines the region within which singularly deflected light paths have a geometric phase delay less than 1 radian and therefore will add constructively to the observed wave. The oscillatory nature of constructive and destructive interference means that there are also higher order Fresnel zones which we shall not consider here.

Conversely, if the phase screen $\phi(\vec{x})$ is inhomogeneous then there is a wide variety of possible propagation behaviours. In the following sections we shall review the cases of a turbulent plasma and a compact gravitational lens.

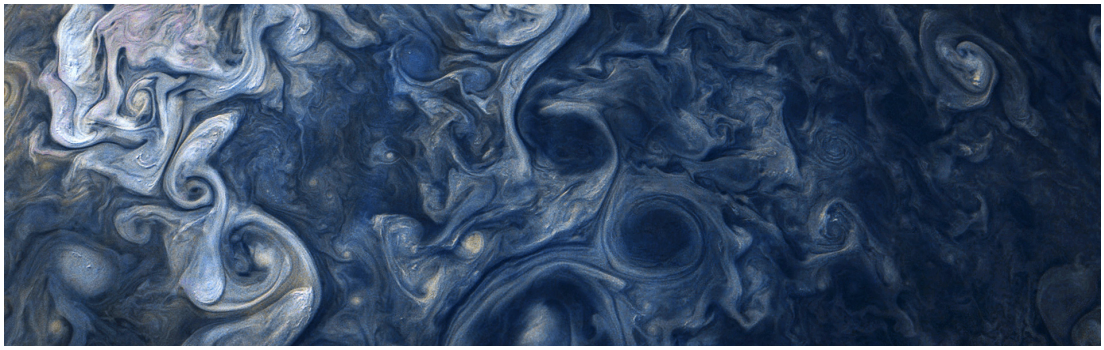

Figure 2.5: Turbulence in the upper atmosphere of Jupiter, as imaged by the NASA's Juno spacecraft (Enhanced Image by Gerald Eichstädt and Sean Doran (CC BY-NC-SA) based on images provided courtesy of NASA/JPL-Caltech/SwRI/MSSS).

2.2.1 Turbulent Media

Turbulence is a common phenomenon in fluids, where a cascade of energy causes self similar behaviour over a vast range of scales (Richardson, 1922). A striking case of this can be seen in Fig. 2.5 which shows vortices in clouds of Jupiter. In this case, energy input from the Sun and Jupiter's rotation drives large scale eddies that gradually break into successively smaller scale eddies until eventually the energy is dissipated as heat. Continuous input of energy into the system then results in eddies over all possible scales being present simultaneously as seen in Fig. 2.5. We expect turbulent flows similar to the Jovian case to occur throughout the Universe, including in the interstellar and intergalactic mediums as well as Earth's own atmosphere. Therefore the effect of a turbulent medium on signal propagation represents an important case study.

By assuming that the turbulence is homogeneous, i.e. that its statistics are spatially invariant we can derive the spectral index of its spatial power spectrum from a dimensional argument. Beginning with a power law form in accordance with the scale invariance of the eddies, the energy density per cubic wavenumber (E) can be expressed as

$$E(k, \psi) = Ck^{\alpha}\psi^{\beta}, \tag{2.13}$$

where C is some constant and ψ is the rate of energy dissipation. Considering

only their temporal (T) and spatial dimensions (L), each of these components can be decomposed as follows

$$k \propto \frac{1}{L} \qquad E \propto \frac{L^5}{T^2} \qquad \psi \propto \frac{L^2}{T^3}. \tag{2.14}$$

Substituting these into the initial form yields

$$\frac{L^5}{T^2} = L^{-\alpha} \left(\frac{L^2}{T^3} \right)^{\beta}, \tag{2.15}$$

from which we can solve for $\beta = 2/3$ and $\alpha = -11/3$. Because the kinetic energy of the turbulence drives the density fluctuations in the medium, α also corresponds to the power spectrum of density fluctuations. Therefore, ideal, spatially homogeneous turbulence can be characterised by a density power spectrum with $\alpha = -11/3$, known as Kolmogorov turbulence (Hallbäck et al., 1996). Typically the power law is bounded by an inner and outer scale corresponding to the minimum and maximum size of the eddies. The largest eddies occur on the scale at which energy is injected into the fluid to drive turbulence. Whereas, the smallest eddies occur on the scale where energy is dissipated as heat.

Within the Milky Way density fluctuations in the interstellar medium (ISM) are broadly consistent with a Kolmogorov spectrum, with observations over nearly twelve orders of magnitude in scale from 10^7 m to 100 pc showing a spectral index $\alpha = -11/3$ (Armstrong et al., 1981; Chepurnov & Lazarian, 2010). In detail however, the ISM often contains significantly more structure than purely homogeneous turbulence. Examples of this can be found in studies such as Rickett et al. (1997), Stinebring (2007), Oosterloo et al. (2020), Wang et al. (2021) and Main et al. (2022) which show evidence for anomalous plasma, filamentary structures and statistically anisotropic densities in the ISM. The extent of these complexities within the ISM is not fully understood, however a Kolmogorov turbulence model of density fluctuations serves as a useful fiducial model.

Using a Kolmogorov spectrum to model the density fluctuations in a cold

plasma we can determine the corresponding phase fluctuations ($\Delta\phi(\vec{x})$) in its thin screen approximation. Assuming that the true medium has a relatively constant thickness, the difference in phase contribution between two points on a turbulent phase screen will be proportional to their difference in phase velocity. The phase velocity will be inversely proportional to the refractive index at each point (as per Eq. 2.3), which, for a cold plasma is given by Eq. 2.5. Assuming once more that the plasma frequency is much less than the observing frequency, the inverse of the refractive index can be Taylor expanded to $1/n(\omega) \approx 1 + (\omega_p/\omega)^2/2$. Following from this and Eq. 2.4, the difference in phase velocity between two points on the screen, $\vec{x_1}$ and $\vec{x_2}$ is given by

$$\Delta v_p(\vec{x_1}, \vec{x_2}) = \frac{ce^2}{2\omega^2 m_e \varepsilon_0} \left[n_e(\vec{x_2}) - n_e(\vec{x_1})\right] \tag{2.16}$$

where $n_e(\vec{x})$ is the electron density in the medium at a point $\vec{x}$. The difference in phase contribution between two points separated by $\vec{r} = \vec{x_2} - \vec{x_1}$, is then proportional to the difference in electron density between those two points $\Delta\phi(\vec{r}) \propto \Delta n_e(\vec{r})$. Therefore, the phase fluctuations from a turbulent, cold plasma medium with a Kolmogorov density power spectrum will follow

$$\Delta\phi(\vec{r}) \propto r^{11/3} \tag{2.17}$$

where r is the scalar magnitude of $\vec{r}$. Normalising this relation and taking the second order moment yields the phase structure function, describing the variance of screen phase as a function of separation (Narayan, 1992)

$$D_\phi(\vec{r}) = \left\langle \left[\phi(\vec{r'} + \vec{r}) - \phi(\vec{r'})\right]^2 \right\rangle = \left(\frac{r}{r_{\text{diff}}}\right)^{\beta-2}, \tag{2.18}$$

where $\beta = 11/3$ for Kolmogorov turbulence, the angular brackets denote the ensemble average over all potential instances of the screen and the diffractive scale (r_{diff}), is the scale over which the root-mean-square (RMS) phase difference

is one radian.

The ratio of the diffractive scale to the Fresnel scale further characterises the effect of the screen on light propagation. When $r_{\rm diff} \gg r_F$, Eq. 2.18 yields $D_\phi(r_F) \ll 1$, indicating that the random phase fluctuations over the Fresnel scale will be small. In this regime, known as weak scattering, an observation will be approximately the same as the homogeneous case. Weak perturbations in phase however, will cause small variations in observed intensity. For further discussion on the behaviours of weak scattering see Narayan (1992).

When $r_{\rm diff} \ll r_F$, Eq. 2.18 yields $D_\phi(r_F) \gg 1$ indicating that phase fluctuations from turbulence will dominate over path length variations on the Fresnel scale. The position of points of stationary phase on the constant phase surface described in Eq. 2.12 will therefore be dominated by the turbulent phase fluctuations. Because the properties of the turbulence do not depend on the position on the screen (i.e. the turbulence is statistically homogeneous) the constant phase surface will contain a large randomly fluctuating component across its extent as seen in Fig. 2.6. The screen will therefore have many points of stationary phase across its surface where the phase surface gradient is randomly zero, as displayed by the red rays in Fig. 2.6.

Previously, the size of a patch on the screen contributing coherently to the observed intensity was limited by geometric path length variations on the Fresnel scale. However, when $r_{\rm diff} \ll r_F$ the phase fluctuations from turbulence will begin to suppress the integral in Eq. 2.10 on much smaller scales. Following from this, r_F ceases to be relevant in the strong scattering regime, with the size of a coherent patch instead set by $r_{\rm diff}$.

As in single slit diffraction, each coherent patch scatters radiation into a diffraction cone with an angle $\theta_{\rm scatt} \sim \lambda / r_{\rm diff}$, where $r_{\rm diff}$ is analogous to the slit's width. An observer then sees radiation from all points of stationary phase within a $\theta_{\rm scatt}$ sized cone projected back onto the screen. For a point source this results in the image being scatter broadened by $\theta_{\rm scatt}$. Furthermore, contributions from

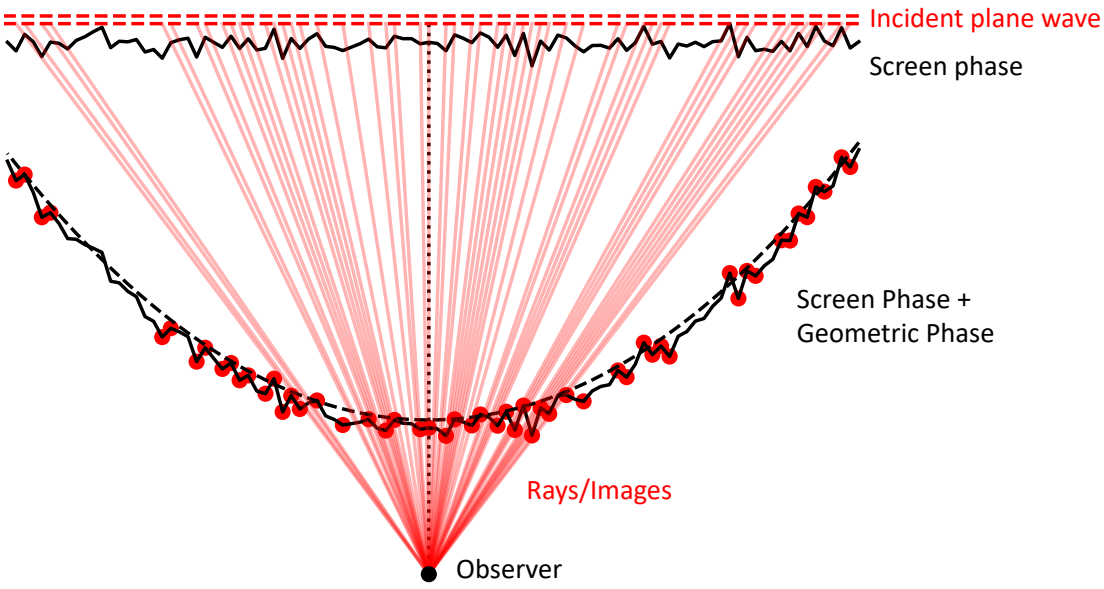

Figure 2.6: Propagation of light through a thin phase changing screen as described in Fig. 2.4, but with a turbulent phase contribution resulting in multi-path propagation.

points of stationary phase further from the optic axis will have a greater path length and therefore the signal will arrive distributed in time. For time varying signals the observed temporal profile will be the intrinsic profile convolved with the impulse response function of the medium. For a two-dimensional screen with a square law phase structure function the impulse response is an exponential profile characterised by the scattering time (Macquart & Koay, 2013)

$$t_{\rm scatt} = \frac{D_{\rm eff}\theta^2_{\rm scatt}}{c} = \frac{1}{ck}\frac{r_F^2}{r^2_{\rm diff}}. \tag{2.19}$$

This temporal smearing from multi-path scattering by a turbulent cold plasma can be seen in Fig. 2.7 which depicts the frequency averaged profile of FRB 20210320. The FRB has a sharp rise time followed by the characteristic exponential decay with $t_{\rm scatt} = 0.233\,$ms as per the best fit model shown in blue. In this case the scattering is likely caused by the ISM in the FRB host galaxy as we explore further in §7.

In the case of pulsars, the thickness of the turbulent ISM is comparable to

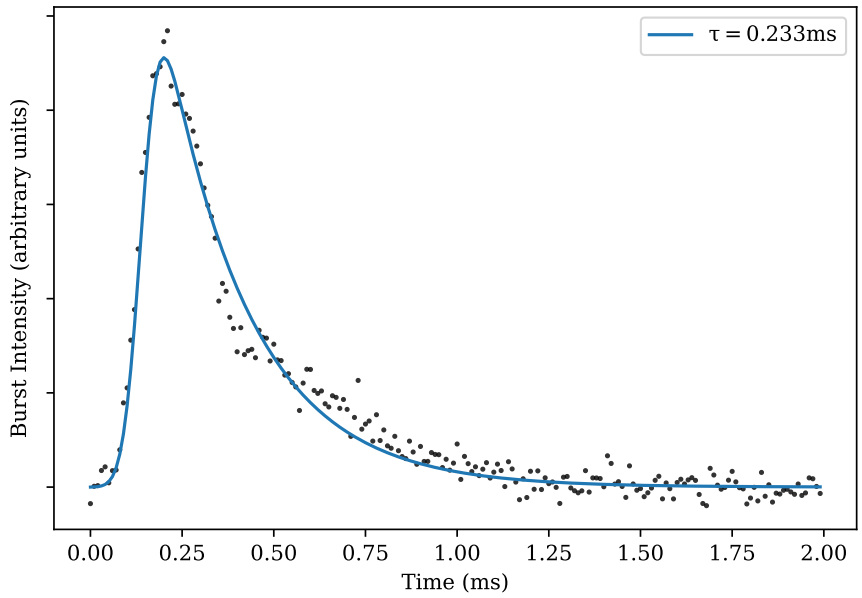

Figure 2.7: Frequency averaged profile of FRB 20210320 shown as black dots as a function of arrival time. Best fit pulse profile shown in blue, modelled as an intrinsic Gaussian convolved with the exponential profile of diffractive scattering at $t_{\rm scatt} = 0.233\,{\rm ms}$.

the distance between the observer and source, violating our assumption of a thin screen. As seen in Eq. 2.19 however, the scattering time ($t_{\rm scatt}$) depends upon $D_{\rm eff}$. The effective distance is maximised halfway between the observer and the source. Following from this, for a statistically uniform medium, the observed scattering time will be dominated by scattering occurring within a relatively small section of the screen at the midpoint. By approximating the extended scattering medium as a thin screen halfway between the observer and source we can still accurately model the scattering effect with a thin screen model.

The phases at each point of stationary phase are effectively uncorrelated from one another. An observer will therefore see a random interference pattern made from the superposition of all contributing points just as in Young's famous double slit experiment. Both the interference pattern, as well as the underlying phase contributions from the plasma are frequency dependent. Over large bandwidths this leads to a pseudo-random frequency modulation of the burst as seen in Fig. 2.8, referred to as scintillation. The bright parts of the modulation, known as

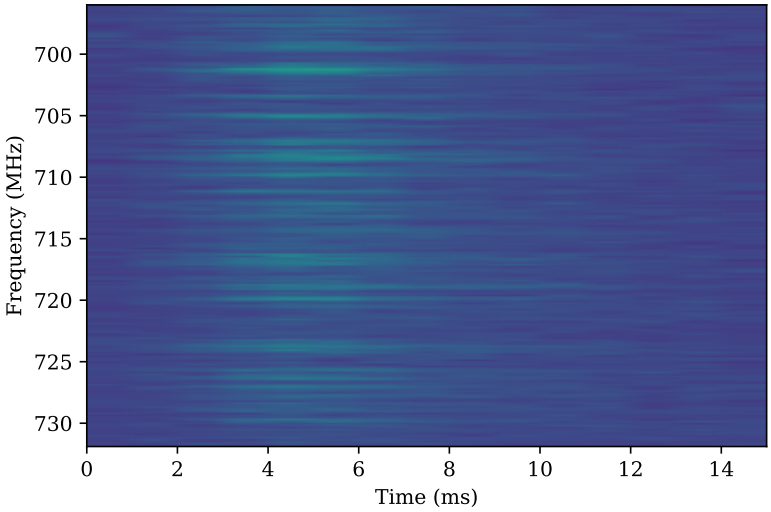

Figure 2.8: Dynamic spectrum of FRB 20201124a.1 showing frequency modulation consistent with diffractive scintillation with a decorrelation bandwidth $\nu_{\rm DC} \sim 0.15\,{\rm MHz}$.

scintles, will be correlated in intensity over a small range in frequency known as the decorrelation bandwidth $\nu_{\rm DC}$. The fractional decorrelation bandwidth is then related to the screen properties through (Narayan, 1992)

$$\frac{\delta\nu_{\rm DC}}{\nu} \approx \left(\frac{r_{\rm diff}}{r_F}\right)^2, \tag{2.20}$$

where for a thin screen and Kolmogorov turbulence the decorrelation bandwidth and scattering time form a Fourier pair as (Lambert & Rickett, 1999)

$$2\pi\nu_{\rm DC}t_{\rm scatt} \approx 1 \tag{2.21}$$

Similarly to a changing frequency, any relative motion between the observer and the screen will lead to intensity fluctuations in time as well. For continuous sources such as quasars (Macquart & Bruyn, 2006) these modulations can be observed simply in continued monitoring. However, in FRBs and pulsars these temporal modulations normally occur on much longer time scales than individual

bursts and so can only be observed by analysing changes over many repeat bursts (Bhat et al., 1999; Main et al., 2022). In both the temporal and spectral cases the modulation index of intensity fluctuations is one for a point source and decreases for extended emissions (Narayan, 1992).

In addition to diffractive scattering, clumps of plasma the size of the angular broadening scale $\sim D_d\theta_{\rm scatt}$ can result in strong refractive scattering (Narayan, 1992). By introducing a large scale phase change refractive scattering can cause focussing or defocussing of the scattered image and an offset of its mean position. Fig. 2.9 depicts this by showing two sets of scattering with and without a large scale change in phase. The addition of a plasma over-density[3], in this case offset from the optic axis, caused a magnification of the scattered image (i.e. more rays were seen by an observer) and deflected the mean position of the scattered image as seen by an observer. These behaviours can also be described as plasma lensing as discussed further in Clegg et al. (1998). In the following section we investigate a simpler case of lensing, without the effects of diffractive scintillation superimposed.

2.2.2 Gravitational Lensing

Similarly to plasma, gravity can also cause the deflection of incident light. This property was initially derived from Newtonian mechanics following the expected behaviour of a massive particle on a hyperbolic orbit (Soldner, 1804). In the limit where the deflection angle ($\hat{\alpha}$) is small, Newtonian mechanics predicts

$$\hat{\alpha}_{\rm N} = \frac{2GM}{c^2 r} \tag{2.22}$$

where G is the gravitational constant, M is the mass of the body causing the deflection and r is the impact parameter of the incident particle. Prior to the understanding that light was massless, Newtonian mechanics predicted that light

[3]As plasma causes the phase velocity of light to increase an over-density of plasma causes a negative phase delay as depicted in Fig. 2.9.

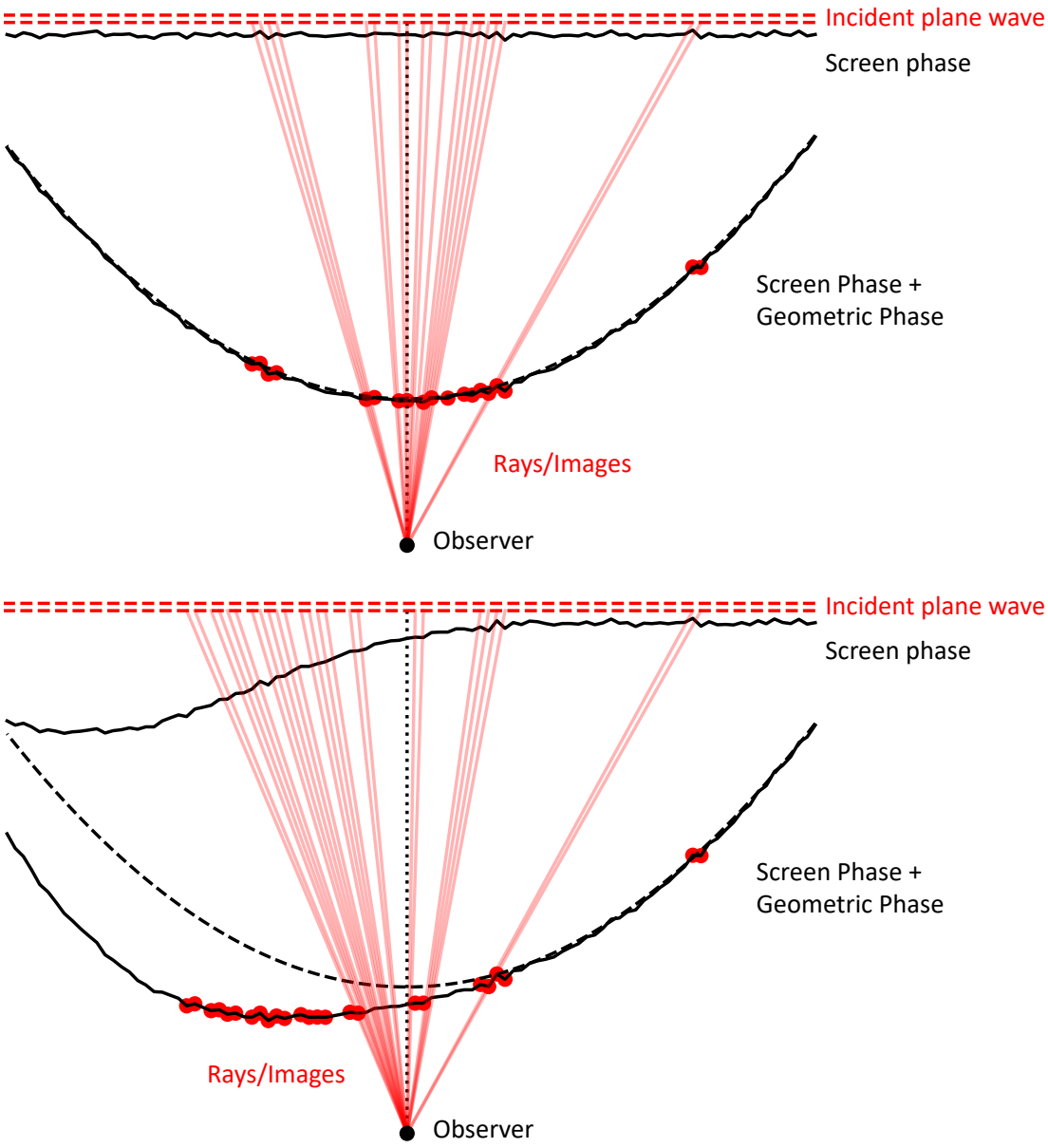

Figure 2.9: Visualisation of the effect of refractive scintillation from a large over-density of plasma. *Top:* Diffractive scintillation for the case of homogeneous turbulence. *Bottom*: Same turbulence as seen in *top* but with the addition of a large scale plasma over-density causing inhomogeneity on the angular broadening scale.

would be deflected by the same amount as it is independent of the mass of the incident particle.

Alternatively Einstein's theory of general relativity predicted a deflection angle of twice as much (Schneider et al., 1992)

$$\hat{\alpha} \approx \frac{4GM}{c^2 r}. \tag{2.23}$$

Early in the 20th century Dyson et al. (1920) measured the deflection angle of background stars during a solar eclipse as they were gravitationally lensed by the Sun. Their results agreed with the value predicted by general relativity, invalidating the simpler Newtonian predictions. In retrospect this result is unsurprising as photons have zero mass and hence are not acted upon by gravitational forces under Newtonian mechanics. Conversely in general relativity gravity can still affect massless particles.

In general relativity the deflection of light in a gravitational field is a natural result of the strong equivalence principle. The strong equivalence principle states that "*the outcome of any local experiment in a free falling reference frame is independent of the velocity of the frame and its location in space-time*". Where space-time is the four-dimensional manifold of the theory of relativity which combines the three spatial dimensions with the extra dimension of time to fully describe the past, present and future space of our Universe with one geometry (Kenyon, 1990). With this principle we can understand gravitational lensing with the following scenario.

Consider the two reference laboratories depicted in Fig. 2.10, one in the vacuum of space, far from all matter and the other free falling in Earth's gravitational field. In each a LASER is pointed horizontally across the room and the difference in height between its emission and impact point on the opposing wall is recorded. Under the strong equivalence principle observers within each laboratory necessarily record the same result of no height difference (the full lined images in Fig. 2.10). From the perspective of a third observer on the Earth's surface however,

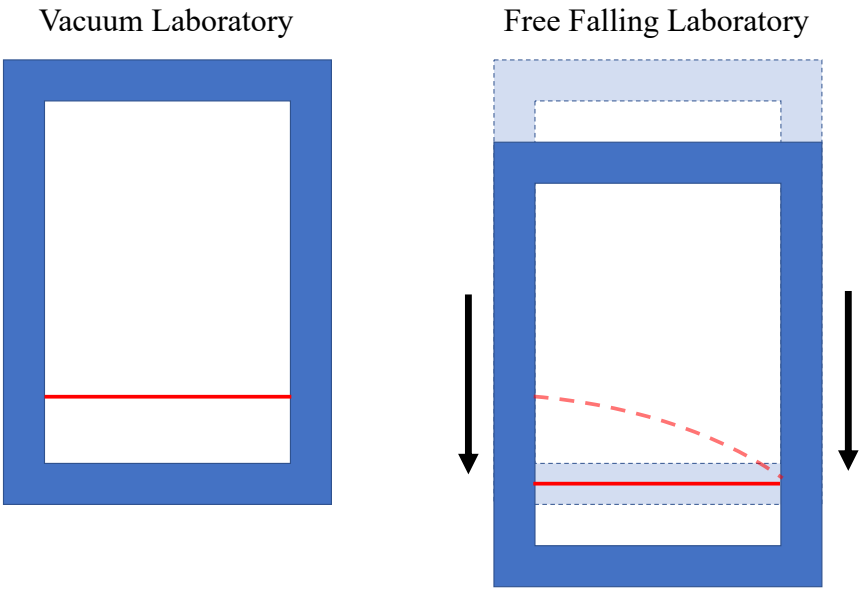

Figure 2.10: Diagram depicting the observed behaviour of a horizontal LASER (red line) in a vacuum and free falling in Earth's gravitational field respectively. Solid line images show the results observed from within each laboratory. Dashed line images show results as seen by an observer on the Earth's surface.

the falling laboratory has moved in the time it takes the light to cross the room. As the results observed from the Earth's surface and from within the free falling laboratory must be the same, the light must have fallen with the laboratory from the perspective of the Earth's surface. We can therefore conclude that light is deflected by gravitational fields as shown by the dashed line in Fig. 2.10.

A subtlety of the above scenario is that the apparent deflection of light in a gravitational field is a result of changing reference frames rather than an action on the light itself. This reflects the theory of general relativity's treatment of gravity as a purely geometric effect (Misner et al., 2018). Within general relativity mass causes the curvature of space-time. As above, a reference frame free-falling through the curvature will seem to be travelling in a locally straight line (Schneider et al., 1992). To an observer external to the masses curvature however, the free falling frame will appear to move under the influence of an apparent gravitational field. Light is no exception to this phenomena and will follow the space-time curvature defined by a mass. For regions where the space-time

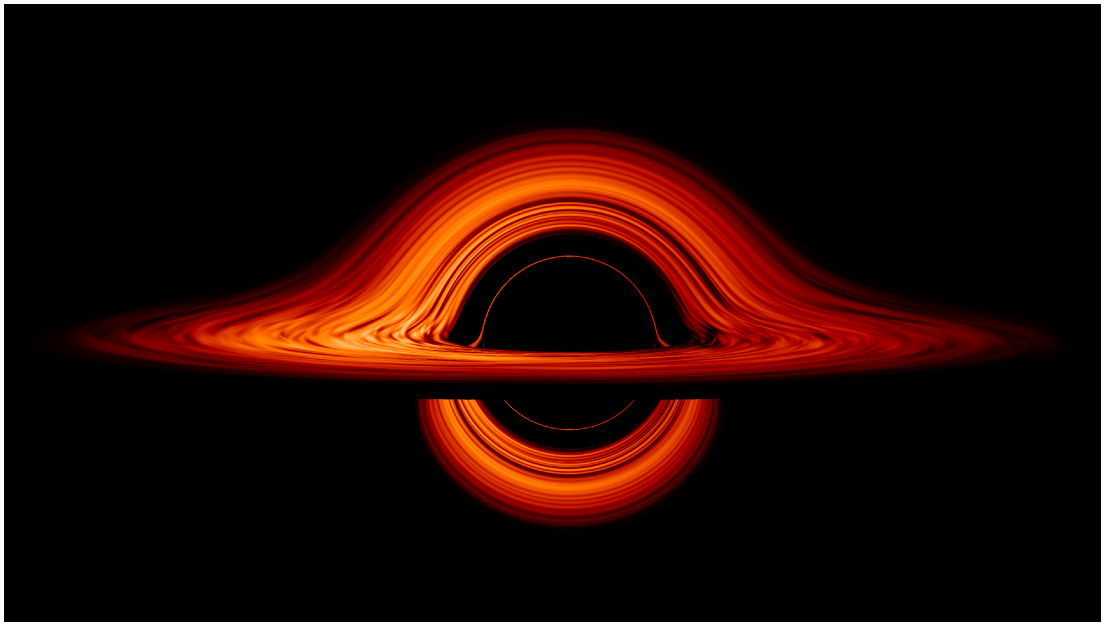

Figure 2.11: Edge on image of a black holes accretion disk simulated with a full three dimensional general relativistic treatment. Credit: NASA's Goddard Space Flight Center/Jeremy Schnittman.

curvature is extreme, such as near the event horizon of a black hole the path of light can become extremely warped as seen in observations of supermassive black holes by the Event Horizon telescope (Event Horizon Telescope Collaboration et al., 2019; The Event Horizon Telescope Collaboration, 2022). Fig. 2.11 shows an example of this in the simulated image of the accretion disk around a black hole. The simulation shows that both the top and bottom of the accretion disk are visible due to the drastic curvature induced around the black hole. In this case the propagation of light requires a fully relativistic treatment beyond the scope of this work (for further reading on visualising strong field light propagation see James et al., 2015). Instead we shall restrict ourselves to light paths well approximated by a single deflection. Below we shall expound upon the formalism used to treat gravitational lensing as presented in Schneider et al. (1992).

As previously, light propagation characterised by a single deflection along the line of sight can be modelled using a thin screen geometry. Fig. 2.12 depicts this

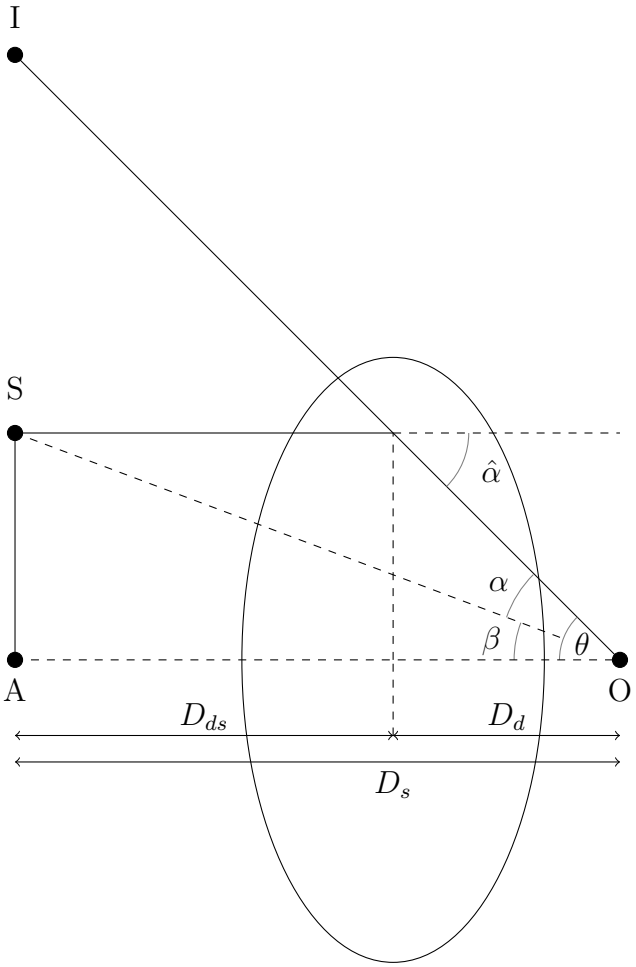

Figure 2.12: Diagram representing the thin screen lensing goemetry. **S** is the source, **O** the observer and **I** the image of the source seen by **O**. **AO** represents the optic axis which is perpendicular to both the source and lens planes, intersecting both at their respective origins.

geometry for the case of a gravitational lensing, from which we can infer

$$\theta D_s = \beta D_s + \hat{\alpha} D_{ds}, \tag{2.24}$$

where θ and β are respectively, the angles of the source and the image on sky. By defining a reduced deflection angle $\alpha = \hat{\alpha} D_{ds}/D_s$ we can then rearrange the above and generalise the expression to angular vectors to arrive at the lens equation

$$\vec{\alpha} = \vec{\theta} - \vec{\beta}, \tag{2.25}$$

which maps the background source plane onto the lens plane viewed by an observer.

This will approximate the true propagation behaviour well when the mass distribution is thin with respect to the D_s and the apparent gravitational potential[4] $|\Phi| \ll c^2$. In this weak field limit the deflection at the screen can be calculated as the gradient of the deflection potential

$$\vec{\nabla}_\theta \psi = \vec{\alpha}, \tag{2.26}$$

where ψ is the Newtonian gravitational potential projected onto the screen

$$\psi(\vec{\theta}) = \frac{D_{ds}}{D_d D_s} \frac{2}{c^2} \int \Phi(\vec{r}) d\ell. \tag{2.27}$$

For a non-rotating point mass potential this yields the deflection angle in Eq. 2.23 seen by Dyson et al. (1920). Unlike the case of a cold plasma in Eq. 2.5, the deflection angle due to gravity is independent of the frequency of incident light. Because gravitational lensing is achromatic it is typically modelled using geometric optics to allow the derivation of general results for all frequencies of light simultaneously. However, for wavelengths of light comparable to the Schwarschild radius of the lens ($R_s = 2GM/c^2$) diffraction effects will be significant and geometric optics will be inadequate to model the observed behaviour.

In general the observed behaviour of a point on the lens screen can be described under geometric optics using the Jacobian of the lens mapping which may be expressed as

$$A_{ij} = \frac{\partial \beta_i}{\partial \theta_j} = \delta_{ij} - \frac{\partial \alpha_i(\vec{\theta})}{\partial \theta_j} = \delta_{ij} - \frac{\partial^2 \psi(\vec{\theta})}{\partial \theta_i \partial \theta_j}, \tag{2.28}$$

where δ is the identity matrix and i and j denote matrix elements. This expression

[4] While there is no physical gravitational field in the theory of General Relativity the apparent field still provides a useful model.

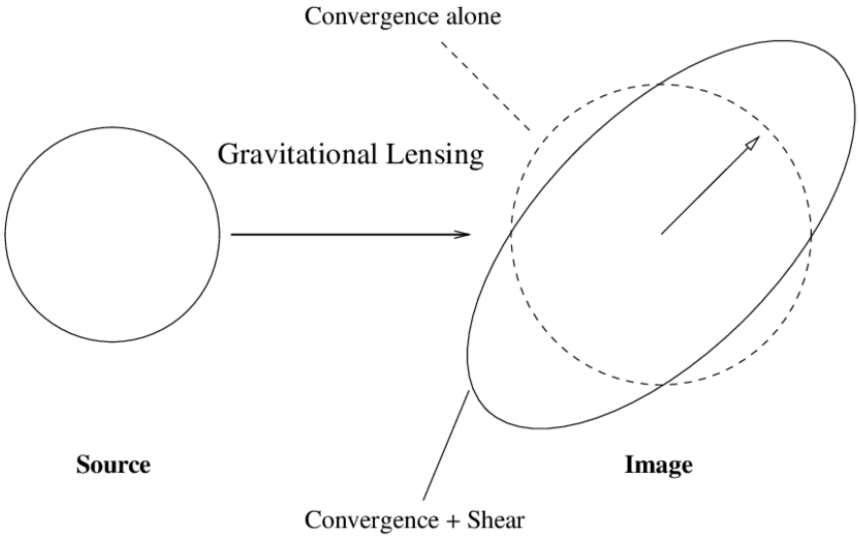

Figure 2.13: Illustration of the effects of convergence and shear on an image of a source adapted from Umetsu (2010).

can be simplified through the following definitions

$$\kappa = \frac{1}{2}\left(\psi_{11} + \psi_{22}\right) \tag{2.29}$$

$$\gamma_1(\vec{\theta}) = \frac{1}{2}(\psi_{11} - \psi_{22}) = \gamma(\vec{\theta})\cos\left[2\varphi(\vec{\theta})\right] \tag{2.30}$$

$$\gamma_2(\vec{\theta}) = \psi_{12} = \psi_{21} = \gamma(\vec{\theta})\sin\left[2\varphi(\vec{\theta})\right] \tag{2.31}$$

$$\tag{2.32}$$

where $\psi_{ij} = \partial^2\psi/\partial\theta_i\partial\theta_j$ and φ denotes the direction of $\vec{\alpha}$ with respect to the coordinate system. These definitions allow the Jacobian to be re-written as

$$A = \begin{bmatrix} 1-\kappa-\gamma_1 & -\gamma_2 \\ -\gamma_2 & 1-\kappa+\gamma_1 \end{bmatrix} \tag{2.33}$$

where κ is the convergence of the mapping and γ_1 and γ_2 are the components of the shear. Within a lensed image, convergence and shear cause different effects. Convergence alone causes a uniform magnification of the source image, whereas the addition of a shear component causes the image to be stretched into an ellipse, as visualised for a circular source in Fig. 2.13.

The exact magnification at any point on the lens plane can be calculated from the determinant of the Jacobian as

$$\mu = \frac{1}{\det(A)} = \frac{1}{(1-\kappa)^2 - \gamma^2}, \tag{2.34}$$

where physically, magnification comes from additional rays of light being focused into the observers line of sight that causes an increase in the observed intensity and apparent angular size of a source. From Eq. 2.34 we can see that formally the magnification will diverge to $\mu = \infty$ when $(1-\kappa)^2 = \gamma^2$. For the special case when $\gamma = 0$, infinite magnification will occur when $\kappa = 1$. From Eq. 2.29 the convergence can be derived from the Laplacian of the deflection potential. If we make the simplifying assumption of a circularly symmetric mass distribution creating a circularly symmetric deflection potential, Eq. 2.29 reduces to

$$\kappa = \frac{1}{2}\left(\psi_{11} + \psi_{22}\right) = \psi_{11} = \psi_{22}, \tag{2.35}$$

as the second order derivatives will be the same in each lens plane direction. From Eq. 2.28 the convergence is then equivalent to the partial derivative of the deflection angle with θ, which neglecting the direction due to the circular symmetry, is given by

$$\kappa = \frac{\partial \alpha}{\partial \theta} = \frac{4GMD_{ds}}{c^2 D_s D_d}\frac{1}{\theta^2}. \tag{2.36}$$

By setting $\kappa = 1$ we can then assert that for a circularly symmetric lens of mass M the magnification will be infinite for images on the lens plane satisfying

$$\theta = \theta_E = \sqrt{\frac{4GMD_{ds}}{c^2 D_s D_d}}, \tag{2.37}$$

where θ_E is known as the Einstein radius. Substituting this value and the function

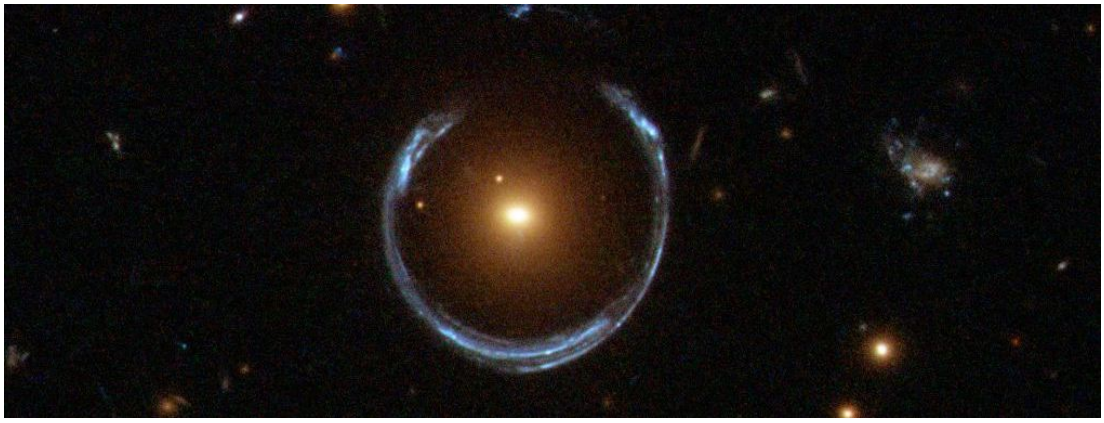

Figure 2.14: A nearly complete Einstein ring observed by the Hubble space telescope. By ESA/Hubble; NASA derivative work: Bulwersator (talk) Public Domain, https://commons.wikimedia.org/w/index.php?curid=17750437.

for $\alpha(\theta)$ into the lens equation we can find the corresponding value of β:

$$\beta = \theta_E - \alpha(\theta_E) \tag{2.38}$$

$$\beta = \sqrt{\frac{4GMD_{ds}}{c^2 D_s D_d}} - \frac{4GMD_{ds}}{c^2 D_s D_d}\frac{1}{\theta_E} \tag{2.39}$$

$$\beta = \sqrt{\frac{4GMD_{ds}}{c^2 D_s D_d}} - \sqrt{\frac{4GMD_{ds}}{c^2 D_s D_d}} \tag{2.40}$$

$$\beta = 0. \tag{2.41}$$

Therefore for a circularly symmetric mass the magnification will be infinite in the special case when the source and lens are perfectly aligned ($\beta = 0$). In this case the action of the lens upon the incident light will be rotationally symmetric and the net shear on the image of the source will be zero, consistent with our initial assumption. Moreover, because of this symmetry the lens mapping $\alpha(\theta_E) = \theta_E$ will be satisfied in all directions from the optic axis. As a result an observer will see the source as a ring of infinite magnification known as an Einstein ring similar to that depicted in Fig. 2.14.

As the circularly symmetric lens is an important approximation in many astrophysical cases the Einstein radius becomes a characteristic quantity in many lensing treatments. In particular, by normalising the lens mass by the square

of the Einstein radius we find that the mean surface density of mass within the Einstein radius is independent of the mass of the lens

$$\frac{M}{\theta_E^2 D_d^2} = \frac{c^2 D_s}{4\pi G D_{ds} D_d} = \Sigma_{\rm cr}, \tag{2.42}$$

where $\Sigma_{\rm cr}$ is known as the critical surface density. By rearranging Eq. 2.36 to be in terms of the critical surface density we find,

$$\kappa = \frac{M}{\theta^2 D_d^2} = \frac{\Sigma}{\Sigma_{\rm cr}} \tag{2.43}$$

allowing for the interpretation of κ as the normalised surface density of the projected mass distribution. An important subtlety here is that M represents the mass interior to θ_E and therefore κ is actually the mean normalised surface mass density interior to θ_E.

In general points on the lens plane of infinite magnification such as the Einstein ring, are known as critical curves, and their source plane equivalents, e.g. the $\beta = 0$ point in the case of an Einstein ring, are known as caustics. Critical curves and caustics are important as they demarcate regions of strong lensing where there are more than one solution to the lens equation, i.e. the lensing causes multi-path propagation. As a source crosses a caustic or an image crosses a critical curve the number of images will change by two. To understand this process we can track the position of images across the image plane.

Under Fermat's principle images will be found at points on the lens plane where the time delay is stationary with respect to image position, i.e. where the gradient of the time delay surface is zero. Each image will have a geometric time delay corresponding to the additional path length associated with its separation from the source position $(\theta - \beta)$. Furthermore, each image will have a Shapiro delay caused by its propagation through a gravitational field. Within the context of General Relativity the Shapiro delay is caused by masses introducing a dilation of space-time in addition to curvature. This gravitational time dilation, which

can be reinterpreted to account for the gravitational redshift effects discussed in §1.1, causes light propagating through a gravitational field to be delayed with respect to light propagating in a vacuum.

Generally, the time delay for an image propagating through a gravitational lens is given by

$$t(\vec{\theta},\vec{\beta}) = \frac{(1+z)}{c}\frac{D_d D_s}{D_{ds}}\left[\frac{1}{2}\left(\vec{\theta}-\vec{\beta}\right)^2 - \psi(\vec{\theta})\right], \tag{2.44}$$

where images will be found at positions satisfying

$$\vec{\nabla}_\theta\left[\frac{1}{2}\left(\vec{\theta}-\vec{\beta}\right)^2 - \psi(\vec{\theta})\right] = 0 \tag{2.45}$$

which is equivalent to the stationary phase approximation in Eq. 2.12.

By interpreting these time delays as phase delays we can visualise strong gravitational lensing in the same way as plasma scattering. Fig. 2.15 shows the transition from weak to strong lensing for a generic gravitational field. Initially, for a source far from the lens, the phase contribution from the lens' gravitational field is too small to cause a zero gradient point and the observer sees only a single, mildly perturbed image along the optic axis. This corresponds to the weak lensing regime. The second panel of Fig. 2.15 shows the scenario where the background point source lies exactly on a caustic of the lens. Here an additional, infinitely magnified image is formed, corresponding to the zero gradient saddle point in the surface of constant phase. This marks the transition into the strong lensing regime. Finally, as the source crosses the caustic and the Shapiro delay begins to dominate over the geometric delay, the previously formed image divides into two separate images of finite magnification. If the lens is transparent an observer in this scenario will now see three images of the source distributed about the lens. Typically however the central image will be obscured by the lens itself, leaving two observable images of the source.

An effective way to identify whether gravitational lensing is causing multiple

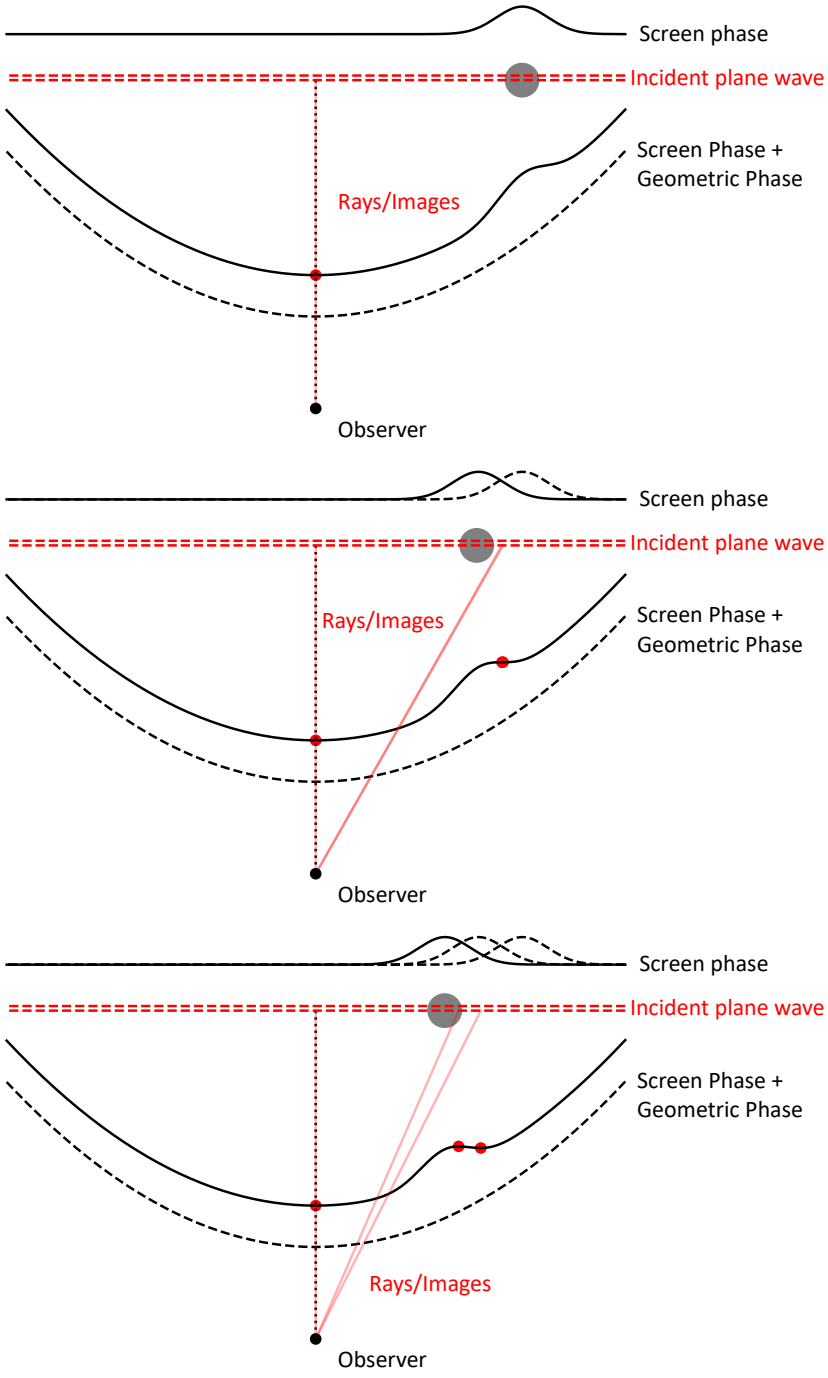

Figure 2.15: Visualisation of propagation through a phase-changing screen, as described in Fig. 2.4, for a screen containing an extended lensing mass. From *top* to *bottom* the lens is moved closer to the line of sight. *Middle* depicts the geometry where the lens is on the caustic and the lensing is transitioning from weak (*top*) to strong (*bottom*).

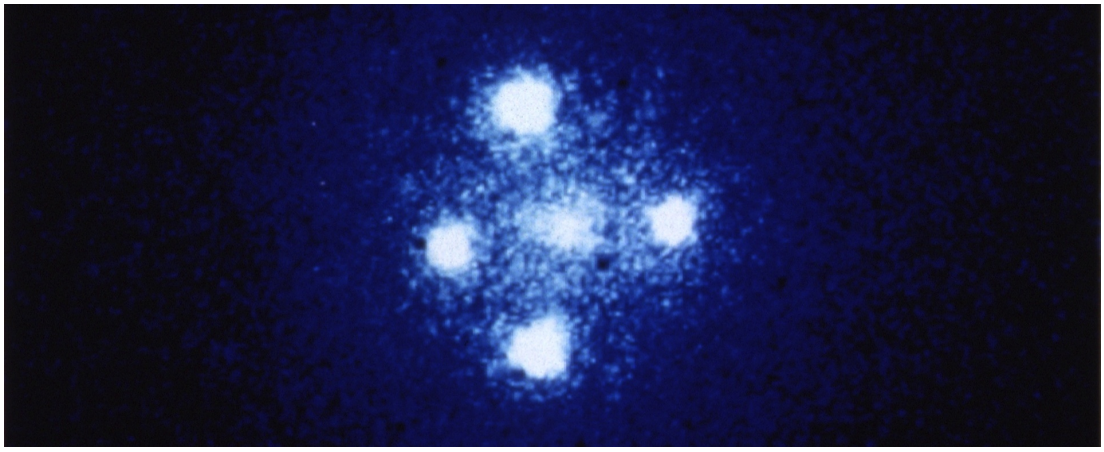

Figure 2.16: Optical image of the Einstein cross, depicting four images of the background quasar surrounding a central image of the foreground lensing galaxy. By NASA, ESA, and STScI - http://hubblesite.org/newscenter/archive/releases/1990/20/image/a/, Public Domain, https://commons.wikimedia.org/w/index.php?curid=2237885.

images is to cross match the spectral properties between images. As gravitational lensing is achromatic each image should share similar[5] spectra. Indeed, the first hints of strong gravitational lensing were detected in QSO 0957+561 (quasi-stellar object), where the spectra of two nearby images were found to be suspiciously similar (Walsh et al., 1979). In the time since this first candidate many cases of strong gravitational lensing have been found, including the Einstein cross depicted in Fig. 2.16. The cross serves as once of the clearest examples of strong gravitational lensing, showing four images of a background quasar surrounding an image of a foreground galaxy, which occludes a theoretical fifth image of the source.

There are also many examples of weak lensing, especially given the long range of gravitational forces (Dark Energy Survey Collaboration 1 et al., 2018; Lewis, 2020). However, within the weak lensing regime the thin screen approximation is not always appropriate as low density regions can have extents comparable to D_s. We will therefore restrict our considerations to the strong lensing regime where

[5]In theoretically ideal circumstances the spectral properties between images will be identical, however because each image traverses a separate path, subsequent propagation effects such as absorption can dilute spectral similarity.

the large densities generally require the extent of the lens to be thin compared to D_s (for a review of weak lensing theory and application see Bartelmann & Schneider, 2001).

In the strong lensing regime an ideal case of interest is the point mass gravitational lens. To visualise lensing from a point mass we can approximate the deflection potential as

$$\psi(\vec{\theta}) \approx \frac{4GM}{c^2} \ln\left(\frac{|\vec{\theta}|}{\theta_E}\right), \tag{2.46}$$

which will model the true potential well for $\theta < \theta_E$. Fig. 2.17 depicts this scenario, showing that the surface of constant phase contains a singularity where the deflection potential approaches infinity as the line of sight approaches the point mass. Formally this means that point mass lenses always cause strong lensing as there will always be a pair of zero gradient points either side of the phase singularity. Furthermore, for a true singularity the phase surface will be undefined for lines of sight coincident with the lens and so no third image will exist. In the second panel of Fig. 2.17 we can see that in the case where the source is aligned with the lens the geometry becomes circularly symmetric, with the two zero gradient points combining to form a zero gradient loop associated with an Einstein ring.

Lensing from a point mass is a useful case study as under Gauss' law the gravitational field from a spherically symmetric mass distribution interior to a given point will be identical to that from a single point of the same mass. We can therefore use the point mass behaviour to model lensing from any spherically symmetric mass distributions. As many mass distributions in astronomy may be accurately modelled as a sphere the point mass model is extremely useful.

For extended mass distributions there will be no phase surface singularity as the mass interior to a given radius will decrease to zero with that radius. This leads to a smooth peak in the surface of constant phase as depicted in Fig. 2.15. However, if the entire mass distribution is contained within the locus of its Einstein ring then it will still create the zero gradient points predicted by a

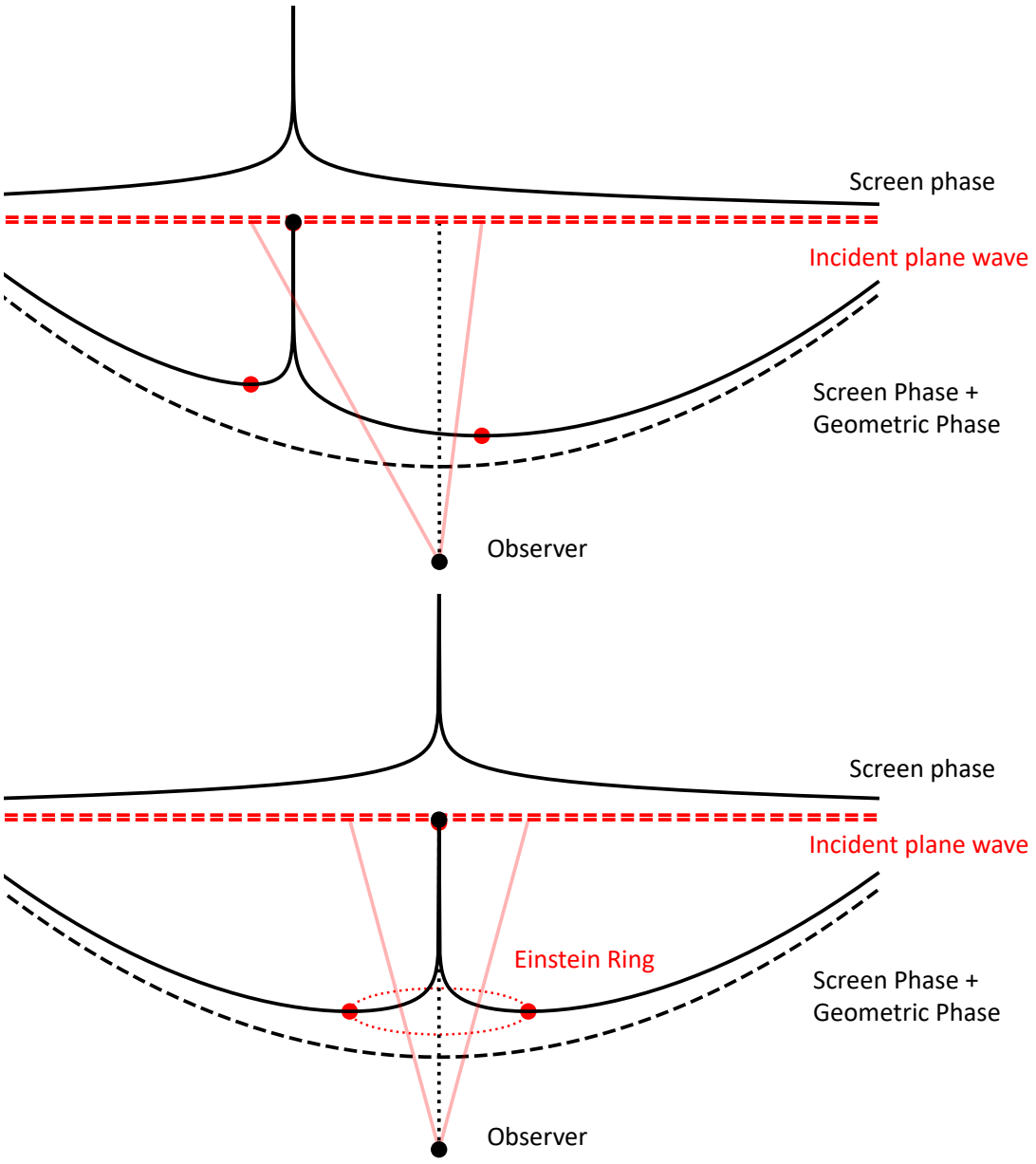

Figure 2.17: Visualisation of the effect of gravitational lensing from a point mass off axis (*top*) and aligned with the source (*bottom*).

point lens model. We can therefore restate the condition for strong lensing as a requirement that the surface density of the lensing mass satisfies $\Sigma > \Sigma_{\rm cr}$.

For compact lenses such as black holes and neutron stars, the mass interior to a given radius will not decrease until within a few Schwarschild radii of the lens. Here the weak field condition will be violated and a more complex treatment required. Therefore, in the regime where a thin screen model is valid, gravitational lensing from compact objects may be approximated with a point mass model.

Using the approximation in Eq. 2.46 the positions of the two images created by a point mass are given by

$$\theta_{\pm} = \frac{1}{2}\left(\beta \pm \sqrt{\beta^2 + 4\theta_E^2}\right) \tag{2.47}$$

each image has a magnification described by

$$\mu_{\pm} = \left(1 - \left[\frac{\theta_E}{\theta_{\pm}}\right]^4\right)^{-1} = \frac{y^2+2}{y\sqrt{y^2+4}} \pm \frac{1}{2} \tag{2.48}$$

where is the normalised angular impact parameter of the source $y = \beta/\theta_E$. Notably, the sign of the image magnifications corresponds to the parity of the images, i.e. images with negative magnification are reflected with respect to the optic axis. The difference between the signed image magnifications is unity, i.e. $\mu_+ - \mu_- = 1$, and the unsigned sum of their magnifications is given by

$$\mu = |\mu_+| + |\mu_-| = \frac{y^2+2}{2y\sqrt{y^2+4}} \tag{2.49}$$

From the solutions given by Eq. 2.47 the difference in time delay between these images is given by

$$\Delta t = \frac{4GM_L}{c^3}(1+z_L)\left[\frac{y}{2}\sqrt{y^2+4} + \ln\left(\frac{\sqrt{y^2+4}+y}{\sqrt{y^2+4}-y}\right)\right], \tag{2.50}$$

where z_L is the redshift of the lens.

The different time delays for each image mean that time variable processes in the intrinsic signal will appear echoed in the observed temporal profile. Each echo will correspond to an image in the spatial domain and by measuring the delays between echoes the lensing geometry may constrained. The larger the amplitude of the intrinsic variation the more significant the echoes will be in the observed profile. Transient signals are therefore the ideal probe of this effect, owing to the full modulation of their signals with time.

From Eq. 2.50 we can see that the time delay increases linearly with the mass of the lens. Therefore the minimum lens mass we can probe to with a given transient depends on the minimum time delay which could be detected between temporal echoes. Without considering wave optics effects at radio frequencies, the minimum detectable time delay will be comparable to the duration of the transient. Initial considerations of temporal echoes proposed looking for SNe lensed by galaxies (Refsdal, 1964). However, the subsequent discovery of much shorter transients such as FRBs and GRBs allows us to look for lensing by lower mass objects such as the primordial black holes introduced in §1.1.

Strong lensing of a fast transient by a lower mass object has potentially already been observed in GRB 950830 (Paynter et al., 2021). Fig. 2.18 displays the temporal profile of the GRB, showing two peaks in the temporal profile consistent with strong lensing by a $\sim 10^4\, M_\odot$ compact object. The key evidence for gravitational lensing, in this case, is the achromatic time delay between the bursts and their consistent spectra. This case provides strong evidence for the occurrence of strong lensing in fast transients and motivates us to explore its impact on fast cosmological transients.

FRBs (which are discussed in detail in §B) in particular would serve as an excellent probe of strong lensing by PBHs, providing many advantages over GRBs and SNe. The simplest among them is the short tens of μs to ms scales of FRB widths and temporal substructures (Farah et al., 2018, see also Fig. 7.2) which could allow temporal echoes from lenses on $0.1 - 10\,\mathrm{M}_\odot$ scales, respectively, to

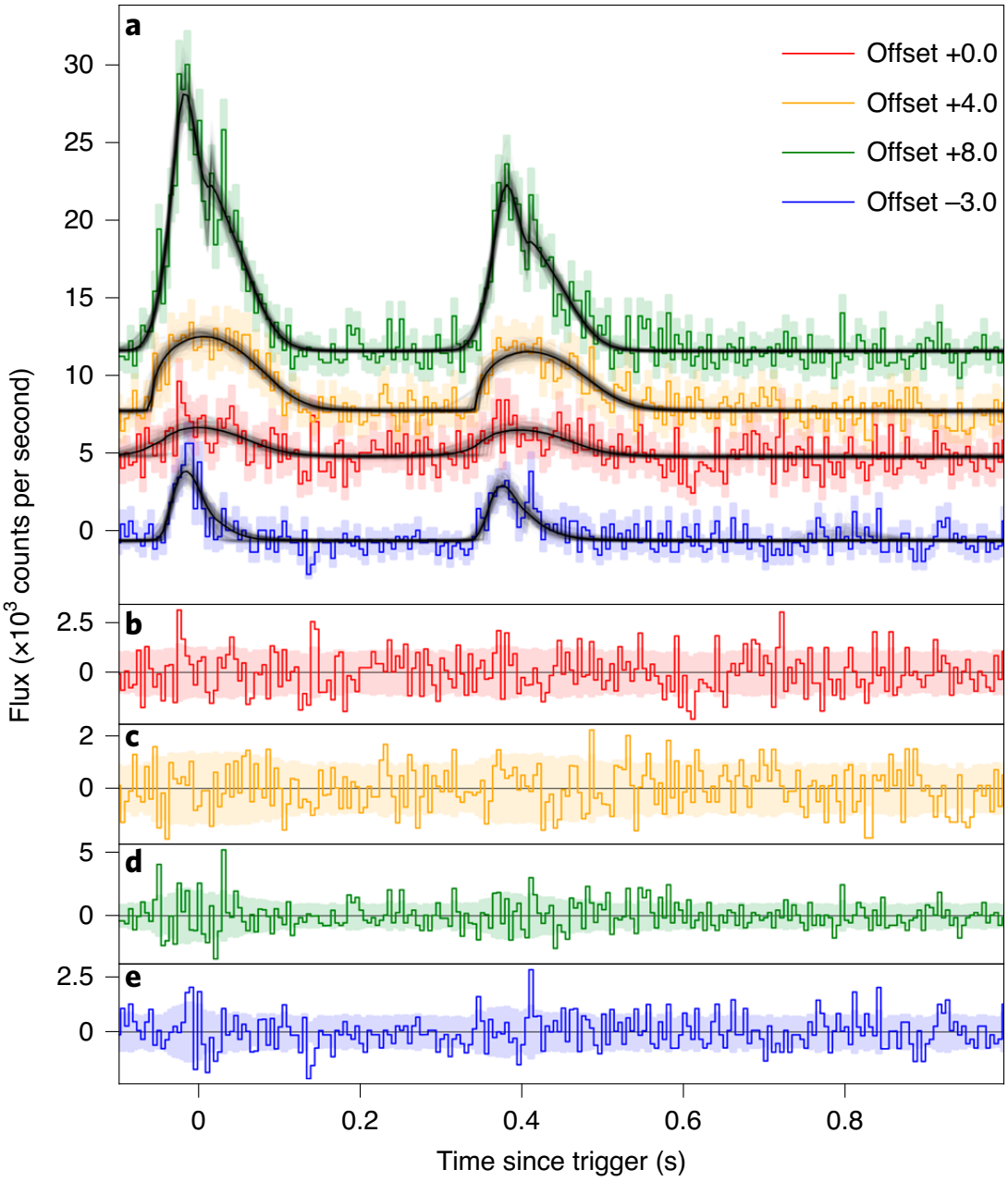

Figure 2.18: Temporal profile at a range of frequencies for gravitationally lensed GRB 950830 taken from Paynter et al. (2021). Panel **a** shows the GRB light curve at energies: 20-60 keV (red); 60-110 keV (yellow); 110-320 keV (green); 320-2000 keV (blue), with 1σ errors depicted by the shaded regions. To aid visual distinction each energy has been offset on the *y-axis* by the amount specified in the legend. Solid black lines show the best fits to the data, where each echo has been fit independently. Panels **b-e** show the residuals to these fits at each energy.

be distinguished using only the observed intensity temporal profile of the burst (assuming a redshift of $z_L = 0.2$ for the lens and $y = 1$). Whereas, the 0.1–10 s scale of structure GRB temporal profiles (Gehrels et al., 2009) corresponds to lensing from 10^3 – $10^5\,\mathrm{M}_\odot$ objects (assuming $z_L = 1$ and $y = 1$, where the larger lens redshift corresponds to the greater mean redshift of GRB distributions (Paynter et al., 2021)). In each of these cases the temporal separations of the echoes correspond to image spatial separations well below the angular resolution of typical observations. For context, with the ~ 0.1 arcsecond resolution achieved by ASKAP when localising FRBs (Bannister et al., 2017), a gravitational lens would need to be $\sim 10^{10}\,\mathrm{M}_\odot$ in order for images separated by $\sim \theta_E$ to have distinct sky localisations (assuming a midpoint lens at $z_L = 0.2$), a mass which rises to $10^{15}\,\mathrm{M}_\odot$ in the case of GRB localisation with Swift-BAT to only arcminute precision (Barthelmy et al., 2005)(assuming a midpoint lens at $z_L = 1$).

Unlike type Ia SNe, neither GRBs nor FRBs are standardisable candles, and therefore the determination of the distance to their sources is significantly more difficult. For both FRBs and GRBs the redshift is often determined from spectroscopic or photometric analysis of the host galaxy associated with the burst itself or the optical afterglow in the case of GRBs (D'Avanzo, 2015; Bannister et al., 2017). The larger estimated mean redshift of the GRB population allows any individual burst to probe a larger portion of the Universe, in some cases up to a redshift $z \sim 9.4$ (Cucchiara et al., 2011). However, as the lens mass can only be determined from the time between temporal echoes to within a factor of $(1 + z_L)$ (see Eq. 2.50), where z_L can range from zero to the redshift of the source, the greater range of potential GRB redshifts compared to FRBs also leads to higher uncertainty in the mass of any lens along the line of sight. Furthermore, GRB redshift determinations from the optical afterglows are somewhat model dependent (Cucchiara et al., 2011), leading to greater uncertainty compared to FRBs source redshifts which often boast many orders of magnitude higher relative precision (Bhandari et al., 2020). Therefore while any given GRB is likely a deeper

probe, FRBs will constrain a lower and more precise range of lensing masses.

Another potential drawback of FRBs is the existence of complex sub-burst temporal structures and in some cases, repeating sources, which create a source of degeneracy that makes the identification of true lensed images more difficult. In general, repeating sources and sub-burst structures are not expected to share identical spectra, whereas, the achromatic nature of gravitational lensing should produce nearly identical spectra for each lensed copy. Therefore, the spectral information recorded along with FRB temporal profiles serves to break some of the degeneracies created by potential repeaters and other complex morphologies. Furthermore, many FRB observatories now routinely collect the raw voltage information associated with the observation of any burst. Using this information, the wavefield of an FRB can be reconstructed, and lensed bursts identified unambiguously from the correlation between gravitationally lensed images, which are expected to have their coherence preserved by lensing (see Kader et al., 2022; Leung et al., 2022, for a precise description of this method). A potential issue with this method is that each image/echo propagates along a distinct path to the observer, potentially encountering different plasma densities and turbulences that may disrupt the coherence of the burst. As discussed in Leung et al. (2022), by cross-correlating the wavefields associated with each image to search for coherent gravitational lensing, we transform the strong gravitational lens into something of an interferometer with a baseline on the order of the image separation scale. In this context, whether scattering prior to the strong lensing suppresses this correlation can be determined by considering whether the scatter-broadened image is resolved out by the gravitational lens interferometer. Furthermore, by reversing this scenario we can determine whether scattering after the strong lensing disrupts the wavefield coherence between images by considering whether the dominant scattering screen resolves the multiple images from the lens as considered by Eichler (2017). In each of these contexts, smaller lens masses usually result in the coherence between images being preserved, as these lenses have smaller im-

age separations, which are both more difficult to resolve and have lower resolving power. Moreover, both Eichler (2017) and Leung et al. (2022) note that even in the case where the relevant lensing/scattering screen is resolved, the correlation may not be completely destroyed. Within this thesis I focus primarily on the geometric effects of lensing and do not consider in-depth, wave-optics effects. I, therefore, leave further consideration of decoherence of the wavefield between strongly gravitationally lensed images to a future study and urge any intrepid readers to see Eichler (2017); Leung et al. (2022); Kader et al. (2022) for further discussion. In addition to disrupting coherence between images, variant scattering and dispersion between paths may lead to the burst profiles between images being different. In principle, both of these effects can be accounted for using coherent dedispersion (Scott et al., 2023) and independent burst fitting (Qiu et al., 2020) to recover the intrinsic shape of each temporal echo. In these cases, the differences in DM, scattering, and perhaps even redshift can potentially be leveraged for a greater understanding of the lensing geometry. Given we will be exploring the small scale case in this thesis, and do not expect the paths of propagation to be different enough to substantially change scattering, DM, or redshift we will leave a more complete consideration of the interaction between lensing and these observables to a future study (see also Er & Mao, 2014; Cordes et al., 2017; Er & Mao, 2022, for additional plasma lensing effects not considered within the scope of this thesis).

Chapter 3

Cosmological Lensing

3.1 Cosmological Distances

In their most general form, distances measure the separation between events along observed photon trajectories (Hogg, 2000). On human scales measuring distances is trivial. As, on these scales, we do not expect environments to evolve significantly over the light travel time, the travel time of observed photons corresponds to the instantaneous distance (proper distance[1]) to a source. On Galactic scales the travel time of light is significant. As a result, the observer-source dynamics can be important to precise determinations of proper distance, however, in general, the light travel time corresponds closely to the proper distance as the Galactic environment is isolated from the Hubble flow. Conversely, on cosmological scales, the Universe expands significantly over the time of flight of a photon. As a result, the proper distance, in general, does not correspond to the travel time of light. The separation of these quantities highlights the need for specialised distance measures in cosmology. Described below are the cosmological distance measures relevant to this work, following the formulae described by Hogg (2000) and Harrison (1993).

Perhaps the most important distance measure is the comoving distance. As

[1]the proper distance is defined as the distance between two events in the frame where they are simultaneous (Weinberg, 1972).

the name suggests, the comoving distance is the distance measure that accounts for cosmological expansion. Specifically, it is the proper distance to a source divided by the ratio of scale factors at emission and observation, and therefore it is constant regardless of expansion. An expression for the comoving distance as a function of redshift can be derived by considering an infinitesimal proper distance, equivalent to the light travel time

$$\ell = c\,dt. \tag{3.1}$$

Dividing by the scale factor at the current time yields an infinitesimal comoving distance

$$dD_c = \frac{c\,dt}{a(t)}. \tag{3.2}$$

Integrating this quantity between emission (t_1) and observation (t_0)

$$D_c = \int_{t_1}^{t_0} \frac{c\,dt}{a(t)}, \tag{3.3}$$

yields the total comoving distance. Cosmological redshift can then be expressed as a function of the scale factor at different times

$$(1+z) = \frac{a(t_0)}{a(t)}. \tag{3.4}$$

Defining the scale factor at the time of observation as $a(t_0) = 1$ then implies $da = -a^2 dz$. Using this and defining $H(z) = \dot{a}/a$, we can then express D_c as a function of redshift, following

$$D_c = \int_{t_1}^{t_0} \frac{c\,dt}{a(t)} = -\int_{a(t_1)}^{a(t_0)=1} \frac{c\,da}{a^2 H(a)} = \int_0^z \frac{c\,dz'}{H(z')} = d_H \int_0^z \frac{dz'}{E(z')}, \tag{3.5}$$

where $d_H = c/H_0$ and $E(z)$ is given by Eq. 1.6. For a homogeneous universe, it then becomes simple to transform the comoving distance into other useful distance measures such as the luminosity distance and the angular diameter distance.

The luminosity distance (D_L) describes the relationship between bolometric luminosity (L) of a source and its observed flux (S):

$$L = 4\pi S D_L^2. \tag{3.6}$$

In the case of spectral luminosity and flux, the relation instead becomes

$$L_{\nu_e} = \frac{4\pi D_L^2 S_\nu}{(1+z)} \tag{3.7}$$

where the additional redshift factor accounts for the effect of cosmological expansion on the observed bandwidth. When working with transients, where the observable of interest is fluence instead of flux, the above relation is divided by another factor of $(1 + z)$ to account for the cosmological time dilation of the burst's duration (Macquart & Ekers, 2018a).

The angular diameter distance (D_A) describes the relationship between a source's physical transverse size (x) and the observed angular size it subtends (θ):

$$D_A = \frac{x}{\theta}. \tag{3.8}$$

D_A can also be used to calculate D_L via Etherington's reciprocal relationship, which asserts that, in any space-time (Etherington, 1933)

$$D_L = (1+z)^2 D_A. \tag{3.9}$$

In a flat homogeneous universe D_A can also be expressed in terms of the comoving distance as

$$D_A = \frac{D_C}{(1+z)} \tag{3.10}$$

and, furthermore, the angular diameter distance of a object at redshift z_2 as

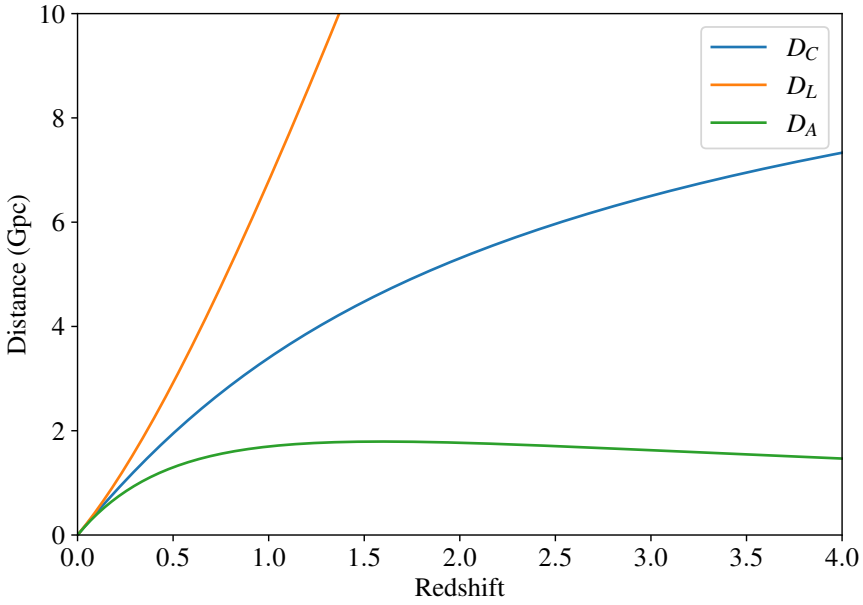

Figure 3.1: Cosmological distance measures for a Planck cosmology.

observed from redshift z_1, $D_{A,12}$, can be expressed as

$$D_{A,12} = \frac{1}{(1+z_2)}\left[D_{C,2} - D_{C,1}\right], \tag{3.11}$$

for a flat universe, where $D_{C,1}$ and $D_{C,2}$ are the corresponding comoving distances. For comparison the above three distance measures are plotted in Fig. 3.1 for a range of redshifts using a Planck cosmology (Planck Collaboration et al., 2018).

As discussed in §2.2.2, gravitational lensing can affect the observed image of a source. Therefore, in a universe with an inhomogeneous distribution of matter, cosmological distance measures determined from observables, i.e angular diameter (D_A) and luminosity distances (D_L), will be impacted by the matter distribution over which they are measured (see Helbig, 2020, for a review). For D_A this can be understood by considering the beam received by an observer and subtended by the source as seen in Fig. 3.2. In a universe with a homogeneous distribution of matter a beam will contain matter at that universe's average density and will have zero convergence (magenta). Conversely, a beam in an inhomogeneous universe, containing a void or a below-average matter density (black), will have a negative

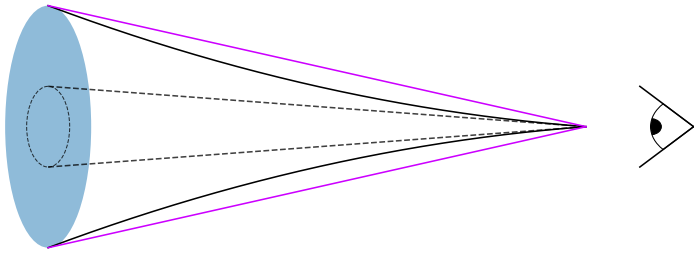

Figure 3.2: Visualisation of the effect of matter on a beam of light subtended by the source. A below average density of matter within a beam causes a negative convergence of the light (black solid line). When compared to the average density, zero convergence case of a filled beam (magenta solid line) this results in a decreased angular source size (black dashed line) associated with the same physical size (blue ellipse). This can be modelled as an apparently larger D_A for the under-dense beam.

convergence caused by that lower density. As found by Fleury et al. (2017), only matter within the beam will contribute to the convergence. This negative convergence presents as an apparently smaller angular size (θ) associated with the same physical source size (x), resulting in an increase to $D_A = x/\theta$ compared to the homogeneous case.

In the context of D_L, this difference manifests as a lower flux observed for the case of an under-dense or empty beam. Etherington's reciprocal relation allows D_L to be easily calculated from the corresponding D_A. Consequently, it is sufficient to discuss the effect of inhomogeneity in the context of D_A[2].

The matter in any universe can be categorised as either homogeneous or inhomogeneous. By convention, we define the fraction of total matter that is homogeneously distributed as η. The two important instances of D_A are then labeled as the empty (D_η) and filled (D_1) beam cases. An empty beam represents the most extreme case of a void, where a beam contains no clumps of inhomogeneous matter, corresponding to the maximal value of D_A in a universe with a smooth matter fraction η. A filled beam refers to the case where all matter in the uni-

[2]Etherington's reciprocal relation holds in all metric theories of gravity (Schneider et al., 1992), for modified theories of gravity this is not necessarily true. In this thesis, I do not consider lensing in the context of modified gravitational theories, for an example of the potential impact of Etherington relation violation in a non-metric theory of gravity, see Giesel et al. (2023).

verse is distributed homogeneously (i.e. $\eta = 1$, hence D_1), and hence the beam contains matter at the average density. Finally, just as a void places sources apparently further away, magnification associated with gravitational lensing from an inhomogeneity within the beam can place the sources apparently closer.

Typically, we assume a homogeneous or 'smooth' universe, and therefore $D_A = D_1$. In reality, our Universe is inhomogeneous on a vast range of scales, from individual particles to galaxy clusters. As a result, a population of sources at a constant redshift will have a complex distribution of D_A depending upon the intervening matter. This distribution will correspond to the probability distribution of gravitational lensing magnifications such as those applied by Zumalacárregui & Seljak (2018) and Garcia-Bellido et al. (2017) to supernova observations. The results of Weinberg (1976); Kaiser & Peacock (2016) indicate that in a transparent universe[3] D_A^2 averaged over direction is unaffected by inhomogeneity provided that the total area of the surface of constant redshift is also unaffected, as found by Breton & Fleury (2020). Therefore, the mean of the magnification distribution must be the magnification corresponding to D_1^2 [4]. Moreover, these magnification distributions are often heavily skewed towards low magnifications with a mode corresponding to D_η (Metcalf & Silk, 1999). As such, D_η and D_1 are crucial to characterising the macroscopic distribution of magnifications (Schneider & Weiss, 1988), with D_η containing information relevant to the bulk of the events, whereas the small distances associated with high magnifications will only pertain to a small fraction.

It is worth noting, however, that a beam will average over fluctuations on scales that are small compared to the beam's volume. Fig. 3.3 depicts this, showing the distribution of D_A in an inhomogeneous universe for both a large (magenta) and small (black) source. The large beam volume associated with the

[3]Some fraction of the distant universe will be obscured by the opaque cross-section of our lens, however as we are considering only compact lenses here and material opacities are generally low for the radio and gamma-ray sources we are interested in, this fraction is likely to be low, so we assume a transparent universe.

[4]Conversely, the directionally averaged value of D_A will not be equivalent to its smooth universe counterpart as D_A is a non-linear function of D_A^2.

large source smooths over the small-scale inhomogeneities (grey dots), rendering D_A indistinguishable from that of a completely smooth universe ($\eta = 1$). Hence as the solid angle subtended by a source increases the value of η will tend to increase and D_A will decrease towards D_1. The minimum mass scale that a given source will be sensitive to lensing from, can then be inferred from the volume of the beam subtended by that source.

3.2 Probed Lens Masses

To derive this minimum mass scale inhomogeneity it is instructive to consider a field of homogeneously distributed clumps of mass M_c composing some fraction (f) of the Universe's total matter density $\Omega_{\rm c} = f\Omega_{M,0}$. We can then characterise the level of inhomogeneity by comparing M_c to $M_{\rm beam}$, the mass enclosed by the beam. For the case of a smooth mass distribution ($\eta = 1$) in a flat universe (k=0),

$$M_{\rm beam} = \rho_{cr,0} d_H^3 \frac{A}{D_A^2(z_s)} \left\{ \Omega_{c,0} \int_0^{z_s} \frac{(1+z)^2 \tilde{D_A}^2(z)}{E(z)} dz \right\}, \tag{3.12}$$

as per the comoving volume equation in Hogg (2000). $\rho_{\rm cr,0}$ is the critical density at $z = 0$, A is the area of the source, d_H is the Hubble distance, $\tilde{D}$ denotes a distance normalised by d_H, $E(z) = H(z)/H_0$, and z_s is the source redshift.

For a $M_c \ll M_{\rm beam}$ the expected number of clumps within the beam will be $\langle N \rangle \gg 1$. As our distribution of clumps has constant co-moving density, the random fluctuations in N will follow Poisson noise with standard deviation of $\sqrt{N}$, making the fractional fluctuation in both N and the total convergence of the beam small for large $\langle N \rangle$. It is therefore unlikely, in the case of $M_c \ll M_{\rm beam}$, to observe D_A significantly different from D_1. As the value of M_c increases, the fractional fluctuation in N also increases, eventually yielding a significant probability of a beam containing no clumps. For the case of $M_c \gg M_{\rm beam}$, a beam is most likely to contain no clumps in which case D_η will apply.

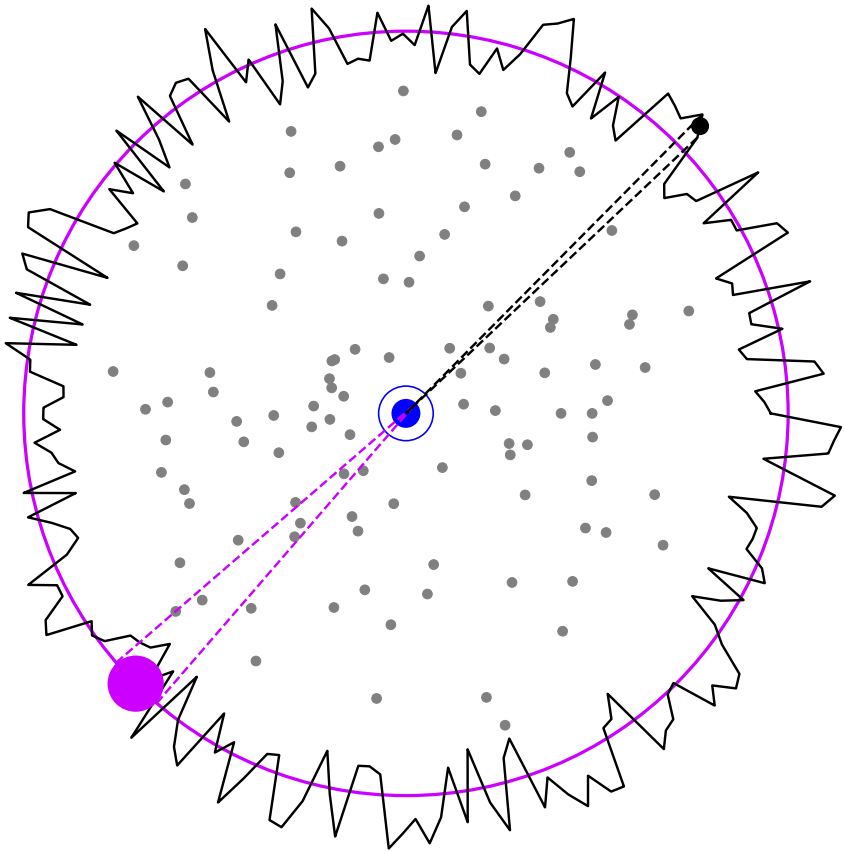

Figure 3.3: Visualisation of the smoothing effect of large source sizes. Grey dots represent clumped matter in an inhomogeneous universe. The magenta solid line is D_A to the magenta source at a constant redshift. The solid black line represents D_A to the compact black source at a constant redshift and the blue sphere represents the observer. To an observer of the extended magenta source, the universe appears smooth as the matter within the large beam volume (magenta dotted lines) remains relatively constant. To an observer of the compact black source the same inhomogeneities cause the D_A to the source to change with the source's position according to how much matter is within the compact beam (black dotted line). As a result, the black curve is noisy following the large random variation of matter within the beam as a function of direction.

3.2.1 Magnification of Extended Sources

The exception to our $M_{\rm beam}$ criteria would be when many clumps lie within the beam and each causes a significant magnification of the source. This scenario may be observationally distinct from the smooth matter case and hence the requirement of $M_c \ll M_{\rm beam}$ is a necessary but not sufficient condition for smoothness. In order to treat a matter distribution as though it were smooth we must also require that the maximum magnification by any lenses within its volume be low. Because the size of lensing masses (M_c) in question are exceedingly low it is appropriate to consider the finite size of even our most compact sources.

Extended sources can be significantly magnified if their angular size (θ_S) is comparable to the Einstein angle of the lens (θ_E). As shown by Schneider et al. (1992), the maximum magnification ($\mu_{\rm max}$) from an extended source is given by,

$$\mu_{\rm max} = \frac{\sqrt{4+r^2}}{r}, \tag{3.13}$$

where $r = \theta_S/\theta_E$. If these two angles are equal ($r = 1$) then $\mu_{\rm max} \approx 2.24$, dropping approximately linearly with r. Using this equivalence, we can determine the mass of clumps, below which only small magnifications will be observed,

$$M_{\rm lens} = \rho_{cr,0} d_H^3 \frac{A}{D_s^2} \left\{ \frac{2}{3} \frac{\tilde{D}_d \tilde{D}_s}{\tilde{D}_{ds}} \right\}. \tag{3.14}$$

Uniform mass distributions with clump masses that are then below both $M_{\rm beam}$ and $M_{\rm lens}$ will have clumps both numerous within the beam and able to affect only a low maximum magnification of the source. Such distributions will be largely indistinguishable from a smooth matter distribution.

The linear density field associated with a uniform distribution of clumps has a vanishing shear due to matter outside the beam (Nakamura, 1997). As such, for $M_c \gg \min[M_{\rm lens}, M_{\rm beam}]$ the assumptions of the ZKDR distance model are satisfied and we can calculate D_A for a beam without clumps using the method

of Kayser et al. (1997) (i.e. $D_A = D_\eta$, with $f = \eta$). We then expect a source averaged magnification with respect to the empty beam $\langle\mu\rangle = \frac{D_\eta^2}{D_1^2}$ and the most likely line of sight to a source to be characterised by D_η.

In the left panel of Fig. 3.4 we visualise the range of clump masses which should and should not be considered smooth by plotting $M_{\rm beam}$ (full lines) and $M_{\rm lens}$ (dotted lines) for various sources. We have used the canonical source sizes for SN Ia, GRBs and FRBs (100 AU, 10^4 km and 10 km, respectively) to calculate each criteria. For SN Ia this canonical size is derived by assuming a $\sim$ 19 day period to reach maximum light (Firth et al., 2015; Riess et al., 1999). For a typical type Ia supernova (SN Ia) expanding uniformly at the canonical velocity of 10^4 km/s (Maoz et al., 2014) this rise time will correspond to a radius of $\sim$ 100 AU and subtend a cosmological volume of $\sim$ 1000 pc^3 at $z \approx 1$ (Fleury et al., 2013). For FRBs the extent of their sources are canonically inferred from the duration of their bursts to be as low as 10 km (corresponding to 10^{-16} pc$^3 \approx 1$ AU^3 at $z \sim 0.5$; Farah et al., 2018; Cho et al., 2020), and for short GRBs it may be as low as 10^4 km (corresponding to 10^{-10} pc^3 at $z \sim 0.5$; D'Avanzo, 2015). Additionally, for the calculation of $M_{\rm lens}$ we assume that $D_{ds} = D_d$ as this will capture the region of lens geometry with the highest contribution to the lensing optical depth (Turner et al., 1984).

As expected from the similarity of equations (3.12) and (3.14), the value of each criteria is relatively similar over the vast range of masses we are considering. For each source $M_{\rm beam}$ is shown to be the dominating criteria over much of the redshift space of interest. Our interest is restricted to source redshifts $1.0 < z_s < 3.0$ as the difference between D_0 and D_1 for $z < 1$ is small as per Fig. C.1 and we expect few sources to be observed at higher redshifts.

We note that a caveat of this model is that as the convergence of the beam fluctuates with N, the apparent angular size of the source will also fluctuate. This leads to changes in both the beam's volume and consequently in N. We do not account for this second order effect, however qualitatively the resulting

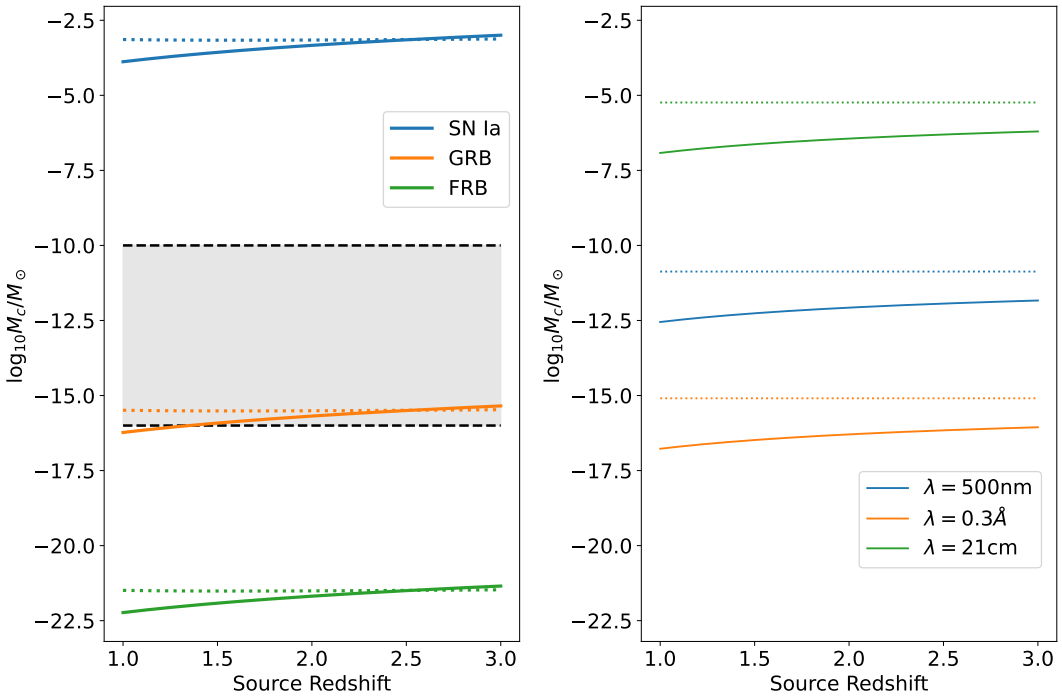

Figure 3.4: $M_{\rm beam}$ and $M_{\rm lens}$ limits to clump mass plotted with full and dotted lines respectively. For $M_c \gg \min[M_{\rm beam}, M_{\rm lens}]$ the mass will appear inhomogeneous and D_η will describe the most likely line of sight to a source. For $M_c \ll \min[M_{\rm beam}, M_{\rm lens}]$ the mass will appear homogeneous and all lines of sight will be described by D_1. *Left*: Constraints are calculated in the limit of geometric optics for source size representing SN Ia (100 AU), GRBs (10^4 km) and FRBs (10 km), using equations (3.12) and (3.14). The shaded region gives the range of PBH masses that are observationally unconstrained *Right*: Limits are calculated considering physical optics for wavelengths representing SN Ia, GRBs and FRBs, using equations (3.15) and (3.16). A mass distribution may be considered smooth if $M_c \ll \min[M_{\rm beam}, M_{\rm lens}]$ for either of the geometric or wave optics limits, hence wave optics will be the dominant limit for FRBs observed at radio frequencies.

change to N will be in the same direction as the original fluctuation. This will cause an increase to the standard deviation of the distribution of N and therefore an increase in the level of inhomogeneity. By neglecting this second order effect our conclusions on the mass range of inhomogeneities each source is sensitive to will be conservative.

Any objects having masses in the stellar range constitute inhomogeneities for SN Ia, GRBs and FRBs, as can be seen from Fig 3.4 (left), and for that reason a large population of such objects is already excluded by the SN Ia data (Helbig, 2015). Visible stars themselves amount to only a small fraction of the average matter density, $\Omega_{\rm stars}/\Omega_{\rm Matter} \sim 0.01$ (Fukugita & Peebles, 2004), and a uniformly distributed population at this low level would not have a substantial effect on the angular diameter distances; this case would be well approximated by the $\eta = 1$ calculations shown in Figure 3. In fact visible stars are far from uniformly distributed; they are concentrated in the central regions of galaxies and so can play a major role as gravitational lenses on some particular lines-of-sight, but have little influence on the background geometry.

The shaded region in Fig. 3.4 (left) corresponds to the range of PBH masses which could theoretically still constitute 100 % of our Universe's dark matter. Notably, this region lies well below $M_{\rm beam}$ for SN Ia, meaning that current observational constraints are insensitive to PBHs in the asteroid to sub-lunar range. Conversely, the region lies far above $M_{\rm beam}$ for FRBs, with a majority being far above $M_{\rm beam}$ for GRBs as well. Thus, if dark matter were comprised mostly of PBHs in the unconstrained range, D_A for FRBs and GRBs would be affected. This suggests that compact cosmological transient such as FRBs and GRBs could provide a new way to constrain dark matter in this unexplored range.

3.2.2 Diffraction Limitations

As suggested by several authors Oguri (2019); Jow et al. (2020) wave effects may also be important to the lensing of FRBs. In the context of our previous

two constraints given by equations (3.12) and (3.14), considering physical optics will have two effects: it will set a minimum probed volume corresponding to the Fresnel scale, and it will set a maximum amplification as described below.

Under wave optics, radiation from the source will sample a transverse area corresponding to the Fresnel scale. Hence, the volume probed by a source cannot be smaller than the Fresnel zone integrated over the line of sight. Using this volume we can recalculate $M_{\rm beam}$ as

$$M_{\rm beam} = \rho_{cr,0}\,\lambda d_H^2 \left\{ \Omega_c \int \frac{\tilde{D_{ds}}\tilde{D_d}}{\tilde{D_s}} \frac{(1+z)^2}{E(z)} dz \right\} \tag{3.15}$$

where λ is the wavelength of the radiation.

Diffraction around a lens will also set the maximum amplification[5] we can observe from a lens' magnification. When the Schwarzschild radius is equivalent to the wavelength of the emitted radiation the maximum amplification will be $I_{\rm max} \approx 3.28$ (Nakamura, 1997). As we did earlier for extended sources we can use this as a fiducial point and calculate the mass below which diffraction will significantly restrict amplification,

$$M_{\rm lens} = \frac{c^2\lambda}{8\pi G}. \tag{3.16}$$

Just as for our previous constraints, clump mass $M_c \ll \min[M_{\rm beam}, M_{\rm lens}]$ will be numerous within the Fresnel volume and have low maximum magnifications allowing their distribution to be effectively treated as smooth for the purpose of calculating distance measures.

The right panel of Fig. 3.4 shows the $M_{\rm beam}$ (full lines) and $M_{\rm lens}$ (dotted lines) criteria calculated for a range of representative wavelengths for the prompt emission from each of the sources in the left panel (500 nm = optical = SN Ia, 0.3Å= gamma-ray = GRB, 21 cm = radio = FRB). Between the two limits we can see that in the redshift range of interest $M_{\rm beam} \gg M_{\rm lens}$. Consequently,

[5]We note that amplification here refers directly to wave amplitude rather than magnification which is defined with respect to the angular size of the image.

for these redshifts it is sufficient to say that if the uniformly distributed clumps are numerous within the Fresnel volume then they may be treated as a smooth distribution of matter. Comparing the results between panels we can see that the mass limits calculated in the geometric optics limit dominate over their physical optics counterparts for both SN Ia and GRBs, i.e. small inhomogeneities will be smoothed over by the source sizes before wave effects become important. For FRBs however, diffraction will smooth over inhomogeneities far larger than what could be probed on the basis of their source size alone. This leaves only a narrow range of possible inhomogeneites they could probe that are not already ruled out from SN Ia observations.

However, despite their curtailed potential in the radio, the results obtained for FRBs in the geometric optics case further motivate multi-wavelength observations of FRBs. Observations of the so called Galactic FRB have shown coincident x-ray emission with the prompt radio burst (Ridnaia et al., 2021; The CHIME/FRB Collaboration, 2020). Such a high frequency counterpart would drastically reduce the diffraction limit associated with FRB observations at 21 cm, allowing FRBs to probe a similar range of inhomogeneities as GRBs.

As shown above, the beam volume for sources at similar redshifts is largely dependent on physical source size. The remaining question is then, for which sources may the matter distribution in the Universe be considered homogeneous? Evidence from SN Ia observations has proved under reasonable conditions that D_A to sources subtending a beam of volume greater than the typical SN Ia is equal to D_1 (Helbig, 2015; Kaiser & Peacock, 2016; Breton & Fleury, 2020). As a relatively compact source, this validates the assumption of homogeneity in many astrophysical cases. Hence, inhomogeneous evaluations of D_A are generally disregarded.

However, as shown in Fig. 3.2, FRBs and GRBs will be sensitive to compact inhomogeneities on scales below that ruled out by SN Ia observations (for an extended discussion on the advantages of FRBs in probing more complex lens mass

distributions see Wagner et al., 2019). Of particular interest in this mass range are sub-stellar mass primordial black holes (PBHs) which, as discussed in §1.1.1, have only been constrained in the nearby Universe. FRBs and GRBs could therefore provide complementary constraints on cosmological scales, thus providing a specific motivation for considering small-scale, macroscopic inhomogeneities. Furthermore, as demonstrated by Kayser et al. (1997) there is a significant difference between D_1 and D_η for $\eta = 0$ at high redshift. This difference could have dramatic effects on the inferred properties of GRBs and FRBs at redshifts above one, as we consider in §6.

3.3 Lensing Probabilities

In order to determine the impact of gravitational lensing on the observed population of a type of cosmological transient, we must determine the probability that a given transient will be lensed. To do so, we will make use of the concept of optical depth.

Optical depth is a dimensionless value that describes the effective thickness of a medium to light. Specifically, it is the natural log of the fraction of incident intensity that is successfully transmitted through a medium (Maoz, 2016). To derive this quantity we must first consider that media of any type are comprised of particles. To characterise the interaction between the incident light and the particles of a medium we need to know the number density of medium particles (n), and how close a photon can be to a particle of the medium before it is absorbed. Typically, the latter is quantified using the absorption cross-section (σ), i.e. the area around a medium particle where a photon would be absorbed. The average distance a photon can travel through the medium before being absorbed is then given by

$$\lambda = \frac{1}{n\sigma} \tag{3.17}$$

where λ is referred to as the mean free path of the photon and is linearly pro-

portional to the fraction of incident light that is absorbed by the medium. To derive the transmitted intensity, I_t, consider a beam of intensity I_0 incident upon a medium with a mean free path λ. For propagation through the medium over a small path length $d\ell$ the decrease in intensity, $-dI$, will be given by the product of the intensity at that position, I, and the path length in units of the mean free path

$$-dI = I\frac{d\ell}{\lambda}. \tag{3.18}$$

Integrating over all path lengths yields

$$-\int_{I_0}^{I_t} \frac{dI}{I} = \int_0^{\ell} \frac{d\ell}{\lambda}, \tag{3.19}$$

where ℓ is the total path length through the medium. Assuming a homogeneous medium, i.e. the mean free path is not a function of ℓ, allows for simple evaluation of this equation as

$$\ln \frac{I}{I_0} = -\frac{\ell}{\lambda} = -n\ell\sigma = -\tau. \tag{3.20}$$

As per the previous definition, this is the optical depth (τ), which we can see can also be represented as the length of the medium in units of the mean free path. Following from this, the probability of a photon being transmitted through a medium (p_t) can be expressed as

$$p_t = \frac{I_t}{I_0} = e^{-\tau} = (1 - p_i), \tag{3.21}$$

where p_i is the probability of interception. As expected, this form is consistent with a Poisson probability of a given photon being intercepted a single time for a mean interception rate given by τ. Furthermore, when $\tau \ll 1$, these can be

Taylor expanded to yield

$$p_t \approx 1 - \tau, \tag{3.22}$$

$$p_i \approx \tau. \tag{3.23}$$

The concept of optical depth can be abstracted to interactions beyond the absorption of light in a medium. By using the number density of lenses in the Universe as n, and the cross-section for significant gravitational lensing as σ, the optical depth of gravitational lensing can be determined. Furthermore, it can be used to evaluate the probability that a given source will be lensed (Schneider et al., 1992). The gravitational lensing cross-section is often defined as the area of the lens plane (see Fig. 2.12 for reference) where a background source would be magnified by greater than some threshold value, $\mu_{\rm min}$ (where μ is the total magnification of all observed images). Where previous studies such as Muñoz et al. (2016) consider the ratio of magnifications between images to avoid the degeneracy between magnification and intrinsic brightness, we will consider the total magnification of both images and later derive observables that take the luminosity function of our sources into account. To calculate the angle around a lens associated with magnifications greater than $\mu_{\rm min}$ Eq. 2.49 can be inverted to yield (Schneider et al., 1992)

$$y(\mu_{\rm min}) = \sqrt{2\left(\frac{\mu_{\rm min}}{\sqrt{\mu_{\rm min}^2 - 1}} - 1\right)}, \tag{3.24}$$

where $y = \beta/\theta_E$ is the normalised angular impact parameter of the source background to the lens. This angle can then be converted into the physical area around the lens as

$$\sigma(\mu_{\rm min}) = \pi y(\mu_{\rm min})^2 \theta_E^2 D_d^2, \tag{3.25}$$

where D_d is the angular diameter distance of the lens plane.

As per the definition in Hogg (2000) (see also Schneider et al., 1992) the

optical depth for a cosmological distribution of objects may be represented as

$$\tau = \int_0^{z_s} d\chi(z_d)(1+z_d)^2 n\sigma(\mu_{\min}), \tag{3.26}$$

which is analogous to the form expressed in Eq. 3.20, where z_s is the redshift of the source, z_d is the redshift of the lens, $\chi(z_s)$ is the comoving distance associated with a redshift of z_s and n is the average comoving number density of lenses over the cosmological volume out to z_s. Following the derivation in B.1, equations 3.24, 3.25 and 3.26 can be combined to express the optical depth as

$$\begin{aligned}\tau = &\int_0^{z_s} dz_d \frac{2\Omega_L \rho_{\rm cr}}{\Sigma_{\rm cr}} \frac{c}{H(z_d)}(1+z_d)^2 \\ &\times \int_{\mu_{\min}}^{\infty} \frac{1}{(\mu^2-1)^{3/2}}\mu,\end{aligned} \tag{3.27}$$

which is equivalent to the form found by Turner et al. (1984), where Ω_L is the average density of lenses in the Universe in units of the critical density $\rho_{\rm cr}$ and $\Sigma_{\rm cr}$ is the critical surface density for strong lensing discussed in §2.2.2, expressed in terms of D_η, discussed in §3.1. Notably, for a circularly symmetric lens mass, the squared Einstein radius is proportional to the enclosed mass, resulting in the optical depth to lensing being independent of the mass of individual lenses. Instead, it depends only on the total mass of lenses in the Universe. Implicitly, this derivation assumes a uniform distribution of point mass lenses in comoving space (Turner et al., 1984). A natural question to arise from the lack of dependence on individual lens mass is, what is the minimum threshold for something to count as a lens? In the greater context of arbitrary density perturbations in an evolving universe, this question becomes complicated significantly beyond the scope of this thesis, requiring the degeneracies between different lens mass distributions to be considered (Wagner, 2018) and the gauge problem to be addressed (Ellis & Bruni, 1989). Here I make only simple considerations of what minimum point mass will

contribute to the lensing optical depth. These considerations are addressed in 3.2, resulting in the conclusion that a clump of mass greater than the mass that would be contained within a cone subtended, at the observer, by the source in a completely homogeneous universe will be counted as a lens for the purpose of determining Ω_L.

3.3.1 Correction for an Inhomogeneous Universe

From τ the probability of gravitational lensing can be derived using Eq. 3.21. However, as Ehlers & Schneider (1986) detail, this derivation implicitly assumes that all lines of sight have equal statistical weight. While this assumption holds in a homogeneous universe (which by definition has no gravitational lenses), in an inhomogeneous universe the distribution of sky magnifications violates this assumption. Ehlers & Schneider (1986) re-derive Eq. 3.20 taking an inhomogeneous universe into account, finding

$$\tau = \langle\mu(z_s)\rangle_a \int_0^{z_s} dz_d \frac{1}{\langle\mu(z_d)\rangle_a} \frac{2\Omega_L \rho_{\rm cr}}{\Sigma_{\rm cr}} \frac{c}{H(z_d)} (1+z_d)^2 \times \int_{\mu_{\rm min}}^{\infty} \frac{1}{(\mu^2-1)^{3/2}} d\mu. \tag{3.28}$$

The expression is different by a factor of $\langle\mu(z_s)\rangle_a / \langle\mu(z_d)\rangle_a$, where $\langle\mu(z)\rangle_a$ is the area averaged magnification with respect to the empty beam introduced in §3.1 at a redshift z. This average can be determined analytically as (Schneider & Weiss, 1988)

$$\langle\mu\rangle_a = \frac{D_\eta^2}{D_1^2}, \tag{3.29}$$

where D_1 is the conventional angular diameter distance, or equivalently D_η for $\eta = 1$. The area-averaged quantity is distinct from the directionally averaged version, which by the definition of magnification is precisely unity (Breton &

Fleury, 2020)

$$\langle \bar{\mu}^{-1} \rangle_\Omega \equiv \frac{1}{4\pi} \int_{4\pi} d^2\theta \frac{d^2\beta}{d^2\theta} = \frac{1}{4\pi} \int_{4\pi} d^2\beta = 1, \tag{3.30}$$

corresponding to the necessity that all background rays are mapped somewhere into the foreground by the lens, i.e. that total flux is conserved (Weinberg, 1976).

3.3.2 Shear Inclusion

So far only the convergence associated with an individual lens has been considered when calculating the probability of lensing above a given magnification. However, in an ensemble population of lenses the shear from other nearby lenses will be non-negligible, especially as the minimum considered magnification is reduced. As seen in Fig. 2.13 shear can change the shape of the observed image, it can also affect the lensing cross-section and therefore the probability of lensing above a given magnification. In a field of lenses these effects are non-linear, however, they are also analytically soluble for a thin screen of lenses as presented by Schneider (1987). This prescription is excellent for describing the lensing effect of an ensemble of compact lenses within an intervening galaxy's halo where the thin screen model is a good approximation. For an extended distribution of lens objects, however, the treatment is inadequate, failing to capture the effect of multiple shears at different redshifts. To fully capture this non-linear behaviour we would require numerical simulations. However, we can model the linear terms in the shear by treating our extended distribution of lenses as an infinite number of 2D lens planes, within each of which the shear is analytically calculable. This calculation is developed in Schneider & Weiss (1988) and we will make use of their work here.

The method of Schneider & Weiss (1988) calculates the probability of a light ray propagating through an extended distribution of point-mass lenses having magnification μ. This subsequently leads to the probability of a source having a given magnification. They derive the following expression for the probability

density of the magnification of a light ray:

$$P_R(\mu) = \frac{\langle\mu\rangle_a}{2\mu^2} \frac{Y(z_s)}{\left[Y(z_s)^2 + \langle\mu\rangle_a (1 - 1/\mu)\right]^{3/2}} \tag{3.31}$$

where $Y(z_s)$ is referred to as the effective optical depth and is calculated from the following Volterra integral equation of the 2nd type

$$Y(z_s) = \frac{D_\eta(z_s)}{D_1(z_s)} - 1 + \int_0^{z_s} dz_d\, \kappa'(z_d) \frac{D_{\eta,ds}(z_d, z_s)}{D_\eta(z_s)} Y(z_d), \tag{3.32}$$

where κ' is given by

$$\kappa'(z_d) = \frac{3H_0^2}{2cH(z_d)} D_1(z_d)\Omega_L(1 + z_d)^2 \tag{3.33}$$

closely resembling optical depth. To solve for Y the integral can be approximated as a sum over n small intervals in redshift

$$Y_n = K + \sum_{i=0}^{n-1} C_i Y_i \Delta x$$

where K and C are constants. This relation can be generalised as

$$Y_n = Y_{n-1} + C_{n-1} Y_{n-1} \Delta x$$

which can be solved easily using an iterative algorithm such as a for loop. As seen in Fig. 3.5 which is duplicated from Schneider & Weiss (1988).

3.3.3 Probability of Source Magnification

As seen in Fig. 2.16, a single source can be associated with multiple images of varying magnifications. For the random field of point masses considered here, there is no way to analytically predict the number of images that will be observed. As a result, there is no general way to relate the probability (P_R) of ray magni-

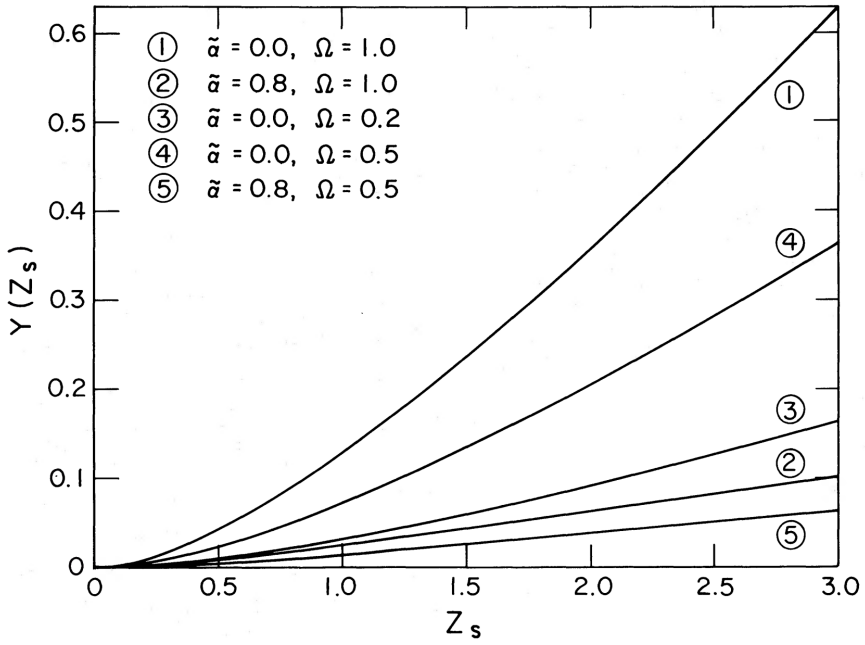

Figure 3.5: $Y(z_s)$ evaluated as a function of source redshift for varying choices of total energy density Ω and smoothness parameter $\eta = \tilde{\alpha}$, duplicated from Schneider & Weiss (1988). In each case the cosmologies are modelled assuming $\Lambda = 0$.

fication (μ) with the probability (P_S) of source magnification (μ_s) (Schneider & Weiss, 1988). In the simple case modelled by Eq. 3.20 the lenses are considered in isolation and hence this model will only be valid at low optical depths where only one lens needs to be considered (Turner et al., 1984). Similarly, the linear shear inclusive model will only be useful for calculating the expected source magnification in the limit where the number of images and their magnifications are well defined. Specifically, we follow Schneider & Weiss (1988), by adopting the hypothesis that in the limit of high magnification ($\mu \gg 1$), images occur in pairs (Refsdal, 1970) with $\mu_1 = -\mu_2$. As a result, the probability of source magnification can be calculated as

$$P_S(\mu_s) = \frac{\langle\mu\rangle_a}{\mu_s} P'_R\left(\mu = \frac{\mu_s}{2}\right) \tag{3.34}$$

$$P_S(\mu_s) = \frac{2\langle\mu\rangle_a^2}{\mu_s^3} \frac{Y(z_s)}{\left[Y(z_s)^2 + \langle\mu\rangle_a\,(1 - 2/\mu_s)\right]^{3/2}} \tag{3.35}$$

however this will only be valid for magnifications $\mu \gg 1$, corresponding to optical depths $\tau \ll 1$.

3.3.4 High Optical Depths

For a distribution of many lenses, such as the scenario of microlensing in a cluster considered by Diego et al. (2018), as the minimum considered magnification decreases towards one, the size of any given cross-section will increase towards infinity, and the optical depth to gravitational lensing will become large ($\tau \gtrsim 1$). At high optical depths, the distribution of magnifications associated with source positions is a caustic network similar to that shown in Fig. 3.6. In this regime, an observer is likely to see images associated with more than one lens, and therefore the simple analytical relations between source and ray magnification used above will no longer be valid (Schneider et al., 1992). Moreover, conversely to regular absorption, where an absorbed photon is effectively removed from the medium, a ray that has been gravitationally lensed continues to propagate through the medium and can be lensed again. This multiple lensing is a highly non-linear process, the general outcomes of which are difficult to predict analytically (Schneider et al., 1992). Recent works, however, have made significant progress towards the analytical treatment of these complex scenarios. Fleury et al. (2015) have shown that stochastic gravitational lensing may be more effectively modelled by treating the lensing matter density fields as white noise and modelling small scale lensing as a diffusion process; a generalised formalism to model the non-linear effects of multiple lensing has been developed by Schneider (2019); furthermore, the impact of finite beam effects in high optical depth scenarios, which could be important when considering lensing on the very small scales considered here, has been investigated in works by Fleury et al. (2017, 2019). These extensions are beyond the scope of this thesis and therefore I do not consider them further, but note that future considerations of small scale lensing may benefit from their consideration. Instead of the significantly more complicated analytical route, numerical

simulations can be used to create accurate empirical models of the magnification probability distribution associated with a caustic network, that can be easily applied.

From the above discussion we conclude that in the case of large magnifications, such as determining the optical depth to strong lensing for cosmological transients dominated by two images, the above equations should be sufficient. Whereas, for treating the effect of gravitational lensing on an ensemble population, a probability distribution valid for all magnifications is needed. In these cases, empirical definitions of the gravitational lensing probabilities from numerical simulations are more suitable as they implicitly handle much of the difficulty associated with the number of images per source and non-linear multiple lensing of those images. To further understand how lensing will affect these populations we must first understand the basics of cosmological populations and their observed source counts.

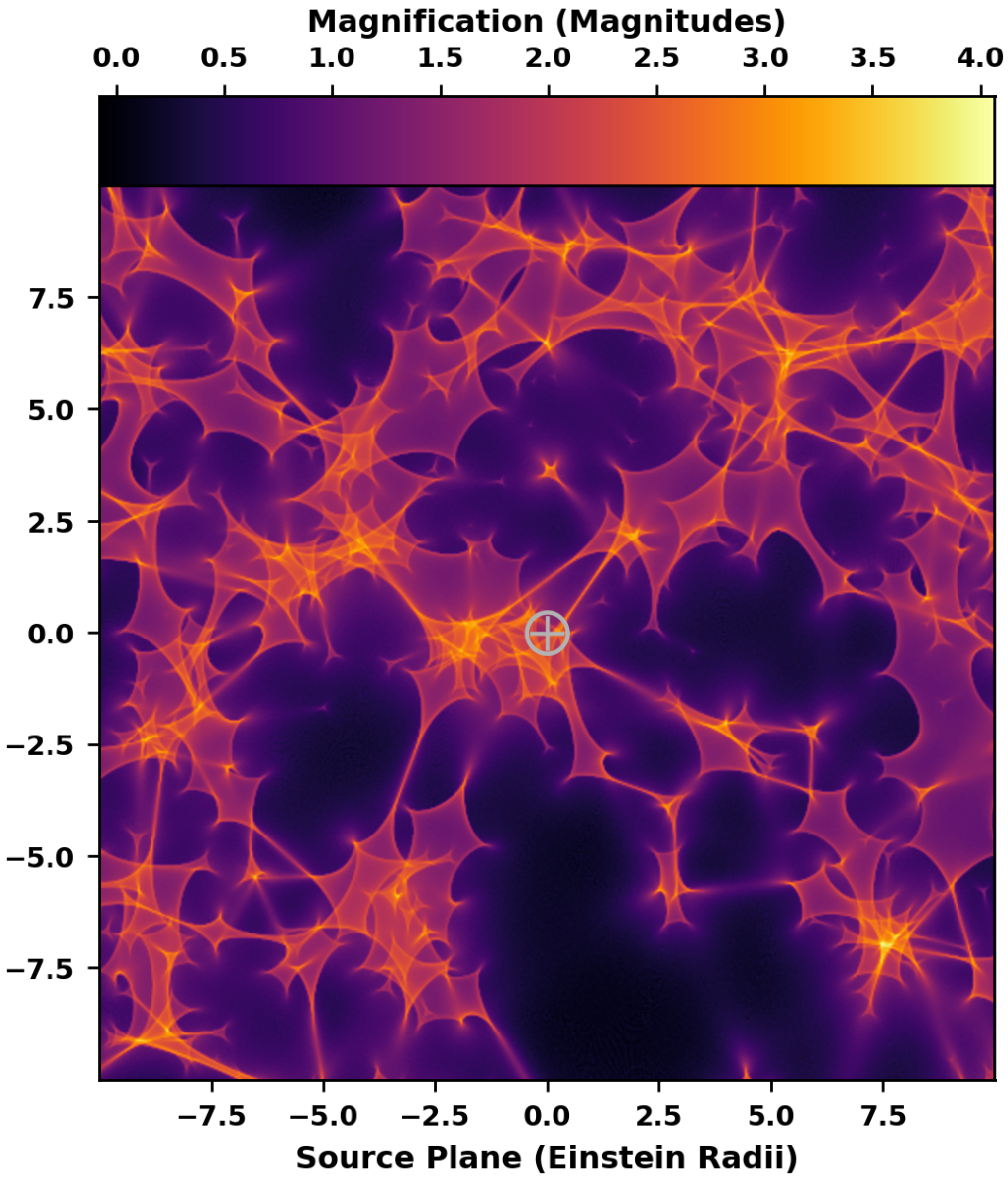

Figure 3.6: Map of source magnification showing the caustic network associated with gravitational lensing by a thin screen of randomly distributed point masses as simulated by Lewis (2020).

Chapter 4

Cosmological Populations

4.1 Source Counts

Source counts are one of the most fundamental observables in cosmology. In their integral form, they are simply the cumulative number of sources (N) observed above a given flux S. The differential form (dN/dS), however, is widely preferred, as the integral counts tend to wash out structure and are not statistically independent from one flux level to the next (Crawford et al., 1970; Jauncey, 1975). Source counts reflect both the intrinsic population of sources and the geometry of the Universe containing them and are thus potentially useful for constraining both (Ellis & Baldwin, 1984; Condon, 1988; Dam et al., 2023).

For the simple case of a Euclidean Universe populated by a uniform density of standard candle sources with luminosity L, the sources will be visible above some limiting flux S out to a distance D. The number of observed sources will be proportional to D^3, and as the observed flux of a source is inversely proportional to its distance squared, the relationship between the observed number and observed flux becomes $N \propto S^{-3/2}$ for the integral counts, and $dN/dS \propto S^{-5/2}$ in the differential case (von Hoerner, 1973).

For the considerably more complex case of a source population with an intrinsic distribution of luminosities in an expanding, homogeneous Universe, the

differential source counts can be expressed as

$$\frac{dN}{dS} = \int 16\pi^2 D_c^4 (1+z)^2 \, \phi(L,z) \frac{dD_c}{dz} dz, \tag{4.1}$$

as per §A.1.1, where $\phi(L,z)$ is known as the luminosity function of the population, describing the number density per unit luminosity as a function of both luminosity and redshift, to allow for an evolving population.

For the case of a non-evolving, standard candle population, the form of Eq. 4.1 can be reduced further to (see §A.1.1.2 for derivation)

$$\frac{dN}{dS} = 16\pi^2 D_c^4(z_0)(1+z_0)^2 N_0 \frac{c}{H(z_0)} \frac{1}{dL(z_0)/dz}, \tag{4.2}$$

where z_0 is the redshift corresponding to a flux S observed from a source of luminosity L, and N_0 represents the local spatial density of sources. For high S observations, where the corresponding z_0 is small, $dN/dS \propto S^{-5/2}$ just as in the Euclidean case (von Hoerner, 1973). For lower S observations, which probe higher z_0 however, the counts will depend only on the Universe's geometry, allowing cosmological parameters such as H_0 and Ω to be determined.

Prior to the determination of cosmological parameters through other means, this was one of the main goals of measuring extragalactic radio source counts (von Hoerner, 1973). In practice, however, the luminosity function and its evolution with redshift are difficult to distinguish from varying choices of cosmology and hence a precise determination of cosmological parameters from radio source counts was never made (Peacock, 1985; Kellermann & Wall, 1987). Extragalactic source counts have also been used to probe cosmic isotropy by measuring the amplitude and direction of the source count dipole. In an isotropic and homogeneous universe, any peculiar motion of the observer relative to the cosmic rest frame will induce a dipole in frequency dependent observables via Doppler shifting (Siewert et al., 2021). Such an effect is thought to be responsible for the prominent dipole observed in the CMB temperature, and a similar dipole was predicted to occur in

radio source counts due to their frequency dependent luminosity function (Ellis & Baldwin, 1984). Current estimates of the source count dipole (Colin et al., 2017; Dam et al., 2023) show it to be in the same direction as the CMB dipole, as predicted, but with a much higher amplitude. The cause of this discrepancy is an area of active research, see (Dam et al., 2023) for further discussion.

With the Universe's cosmology independently determined, source counts can also be used to study the luminosity functions and redshift distributions of source populations in their own right. The redshift and luminosity dependence of $\phi(L, z)$ are typically considered separately as $\phi_L(L)$ and $\phi_z(z)$. $\phi_L(L)$ is often assumed to have a power law form with an index γ, and is referred to as shallow or steep depending on whether $\gamma > -2.5$ or $\gamma < -2.5$ respectively. This division is made due to the qualitatively different behaviour expected for shallow and steep populations in a Euclidean geometry. Assuming no upper or lower luminosities, for $\gamma > -2.5$, observations of dN/dS will be dominated by observing fewer luminous sources at large distances as S increases. Conversely, for steep ϕ_L, dN/dS will be dominated by observing fewer weak sources nearby as S is increased. For a critical dependence of $\gamma = -2.5$, every S will be comprised of the same distribution of source luminosities and redshifts. These same conclusions apply locally for a non-Euclidean Universe, with the critical, $\gamma = -2.5$, limit changing at higher redshifts (Kellermann & Wall, 1987; Wall & Peacock, 1985).

For sources born through a stellar evolution channel, such as SNe, GRBs and FRBs, ϕ_z is often expressed with respect to the cosmic star formation rate (CSFR), ψ (Dahlén & Fransson, 1999; D'Avanzo, 2015; James et al., 2021b). Modelled in depth in Madau & Dickinson (2014), the CSFR is the functional form describing the average star formation rate over a cosmological volume as a function of redshift. Plotted in Fig. 4.1, the rate climbs from the present until approximately redshift $z \sim 2$, referred to as cosmic noon, before slowly decreasing towards earlier times. Physically, the relation between ϕ_z and ψ can be an indication of how the source evolved and how long it is expected to live.

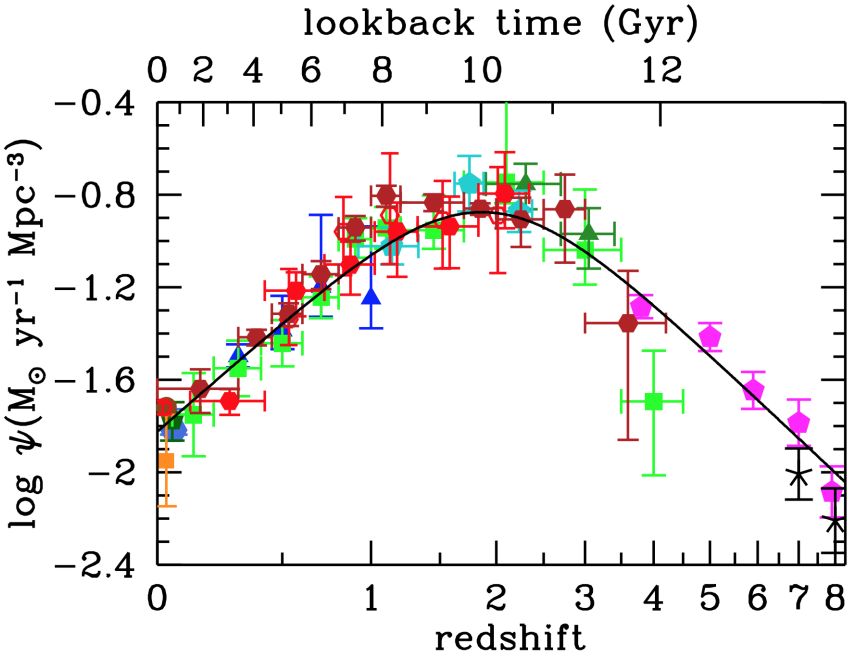

Figure 4.1: CSFR as a function of redshift and lookback time as plotted in Madau & Dickinson (2014). Data points are far ultraviolet and infrared measurements used to fit the model. For more discussion see associated paper. A tabular legend can be found in §A.1.

For $\phi_z \propto \int \psi$, the density of sources is proportional to the total number of stars created over cosmic time, suggesting that the progenitor must be extremely long-lived, such as a black hole (Fishbach et al., 2018). Alternatively, if $\phi_z \propto \psi$ the source must be short-lived and evolve swiftly from its stellar progenitor, such as core-collapse SNe evolving from a massive, short-lived star (Strolger et al., 2015).

By measuring the number of sources using source counts we can constrain both ϕ_L and ϕ_z, and therefore investigate the intrinsic nature of the source population. This is particularly important for sources such as FRBs whose progenitors are unknown. While the above is discussed for continuous sources, the same treatments apply to transient sources by simply replacing the total source count with the observed rate R as done in (Macquart & Ekers, 2018a). In order to make the correct inferences about the underlying population using the source counts, propagation effects such as gravitational lensing must also be taken into account. We discuss the impact of lensing on the observed event rate of transients such as

FRBs in §6, but first, we shall use the proceeding chapter to introduce FRBs.

4.2 Fast Radio Bursts

Fast radio bursts (FRBs) are bright, millisecond duration signals observed at radio wavelengths, originating from outside the Galaxy. Discovered in archival pulsar survey data by Lorimer et al. (2007), the first FRB (depicted in Fig. 2.1) displayed a DM more than ten times larger than the predicted Galactic DM value for this line of sight (Cordes & Lazio, 2003). As we discussed in §2.1, DM is equivalent to the integrated column density of electrons along the line of sight. Therefore, by assuming that the distribution of electrons is relatively uniform, DM can be used as a proxy for distance. Evidence in favour of this interpretation can be found in Shannon et al. (2018), where the authors note a relationship between DM and the fluence of bursts as shown in Fig. 4.2. Where flux is the relevant observable for continuous sources, fluence is the relevant observable for transient sources, representing the power per unit area, integrated over the duration of the burst. For FRBs, the fluence per unit bandwidth is a typical measurement, often reported in units of Jansky milliseconds (where a Jansky = Jy = 10^{-26}W m^{-2} Hz^{-1}). Fig. 4.2 shows that on average, lower fluence bursts tend to have large DMs. Also shown are two obvious groups of bursts, the blue bursts observed by ASKAP (Australian Square Kilometre Array Pathfinder) and the black bursts observed by Murriyang. The burst groups are separated in fluence due to the differing sensitivities and fields of view between the instruments. Dashed lines of constant spectral energy inferred from the ASKAP FRBs overlap with the bursts observed by Murriyang. This suggests that the Murriyang bursts have a similar distribution of intrinsic energies, but are observed at greater distances, leading to their lower observed fluence (Shannon et al., 2018). There is, therefore, a positive correlation between distance and DM.

The Lorimer burst was detected with a DM far in excess of other Galactic sources at similar positions. Therefore, Lorimer et al. (2007) contended that the

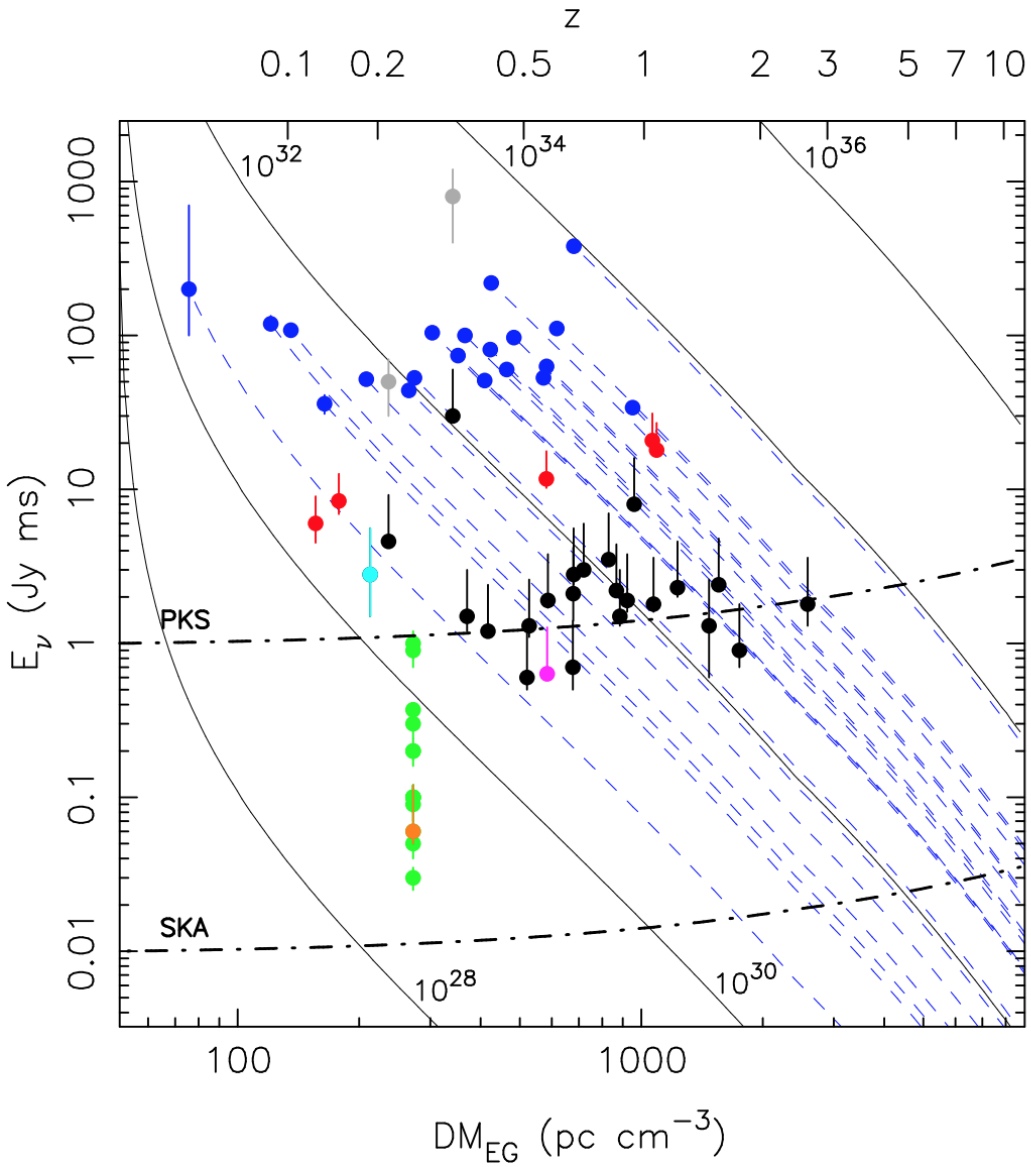

Figure 4.2: Estimated extragalactic DM, redshift (z), and observed fluence of all published FRBs at the time of publication ($\sim$ 50)(adapted from Shannon et al., 2018). FRBs are shown as dots and colour coded according to the instrument that observed them: ASKAP (blue), Murriyang/Parkes (black), UTMOST (red), GBT (magenta), Arecibo (green)(the repeater). The remainder are also observed by Murriyang, grey points are those where an instrumental correction displaced their position and the cyan point is suspected to be a Galactic source. Black contours depict lines of constant spectral energy. Blue dashed lines trace constant spectral energy for ASKAP FRBs. The dash-dotted lines show the constant fluence 10σ detection thresholds for ASKAP and Murriyang, including a cosmological time dilation correction for extreme distances associated with large dispersion measures.

burst likely originated from outside our Galaxy. Subsequent detections of other FRBs by Thornton et al. (2013) supported this claim, with their similarly large DMs and a seemingly isotropic sky distribution being inconsistent with a Galactic population. Both Lorimer et al. (2007) and Thornton et al. (2013) also posited that if FRBs were extragalactic, they may constitute an important probe of our Universe's baryonic content.

All of these initial FRB detections (Lorimer, 1998; Thornton et al., 2013) were made using the multi-beam system on Murriyang (Parkes), until FRB 20121102, which was observed by Spitler et al. (2014) using Arecibo. Confirmation of measurement at a separate observing site allayed any remaining concerns of a terrestrial signal origin, and subsequent study of this source revealed that FRBs can repeat, with the observation of 10 additional bursts (Spitler et al., 2016). Unlike the previous, apparently non-repeating, FRBs which were found using single dish instruments, *the repeater* (FRB 20121102) could be followed up with an interferometer, allowing it to be localised unambiguously to a host galaxy at a redshift of $z = 0.19273$ (Chatterjee et al., 2017; Tendulkar et al., 2017). This association confirmed the extragalactic nature of FRBs and associated *the repeater* with a persistent radio source (PRS) thought to be consistent with emission from the environment surrounding a compact object (Chatterjee et al., 2017; Chatterjee, 2021).

In the years following these initial discoveries, many FRB detections have been made. At the time of writing over 660 FRBs have been observed, with 50 known to repeat and 27 localised to host galaxies (Nimmo & Chatterjee, 2023). The largest single sample of FRB sources has been observed by the CHIME radio telescope (The CHIME/FRB Collaboration et al., 2021), which benefits from a large field of view at the cost of poor localisation on the sky. Identified repeaters have since been followed up by sensitive single-dish instruments such as Arecibo (Hewitt et al., 2021) and FAST (Xu et al., 2022) as well as very long baseline interferometers (VLBI) like the European VLBI network (EVN) (Nimmo et al.,

2022b), resulting in some repeaters being localised to sub-arcsecond precision, with hundreds of recorded bursts. For once-off bursts, similar localisations have been made by ASKAP, which boasts both a 31 $\deg^2$ field of view and arcsecond localisation (Hotan et al., 2021; Bannister, 2018). This allows for a high rate of FRBs to be observed and for each to be localised precisely from a single observation. As a result ASKAP has provided the greatest number of localised FRBs, most of which are apparently non-repeating (Petroff et al., 2022; Chatterjee, 2021).

By following up FRB host galaxies with spectroscopic instruments the redshifts of FRBs can be determined independently of the distance inferred from their DM. This allows the DM–redshift relationship, hereafter known as the Macquart relation, to be quantified and the fraction of ionised matter present in the IGM to be constrained (Macquart et al., 2020). More than 75% of the Universe's baryonic content was thought to exist in the IGM in a hot diffuse state, however, the diffuse nature of this matter made this hypothesis difficult to confirm (Fukugita & Peebles, 2004). As DM measurements are equally sensitive to all free electrons along the line of sight, regardless of their position or energy, it was the ideal probe to resolve this *missing baryon problem*. Using a sample of FRBs localised by CRAFT, Macquart et al. (2020) constrained the fraction of baryons in the IGM, resolving a significant problem in cosmology and demonstrating the potential of FRBs as a cosmological probe (see Cordes & Chatterjee, 2019; Chatterjee, 2021, for a review of the potential of FRBs as cosmological probes).

Subsequent studies of the Macquart relation have found that the contribution to DM from host galaxies is a significant source of error when estimating redshifts from DM (James et al., 2021a). As discussed in §2.1, the DM is simply the integrated electron column density along the line of sight, and therefore the total observed DM can be thought of as a summation of each major contribution

$$\mathrm{DM} = \mathrm{DM_{MW}} + \mathrm{DM_{IGM}} + \mathrm{DM_{Host}}, \tag{4.3}$$

where these sub-components denote the Milky-Way, IGM and host galaxy contributions respectively. Within the Milky-Way, measurements of DM have been made from pulsar observations (Cordes & Lazio, 2003) allowing this component to be estimated for any given FRB line of sight. As FRBs are often found at high Galactic latitudes this is often only a moderate contribution in the range of 10–100 pc cm^{-3}[1]. From the Macquart relation the contribution from the DM is to first order expected to increase linearly, with a rough rule of thumb yielding $\mathrm{DM_{IGM}} \sim 1000\, z_S$ (where z_S is the source redshift). As measurements of local galactic DM cannot be made in the host galaxy, this contribution is often more difficult to constrain, leading some studies to include it with $\mathrm{DM_{IGM}}$ as a total extragalactic DM term. Fig. 4.3 shows relative detection rates for FRBs as a function of extragalactic DM and source redshift, estimated from localised and unlocalised FRBs observed by both ASKAP and Murriyang (James et al., 2021a). The figure highlights the wide range of possible extragalactic DMs that correspond to any given redshift, and hence the difficulty in inferring a redshift from DM measurements.

Measuring the redshifts of FRBs directly from their host galaxies is a resource-intensive process that becomes increasingly difficult at large distances where FRBs are most useful for cosmological applications such as constraining H_0 (Hagstotz et al., 2022; James et al., 2022; Wu et al., 2022). Therefore, understanding host galaxy electron distributions and how they contribute to extragalactic DM is an active area of research that could allow for better redshift estimation of distant FRBs without host galaxy localisations. A potential avenue to improve estimates of $\mathrm{DM_{host}}$ is by constraining the position of the dominant scattering screens which contribute to the temporal broadening of FRBs. As described in §2.2, the scattering time induced by multi-path scattering through an extended, statistically uniform medium, will peak in at its geometric centre. Therefore it may be reasonable to expect that most of the observed scattering in FRBs comes

[1] Although for low Galactic latitudes the contirbution can be significantly greater.

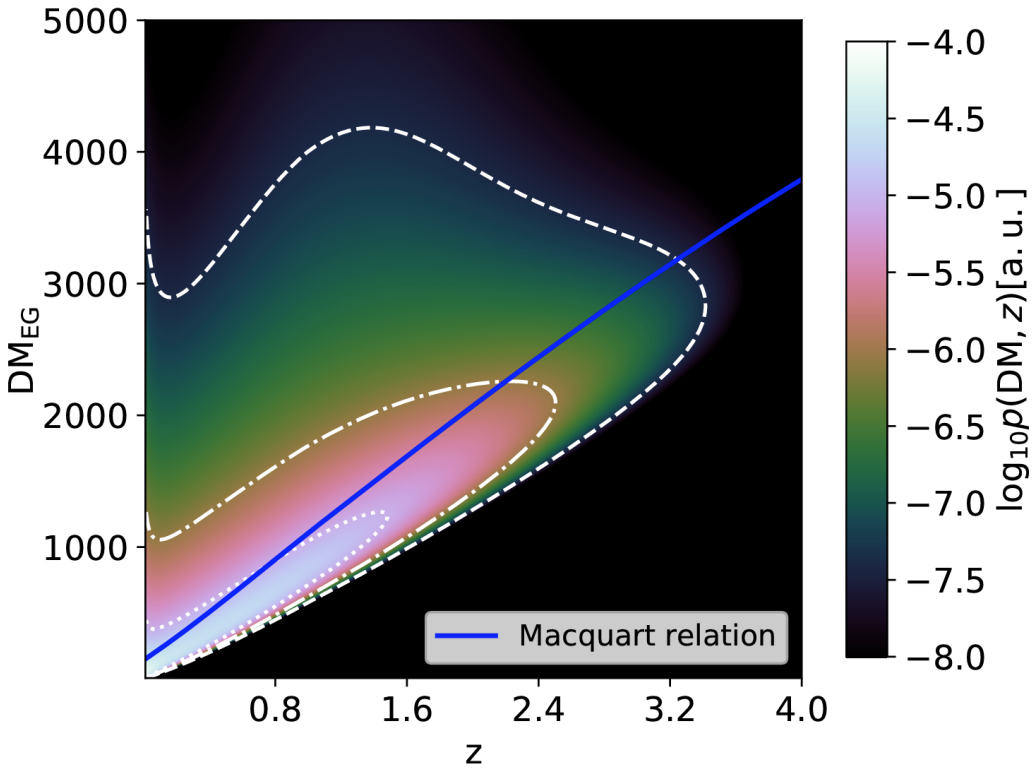

Figure 4.3: z–DM relation reproduced from James et al. (2021a). Depicted is the relative rate of FRB detections as a function of redshift z and extragalactic dispersion measure $\mathrm{DM_{EG}}$. Contours delineate 99% (dashed), 90% (dash-dotted) and 50% (dotted) of the observed population. Overplotted in blue is the linear Macquart relation (Macquart et al., 2020). This determination does not account for observational biases such as the effect of beam shape and burst width, and uses the best fit population parameters described in James et al. (2021a).

from the middle of the path, somewhere in the IGM. However, generally the IGM is expected to have very low plasma densities and therefore contribute negligibly to the scattering observed in FRBs (Macquart & Koay, 2013). Instead the dominant contribution may come from the host galaxy's ISM. This can be useful as, if the same plasma that contributes to $\mathrm{DM_{host}}$ causes the observed temporal broadening in an FRB, measurements of its scattering time could be used to constrain $\mathrm{DM_{host}}$ (Cordes et al., 2022). Recent studies suggest however that the dominant scattering observed in FRBs may come from much closer to the burst's source, and therefore are not useful for constraining the host galaxies ISM (Chawla et al., 2022; Ocker et al., 2022c,b). I investigate the position of FRB scattering screens further in §7.

Deriving the distance to an FRB also allows its intrinsic energy to be estimated from its fluence which is important to modelling the FRB progenitor population. From the energies inferred in Fig. 4.2, the population of FRBs must have a distribution of intrinsic energies analogous to the luminosity functions described in §4.1 (Petroff et al., 2022). However, inferring the intrinsic energy distribution from the observed fluences is non-trivial as the distribution of fluences we observe is affected by many biases (Connor, 2019). Early on, Macquart & Ekers (2018b) highlighted the discovery bias associated with including the initial Lorimer burst in statistical samples and discussed the detrimental effect of correcting for beam attenuation only in the brightest FRBs. Currently, using the model of Connor (2019), James et al. (2021b) and Luo et al. (2020) provide the most thorough estimates of the population parameters governing the luminosity function and redshift distribution of FRBs. Assuming a power law form, James et al. (2021b) find the distribution of intrinsic FRB energies is best fit by an index of $\gamma \approx -2$, in agreement with Luo et al. (2020), and they find the redshift distribution to be consistent with the CSFR, or a distribution that evolves faster with redshift.

As discussed in §4.1, a redshift distribution that follows the CSFR indicates that FRB sources must form quickly and be relatively short-lived. The currently

favoured FRB progenitor, the magnetar, is thought to be consistent with this picture (Zhang, 2022). A magnetar is a variation of a neutron star with an extreme magnetic field, typically defined as $\gtrsim 10^{14}\,\mathrm{G}$ (Zhang, 2022). Magnetars are expected to form quickly from massive stars, and their magnetic fields are thought to decay a short duration after their birth ($10^4\,\mathrm{yrs}$) (Colpi et al., 1999). As such the magnetar redshift distribution is expected to match the CSFR (Zhang et al., 2021), consistent with current constraints on the FRB progenitor population (James et al., 2021b). Along with many other potential progenitors (Platts et al., 2019; Cordes & Chatterjee, 2019; Chatterjee, 2021), magnetars were proposed early (Popov & Postnov, 2010), with their extreme magnetic fields providing the large energy required to generate an FRB (Lyubarsky, 2014; Beloborodov, 2017; Metzger et al., 2019). However, interest in the candidate progenitor was renewed in late 2020 with the detection of the so-called *Galactic FRB* (The CHIME/FRB Collaboration, 2020; Bochenek et al., 2020). While not as energetic as an extragalactic FRB, it has remarkably similar burst morphology and, notably, was detected coincident with x-ray emission from the Galactic magnetar SGR 1935+2154 (Ridnaia et al., 2021).

Another consistency with the magnetar picture is the presence of strong magnetic fields along the line of sight to some FRBs, inferred from their rotation measures (RM). Similarly to DM, RM is a measure of the product of the density of electrons with the parallel magnetic field component integrated along the line of sight, i.e. (Lyne & Graham-Smith, 2012)

$$\mathrm{RM} = \int n_e B_{||} d\ell, \tag{4.4}$$

where $B_{||}$ represents the magnetic field strength parallel to the line of sight integration element $d\ell$.

RM results from differential Faraday rotation of a signal's polarisation with frequency due to propagation in a magnetic field, and therefore manifests as a

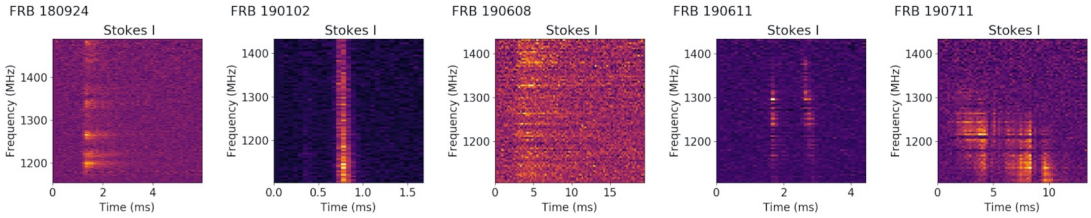

Figure 4.4: Stokes I dynamic spectra of five high-time resolution FRBs observed by CRAFT. Reproduced from Day et al. (2020).

varying linear polarisation angle in a signal's spectrum,

$$\mathrm{RM} = \frac{\theta_p}{\lambda^2}, \tag{4.5}$$

where θ_p is the angle of polarisation rotation. More than 10 FRBs have been observed to have RMs significantly in excess of the expectation for their lines of sight (Petroff et al., 2022), including both repeating (Marcote et al., 2020) and non-repeating (Masui et al., 2015; Day et al., 2020) sources. Moreover, the RMs of several repeating FRBs have been seen to fluctuate strongly on short time periods, indicating a dynamic local environment (Hilmarsson et al., 2021), or in some cases the re-orientation of local magnetic fields (Anna-Thomas et al., 2022). These cases suggest that the circum-burst environment of FRBs sometimes contains a high density of turbulent magneto-ionic material, consistent with what would be expected for a nebula-embedded magnetar (Margalit & Metzger, 2018). However, despite the aforementioned consistencies, there remains insufficient evidence to conclude that magnetars are dominantly responsible for the extragalactic FRB emission we detect (Zhang, 2022).

FRBs display a wide variety of observed pulse morphologies. As shown in Fig. 4.4, FRBs burst widths can range from several 10s of microseconds to several 10s of milliseconds, and they can be a single pulse or comprised of several overlapping components of various shapes and sizes in time and frequency space. A significant complexity when interpreting an observed dynamic spectrum is in the attribution of these complex behaviours to intrinsic phenomena associated

with the emission process or to propagation effects. By understanding the signature of propagation effects such as dispersion, its effect can often be accounted for, such as in dedispersion, leaving only the emission-relevant behaviours behind. The observed propagation effects also often carry information about the intervening medium, such as the baryonic content of the IGM, in the case of dispersion (Macquart et al., 2020). Furthermore, this information can also be of indirect use to constraining FRB progenitors, by constraining the kinds of environments to host them, e.g. observations of high RM hinting at a strongly magnetised source environment (Masui et al., 2015). At every turn, it is clear that understanding the propagation of FRBs is crucial to identifying their progenitors and probing new astrophysical regimes. Therefore, in this work, we aim to further explore the effect of lensing, scattering, and scintillation as they pertain to cosmological transients such as FRBs.

4.3 ASKAP Data Acquisition

To study the effects of propagation on FRBs we analyse FRBs observed by the CRAFT (Commensal Real-time ASKAP Fast Transient; Macquart et al., 2010) survey using ASKAP. ASKAP is a 36-element interferometer located at Inayarrimanha Ilgari Bundara, the CSIRO Murchison Radioastronomy Observatory in Western Australia. Each element of the interferometer is a 12 m dish capable of observing 31 square degrees of the sky simultaneously by using a phased array feed (PAF) to form 36 digital beams across the focal plane (Hotan et al., 2021).

FRBs are initially detected in real-time by searching intensity dynamic spectra summed incoherently over each of the two polarisations and each antenna (Bannister et al., 2019b). The dynamic spectra are comprised of 336 one MHz channels. The search algorithm, FREDDA (Bannister et al., 2019a), trials 4096 dispersion measures, up to a maximum of $\sim 4000\,\mathrm{pc\ cm^{-3}}$[2]. For each trial, the

[2]DMs of several hundred are typical for FRBs, with the largest DM for published ASKAP FRBs being 1457.624 pc cm^{-3} (Ryder et al., 2022).

result is integrated over frequency and FREDDA calculates the S/N ratio for convolutions of the de-dispersed time series with boxcars of lengths between 1 and 32 time samples. Instances with S/N ratio greater than 9 are treated as FRB candidates and trigger a download of the 3.1 s of voltage data immediately preceding the trigger, as saved by the ring buffer on each antenna for each of the two orthogonal polarisations (Bannister et al., 2019b). Only the voltages for the beam on each antenna containing the FRB candidate are saved.

The voltage data allow for both precision localisation (Bannister et al., 2019b; Prochaska et al., 2019a; Day et al., 2021; Ryder et al., 2022) of the FRB source and high-resolution analysis of burst morphology (Cho et al., 2020; Day et al., 2020). To localise an FRB the voltages are cross-correlated between antennas, flux calibrated against voltage data of a well-known calibrator source, and interferometrically imaged as described by Scott et al. (2023). Natively, the voltages are stored as coarse channel dynamic spectra with 336 MHz of bandwidth at 1 MHz resolution (Scott et al., 2023). To access high-resolution dynamic spectra, the voltage data from each antenna are beamformed towards the FRB's apparent position and the coarse channelisation of the voltages is undone through polyphase filterbank inversion (for technical details on PFB inversion see Cho et al., 2020). During the PFB inversion process, the data are also calibrated and coherently de-dispersed. Conversely to incoherent de-dispersion, which is the simple shifting of frequency channels by discrete time steps to account for dispersion (Zackay & Ofek, 2017), coherent de-dispersion rotates the complex voltages as a function of frequency to perfectly compensate for the dispersion introduced into the signal by cold plasma along the line of sight as detailed in §2.1. The ultimate result of the above processes is 3.1 s of complex-valued, de-dispersed time series, sampled at the inverse bandwidth $(336\,\mathrm{MHz})^{-1} \approx 3\,\mathrm{ns}$, for the two orthogonal polarisations. From this complex time series, intensity dynamic spectra containing the FRB can be formed at any time (Δt) and frequency ($\Delta\nu$) resolution such that $\Delta\nu\Delta t = 1$.

In addition to the FRB, the rendered dynamic spectra often contain frequency-

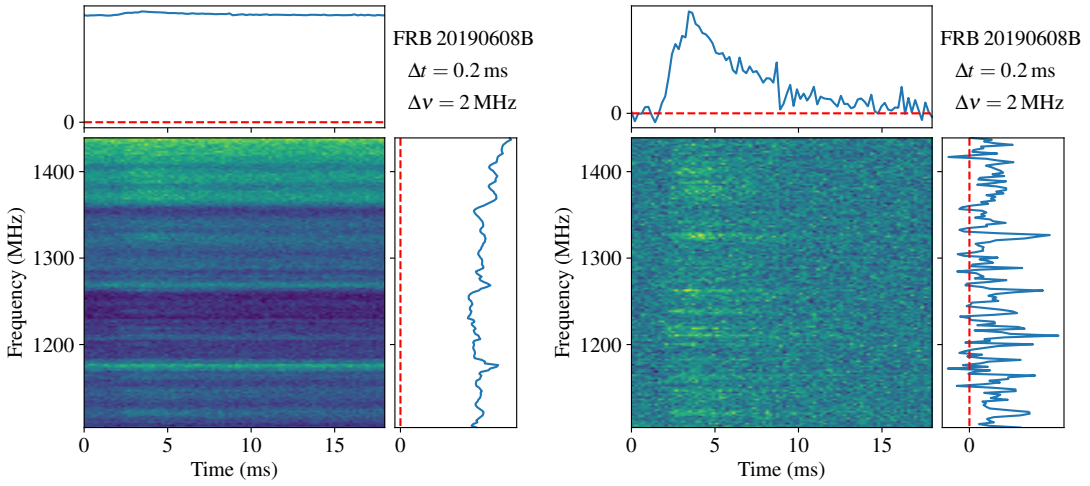

Figure 4.5: Dynamic spectra of FRB 20190608B rendered at a time and frequency resolution labeled in the top right-hand corner of each plot. Top sub-panels show the dynamic spectra integrated over the bandwidth, right hand sub-panels show the dynamic spectra integrated in time. *Left*: Unnormalised intensities containing RFI, seen as bright spectral channels which are stationary in time. *Right*: Intensities normalised by off-pulse spectrum.

dependent instrumental effects and radio frequency interference (RFI) from artificial sources which contaminate the astrophysical signal. To mitigate these effects we measure the mean and variance in intensity within each spectral channel in an off-pulse region that does not contain the FRB and then normalise the entire measurement by these values, subtracting the off-pulse mean and dividing by the off-pulse standard deviation. As shown in Fig. 4.5, this process removes any unwanted contamination in the measured burst spectra and converts the measured intensities to S/N for ease of interpretation. An implicit assumption in this method is that any instrumental effect or RFI signal is stationary in time, which can easily be verified by inspecting the unnormalised dynamic spectra. The normalised dynamic spectra constitute the final data product analysed in §5 & 7.

Chapter 5

First Constraints on Compact Dark Matter From Fast Radio Burst Microstructure

This chapter is comprised of a pre-copyedited, author-produced version of an article accepted for publication in *The Astrophysical Journal* following peer review. The version of record: Mawson W. Sammons, Jean-Pierre Macquart, Ron D. Ekers, Ryan M. Shannon, Hyerin Cho, J. Xavier Prochaska, Adam T. Deller and Cherie K. Day, First Constraints on Compact Dark Matter from Fast Radio Burst Microstructure, *The Astrophysical Journal*, Volume 900, Issue 2, id. 122, December 2022, is available online at: https://doi.org/10.3847/1538-4357/aba7bb. This work was motivated and supervised by A/Prof. Jean-Pierre Macquart. Initial calibration and pre-processing of data, including PFB inversion and dedispersion, was performed by Prof. Adam Deller, Dr Cherie Day and Ms. Hyerin Cho. I performed all analyses of the processed data, making use of code written by Prof. J. Xavier Prochaska to evaluate Galactic intersection probabilities. Prof. Ron Ekers and A/Prof. Ryan Shannon motivated sections on clumpy dark matter. Apart from Figure 3, which was generated for publication by Ms. Hyerin Cho, the draft manuscript was written by me and distributed to co-authors for

critique. All co-authors provided input over several iterations of feedback until the manuscript was complete.

5.1 Abstract

Despite existing constraints, it remains possible that up to 35% of all dark matter is comprised of compact objects, such as the black holes in the 10-100 $M_\odot$ range whose existence has been confirmed by LIGO. The strong gravitational lensing of transients such as FRBs and GRBs has been suggested as a more sensitive probe for compact dark matter than intensity fluctuations observed in microlensing experiments. Recently ASKAP has reported burst substructure down to 15μs timescales in FRBs in the redshift range $0.3 - 0.5$. We investigate here the implications of this for the detectability of compact dark matter by FRBs. We find that a sample size of ~ 130 FRBs would be required to constrain compact dark matter to less than the existing 35% limit with 95% confidence, if it were distributed along $\gtrsim 1$ Gpc-long FRB sightlines through the cosmic web. Conversely, existing constraints on the fraction of compact dark matter permit as many as 1 in ≈ 40 of all $z \lesssim 0.4$ FRBs to exhibit micro-lensed burst structure. Approximately 170 FRBs intercepting halos within ~ 50 kpc would be required to exclude the fraction of compact dark matter in each intercepted halo to a similar level. Furthermore, we consider the cumulative effects of lensing of the FRB signal by a macroscopic dark matter distribution. We conclude that lensing from a uniform distribution of compact objects is likely not observable, but suggest that FRBs may set meaningful limits on power-law distributions of dark matter.

5.2 Introduction

Dark matter comprises 24% of the energy density of the Universe (Bennett et al., 2013), yet its indeterminate form represents one of the largest unsolved problems in astrophysics. Exotic particles from outside the standard model, such as Weakly

Interacting Massive Particles (WIMPs) or axions have been invoked as possible explanations (see Bertone et al. (2005) for a review). However, some fraction of dark matter could reside in the Universe as compact objects, such as black holes or neutron stars.

Decades of extensive research has constrained the fraction of dark matter present in compact objects over a range of masses. Low mass objects ($10^{-7} M_{\odot} \lesssim M \lesssim 10\mathrm{M}_{\odot}$) are excluded as the dominant form of dark matter in the Milky Way and environs based on the absence of stellar variability caused by gravitational microlensing (Tisserand et al., 2007; Wyrzykowski et al., 2011; Alcock et al., 1997). High mass objects ($\gtrsim 100\mathrm{M}_{\odot}$) are excluded by the lack of expected kinematic perturbations to wide binary orbits and ultra faint dwarf galaxies (Quinn et al., 2009; Brandt, 2016).

The only population of compact objects that are not well constrained lie in the range of 10 to $100\mathrm{M}_{\odot}$. There is a known population of black holes in this mass range; gravitational wave observations by LIGO have detected several mergers of these black holes (LIGO Scientific Collaboration and Virgo Collaboration et al., 2019). Subsequent theories suggest that dark matter composed of $\sim 30\mathrm{M}_{\odot}$ primordial black holes could explain the merger event rates observed by LIGO (Bird et al., 2016; Clesse & García-Bellido, 2017; Sasaki et al., 2016). Better constraints on the fraction of compact dark matter within the 10-$100\mathrm{M}_{\odot}$ range could therefore be key in identifying some fraction of dark matter.

The strong gravitational lensing of extragalactic transients provides a way to either detect or to place more stringent constraints on dark matter. The strong lensing of type Ia supernovae has been used to limit the compact dark matter fraction to less than 35% for all objects more massive than $0.01\mathrm{M}_{\odot}$ (Zumalacárregui & Seljak, 2018). Recently, it has been realised that cosmological transients such as Gamma Ray Bursts (GRBs) and Fast Radio Bursts (FRBs) will allow constraints to be placed at a much higher significance (Ji et al., 2018; Laha, 2020).

In both cases strong lensing creates multiple images of the source. Unlike the gravitational lensing of quasars by foreground galaxies (Wong et al., 2019), the images formed by a compact object would be too close to be spatially resolved. However, the images of the source will arrive separated in time due to different gravitational and geometric time delays along each path. This temporal separation (Δt) is linearly dependent upon the lens mass, whereas the magnification ratio is mass independent. The lens mass and geometry can be constrained using these two observables. Due to the achromatic nature of gravitational lensing the same formalism initially suggested by Muñoz et al. (2016) for FRBs can be applied at all wavelengths. The formalism ignores the effect of physical optics, which becomes important when the Einstein radius of the lens is smaller than the Fresnel scale, $\sim \sqrt{D_{\rm eff}\lambda/2\pi}$, where $D_{\rm eff}$ is the effective distance to the lens. This occurs for lens masses less than $\sim 10^{-5}\mathrm{M}_{\odot}$ at a frequency of 1 GHz, and is well below the masses considered here; hence a full wave optics treatment, such as that explored by Jow et al. (2020), is not yet warranted.

Several thousands of GRBs have been discovered at redshifts $z \sim 1$ by dedicated GRB observatories such as *Swift*, *BATSE*, and *Fermi*. The cosmological distances they traverse allow them to probe a large volume of the Universe for compact dark matter. GRBs have a broad temporal profile ranging from milliseconds to minutes (Ji et al., 2018), and as a result, distinguishing multiple images is more difficult as the time delay between signals lensed by a $10\mathrm{M}_{\odot}$ compact object will be less than the duration of the GRB. Ji et al. (2018) have proposed auto-correlating the light curve as a method of detecting lensing. They conclude, however, that current GRB observatories would need to reduce their noise power by at least an order of magnitude to be able to detect lensing in the 10-$100\mathrm{M}_{\odot}$ mass range.

In contrast, FRBs have temporal profiles ranging from tens of microseconds (Cho et al., 2020) to several milliseconds, which is often shorter than the anticipated delay ($\sim$ 1ms) for lensing by compact objects in the mass range under

consideration here. This enables multiple images to be clearly distinguished, hence rendering FRBs considerably cleaner probes of compact structure along their sightlines. FRBs are highly luminous, extragalactic radio pulses, and those such as FRB 181112 (Cho et al., 2020) with substructure on timescales of a few tens of microseconds provide, to date, the finest timescale probe of sightlines at cosmological distances. Moreover, a unique capability of radio interferometric observations of such bursts is their ability to directly capture the *wavefield* of the each FRB at extremely high time resolution (3 ns; see Cho et al., 2020). This affords a powerful new diagnostic of the presence of gravitational lensing. The wavefield, which is directly observable at radio wavelengths, of any pair of paths in the lensed signal should be correlated, whereas burst substructure intrinsic to the FRB would not.

Of the FRBs localised to host galaxies so far, all have been at redshifts $z < 1$, placing the current sample generally closer in the Universe than GRBs (Ji et al., 2018; Coward et al., 2013; Bannister et al., 2019b; Prochaska et al., 2019a). However, this limitation can be overcome by inferring source redshifts from the dispersion measures of non-localised FRBs (Macquart et al., 2020); the existence of FRBs with dispersion measures exceeding $2000\,\mathrm{pc\,cm^{-3}}$ (e.g. Bhandari et al., 2018) ostensibly places some fraction of the population at $z > 2$.

To detect strong lensing, the temporal separation must be sufficiently large to allow each image to be distinguished. This is constrained by the shortest distinct temporal structure in the signal. In this paper we examine the implications of the high-time resolution structure observed in the FRBs 180924 and 181112. In FRB 180924 the shortest timescale corresponds to its rise time of only 30μs (Farah, 2020). FRB 181112 has recognisable temporal structure on the scale of 15μs, the shortest structure observed in an extragalactic radio signal (Cho et al., 2020). The resolution of temporal structures of $\sim 10\mu$s enables searches for lensing at temporal separations an order of magnitude below those considered in previous treatments (0.1 ms; Muñoz et al., 2016; Laha, 2020). The S/N of recorded

FRBs allows us to consider magnification ratios an order of magnitude above previous treatments (<5; Muñoz et al., 2016; Laha, 2020). Additionally, if the FRB passes close to an intervening galaxy, as it did for FRB 181112 (Prochaska et al., 2019a), it opens up the possibility of examining lensing attributable to a specific galaxy along the burst sightline, other than the host galaxy or the Milky Way. Muñoz et al. (2016) and Laha (2020) report that a sample of 10^4 FRBs would be required to exclude the compact dark matter fraction to less than 1%. Assuming a ΛCDM cosmology, we apply the same formalism to estimate the constraining potential of detected high time resolution FRBs comparable to FRBs 181112 and 180924.

5.3 Theory

In the weak field limit, where the gravitational potential $|\Phi| \ll c^2$, gravitational lensing can be modelled as an achromatic deflection of incident light by a thin screen. Under this treatment, a point mass lens will produce two images on the lens plane. The temporal separation, magnification ratio and position of these images are determined by the angular impact parameter of the source (β) normalised by the characteristic Einstein radius of the lens ($y = \beta/\theta_E$).

Here we briefly review previous theory as expounded by Muñoz et al. (2016) and Laha (2020). Following this formalism, the difference in arrival time between the images (Δt) and the ratio of each magnification (R_f) correspond to unique normalised angular impact parameters of the source $y_{\Delta t}$ and y_{R_f}, respectively. The relation between y_{R_f} and R_f can be expressed analytically as (Muñoz et al., 2016),

$$y_{R_f} = \sqrt{\frac{R_f + 1}{\sqrt{R_f}} - 2}, \tag{5.1}$$

which is notably independent of the lens mass. Conversely, $y_{\Delta t}$ cannot be derived

analytically and is found numerically from Muñoz et al. (2016):

$$\Delta t = \frac{4GM_L}{c^3}(1+z_L)\left[\frac{y}{2}\sqrt{y^2+4}+\ln\left(\frac{\sqrt{y^2+4}+y}{\sqrt{y^2+4}-y}\right)\right], \tag{5.2}$$

where M_L and z_L are the mass and redshift of the lens, respectively.

To detect gravitational lensing, we require the normalised angular impact parameter to be within the observable range ($y_{\rm min}$–$y_{\rm max}$). This range is defined by two conditions: (1) The associated time delay calculated from Eq. 5.2 must be less than the maximum observable time delay $\Delta t_{\rm max}$ and greater than the minimum distinguishable separation $\Delta t_{\rm min}$. The length of the observation sets $\Delta t_{\rm max}$, and $\Delta t_{\rm min}$ is set by the structure in the pulse profile (Muñoz et al., 2016). (2) The magnification ratio must be below the maximum ($\bar{R_f}$) set by the detection threshold (Muñoz et al., 2016).

For the thin screen approximation to be valid, the gravitational field at the impact parameter must also satisfy the weak field condition:

$$y_{\rm min} \gg \frac{R_S}{D_L\theta_E} \tag{5.3}$$

where R_S and D_L are respectively, the Schwarzschild radius and angular diameter distance of the lens. $y_{\rm min}$ and $y_{\rm max}$ define the annulus of the cross section to observable lensing. This cross section can then be used to calculate the observable lensing optical depth. Details on this calculation are provided in the following subsections for different environments. If the fraction of all dark matter that is compact ($f_{\rm DM}$) is assumed to be constant over redshift, the probability of observing lensing (P_L) at least once in a set of N FRBs can then be calculated as

$$P_L = 1 - \exp\left[-\sum_i^N \tau_i\right]. \tag{5.4}$$

where τ_i is the optical depth of the ith FRB in the set. To exclude compact dark matter fractions of $\geq f_{\rm DM}$ with 95% confidence, we require a null observation

of lensing in a set of FRBs with a cumulative observable lensing optical depth of 3.0. If lensing is rare we expect $\tau_i \ll 1$, however, a precise evaluation of the observable lensing optical depth probed by an FRB depends on our assumptions of where the lenses are distributed.

5.3.1 Lensing in Galaxy Halos

If we assume that compact dark matter takes the form of MACHOs (MAssive Compact Halo Objects), the only contribution to the lensing optical depth will come from the intervening galactic halos. In the local potential of a galaxy, the Hubble flow can be ignored and the optical depth calculated simply as

$$\begin{aligned}\tau &= \frac{f_{\rm DM}\Sigma_{\rm halo}}{M_L}\sigma \\ &= \frac{4\pi G f_{\rm DM}\Sigma_{\rm halo}}{c^2}\frac{D_L D_{LS}}{D_S}\left[y^2_{\rm max} - y^2_{\rm min}\right]\end{aligned} \tag{5.5}$$

where $\Sigma_{\rm halo}$ is the halo mass surface density, which will determine the number density of M_L mass compact lensing objects within the halo; D_L, D_{LS}, and D_S are the angular diameter distances from the observer to the lens, from the lens to the source and from the observer to the source respectively; and σ is the observable lensing cross section, as described by Laha (2020). We assume a Navarro-Frenk White (NFW) dark matter distribution (Navarro et al., 1996) for which $\Sigma_{\rm halo}$ has been derived by Bartelmann (1996). Implicitly this method assumes that the cross section of an individual lens is unaltered by the potential of the galaxy, given we are considering images separated by at most ~ 1 second, we find this to be a reasonable assumption.

5.3.2 Lensing in the Intergalactic Medium

Stellar remnants unbound from their host galaxies via natal kicks or gravitational interactions present a possible source of lensing in the intergalactic medium (IGM)(Atri et al., 2019), as do primordial black holes. Here, the effects of the

Hubble flow cannot be ignored. As derived in Muñoz et al. (2016) and Laha (2020), the optical depth to lensing of a single source by a single compact object in the IGM is

$$\begin{aligned}\tau &= \int_0^{z_s} d\chi(z_L)(1+z_L)^2 n_{\rm IGM}\sigma \\ &= \frac{3}{2} f_{\rm DM}\Omega_c \int_0^{z_s} dz_L \frac{H_0^2}{cH(z_L)} \frac{D_L D_{LS}}{D_S}(1+z_L)^2[y_{\rm max}^2 - y_{\rm min}^2],\end{aligned} \tag{5.6}$$

where χ is the co-moving distance, $n_{\rm IGM}$ is the average co-moving number density of the lens, $H(z_L)$ is Hubble's constant at the lens redshift and Ω_c is the current density of dark matter.

Both the halo and IGM lensing optical depths are separated into magnification and time-delay-limited domains over which $y_{\rm max}$ is limited by the corresponding condition. At low masses, $y_{\rm min}$ increases until $y_{\rm min} = y_{\rm max}$, and the optical depth to lensing becomes zero. The halo and IGM lensing optical depths are mass independent over a large range of lens masses. This can be understood by considering equations 5.5 and 5.6, respectively. The product of the Einstein radius squared and the projected number density is mass independent[1]. Hence, by expressing the cross section in terms of the normalised angular impact parameters $y_{\rm min}$ and $y_{\rm max}$, the source of the mass dependence in each optical depth becomes isolated to $y_{\rm min}$ and $y_{\rm max}$. In the magnification-limited domain, $y_{\rm max}$ is given by y_{R_f} and will be independent of the mass (Eq. 5.1). If y_{max} is also much greater than $y_{\rm min}$, then the optical depth to observable lensing in either the halo or IGM case will be effectively mass independent. The domain of this mass independent regime is determined by the minimum and maximum temporal separations.

[1]We highlight that this relies strongly on the assumption of a circularly symmetric lens potential, and therefore, in this work, we restrict ourselves to this case.

FRB	$\Delta t_{\rm min}(\mu{\rm s})$[1]	$\Delta t_{\rm max}(\mu{\rm s})$	$\bar{R}_f$[2]	z_s[3]
181112[4]	15	1.369	73.3	0.47550
180924	30	1.445	64.7	0.3214

Table 5.1: Observational parameters for localised high time resolution FRBs. $\Delta t_{\rm min}$ and $\Delta t_{\rm max}$ are defined respectively as the minimum and maximum observable time delays. $\bar{R}_f$ is defined as the maximum magnification ratio, set by the detection threshold. z_S is the source redshift. We highlight that FRB 181112 intercepted a foreground galaxy at $z = 0.3674$.

5.4 Results

The determination of the redshift of an FRB, either by localisation or by inference from its dispersion measure (Macquart et al., 2020), allows the formalism outlined in Section 5.3 to be applied. Here, we calculate the halo and IGM lensing optical depth for localised FRBs 181112 (Prochaska et al., 2019a) and 180924 (Bannister et al., 2019b). The temporal microstructure of these bursts has been resolved, enabling us to probe to the minimum value of $y_{\rm min}$ allowed by the burst structure. FRBs 181112 and 180924 probe a similar range of masses ($0.1{\rm M}_\odot \lesssim {\rm M} \lesssim 10^4{\rm M}_\odot$) due to their similar minimum and maximum temporal separations (Table 5.1). Over this range of masses, Eq. 5.3 is satisfied, and the strong field region is orders of magnitude smaller than the spatial scale probed by a temporal separation of $10\,\mu$s. This is the scale of the smallest distinguishable temporal separation amongst known FRBs; therefore, the weak field approximation is valid for all cases considered here.

The spectra of FRB 181112 shown in Fig. 5.1 (see also Cho et al., 2020) exhibits multi-peaked structure that could potentially be explained by gravitational lensing. Indeed, if the two major peaks are assumed to be two images, the temporal profile is consistent with gravitational lensing by a $\sim 10{\rm M}_\odot$ compact object in the halo of the foreground galaxy (hence referred to as FG 181112). Cho et al. (2020) test for the presence of microlensing by searching for correlations in the

burst wavefield with time; in the case of FRB 181112 no fringes between sub-pulses were seen, suggesting the pulse multiplicity is more likely intrinsic to the burst, rather than multiple lensed copies of the same burst. However, the absence of a correlation is not definitive since other effects, notably due to differences in any turbulent cold plasma encountered along the slightly separated sightlines of the lensed images, could scatter the radiation in different manners, and thus destroy the phase coherence between the lensed signals. However, in the present instance Cho et al. (2020) also find that the polarization properties of the sub-bursts differ in detail, particularly in their circular polarization, an effect which is difficult to attribute to lensing [2].

As recorded in Table 5.1, FRB 181112 had an extremely narrow pulse profile, with its shortest temporal structure being 15 μs. FRB 180924 had an extended scattering timescale of 580 μs but a short rise-time of 30 μs. Were any delayed lensed signal present, it would also have a sharp 30 μs rise time which would have been detectable within the tail of the overall pulse envelope. The maximum magnification ratios ($\bar{R}_f$) and redshifts are similar for each burst. To calculate $\bar{R}_f$, the S/N (signal-to-noise ratio) of the primary peak is divided by the detection threshold (3σ). A key difference between the two is that FRB 181112 passed within 29kpc of FG 181112, allowing it to probe a longer path through a galactic halo. In the following optical depth calculations these parameters are used to determine $y_{\rm min}$ and $y_{\rm max}$ from the equations defined in Section 5.3. For all following calculations, we use values for H_0 and the cosmological density parameters from the Planck 2018 results (Planck Collaboration et al., 2018).

[2]We can exclude circular polarization differences due to the existence of any relativistic plasma from a neutron star along the sightline, except at the source (where its presence would be irrelevant for the present argument). The lens mass of $10M_\odot$ required to explain the sub-burst time delays is significantly above the largest observed neutron star mass of $2.14M_\odot$ (Cromartie et al., 2020), ruling out neutron stars as potential lens candidates, and the effects of any relativistic plasma associated with them.

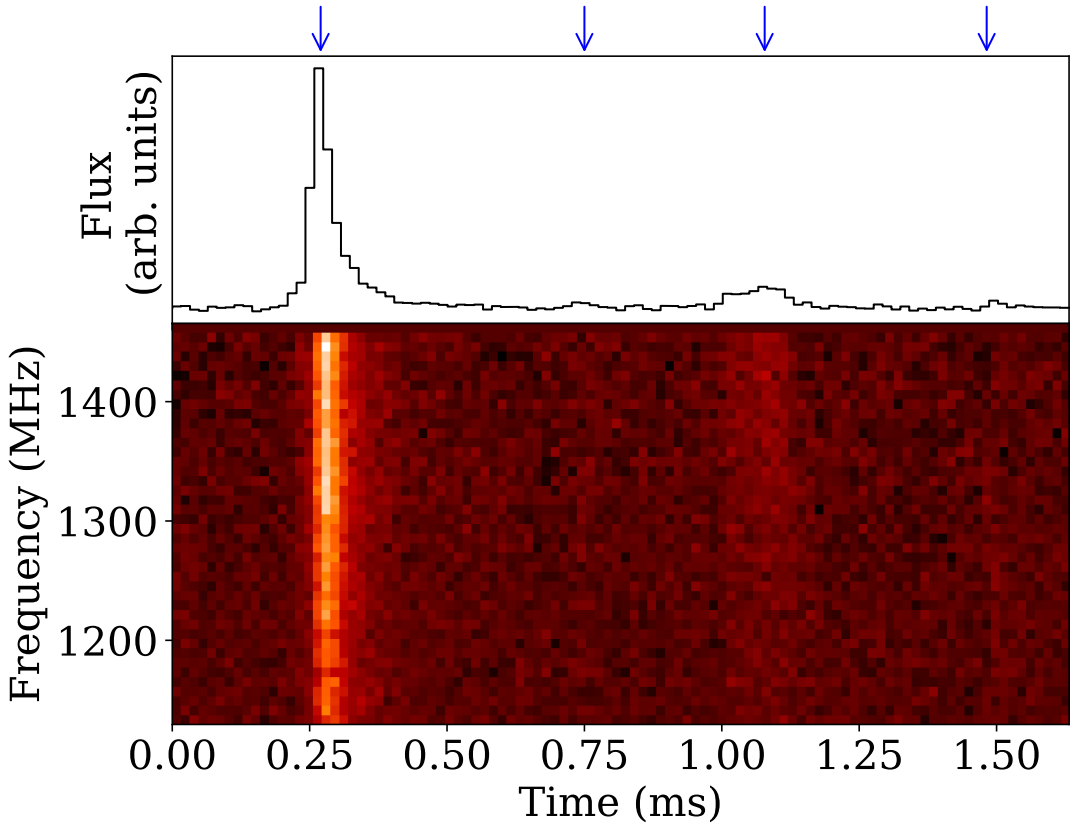

Figure 5.1: The pulse profile (top) and dynamic spectrum (bottom) of FRB 181112 at 16μs and 8MHz temporal and spectral resolution respectively (This representation is smoothed to 16μs to optimise the S/N, it is not the instrumental resolution). The pulse is seen to consist of two bright sub-pulses, at $t = 0.25$ ms and 1.1 ms, and two weaker sub-pulses at $t = 0.75$ ms and 1.50 ms, as indicated by the blue arrows.

5.4.1 Halo Lensing Optical Depth

The observable lensing cross section peaks approximately midway between the source and the observer and is minimal in both the host galaxy and the Milky way. Using the code of Prochaska et al. (2019b) we expect approximately one in 20 FRBs to intercept a foreground halo larger than $10^{12}\mathrm{M}_{\odot}$ within 50 kpc. This is consistent with recent optical followups of arcsecond-localised FRBs, including FRB 180924, which do not intercept massive galaxy halos within ~ 50 kpc (Bannister et al., 2019b; Chatterjee et al., 2017; Marcote et al., 2020). Consequently, these FRBs are of negligible value in constraining the dark matter halos of specific galaxies. FRB 181112, however, passes through a foreground galaxy where the cross section to lensing is much greater, making it an ideal candidate to constrain halo lensing.

Fig. 5.2 displays the optical depth to observable lensing by MACHOs probed by FRB 181112. This optical depth is dominated by the contribution from the halo of FG 181112. FG 181112 is classified as a Seyfert galaxy with an old $10^{10.69}\mathrm{M}_{\odot}$ stellar population (Prochaska et al., 2019a).

The white dotted line in Fig. 5.2 marks where the cross section to lensing becomes zero ($y_{\mathrm{min}} = y_{\mathrm{max}}$). Between this cutoff and a lens mass of $\sim 1\mathrm{M}_{\odot}$, y_{min} and y_{max} are comparable, and the optical depth to observing lensing depends on the mass of the lens. Above a lens mass of $\sim 1\mathrm{M}_{\odot}$, $y_{\mathrm{max}} \gg y_{\mathrm{min}}$ and the optical depth in the magnification-limited domain is approximately independent of mass. In the time-delay-limited domain, the optical depth decreases sharply as a function of mass. We estimate that to conclude with 95% confidence that the MACHO dark matter fraction is less than 35%, we require ~ 170 FRBs that intersect a foreground galaxy similar to FRB 181112. This estimate is projected from the optical depth $\tau \approx 0.018$ probed by FRB 181112 at $f_{DM} = 0.35$. Additionally, we can conclude with 90% confidence that the total mass, in the halo of the FG galaxy of FRB 181112, contained in uniformly distributed compact objects may be no more than $4.5 \times 10^{13}\mathrm{M}_{\odot}$. Prochaska et al. (2019a) estimate the halo mass of

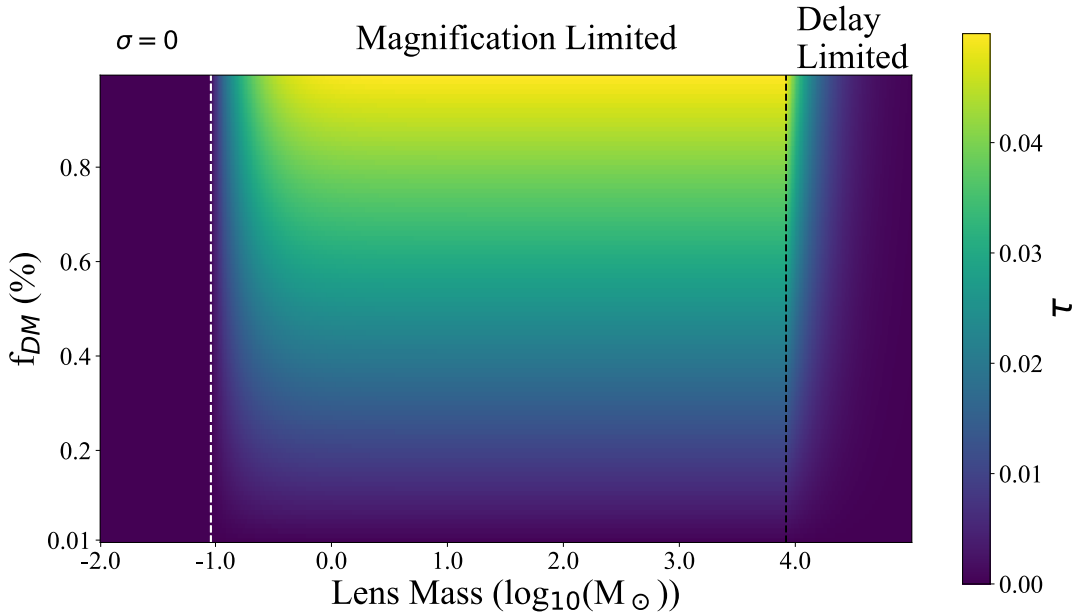

Figure 5.2: Optical depth to observable strong gravitational lensing by a point mass compact object of mass M_L probed by FRB 181112. For masses below the black dotted line $y_{\rm max}$ is limited by the maximum magnification ratio, above $y_{\rm max}$ is limited by the maximum time delay. The white dotted line marks the mass where $y_{\rm min}$=$y_{\rm max}$ and $\sigma = 0$. This calculation assumes an NFW distribution of compact objects of a single mass M_L, comprising a fraction $f_{\rm DM}$ of the host, Milky Way and foreground galaxies. FG 181112 is modelled to have a halo virial mass $M_{\rm halo} = 10^{12}{\rm M}_\odot$ (Prochaska et al., 2019a) and a concentration parameter of $c \sim 7$.

FG 181112 to be $M_{\rm halo} \approx 10^{12.3}\,{\rm M}_\odot$, and therefore this limit is not constraining. Alternatively stated, a single burst probes an insufficient lensing optical depth to be informative.

5.4.2 Lensing by Structure in the Cosmic Web

Fig. 5.3 displays the optical depth to lensing by a compact object due to any compact dark matter present throughout the cosmic web by FRB 181112 and FRB 180924, assuming that the dark matter density along their sightlines are representative of the mean cosmological dark matter density $\Omega_{\rm DM}$. This case shows the same trends as the halo lensing case, albeit with a much higher overall optical depth. Unlike in the halo lensing case, compact objects can be encountered

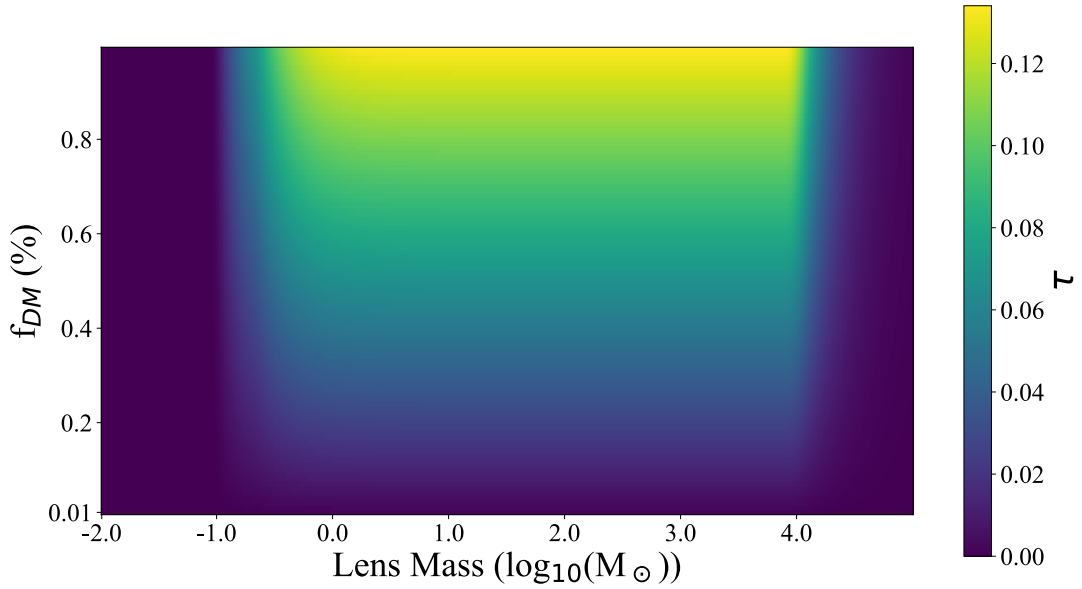

Figure 5.3: Cumulative optical Depth to observable strong gravitational lensing by a point mass compact object of mass M_L in the IGM probed by FRB 181112 and FRB 180924. We assume a uniform distribution of M_L mass compact objects in co-moving space comprising a fraction $f_{\rm DM}$ of the total dark matter of the Universe.

anywhere in the path of an FRB. As a result, FRBs probe a much greater optical depth to lensing in this scenario. We estimate that to exclude compact dark matter fractions above 35% with 95% confidence, a comparatively smaller sample of ~ 130 FRBs would be required. Furthermore, this sample may be comprised of any observed FRBs. This estimate is projected from the average optical depth $\tau \approx 0.024$ probed by FRB 181112 or FRB 180924 at $f_{DM} = 0.35$. Under a different assumed FRB redshift distribution, Laha (2020) and Muñoz et al. (2016) estimate that to exclude $f_{DM} \geq 1\%$ with 99% confidence, 10^4 FRBs would be required.

5.4.3 Gravitational Scattering

So far our treatment has been restricted to lensing by a single point mass. However, it is possible in principle that an ensemble of low mass clumps could collectively lens an FRB signal, characterising it with an achromatic, exponential scattering tail (Macquart, 2004).

We are thus motivated to examine whether gravitational scattering, caused by a cloud of substructure within a dark matter halo is observable. Within FRB 181112, we do not observe a clear exponentially decaying scattering tail, placing an upper limit to the scattering timescale $\sim 20\mu$s (Cho et al., 2020). The lack of this feature was interpreted as a lack of turbulent plasma along the line of sight, as discussed in Prochaska et al. (2019a). However, it also places a constraint on the mass of lensing substructure in the intervening halo. Here we introduce the relevant theory and present some cursory constraints, leaving a more exhaustive treatment to a future paper. In the limit where a large number of lenses exist within the coherence area, a statistical approach is mandated, and the characteristic delay timescale is, analogous to scattering in an inhomogeneous plasma (Macquart, 2004),

$$t_{\rm scatt} = \frac{1}{2\pi\nu}\frac{r_F^2}{r_{\rm diff}^2}, \tag{5.7}$$

where r_F is the Fresnel radius given by

$$r_F^2 = \frac{cD_L D_{LS}}{2\pi\nu D_S(1+z_L)} \tag{5.8}$$

and $r_{\rm diff}$ is the length scale over which the mass density fluctuations cause the gravitational phase delay to fluctuate by one radian RMS.

To solve for the diffractive scale we must consider the RMS phase difference in the fluctuations over varying scales of the mass distribution. This quantity can be calculated from phase structure function (Macquart, 2004)

$$D_\psi(r) = \langle[\psi(\vec{r'}-\vec{r}) - \psi(\vec{r'})]^2\rangle = 2K^2 \int d^2\vec{q}\left[1 - e^{i\vec{q}\cdot\vec{r}}\right] q^{-4}\Phi_\Sigma(\vec{q}), \tag{5.9}$$

which is the means square difference in phase fluctuations as a function of the separation ($\vec{r}$), spatial wavevector ($\vec{q}$) and the mass surface density power spectrum ($\Phi_\Sigma(\vec{q})$), in keeping with our thin screen approximation.

In a simple model, where we assume a Poisson distribution of clumps (i.e. the number of clumps in any given area will be sampled from a Poisson distribution

with an average density of Σ), Eq. 5.9 gives (see, e.g., Macquart, 2004)

$$r_{\rm diff} = 2.2 \times 10^2 (1+z_L)^{-1} \nu^{-1} \left(\frac{M}{1\,{\rm M}_\odot}\right)^{-1} \left(\frac{\Sigma}{100\ {\rm clusters\ pc}^{-2}}\right)^{-1/2} {\rm pc}, \quad (5.10)$$

where Σ is the projected number density of clusters, assumed to be locally uniform. To achieve a smooth scattering tail, the number of lenses must exceed unity within the coherence area $\sim \pi r_F^2$, to the point where the discrete contributions of individual lenses would be indiscernible. Assuming that the halo of FG 181112 obeys a NFW profile with a scale radius $R_s = 24\,{\rm kpc}$ and a virial mass $10^{12}\,{\rm M}_\odot$(Prochaska et al., 2019a), this would require a lens mass $M_L \ll \Sigma \pi r_F^2 \approx 3.7 \times 10^{-8} {\rm M}_\odot$ for a Fresnel scale of $\sim$ 3AU and an impact parameter of 29 kpc (even if all the matter were contained in clumps of this size). The characteristic time delay for gravitational scattering at 1.2 GHz would therefore be much less than $\sim 3.3 \times 10^{-14}$s (from Eq. 5.7). Thus, we do not expect to observe any scattering tail associated with the lensing from a distribution of compact objects with a uniform density.

Under a CDM/WDM treatment, it is plausible that galactic dark matter could cluster following a spatial power law (Macquart, 2004), similarly to turbulent distributions of neutral gas and ionised plasma, which have been observed to have spectral indexes of $3 \lesssim \beta \lesssim 4$ (Armstrong et al., 1995; Dickey et al., 2001; Stanimirović & Lazarian, 2001; Macquart, 2004). A power law spectrum of mass density fluctuations can be projected onto a screen of thickness ΔL to give the mass surface density power spectrum required in Eq. 5.9. Following the derivation of the phase structure function in Macquart (2004), for a power spectrum with an index β, between some inner ($l_0 = 1/q_{\rm max}$) and outer ($L_0 = 1/q_{\rm min}$) scales gives:

$$D_\psi(r) \approx \frac{4\pi^2 (3-\beta) K^2 \Delta L M_\sigma^2}{\beta} r^2 \times \begin{cases} L_0^{-3} \left(\frac{L_0}{l_0}\right)^{\beta-3} & \beta < 3 \\ -L_0^{-3} & \beta > 3 \end{cases} \quad (5.11)$$

where $K = -8\pi(1+z_L)G/(\lambda c^2)$ and M_σ is the RMS of the matter fluctuations

within a cell of size L_0^3.

If $\beta > 3$, as suggested by Macquart (2004), the mass variance is dominated by fluctuations at the outer scale, rendering a diffraction length of (Macquart, 2004)

$$r_{\rm diff} = 1.29 \times 10^{-11} \left(\frac{\beta-3}{\beta}\right)^{-1/2} (1+z_L)^{-1} \left(\frac{\nu}{1{\rm GHz}}\right)^{-1} \times \left(\frac{M_\sigma}{10^9 M_\odot}\right)^{-1} \left(\frac{\Delta L}{10{\rm kpc}}\right)^{-1/2} \left(\frac{L_0}{10{\rm kpc}}\right)^{3/2} {\rm pc}. \quad (5.12)$$

We calculate M_σ from the average density within the cell at a radius equal to the FRB's galactic impact parameter. The screen thickness (ΔL) is set such that the product, $M_\sigma \Delta L / L_0$ is equal to the RMS mass along the FRB's path, $M_\sigma \Delta L / L_0 \approx 5.7 \times 10^9 M_\odot$. Assuming again that the halo of FG 181112 obeys a NFW profile with a scale radius $R_s = 24\,{\rm kpc}$ and a virial mass $10^{12}\,{\rm M}_\odot$ (Prochaska et al., 2019a), Eq. 5.12 yields a diffractive scale of 1.0×10^{-10}pc and a scattering timescale of $t_{\rm scatt} = 280s$ for $\beta = 3.5$ and $L_0 = 10\,{\rm kpc}$. The scattering timescale has a shallower than linear dependence upon the index β (note that the singularity at $\beta = 3$) and is linearly proportional to L_0^3. The absence of an exponential scattering tail longer than $\sim 20\mu$s allows us to exclude, in the halo of FG 181112, the presence of hierarchically clustered dark matter of a power law index $3 < \beta < 4$ with an outer scale $L_0 \gtrsim 70$ pc.

For a value of beta $0 < \beta < 3$ fluctuations at the outer scale no longer dominate the variance in the phase difference across the scattering screen and we must account for contributions at the inner scale. A derivation of the diffractive scale equation yields

$$r_{\rm diff} = 1.29 \times 10^{-5} 10^{-2\beta} \left(\frac{3-\beta}{\beta}\right)^{-1/2} (1+z_L)^{-1} \left(\frac{\nu}{1\,{\rm GHz}}\right)^{-1} \times \left(\frac{M_\sigma}{10^9 M_\odot}\right)^{-1} \left(\frac{\Delta L}{10{\rm kpc}}\right)^{-1/2} \left(\frac{l_0}{\rm pc}\right)^{\frac{\beta-3}{2}} \left(\frac{L_0}{10{\rm kpc}}\right)^{\frac{6-\beta}{2}} {\rm pc}. \quad (5.13)$$

This derivation is outlined by Macquart (2004), however his result is incorrect by

a factor of l_0^2/L_0^2 (algebraic error). For the case of FG 181112, Eq. 5.13 yields a diffractive scale of 3.8×10^{-9} pc and a scattering timescale of $t_{\rm scatt} = 1.9$ ms for $\beta = 1.5$, $L_0 = 10$ kpc and $l_0 = 1$ pc. In this regime the scattering time has a steep, non-linear dependence on β, with scale dependence shifting slowly from the inner to the outer scale as β increases from zero to three. Clearly the scattering time is degenerate with the choice of inner (l_0) and outer (L_0) scales and the index of the power law distribution (β), reducing the possible inferences which can be made regarding the hierarchically distributed dark matter in FG 181112. However, from the observation of FRB 181112 and Eq. 5.13 we can form a bounding surface to constrain the possible values of L_0, l_0 and β, as given by:

$$l_0 < \left(88.14 \times 10^{-2\beta} \left(\frac{3-\beta}{\beta}\right)^{-1/2} \left(\frac{L_0}{10\,\mathrm{kpc}}\right)^{-\beta/2}\right)^{2/(3-\beta)} \mathrm{pc}. \tag{5.14}$$

Crucially, for a warm dark matter model, the inner scale is the free streaming scale, below which all structure is suppressed by the dynamics of a collisionless dark matter fluid. The free-streaming scale has been related to the particle mass of some dark matter candidates (Padmanabhan, 2000), opening the door for FRBs to directly constrain particle mass in select dark matter models.

5.5 Discussion

As a consequence of the greatly improved temporal resolution of FRBs 181112 and 180924 we have been able to probe to much smaller mass scales than considered in previous treatments. Longer observation of FRBs would allow greater maximum temporal separations to be observed, extending the mass independent regime of any constraints to higher masses. Improvements to sensitivity will boost S/N and increase $y_{\rm max}$ in the magnification-limited regime. A larger $y_{\rm max}$ yields a larger cross section and consequently a greater observable lensing optical depth, thus providing a more sensitive probe to small scale structure.

FRBs captured at high time resolution represent an opportunity to explore

fine structure of galaxy halos and clusters on unprecedented scales. We have focused here on the potential for FRBs to detect compact objects and derived simple constraints on non-baryonic dark matter models. The favoured ΛCDM cosmology is well known for its success describing the large scale structure of our Universe, but it faces a number of challenges on length scales below 1 Mpc (Bullock & Boylan-Kolchin, 2017). To meet these challenges, the substructure of dark halos must be understood, and, as shown, high time resolution FRBs provide us with the means to do so by directly constraining the inner scale of hierarchically clustered dark matter.

To exclude lensing with 95% confidence, a cumulative optical depth of 3.0 is required. From Figures 5.2 and 5.3, we estimate the optical depth probed by an FRB similar to those considered here at a range of compact dark matter fractions. The cumulative optical depth probed by a set of FRBs is simply the summation of their individual optical depths as per Eq. 5.4. Hence, we can predict the number of FRBs that would be required to make a desired constraint. The number required varies with $f_{\rm DM}$, the desired confidence level and the assumed distribution (e.g. in halos or distributed throughout the cosmic web). The cumulative optical depth required is non–linear with the desired level of confidence, and, hence, a lesser constraint of 80-90% would require a sample of 54-77% the size, respectively. Conversely, the cumulative optical depth required, is linear with the compact dark matter fraction, i.e. to exclude the compact dark matter fraction with the same confidence to below $0.5 f_{\rm DM}$ requires a sample twice the size.

In summary, recent FRBs detections, made at high time resolution, have revealed the potential of FRBs to probe dark matter within our Universe. The fact that FRBs have narrower temporal structure than previously assumed in gravitational lensing studies, allows searches for smaller lens masses than previously considered. The probability of observing halo lensing, in an FRB similar to FRB 181112, is ~ 0.017 (assuming $f_{DM} \leq 0.35$). To exclude $f_{DM} \geq 0.35$, in galaxy halos, would require a sample of ~ 170 FRBs like FRB 181112. The probability of

observing lensing anywhere along the sightline, in an FRB similar to FRB 181112 or FRB 180924, is ~ 0.023 (assuming $f_{DM} \leq 0.35$). This is a lower limit, in the sense that a large fraction of FRBs have dispersion measures that place them at higher redshifts than these two bursts and it ignores the possibility that the sample of already detected bursts favours lensed events through magnification bias. Thus, it is possible that a significant number of the sample of > 100 FRBs known to date have been lensed, although the lower time resolution and lower S/N of a large fraction of these previous detections would substantially hinder the discoverability of any lensing signal. To exclude $f_{DM} \geq 0.35$, in the IGM, would require detection of ~ 130 FRBs similar to FRB 181112 or FRB 180924. Compared to similar constraints made recently by Paynter et al. (2021) using a sample of ~ 2700 GRBs, a sample of FRBs similar to those measured here would need to be approximately six times larger in size to yield comparable limits for the range of PBH masses considered here. This difference is due mostly to the mean GRB redshift assumed by Paynter et al. (2021) being substantially higher, at $\langle z \rangle \approx 2$, than the mean of our sample $\langle z \rangle \approx 0.4$. Conversely, the number of FRBs required to form limits competitive with those from type Ia supernovae is approximately an order of magnitude lower (Zumalacárregui & Seljak, 2018), although the fundamental differences in methodology make a direct comparison of the value of individual events difficult. Finally, we conclude that when distributed as a uniform field of compact objects, the volume filling factor of dark matter in FG 181112 is likely insufficient to contribute to the temporal scatter-broadening of FRBs on nanosecond to microsecond timescales. However, the gravitational scattering of FRBs does present a promising probe of hierarchically clustered dark matter.

Chapter 6

The Effect of Gravitational Lensing on Fast Transient Event Rates

This chapter is comprised of a pre-copyedited, author-produced version of an article accepted for publication in *Monthly Notices of the Royal Astronomical Society* following peer review. The version of record: Mawson W Sammons, C W James, C M Trott, M Walker, The effect of gravitational lensing on fast transient event rates, *Monthly Notices of the Royal Astronomical Society*, Volume 517, Issue 4, December 2022, Pages 5216–5231 is available online at: https://doi.org/10.1093/mnras/stac3013. Its contents are my own work, except for the input and supervision from Prof. Cathryn Trott, Dr. Clancy James and Dr. Mark Walker during the modelling of lensing probabilities and implementation of numerical integration routines. I wrote the draft of the paper and distributed copies to all co-authors for critique. All co-authors provided input over several iterations of feedback until the manuscript was complete.

6.1 Abstract

Fast cosmological transients such as fast radio bursts (FRBs) and gamma-ray bursts (GRBs) represent a class of sources more compact than any other cosmological object. As such they are sensitive to significant magnification via gravitational lensing from a class of lenses which are not well-constrained by observations today. Low-mass primordial black holes are one such candidate which may constitute a significant fraction of the Universe's dark matter. Current observations only constrain their density in the nearby Universe, giving fast transients from cosmological distances the potential to form complementary constraints. Motivated by this, we calculate the effect that gravitational lensing from a cosmological distribution of compact objects would have on the observed rates of FRBs and GRBs. For static lensing geometries, we rule out the prospect that all FRBs are gravitationally lensed for a range of lens masses and show that lens masses greater than $10^{-5}M_{\odot}$ can be constrained with 8000 un-localised high fluence FRBs at 1.4GHz, as might be detected by the next generation of FRB-finding telescopes.

6.2 Introduction

The observed number of sources as a function of flux (the 'logN–logS' relation) is perhaps the most fundamental quantity to population studies across astronomy. Encoded within them are the properties of the source population: luminosity function, spectra and redshift distribution (Longair & Scheuer, 1966). Constraining the population functions of fast radio bursts (FRBs) and gamma-ray bursts (GRBs) has been an area of particular interest in modern astronomy (Macquart & Ekers, 2018a; Sun et al., 2015). These bursts are often produced in exotic systems or cataclysmic circumstances(Abbott et al., 2017; Woosley & Bloom, 2006; Platts et al., 2019) and therefore represent an important tracer of rare systems.

Propagation effects can however serve to obfuscate the intrinsic behaviours of a transient source. For higher energy transients such as GRBs and super-

novae, influential propagation effects include absorption (Frontera et al., 2000) and extinction (Riess et al., 1998). Whereas for radio transients, scattering, and dispersion are more relevant (Ocker et al., 2022a; Macquart & Koay, 2013; Macquart & Ekers, 2018a). In order to correctly model the population functions from the observations, these propagation effects must be taken into account. Due to the achromatic nature of its effect, gravitational lensing is one such propagation effect that is relevant for both high and low-energy transients.

Gravitational lensing is important to consider because it can magnify source objects, significantly amplifying their observed flux, potentially resulting in erroneously inferred luminosities. Many examples of lenses magnifying, distorting or even multiply imaging individual sources have been recorded, including for quasars (Walsh et al., 1979), GRBs (Paynter et al., 2021) and supernovae (SNe) (Kelly et al., 2015). However, the influence of gravitational lensing on the source counts of a population is typically slight; the fraction of quasars undergoing strong lensing is expected to be only a few percent of quasars beyond redshift six (Pacucci & Loeb, 2019; Yue et al., 2022) and for SNe (Porciani & Madau, 2000; Jönsson et al., 2010) the fraction of lensed bursts is constrained to be small.

The lack of observed gravitational lensing can be used to infer constraints on the population of lenses. Zumalacárregui & Seljak (2018) placed strong constraints on the fraction of dark matter in primordial black holes (PBHs) using type Ia SNe. The authors model the probability of magnification convolved with the spread in supernova magnitudes and compare with the observed spread to constrain the population of lenses at cosmological distances. They find that the observations are inconsistent with a large population of lenses and therefore restrict the fraction of dark matter in PBHs to be less than 0.3 for PBH masses greater than $0.01 M_{\odot}$. Strong constraints can be placed in the case of SNe Ia observations because of the narrow distribution of intrinsic SNe Ia energies (i.e. because SNe Ia are standardisable candles).

These results do not mean that lensing will be unimportant for FRB and GRB

source counts. The smaller angular size of GRBs and FRBs compared to SNe Ia makes them sensitive to even lower mass lenses. The uncertainty surrounding the emission mechanism of most fast transients, however, makes it difficult to separate potential propagation effects from potential emission mechanism effects. For example, it is difficult to distinguish a highly magnified event from an intrinsically luminous burst. Thus, lensing searches have been restricted to searches for multiple source images, be it in the spatial or temporal domain (Muñoz et al., 2016; Wagner et al., 2019; Laha, 2020; Oguri, 2019; Sammons et al., 2020; Paynter et al., 2021; Leung et al., 2022; Kader et al., 2022; Connor & Ravi, 2022).

As we shall show, the luminosity of GRBs and FRBs are sensitive to lens masses much too small to produce resolvable multiple images: as small as $10^{-15}M_\odot$ and $10^{-5}M_\odot$ respectively, and there is little evidence to rule out the presence of a cosmological population of lenses on these low mass scales. Constraints on primordial black holes (PBHs) still allow for 100% of dark matter to be comprised of PBHs in the asteroid to sub-lunar mass regime ($10^{-15}M_\odot \leq M_L \geq 10^{-10}M_\odot$; Carr & Kühnel, 2020). The sub-lunar to sub-stellar ($10^{-10}M_\odot \leq M_L \geq 10^{-2}M_\odot$) regime is also of interest as it is only constrained for our own galaxy halo, with $\sim 10^{-5}M_\odot$ lenses potentially existing locally in appreciable density.

To account for lensing effects on the source counts of fast transients, and estimate how this may be used to constrain the number of PBHs, we create a generic model for differential rates of fast transients with fluence, dR/dF, in an inhomogeneous universe and compare it to its smooth universe counterpart, considering only the total magnification caused by inhomogeneity.

This paper is structured as follows: §6.3.1 & §6.3.2 introduce the lensing theory, §6.3.3 & 6.3.4 introduce the differential event rates formalism, §6.3.5 discusses our numerical method and justifies our model's assumptions, in §6.5 we characterise the response of our model to variation of the input parameters, §6.6 explores the possibility that all FRBs are highly magnified, §6.7 contains explicit calculations of the changes to FRB and GRB event rates in universes of varying

inhomogeneity and finally, we discuss the implications of these results in §6.8 and explore how many FRBs would be needed to place constraints on the PBH parameter space.

6.3 Method

6.3.1 Lensing Basics

Gravitational lensing is a result of perturbations in the mass of a smooth universe deflecting the emission of background sources. By convention we define the fraction of matter in the Universe which may be considered as smoothly distributed as η. A completely homogeneous universe ($\eta = 1$) will be devoid of any gravitational lensing, i.e. the flux from a source at a given redshift will be constant for every line of sight. Whereas, an inhomogeneous universe will have a fraction of its total energy density $(1-\eta)\Omega_M$ in lensing objects and a corresponding distribution of possible magnifications associated with a given redshift.

In general lensing causes a rich variety of effects on source images and temporal profiles of transients (for a detailed review of which we refer the reader to Schneider et al., 1992). In this work we restrict ourselves to consideration only of the total magnification of a source by a lens,

$$\mu = \frac{F}{F_0}, \tag{6.1}$$

where F is the sum of the fluence from all images and F_0 is the fluence observed from a source along an 'empty beam'. The empty beam is defined as the path of propagation which lies far from all clumps of inhomogeneous matter. D_η is the value of angular diameter distance D_A along the empty beam and it represents the background value ($\mu = 1$) of D_A in a universe with a smooth matter fraction η. Following the method outlined by Kayser et al. (1997), D_η can be calculated numerically for a general choice of both cosmology and η (see appendix C.1 for

extended discussion).

A critical quantity of the magnification distribution is the mean source magnification at a given redshift,

$$\langle \mu \rangle = \frac{D_\eta^2(z)}{D_1^2(z)}, \tag{6.2}$$

where D_1 represents the typical angular diameter distance of a smooth universe ($\eta = 1$). As η is increased and the universe becomes homogeneous, D_η tends towards D_1 and we recover the smooth universe behaviour of $\langle \mu \rangle$=1. The mean magnification determines the shape of the magnification probability density function (PDF) we apply from Rauch (1991).

6.3.2 Magnification Probability Density Function

To determine the effects of gravitational lensing on observed fast transient event rates, we require a functional form for the magnification PDF. In this work we make use of the analytical approximation detailed in Rauch (1991),

$$p(\mu) = 2\sigma_{\text{eff}} \left[\frac{1 - e^{-b(\mu-1)}}{\mu^2 - 1} \right]^{1.5}, \tag{6.3}$$

where parameters σ_{eff} and b are chosen such that the PDF is normalised and has a mean magnification $\langle \mu \rangle$ as given by 6.2. The form of the PDF is derived empirically by fitting to simulations of lensing rather than being motivated physically. However, by doing so it implicitly accounts for multiple lensing and shear which are significant complexities to hurdle when deriving a more physical model (Schneider & Weiss, 1988).

As stated in Rauch (1991) this approximation is only valid for low mean magnifications and point sources ($\langle \mu \rangle \lesssim 1.2$, corresponding to $z \sim 1.2$ in a Planck cosmology with $\eta = 0$). However, even for large mean magnifications where the lensing enters the complex regime associated with an intricate caustic network, the approximation by Rauch provides a simple way to capture broad behaviour of the magnification probability distributions found by numerical simulations (e.g.

Fleury & García-Bellido, 2020). Given the relative uncertainties associated with both FRB and GRB luminosity functions (James et al., 2021b; Banerjee et al., 2021) particularly FRBs as their progenitor/s remain unknown, we will make use of this simple empirical model as opposed to vastly more computationally intensive numerical simulations. Finally, we note that this model is only valid for static lensing geometries. If the magnification of a source can change significantly over time due to its motion relative to the lens then the probability of a given magnification must be reconsidered under a different formalism. We assume that both lenses and sources are stationary relative to the observer for the remainder of this work.

6.3.3 Rates in a Smooth Universe

The impulsive nature of fast transient events means that burst rates rather than source counts are the fundamental quantity to consider when characterising the population. Furthermore, the observable directly relevant to transient events is fluence rather than flux which is typical for continuous sources. We use the fluence–energy relation outlined in Macquart & Ekers (2018a).

The observed rate of a transient population is primarily governed by the intrinsic event rate energy function which depends on the redshift of the burst as well as its spectral energy and frequency in the emission frame $\Theta_E(z, E_{\nu_e}, \nu_e)$. This function yields the event rate per spectral energy per co-moving volume. Assuming that the redshift, spectral energy and emission frequency of a burst are independent, it can be separated into the population functions describing each dimension,

$$\Theta_E(z, E_{\nu_e}, \nu_e) = \phi_z(z)\ \phi_E(E_{\nu_e}, E_{\nu_e,\max}, \gamma)\ \phi_{\nu_e}(\nu_e, \alpha), \tag{6.4}$$

allowing us to motivate the form of the ϕ_x functions separately, depending on which transient we are considering. Above we have labelled each of the functions

with their typical arguments. Generally, the source evolution function, ϕ_z, will depend only on z; the energy analogue to the luminosity function, ϕ_E, will have a power law dependence on E_{ν_e} described by index γ (where broken power laws are used, γ is subscripted accordingly) up to a hard cutoff at the maximum spectral energy $E_{\nu_e,\max}$; and the spectrum, ϕ_{ν_e}, will have a power law dependence on ν_e described by index α (and β where broken power laws are used).

Following the work of Macquart & Ekers (2018a), the intrinsic event rate energy function can be related to the differential observed rate with fluence via

$$\frac{dR}{dF} = \int dz\ 16\pi^2 D_c^2 D_L^2 \frac{1}{(1+z)^3} \frac{dD_c}{dz} \Theta_E(z, E_{\nu_e}, \nu_e), \tag{6.5}$$

where D_L and D_c are the comoving and luminosity distances respectively — for a complete derivation see appendix C.3.1.

6.3.4 Rates in a Clumpy Universe

In an inhomogeneous universe the relation between observed fluence and emitted energy is more complicated. Naturally it is dependent on the total magnification of the source. However as our magnification is with respect to the empty beam case, the luminosity distance cannot be calculated for a smooth universe as in §6.3.3. Instead it must be expressed as a function of D_η via Etherington's reciprocal relationship ($D_L = D_\eta(1+z)^2$) (Etherington, 1933).

The probability of any given line of sight to a source at redshift z having magnification μ is given by the PDF described in Eq. 6.3. For most of our calculations we assume the lensing is well characterised by geometric optics. At radio wavelengths this assumption may break down as we show in §C.2 (see also Grillo & Cordes, 2018, for more discussion on the breakdown of geometric optics).

Combining these elements as elaborated in the derivation in appendix C.3.2 the differential rate with fluence for transients in an inhomogeneous universe with

a smooth matter fraction η is

$$\frac{dR}{dF} = \int dz\, 16\pi^2 D_c^2 \left(D_\eta (1+z)^2\right)^2 \frac{1}{(1+z)^3} \frac{dD_c}{dz} \times \int d\mu\, p(\mu, z) \Theta_E(z, E_{\nu_e}, \nu_e) \frac{1}{\mu}\,. \tag{6.6}$$

6.3.5 Numerical Implementation

To evaluate the differential rates we used SciPy's implementation of the FORTRAN quad pack numerical integration. For the smooth universe calculation of dR/dF we integrate in log space over the domain $[z_{\rm min},\, z_{\rm max}]$. In our physical picture the calculated value dR/dF then corresponds to a hollow sphere between redshifts $[z_{\rm min},\, z_{\rm max}]$.

In line with the expectations in a ΛCDM universe, we assume that on large scales the Universe is homogeneous, hence we set a minimum redshift condition of $z_{\rm min} = 0.001$ (D$\sim$ 4 Mpc), corresponding to the scale between galaxies. We do not model the contribution to the event rate from below this scale, as the local structure of our Universe would need to be accounted for. Even with $z_{\rm min}$ set at 0.001, our hollow sphere still well approximates the volume of filled sphere out to $z_{\rm max}$.

The upper redshift boundary corresponds to the designated spatial distribution, e.g. for $\phi_z \propto$ cosmic star formation rate (CSFR; throughout this paper we make use of the CSFR outlined in Madau & Dickinson, 2014) we set $z_{\rm max} = 100$ where star formation is negligible.

In the case of a clumpy universe our redshift integration must be restricted to a higher minimum, $z_{\rm min,\ lensed}$, to ensure stable integration. As seen in Eq. (6.2), $\langle\mu\rangle$ is dependent upon redshift and the smooth matter fraction, η. For high values of η and low redshifts $\langle\mu\rangle - 1$ will be small. To have a magnification PDF of the form of Eq. (6.3) with a small mean magnification requires that the PDF be extremely concentrated around $\langle\mu\rangle$. For mean magnifications $\langle\mu\rangle - 1 \lesssim 10^{-5}$ this peak can be missed in the integration domain, destroying the validity of the

result. For inhomogeneous universes ($\eta < 1$) we set $z_{\text{min, lensed}} \geq z_{\text{min}} = 0.001$ to ensure a valid result. For lower values of η, $z_{\text{min, lensed}}$ is decreased such that the minimum $\langle\mu\rangle$ remains constant. Given the extremely low mean magnification in this low redshift regime the clumpy and smooth universe results are unlikely to vary significantly. Therefore, when $z_{\text{min, lensed}} > z_{\text{min}}$ we add the smooth universe result over the domain $[z_{\text{min}}, z_{\text{min, lensed}}]$ to the clumpy integral result to keep the smooth and clumpy dR/dF results consistent.

For the clumpy universe calculation the inner integral in Eq. 6.6 is performed in log space over the transformed domain of $\Delta\mu = \mu - 1$ to aid numerical integration by spreading out the sharply varying behaviour of the magnification PDF over a greater dynamic range. This integration is performed over the domain $[\Delta\mu_{\text{min}}, \Delta\mu_{\text{max}}]$, where $\Delta\mu_{\text{min}} = 10^{-15}$ as restricted by float precision [1] and $\mu_{\text{max}} = 10^{20}$, beyond which we expect negligible contribution to the integration.

6.4 Fractional Change Due to Lensing

Here and in following sections we illustrate dR/dF using plausible values of the population functions for FRBs (James et al., 2021b; Luo et al., 2020), and vary individual parameters over a broad range of typical values.

Fig. 6.1 plots dR/df as a function of f for a smooth universe, where f is the observed fluence normalised to what would be observed for an $E_{\nu_e,\text{max}}$ burst at redshift $z = 1$ in a smooth universe. We normalise the rates to the expected dR/df for a Euclidean universe, $R_0 f^{-2.5}$ where R_0 is the rate density in the local universe.

Fig. 6.1 shows that dR/df in a smooth universe has roughly two fluence domains of behaviour for event rate energy functions with $\gamma > -2.5$. We define these regions about a break fluence $f_{b,1} = 10^{-1.16}$ which is the fluence corresponding to $E_{\nu_e,\text{max}}$ at z_{max}. At the high fluence end ($f > f_{b,1} = 10^{-1.16}$) the maximum

[1] Technically the float precision of the exponential term in Eq. (6.3) is violated significantly before $\Delta\mu = 10^{-15}$, however the impact on the accuracy of the result is negligible.

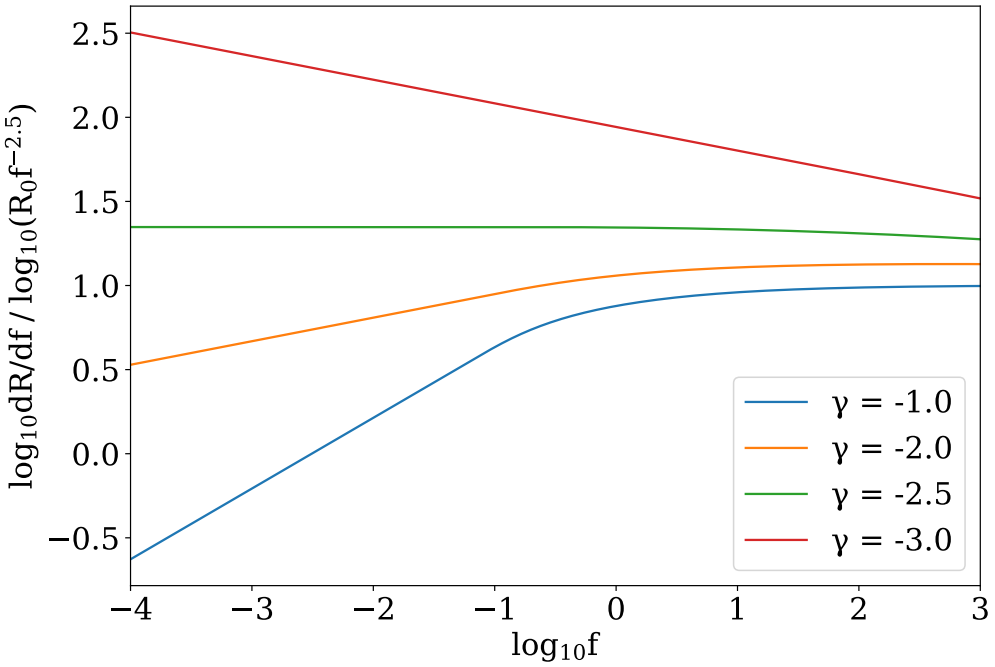

Figure 6.1: Observed differential event rate as a function of normalised fluence in a smooth universe for an event rate energy function with $\alpha = -1.0$, $E_{\nu_e,\max} = 10^{33}$erg/Hz, a uniform comoving spatial density and a range of γ values given in the legend and $z_{\max} = 100.0$. We normalise the result to the Euclidean expectation given by $R_0 f^{-2.5}$.

redshift is determined by $E_{\nu_e,\max}$. Because the power law index of the energy function, $\gamma > -2.5$ is shallower than the expected Euclidean evolution $\propto f^{-2.5}$ the change in rate with fluence is dominated by the change in sources due to a restricted redshift, as opposed to having fewer bursts at higher energies. Therefore dR/df in a smooth universe has a power law index at the high fluence end approaching the Euclidean expectation.

On the low fluence end ($f < f_{b,1} = 10^{-1.16}$), where $z_{\max}$ is instead restricted by the spatial distribution ϕ_z, a change in the observed fluence does not affect $z_{\max}$ and the change in the observed rate is dominated by seeing fewer bursts at higher energies. Therefore at the low fluence end dR/df adopts the power law index seen in the energy function of γ. If the energy function has a steeper index, $\gamma \leq -2.5$ then for a uniform spatial distribution the change in the number of bursts due to the energetics will dominate across all fluences and the Euclidean behaviour will never be recovered.

In a clumpy universe dR/df depends on the convolution of the intrinsic energy function with $p(\mu)/\mu$ as per Eq. 6.6. For gravitational lensing this convolution kernel is generally $\propto \mu^{-4}$ in the high magnification limit. Therefore, for all energy functions with $\gamma > -4$[2] this convolution will be dominated by the intrinsic energy function, and the behaviour of dR/df will be well approximated by the smooth universe behaviour described above. The exception will be the case where all events are highly magnified as we shall discuss in §6.6 and the edge effects we describe below.

To discern the effect of lensing we express our results as the differential event rate (dR/df) in a clumpy universe with a smooth matter fraction $\eta < 1$, normalised by the differential event rate in a smooth universe ($\eta = 1$). Fig. 6.2 shows the $\eta = 0$ case, depicting a $1 - 10\%$ fractional change in dR/df due to lensing that has a characteristic shape common to all values of γ.

[2]We only calculate dR/df in a clumpy universe for $\gamma > -4$. Because $p(\mu)/\mu \propto \mu^{-4}$ at high μ, for $\gamma \leq -4$, the inner integral of Eq. 6.6 would not converge, as described later, none of the intrinsic energy functions for source populations we consider have $\gamma \leq -4$.

Fig. 6.2 shows the low fluence regime for all values of γ and all fluences for $\gamma \leq -2.5$ to have approximately constant fractional difference between the lensed and unlensed differential rates. dR/df in these regions are dominated by the energetics and hence show similar behaviour despite any lensing, consistent with our expectation.

The fluctuation structure is comprised of an initial decrease, before a sharp increase which then tends back towards unity. To understand why this structure appears we must look to the break fluence f_b. For $f > f_b$, the maximum redshift becomes restricted by $E_{\rm max}$ and dR/df becomes dominated by a reduction of the volume out to which sources can be observed as discussed previously. In a smooth universe this occurs at $f_{b,1} = 10^{-1.16}$, shown as a dotted line in Fig. 6.2. In a clumpy universe however this occurs at a lower fluence of $f_{b,\eta} = 10^{-3.69}$, shown as a dashed line in Fig. 6.2. The lower fluence is due to a demagnification of $1/\langle\mu\rangle$ (from Eq. (6.2), $D_1^2(z_{\rm max} = 100)/D_0^2(z_{\rm max} = 100) = 0.00295 \approx 10^{-3.39}/10^{-1.16}$) associated with viewing along an empty beam in a clumpy universe compared to a smooth one. Therefore, as we increase fluence dR/df becomes dominated by the reduction to $z_{\rm max}$ in a clumpy universe before it does so for a smooth universe, resulting in the dip. Once we hit $f = 10^{-1.16}$, the smooth universe also becomes dominated by reduction to $z_{\rm max}$ resulting in an inflection point in the fractional change in accordance with $z_{\rm max}$ decreasing faster in a smooth universe. As the fluence increases and the maximum redshift approaches the nearby universe, the mean magnification decreases and clumpy and smooth universes become indistinguishable, resulting in dR/df values that converge as seen on the high fluence end of Fig. 6.2.

6.5 Intrinsic Parameter Variation

Apart from γ, our model takes in a number of input parameters as discussed in §6.3.3. Below we characterise the response of dR/df to variation of these parameters.

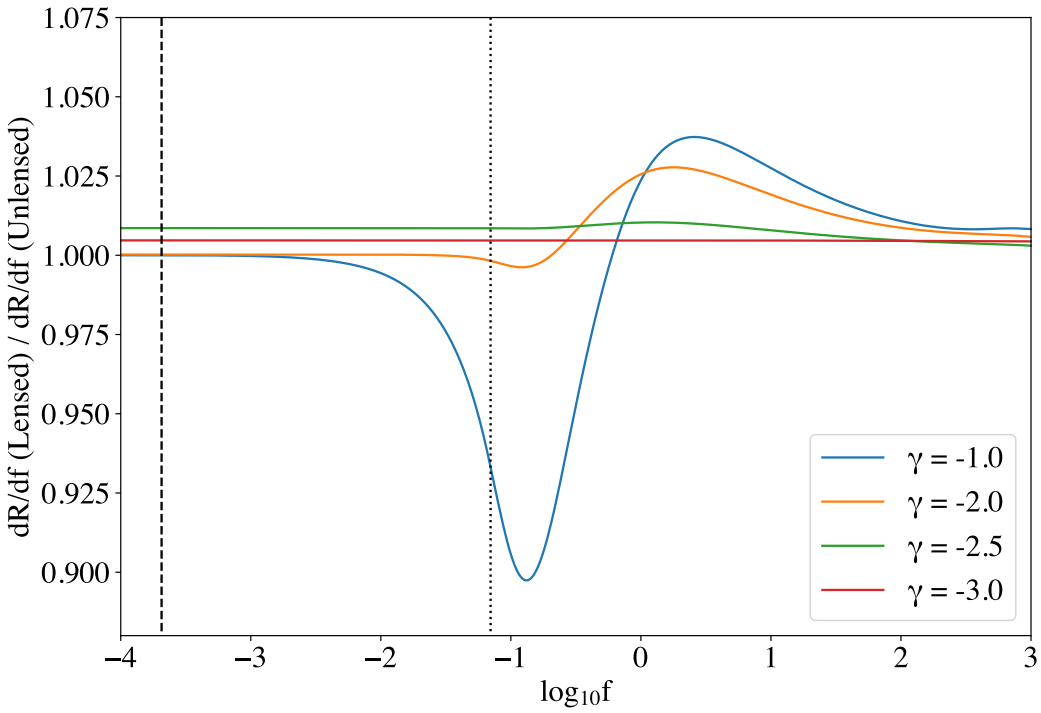

Figure 6.2: Differential rates for a clumpy universe from Fig. 6.1 normalised by the corresponding values in a smooth universe. Dashed and dotted lines denote the break fluences $f_{b,\eta}$ and $f_{b,1}$ for clumpy and smooth universes respectively.

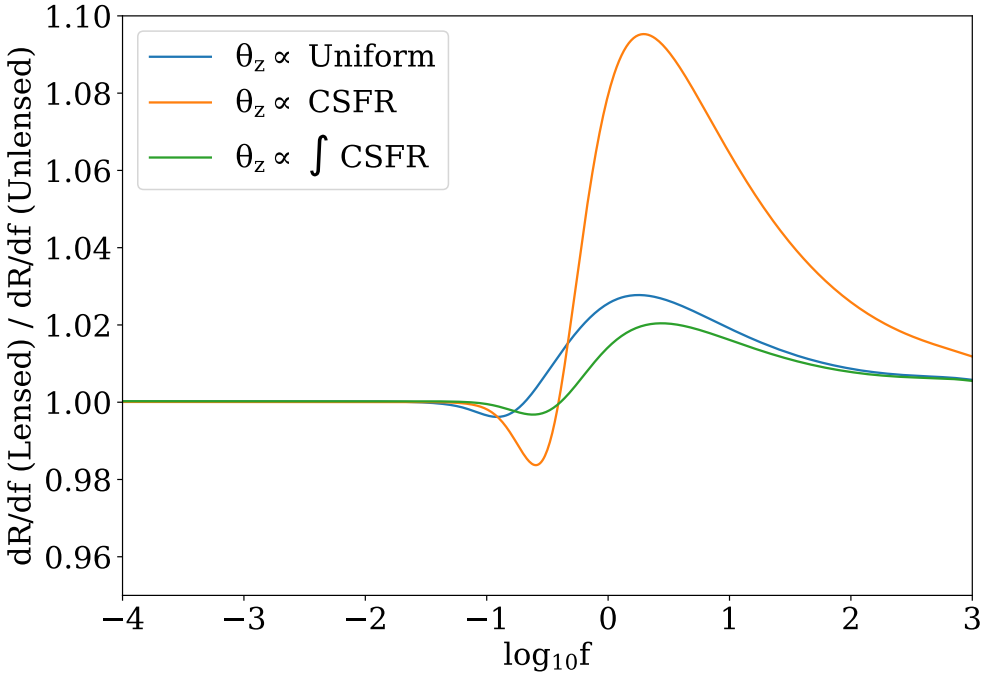

Figure 6.3: Differential rates for a clumpy universe normalised by their smooth universe equivalents for a selection of spatial distributions ϕ_z. Other parameters of the population functions are identical to those in Fig. 6.1 with $\gamma = -2.0$.

6.5.1 Spatial Distributions

Our calculations so far have been restricted to an intrinsic rate with a uniform comoving spatial distribution. More realistically ϕ_z is likely to be proportional to some integral over the CSFR, owing to the stellar origin of the extreme environments that produce (or are candidate progenitors for) many extragalactic transients (Gehrels et al., 2009; Platts et al., 2019). For progenitors that are short lived this integral will be over a small portion of the CSFR and hence the result proportional to the CSFR itself. Conversely, progenitors that emit bursts over a time period comparable to the age of the universe will have ϕ_z proportional to the current number of stars, i.e. the CSFR integrated over all redshifts above z. Taking $\gamma = -2.0$ we plot dR/df for these spatial distributions in Fig. 6.3.

Fig. 6.3 shows that for spatial distributions proportional to the CSFR or its

integral, the minimum fractional change occurs at a higher fluence than for a uniform spatial distribution. This is because the CSFR shows a gradual decline beyond $z \sim 2$ rather than a hard edge at $z \sim 100$. Also of note is that the fractional increase in dR/df from lensing is much larger for the case of $\phi_z \propto$ CSFR than other spatial distributions.

To see why, it is informative to decompose the fractional change due to lensing for a uniform spatial distribution into its components in redshift space. Fig. 6.4 shows that in the case of a ϕ_z which is uniform in comoving space, a majority of the fractional increase due to lensing comes from the $z = 0.72 - 3.728$ region. This is the same region in redshift space where the CSFR peaks and hence for $\phi_z \propto$ CSFR the rate of bursts coincidentally peaks where the fractional change due to lensing is greatest, enhancing the effect of lensing.

6.5.2 Spectral Indices

Fig. 6.5 shows that the fractional change due to lensing varies with the spectral index α similarly to the energy index γ. Steep, negative spectral indices rapidly decrease the burst rate at high frequencies which suppresses the burst rate at higher redshifts where the emission frequency associated with any given observed frequency is higher by a factor of $(1+z)$. Because all significant lensing effects occur in the distant universe where the mean magnification is higher, a suppression to the intrinsic rate at high redshifts restricts the effect of lensing as shown.

6.5.3 $E_{\mathbf{max}}$

The maximum energy of a burst $E_{\nu_e,\mathrm{max}}$ defines where f_b will lie and so will affect where the structure in the above figures will be in fluence. As shown in Fig. 6.6 increasing or decreasing $E_{\nu_e,\mathrm{max}}$ shifts the fluctuations in fractional change linearly with f. Apart from translation, the impact of changing $E_{\nu_e,\mathrm{max}}$ is negligible.

The shape of the structures seen in Fig. 6.6 is caused somewhat by the sharpness of the hard cutoff at $E_{\nu_e,\mathrm{max}}$. Because a hard cutoff is a rather unrealistic

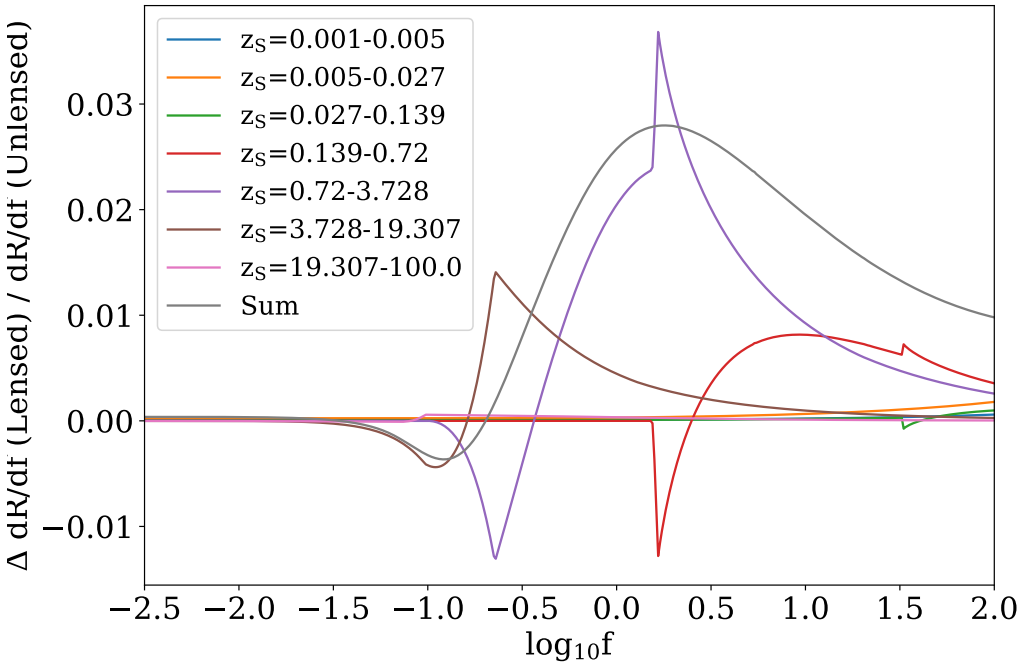

Figure 6.4: Components in redshift space of fractional change in dR/df due to lensing in a $\eta = 0.0$ universe. Components depicted in logarithmically spaced redshift bins. Number of bins is chosen to show a range of redshift behaviours while preserving visual distinction. Sum is equivalent to those shown in Fig. 6.2 and 6.3 for a uniform spatial distribution with $\gamma = -2.0$. The sharp peaks seen in the curves representing each redshift bin are the result of constructing hard bin boundaries in redshift space.

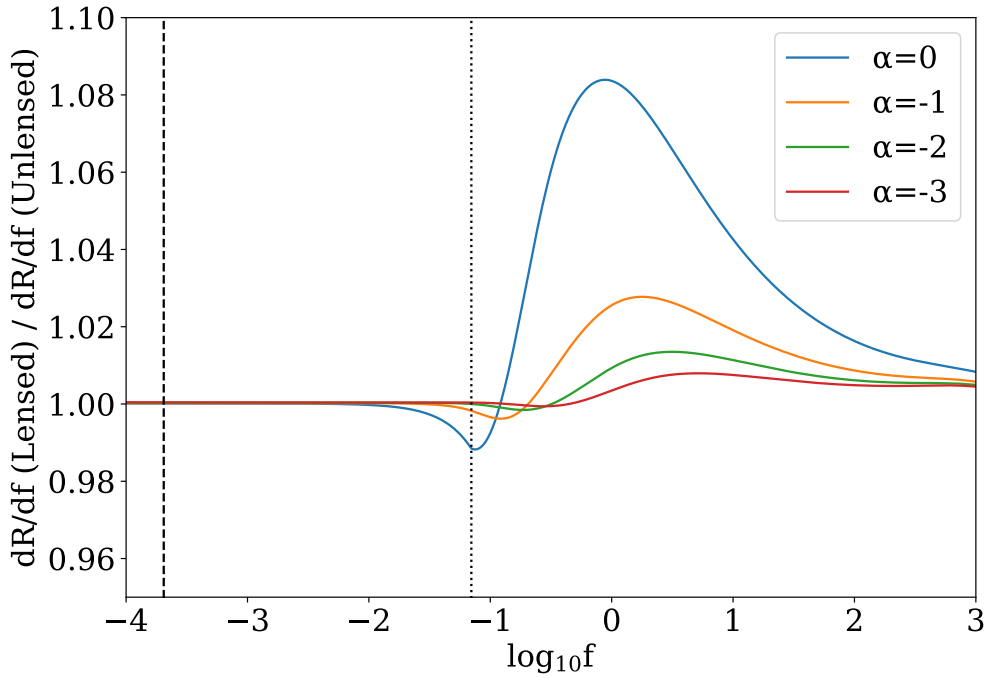

Figure 6.5: Differential rate in an $\eta = 0$ universe normalised by the smooth universe equivalent. We select our parameters to be the same as Fig. 6.1 with $\gamma = -2.0$ but for a variety of α values.

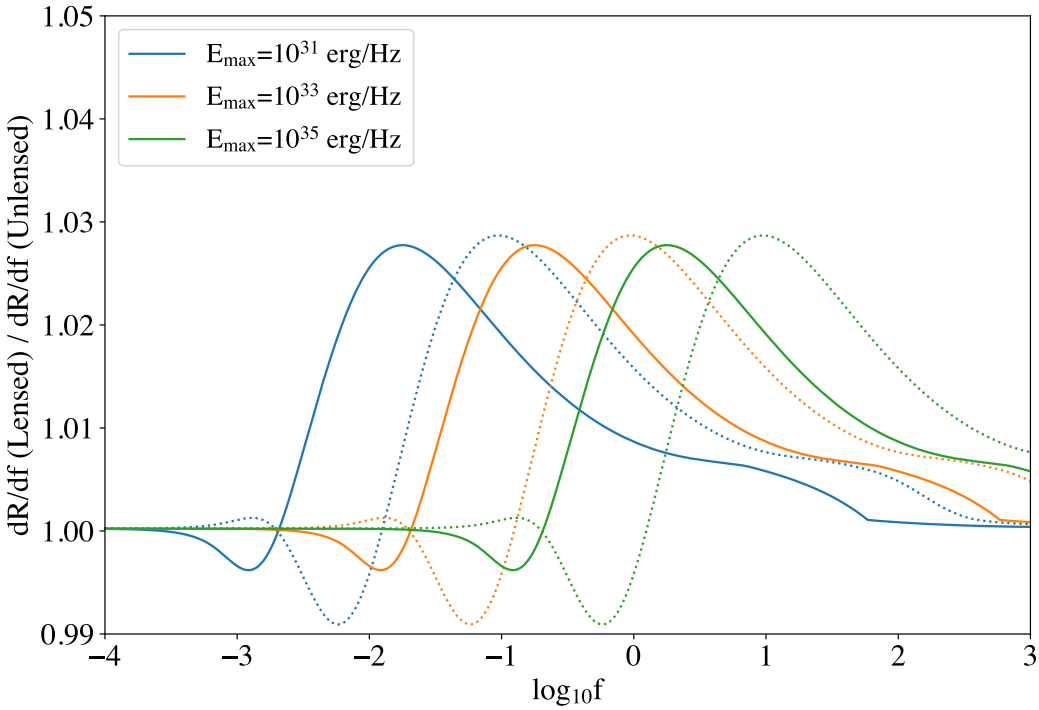

Figure 6.6: As per Fig. 6.1 with $\gamma = -2.0$ but a varying $E_{\nu,\max}$. Dotted lines represent the case of an exponential cutoff in ϕ_E above $E_{\nu,\max}$ as opposed to a hard boundary.

feature of an energy function we have also calculated Fig. 6.6 for an exponential cutoff at the same boundary. The results of this calculation are also contained in Fig. 6.6 as the dotted lines. The figure shows only mild differences from a hard cutoff, including a short rise before deeper decreases, each structure is also shifted to higher fluences. The small scale of these changes shows that the hard cutoff in energy we use is a good approximation for a more realistic sharp decrease in rate beyond $E_{\nu_e,\max}$.

6.5.4 Cosmology

Our results will also depend upon the choice of cosmology used in the model. To demonstrate how changes in cosmology will affect the results we compare the Planck cosmology to the extreme case of an Einstein De-Sitter cosmology that has zero cosmological constant and all of its energy density contained in matter ($\Omega_m = 1$). The Hubble constant for each is that given by the Planck constraints. Both are calculated for the case where $\eta = 0$, giving a density in lenses of Ω_L=Ω_m (we highlight that $\Omega_L = \Omega_m$ is not inconsistent with a macroscopically homogeneous universe, as the small scale inhomogeneities, which cause lensing and comprise this density, will be homogeneous on large scales). Fig. 6.7 shows the fractional change due to lensing for each of these choices. It shows only a mild difference between the two cosmologies, with the Einstein De-Sitter universe having a greater peak. Fig. 6.7 also shows that the fractional fluctuation in dR/df due to lensing in an Einstein De-Sitter universe is shifted to a higher fluence. This is expected as an $\Omega = 1$ universe has a lower luminosity distance at a given redshift, giving a commensurately higher f_b in both the lensed and unlensed case.

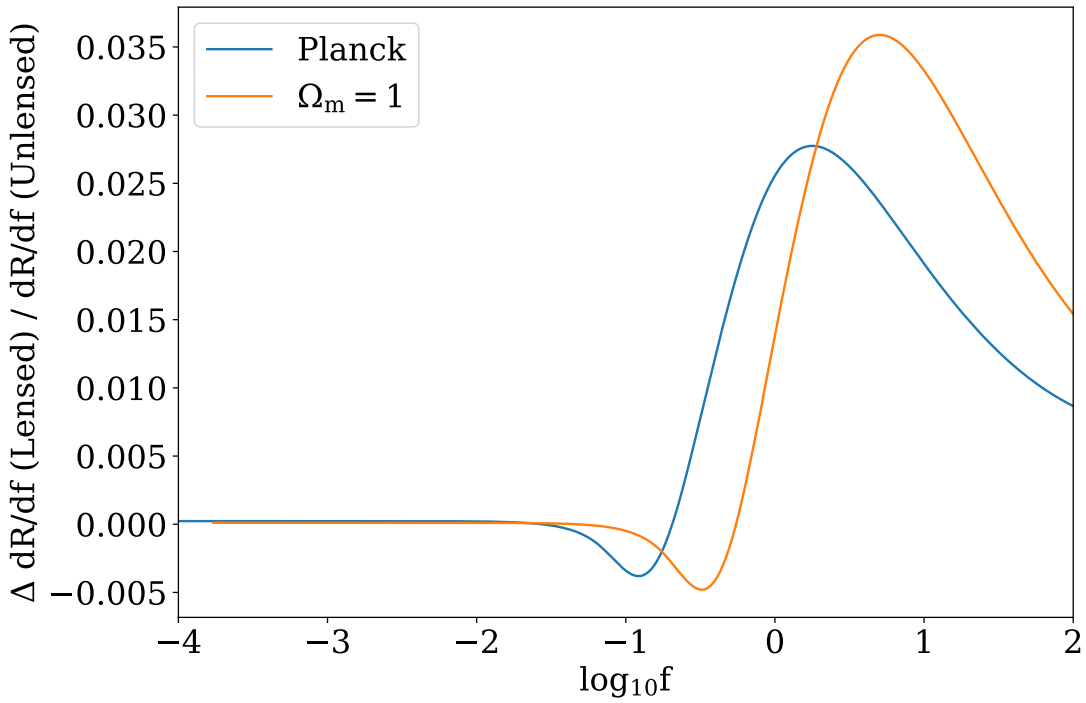

Figure 6.7: Comparison of the fractional change in dR/df due to lensing between a Planck cosmology and an Einstein De-Sitter universe (i.e. a universe with $\Omega_m = 1$). Other parameter choices are as seen in Fig. 6.1 with $\gamma = -2.0$.

6.6 Are All FRBs Lensed ?

Above we have describe the scenario where a burst population which could be observed in a smooth universe is altered by lensing. However, an alternative scenario which has been discussed in the FRB community is the possibility that bursts are only observed because of gravitational lensing, i.e. all observed bursts are intrinsically low energy but highly magnified. In such a situation the minimum redshift becomes important. We define $f_{\rm max}$ as the largest fluence where an observer will see a burst with $\mu = 1$, corresponding to $E_{\nu_e,\rm max}$ at $z_{\rm min}$. For $f > f_{\rm max}$ only magnified bursts are observed, and because the entire spatial domain contributes, the behaviour of dR/df with fluence will be determined entirely by the inner integral over magnification in Eq. (6.6). As f increases, the intrinsic energy required at each magnification will increase and the observed rate will decrease following ϕ_E with index γ (fewer bursts at higher energies). Additionally, the minimum observed magnification will increase with f, resulting in a decrease to dR/df. For a general PDF with a factor $1/\mu$ that behaves as a power law $p(\mu)/\mu \propto \mu^{\xi-1}$ (as it does in the high magnification limit) the integration from $[\mu_{\rm min}, \infty]$ will vary with $\mu_{\rm min}$ following an arbitrary negative power law of index ξ. Therefore as f increases and $\mu_{\rm min}$ increases, dR/df will also vary with index ξ. These behaviours will occur simultaneously, however if one is significantly steeper we expect that it will dominate the change to dR/df, e.g. for $\xi \ll \gamma$, dR/df will be approximately $\propto f^{\xi}$, and vice versa.

Given that in the geometric optics limit for static lensing geometries our chosen PDF varies as $p(\mu) \propto \mu^{-3}$, the expected behaviour for all $\gamma \geq -3$ is to have dR/df vary with a power law index of -3. This is precisely what we find when calculating dR/df for the same selection of ϕ_E functions used earlier but with $E_{\nu_e,\rm max} = 10^{26}$ erg/Hz, which is more in line with the spectral energy observed for the Galactic FRB (The CHIME/FRB Collaboration, 2020).

If all FRBs were highly magnified in a static lensing geometry, the behaviour of dR/df would be consistent with a $\gamma = -3$ intrinsic energy function in a smooth

universe. Estimates of γ outside the context of lensing would therefore yield $\gamma = -3$. Best estimates of γ from observed FRBs give $\gamma \approx -2$ (James et al., 2021b; Luo et al., 2020), which never has dR/df behaviour consistent with a $\gamma = -3$ model and therefore allows us to refute a scenario where FRBs are only observable due to high magnifications from stationary gravitational lenses.

In appendix C.2 we show that as a result of wave optics low mass lenses may not follow $p(\mu) \propto \mu^{-3}$. Given this potential departure from the $p(\mu) \propto \mu^{-3}$ behaviour we can only use $\gamma \neq -3$ to refute that all FRBs are highly magnified by lenses of certain mass. The range of masses which are constrained depends on the magnification required to make the bursts observable, i.e. the maximum apparent energy normalised by the maximum intrinsic energy $\mu_{\rm max} = E_{\rm max,\,obs}/E_{\rm max,\,int}$. For low lens masses the maximum magnification will be insufficient to make low intrinsic energy bursts observable, allowing us to rule them out by default. For higher intrinsic energies and higher lens masses the lensing behaviour will approach the geometric expectation, $p(\mu) \propto \mu^{-3}$, which are then ruled out as FRB $\gamma \neq -3$. We plot these conditions in Fig. 6.8, assuming that magnifications $\mu < \mu_{\rm max}/10^{1.5}$ have $p(\mu) \propto \mu^{-3}$ as describe in appendix C.2. The figure shows the excluded regions for FRBs, with the intermediate region in grey. Here lensing is of sufficient magnification to make bursts observable but close enough to the maximum magnification to have prominent fringes in the cross section that change the behaviour from $p(\mu) \propto \mu^{-3}$. In this region of the parameter space, we cannot rule out that all FRBs are highly magnified on the basis of γ alone.

6.7 How Does Lensing Affect Fast Transient Rates

Assuming that both FRB and GRB populations are intrinsically transient, and not all highly magnified, we have shown in §6.4 that any effect on their differential rates from lensing will be small. Therefore, estimates of their intrinsic parameters, i.e. γ, α and ϕ_z, made without accounting for the possibility of lensing will approximate the true population parameters well even if all of the Universe's

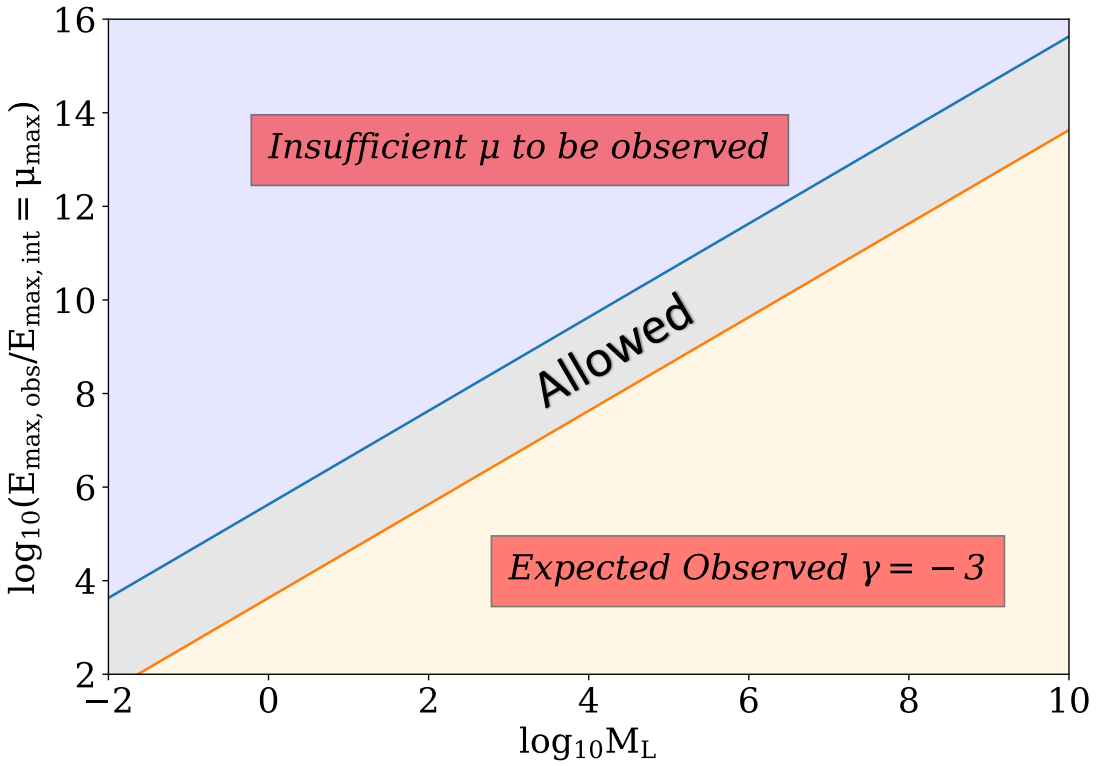

Figure 6.8: Range of lens masses excluded from highly magnifying all FRBs. Blue line is set by the maximum magnification under wave optics for a 1GHz FRB lensed by an M_L mass point lens. Orange line corresponds to the magnification 1.5 orders of magnitude below the maximum. Orange and blue regions highlight parts of the parameter space excluded by observed γ or required magnification respectively. Gray region highlights the unconstrained area of the parameter space associated with prominent intereference fringers in the cross section.

matter were to be contained in lenses[3]. It is therefore appropriate to use the observed population parameters as inputs to our model when calculating the expected dR/df for transient populations in a clumpy universe. In this section we calculate dR/df specific to each transient class for universes with varying η. We display these rates normalised to what a uniform spatial distribution at the local rate would yield, as well as the fractional differences due to lensing.

We model the effect of lensing on FRBs, long GRBs and short GRBs. We use literature values to build fiducial event rate energy functions in each case as discussed in the following sections. We stress that these models are simplified for the purpose of demonstrating the effect of lensing.

6.7.1 Short GRBs

To model SGRBs we use the empirical redshift distribution of Sun et al. (2015, see Eq. (21)) as our ϕ_z. For consistency we'll also make use of the best fit luminosity and spectral functions from Sun et al. (2015), i.e. a single power law with $\gamma = -1.6$, and a Band energy function (Band et al., 1993) with $\alpha = -0.5$ and $\beta = -2.3$ for ϕ_ν. Sun et al. (2015) takes these luminosities to be isotropic and bolometric, using a $1 - 10^4$ keV bandwidth. We also impose a hard maximum luminosity at $L_{\rm max} = 10^{51}$ erg/s which corresponds to the upper bound of the typical energy range for SGRBs (D'Avanzo, 2015). To convert these luminosity conditions to spectral energies consistent with our model we divide these luminosities by the assumed $\simeq 10^4$ keV bandwidth and assume that as the peak spectral luminosity at a frequency corresponding to a photon energy of 200 keV. Furthermore, we assume all GRBs to have a duration given by the mode of the *Swift* burst width distribution (SGRBs = 0.1s, LGRBs = 20s; Gehrels et al., 2009).

Fig. 6.9 shows dR/df calculated for the above SGRB event rate energy function. The top panel normalises the result to dR/df for the same ϕ_E and ϕ_ν but a uniform ϕ_z, whereas the bottom panel shows the result normalised to dR/df

[3]With the exception of $E_{\rm max}$ which may be drastically affected by lensing but has little impact on the inferred value other parameters.

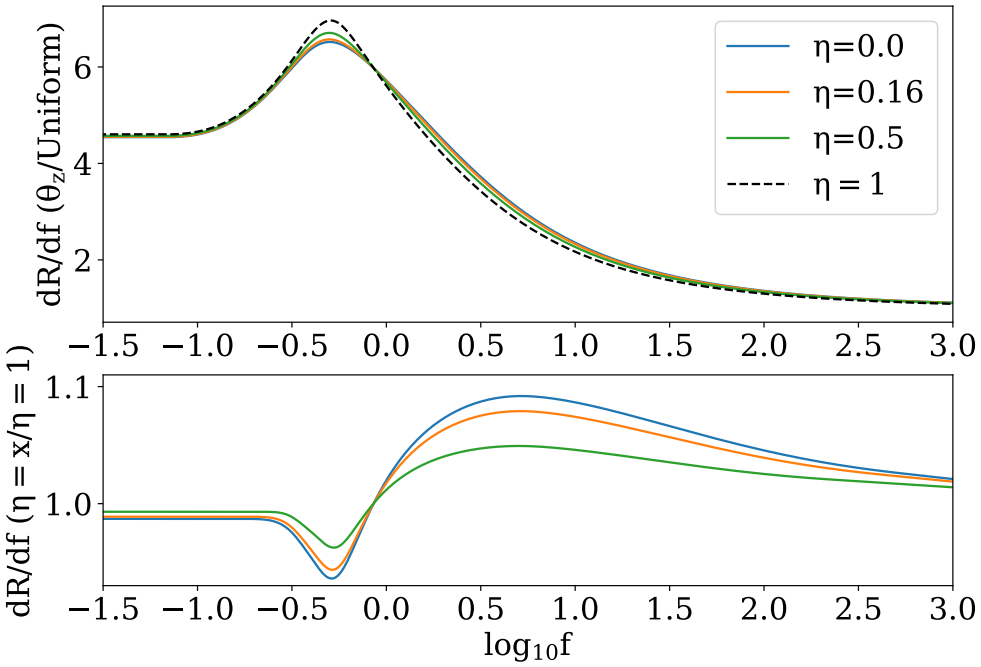

Figure 6.9: Top panel: dR/df normalised to the differential rate expected for a uniform spatial distribution. Bottom Panel: Fractional change in dR/df due to lensing, i.e. normalised by dR/df in an $\eta = 1$ universe. Both panels show results for η values of 0, 0.16 and 0.5 the middle of which corresponds to $\Omega_L = \Omega_{\rm DM}$ in a Planck cosmology.

for the same Θ_E in a smooth universe $\eta = 1.0$. In both panels we see the high fluence end tending towards 1.0, in line with our expectation for the local rate, which should be the same regardless of the choice of universe or spatial evolution. Moreover the results shown in the top panel can be easily scaled to any choice of normalisation corresponding to different estimates of the local rate of SGRBs (or indeed any of the other transients which we will display similarly). The top panel of Fig. 6.9 shows the differential rate falling at higher fluences, in accordance with the CSFR decreasing towards lower redshifts.

Fig. 6.9 shows that the observed dR/df for our representative SGRB model can fluctuate up to $\approx 10\%$ due to lensing with the scale of these fluctuations decreasing linearly with increasing η.

6.7.2 Long GRBs

Those GRBs with a duration above $\sim$ 2s are categorised as long (LGRB) and originate from core collapse supernovae explosions (ccSNe). Given the short lifetime of stars which produce ccSNe, LGRBs should trace star formation closely and hence we model $\phi_z \propto$ CSFR. Observations of LGRBs constrain their luminosity function to be a triple power law with indices $\gamma_1 = -1.7$, $\gamma_2 = -1.0$ and $\gamma_3 = -2.0$ in the respective zones between two break luminosities $L_{b,1} = 10^{51}$ erg/s and $L_{b,2} = 7.8 \times 10^{52}$ erg/s (Sun et al., 2015). We also impose a hard maximum luminosity at $L_{\max} = 10^{54}$ erg/s which corresponds to the highest luminosity LGRB observed (Frederiks et al., 2013). We convert these bolometric luminosities into spectral energies as per the method for SGRBs (with the LGRB width). We also assume all LGRBs to have a spectrum given by the Band energy function with indices $\alpha = -1$ and $\beta = -2.3$.

Fig. 6.10 shows dR/df calculated for the LGRB event rate energy function described above. Similarly to the case of SGRBs, the absolute rate decreases towards higher fluences in line with the CSFR decreasing at lower redshifts, however the LGRB rate does not decrease as significantly towards lower fluences. The

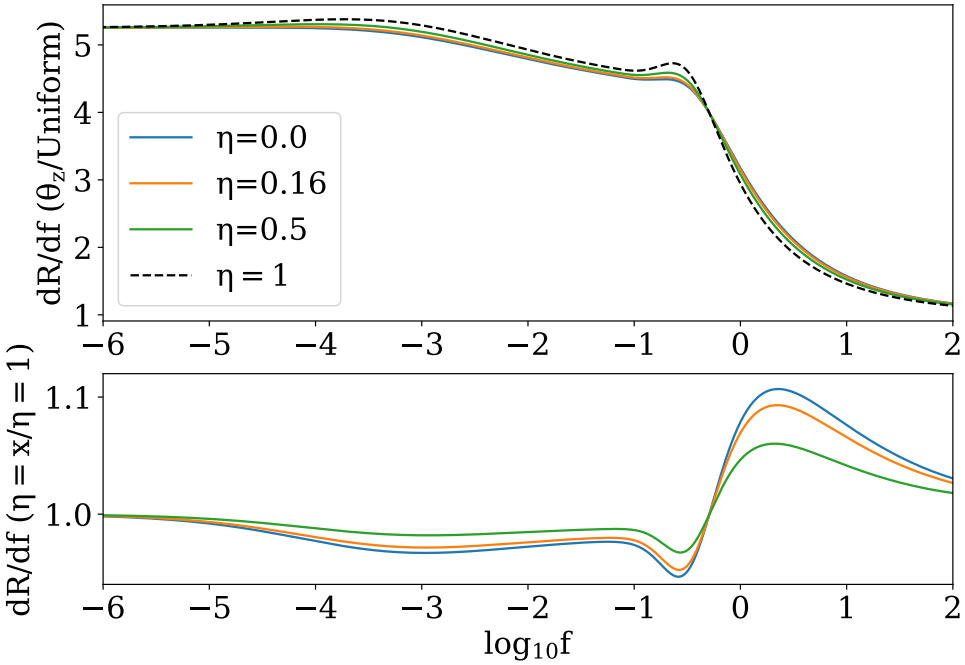

Figure 6.10: Same as Fig. 6.9 but computed for LGRBs.

effect of lensing on the observed LGRB differential rate is similar to SGRBs at a maximum of $\approx 10\%$. The fractional change shows slightly more structure for the case of LGRBs due to the triple power law of ϕ_E but this does not substantially influence the effect from lensing, with any relative differences capped at a few percent.

6.7.3 FRBs

For FRBs we assume that both ϕ_E and ϕ_ν have single power law form described by indices γ and α respectively. ϕ_E is also bounded by a hard cutoff at the maximum spectral energy $E_{\nu_e,\max}$. Leading theories for FRB progenitors (Platts et al., 2019) suggest that the central engine of FRBs is a compact stellar remnant such as a young magnetar. Such objects are also connected to massive star formation and hence, similarly to long GRBs, FRBs are expected to follow the CSFR.

From James et al. (2021b) the best fit values of these parameters are $\gamma =$

$-2.16^{+0.11}_{-0.12}$, $\alpha = -1.5$ and $E_{\nu_e,\max} = 10^{32.84}$ erg/Hz. James et al. (2021b) also allow for a redshift evolution on top of star formation by scaling the CSFR to the power of n. They find the best fit value of $n = 1.77$ under the assumption that ϕ_ν describes the change in energy of FRB bursts with frequency and not a change in the rate of bursts with frequency. Others within the field find differing model parameters. Luo et al. (2020) assume a flat spectral distribution, and find $\gamma = -1.79^{+0.31}_{-0.35}$, neglecting evolution (i.e. $n = 1$) and Shin et al. (2022) find a shallower $\gamma = -1.3^{+0.7}_{-0.4}$. Both James et al. (2021a) and Shin et al. (2022) use a similar model to calculate their values, which improves upon the model of Luo et al. (2020) by using an unbiased sample of FRBs, accounting for the full telescope beam shape, including the cosmological variance of DM, making use of the measured S/N of bursts and allowing the FRB event rate density to evolve with redshift. Shin et al. (2022) uses the first CHIME catalog of FRBs, making it the largest and only homogeneous sample among them. James et al. (2021a) treatment yields more precise results however, owing to the greater number of localised bursts with associated redshifts. Despite these differences, the results of all three are in broad agreement, for simplicity and to capture the small differences between them, our fiducial model will be $\gamma = -2.0$, $\alpha = -1.0$, $n = 1.0$ and $E_{\nu_e,\max} = 10^{33}$ erg/Hz.

The dR/df values resulting from the above calculations are depicted in Fig. 6.11. The results show behaviour very similar to that of the GRB calculations, with a slightly higher minimum in the fractional change due to lensing. This similarity is unsurprising because we have assumed that both types of transient are related to star formation.

6.8 Discussion

Understanding the effects of gravitational lensing on dR/df is crucial if the increasing number of recorded bursts with no redshift information are to be used to constrain Θ_E. Most of the lensing effects we have derived here are small. In

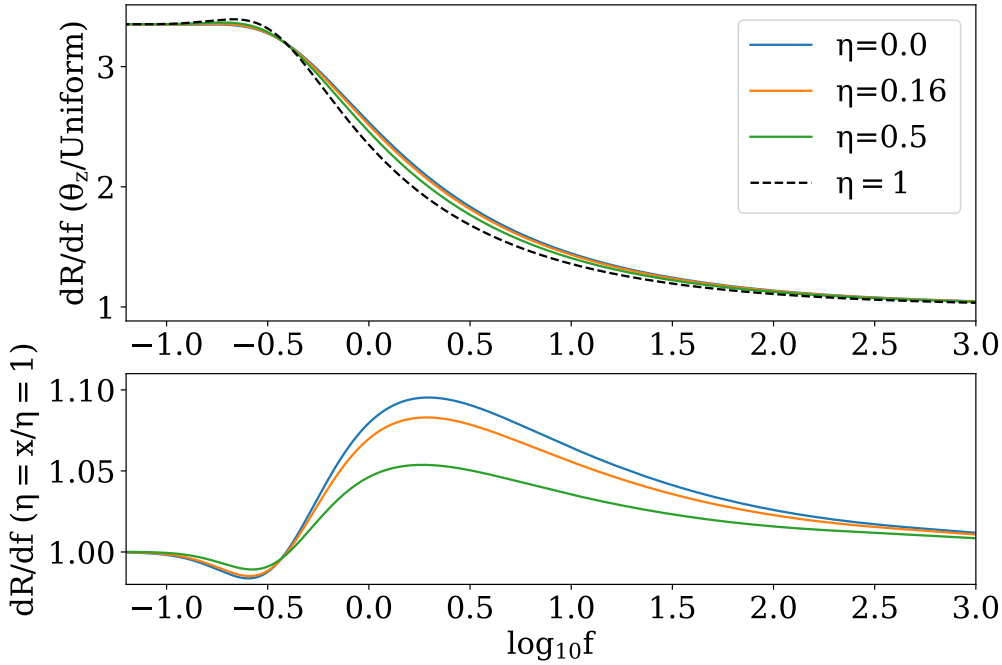

Figure 6.11: Sam as Fig. 6.9 but computed for FRBs.

the current context of observational constraints on Θ_E, for any of the transients mentioned here, the lensing effects are negligible compared to other sources of uncertainty. Hence, lensing may in most cases be ignored when calculating the expected differential rates from a Θ_E model.

Provided that there is a sharp[4] cutoff in the intrinsic rate at some critical energy $E_{\nu_e,\max}$, lensing will cause a fluctuation in dR/df relative to what is expected in a smooth universe, effectively independent of the transients underlying Θ_E. This fluctuation, seen in figures 6.9, 6.10 and 6.11, is a unique effect of lensing and could be used to constrain the value of η which affects its scale. Such constraints on η and the corresponding fluctuation in dR/df relative to a smooth universe would be of direct relevance to current cosmological problems, such as the anomalous amplitude of the cosmic matter dipole found in QSOs (quasi-stellar

[4]We take sharp to mean steeper than the power law dependence (ξ) of the magnification PDF with μ. In the geometric limit $\xi \approx= -3$.

objects), SN Ia and radio galaxies (see Aluri et al., 2023, for a review), for which the effect of lensing has not been explored in great detail.

A comparison between the figures in §6.5 shows that the scale of the fluctuation is also dependent on ϕ_z, α and γ. Due to this degeneracy, the intrinsic population parameters must be well known if η is to be constrained from the observed rates. Given the strong dependence of the absolute rates on these parameters however, they will require far fewer transients to be well constrained. To avoid lensing effects when constraining the intrinsic parameters of Θ_E, they should be modelled from low fluence bursts where the effect of lensing is negligible. To define a low fluence we require $f_{b,\eta}$, the break fluence defined in §6.4. Without knowing $E_{\nu_e,\max}$ this becomes more difficult, however we can approximate a minimum value of $E_{\nu_e,\max}$ and f_b by considering the magnification decomposition of the fractional change in dR/df due to lensing. For the FRB case shown in Fig. 6.11 this magnification decomposition is plotted in Fig. 6.12. It shows that across all fluences there is very little contribution from magnifications above $\mu = 10^2$. A lack of high magnification bursts means that $E_{\nu_e,\max}$ is unlikely to be lower than $1/10^2$ the apparent maximum. By establishing a lower limit on $E_{\nu_e,\max}$ and setting $f_{b,\eta}$ to correspond to this approximate maximum at a redshift of negligible star formation in a universe $\eta = 0$ we can safely assume $f < f_{b,\eta}$ to be in the low fluence regime.

Assuming that the population parameters are well constrained by these low fluence bursts, the intrinsic model could be extrapolated to the high fluence regime for the case of a smooth universe and compared to the observed differential event rates to place a lower limit of the value of η. Averaging over the expected fluctuation for all fluences higher than $f_{b,\eta}$, and below the fluence for a maximum energy burst at $z = 0.001$, we can determine the number of high fluence bursts that would be required to statistically distinguish the expected average fluctuation. We plot this number for FRBs for varying values of η and varying intrinsic γ and α values in Fig. 6.13. We assume that the observed bursts are dis-

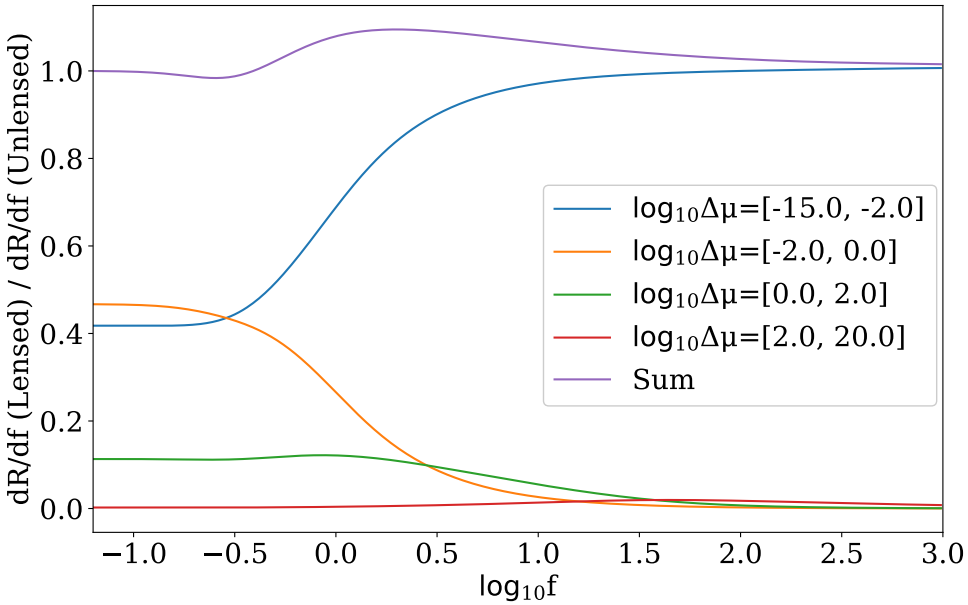

Figure 6.12: Fractional change in dR/df due to lensing, as plotted in Fig. 6.11 decomposed into components of varying magnification. Upper and lower bounds correspond to the limits of our numerical method as described in §6.3.5.

tributed log-uniformly and calculate the relative error on the observed number as $1/\sqrt{N}$. We then calculate the number that would be required for the average of the absolute value of the fluctuation to be significant at the 95% confidence level for a normal distribution (given the large number of bursts required we expect normality in the uncertainty).

As expected from Fig. 6.2 and Fig. 6.5 the number of bursts required to distinguish a universe with a smooth matter fraction η from a completely homogeneous universe $\eta = 1$ generally increases with decreasing γ and α with smoother universes naturally requiring more bursts. For the fiducial FRB population of $\gamma = -2.0$, and $\alpha = -1.0$ a universe comprised entirely of lenses can be ruled out using 8000 high fluence FRBs. Conversely a nearly smooth universe with 5% of its matter in lenses would require some 3.5×10^5 FRBs to distinguish from the smooth case.

Planned instruments such as CHORD or the proposed coherent all sky monitor

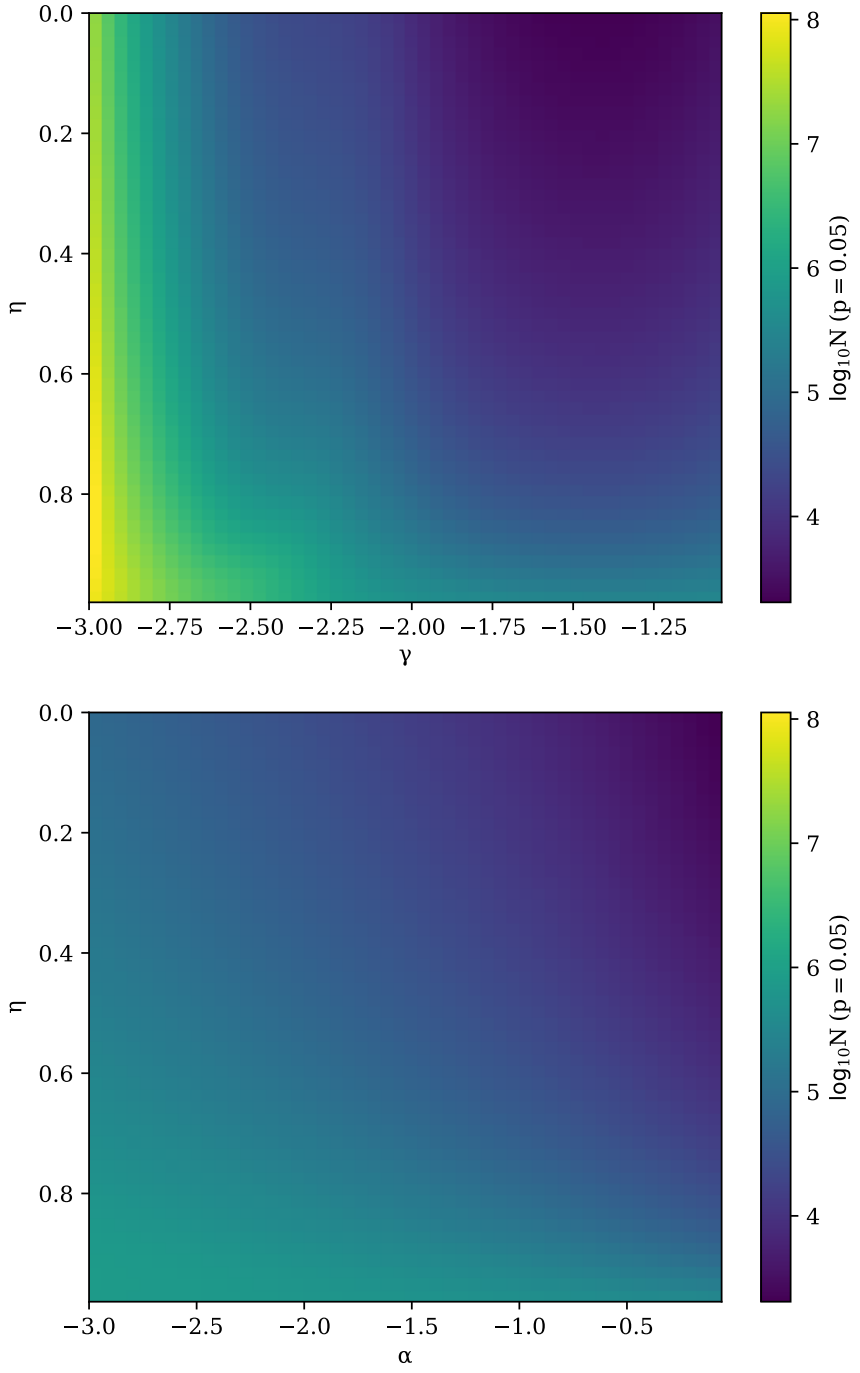

Figure 6.13: Number of high fluence FRBs required to distinguish a universe with a smooth matter fraction η from the $\eta = 1$ case with 95% confidence, assuming the intrinsic population parameters ϕ_z, α and γ are known. *Top:* Plotted for varying values of γ with an $\alpha = -1.0$ and $\phi_z \propto$ CSFR. *Bottom:* Plotted for varying values of α with an $\gamma = -2.0$ and $\phi_z \propto$ CSFR.

(CASM) BURSTT (Lin et al., 2022) have predicted detection rates of $\sim 10^4$ per year (Connor & Ravi, 2022). Several such instruments observing over the course of ten years could reasonably achieve our desired 3.5×10^5 high fluence FRBs, especially given the low-sensitivity – high field of view mode of operation for CASMs. This would allow formation of broad and stringent constraints over parts of the PBH space that have only been probed locally. To show which masses the constraints apply over we must consider both source extension and wave optics effects as detailed in appendix 3.2. Doing so we calculate the PBH dark matter fraction constraints shown in Fig. 6.14 for 3.5×10^5 high fluence FRBs observed at 1.4GHz. We highlight that the only observables required for each of these FRBs are the booleans $f > f_{b,\eta}$ and $\nu > \nu_{\min}$[5]; a precise fluence measurement is not required, neither is a localisation or redshift. If these FRBs are observed at higher frequencies, these constraints will extend down to lower masses, with an infinite frequency FRB counterpart extending all the way down to $10^{-22} M_\odot$. Assuming a FRB-like functional form for the GRB intrinsic Θ_E, a similar number of GRBs could constrain PBHs down to $10^{-15} M_\odot$ as displayed in the figure.

Constraining $E_{\nu_e,\max}$ is an area of particular import in an inhomogeneous universe as lensing can have a large effect on the apparent maximum energy of a burst. $E_{\nu_e,\max}$ is often taken to be the greatest apparent energy amongst observed bursts, which in an inhomogeneous universe can be a large overestimation. The compact nature of fast transient sources means they are susceptible to lensing by low mass objects. Such objects may leave no observational trace of the magnification they are causing. This makes it impossible to know the magnification of an individual burst and thus impossible to confidently approximate the intrinsic $E_{\nu_e,\max}$ based on the largest apparent energy. Variation of $E_{\nu_e,\max}$ however, is not degenerate with η and hence may be constrained if sufficient data are collected to distinguish a fluctuation in dR/df due to lensing.

[5]where this minimum frequency is used the establish the minimum probed lens mass.

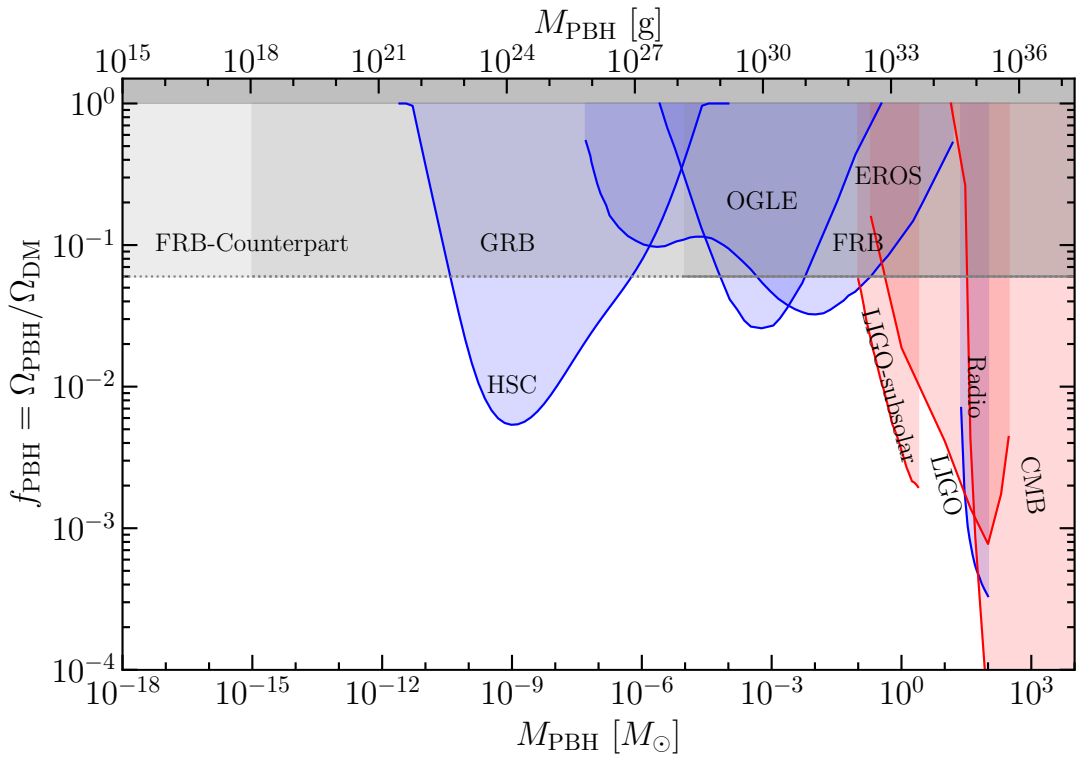

Figure 6.14: Current and potential constraints on the allowed fraction of dark matter in PBHs with a monochromatic mass function centred on M_{PBH}. Constraints based on measurements from our local galactic environment are shaded blue. Constraints that are cosmological in origin are shaded red. Our proposed constraints from 3.5×10^5 high fluence transients are shown in grey. These extend to varying lower mass limits based on observed frequency and source extent as detailed in appendix 3.2. We note that $\eta = 0.95$ corresponds to a maximum f_{PBH} of $\approx 6\%$ (for a Planck cosmology). This plot was made using code from the github repo `https://github.com/bradkav/PBHbounds` (Kavanagh, 2019, and references therein).

6.9 Conclusion

Gravitational lensing is one possible propagation effect to consider when modelling the differential events rate of fast transients from their intrinsic population functions. In doing so we have shown that, for static lensing geometries:

1. Except for the mass-energy range with prominent fringes shown in Fig. 6.8, FRBs are not all intrinsically low luminosity events highly magnified by gravitational lensing from point masses.

2. Given current observational uncertainties, intrinsic population function parameters (other than $E_{\nu,\max}$) inferred from observations without accounting for lensing will not significantly differ in a completely inhomogeneous universe ($\eta = 0$)

3. Wave optics may cause magnification PDFs to differ from the familiar μ^{-3} behaviour at high magnifications.

4. For masses above 0.01 solar masses geometric optics will suffice for modelling the dR/df of FRBs in an $\eta = 0$ universe.

5. Using low fluence ($< f_{b,\eta}$) observations of dR/df to estimate Θ_E will be free from the effects of lensing. A further comparison with high fluence observations can be used to extract the influence of gravitational lensing. In this way the compactness of FRBs and GRBs can be exploited to constrain unexplored regions of dark matter parameter space such as low mass primordial black holes. We expect that 8000 high fluence, unlocalised FRBs would be required to rule out a completely clumpy universe, with 3.5×10^5 required to exclude more than 6% of dark matter being in PBHs in the relevant mass range.

Acknowledgements

We thank Geraint F. Lewis and Ron Ekers for productive discussions on lensing. CMT is supported by an Australian Research Council Future Fellowship under project grant FT180100321. CWJ acknowledges support from the Australian Government through the Australian Research Council's Discovery Projects funding scheme (project DP200102545).

Data Availability

The data underlying this article are available in the article and in its online supplementary material.

Chapter 7

Two-Screen Scattering in CRAFT FRBs

This chapter is comprised of a pre-copyedited, author-produced version of an article accepted for publication in *Monthly Notices of the Royal Astronomical Society* following peer review. The version of record: Mawson W Sammons, Adam T. Deller, Marcin Glowacki, Kelly Gourdji, C. W. James, J. Xavier Prochaska, Hao Qiu, Danica R. Scott, R. M. Shannon and C. M. Trott, Two-Screen Scattering in CRAFT FRBs, *Monthly Notices of the Royal Astronomical Society*, is available online at: https://doi.org/10.1093/mnras/stad2631. I motivated this work, which was supervised by Prof. Cathryn Trott and Dr Clancy James. A/Prof. Ryan Shannon contributed to the initial discovery of the FRBs used in the analysis. Initial calibration and pre-processing of data was performed by Ms. Danica R. Scott, Prof. Adam Deller, Dr Kelly Gourdji and Dr Marcin Glowacki. I performed all analyses of the processed data, making use of code written by Dr Hao Qiu to characterise burst morphology. Prof. J. Xavier Prochaska motivated additional extragalactic scattering constraints. The draft manuscript was written by me and distributed to co-authors for critique. All co-authors provided input over several iterations of feedback until the manuscript was complete.

7.1 Abstract

Temporal broadening is a commonly observed property of fast radio bursts (FRBs), associated with turbulent media which cause radiowave scattering. Similarly to dispersion, scattering is an important probe of the media along the line of sight to an FRB source, such as the circum-burst or circum-galactic mediums (CGM). Measurements of characteristic scattering times alone are insufficient to constrain the position of the dominant scattering media along the line of sight. However, where more than one scattering screen exists, Galactic scintillation can be leveraged to form strong constraints. We quantify the scattering and scintillation in 10 FRBs with 1) known host galaxies and redshifts and 2) captured voltage data enabling high-time resolution analysis. We find strong evidence for two screens in three cases. For FRBs 20190608B and 20210320C, we find evidence for scattering screens less than approximately 16.7 and 3000 kpc respectively, from their sources, consistent with the scattering occurring in the circum-burst environment, the host ISM (inter-stellar medium) or the CGM. For FRB 20201124A we find a low modulation index that evolves over the burst's scattering tail, indicating the presence of a scattering screen $\approx$ 9 kpc from the host, and excluding the circum-burst environment from potential scattering sites. By assuming that pulse broadening is contributed by the host galaxy ISM or circum-burst environment, the lack of observed scintillation in four FRBs in our sample suggests that existing models may be poor estimators of scattering times associated with the Milky Way's ISM, similar to the anomalously low scattering observed for FRB 20201124A.

7.2 Introduction

Fast radio bursts (FRBs) are short duration (μs – ms), extragalactic, radio frequency bursts (Lorimer et al., 2007; Thornton et al., 2013). In addition to intrinsic time-frequency structure, FRBs are dispersed and often contain the hallmarks of multi-path propagation, arising from propagation through a turbulent medium.

While the intergalactic medium (IGM) is often responsible for a sizeable portion of FRB dispersion (Macquart et al., 2020), due to its tenuous density, it is not expected to contribute significantly to the scattering, with estimates typically as low as $\sim 10\,\mu$s at 1 GHz (Macquart & Koay, 2013; Cordes et al., 2022). This conclusion is supported by the observed lack of correlation between FRB dispersion measures (DM) and scattering times (Chawla et al., 2022; Gupta et al., 2022).

Similarly, the Milky Way interstellar medium (ISM) is not expected to dominate the scattering observed in FRBs at high Galactic latitudes, with scattering times inferred from pulsars (Cordes & Lazio, 2003) being $\lesssim 10\mu s$ for lines of sight more than 30° away from the Galactic plane. Assuming that the host galaxies of FRBs are similar to the Milky Way, the symmetry of the scattering process leads to the conclusion that, on average, host galaxy ISMs are also unlikely to be singularly responsible for the observed FRB scattering (Simha et al., 2020; Chawla et al., 2022).

Due to their large geometric leverage, intervening galaxies are a potential source of large scattering in FRBs. For a high redshift population ($z \sim 5$), intervening galaxies have been forecast to be the dominant source of scattering (Ocker et al., 2022b). For FRBs with $z \lesssim 1$, however, the probability of intersecting a foreground galaxy is insufficient for them to be the dominant source of scattering in the population (Macquart & Koay, 2013; Prochaska & Neeleman, 2018; Chawla et al., 2022; Ocker et al., 2022b).

A potentially important scattering region is within the circum-burst environment, which has long been suggested as the site of the $\gtrsim$ ms scattering times and $\gtrsim$ 100 rad m^2 rotation measures (RMs) observed in some FRBs (Masui et al., 2015). Measurements of RM variability in some repeating FRBs have supported this scenario, with large variations over short durations requiring a dense, magnetised medium near the source (Michilli et al., 2018; Hilmarsson et al., 2021; Anna-Thomas et al., 2022). Recent measurements of scattering variability in FRB 20190520B provide the tightest limits yet, with variation on minute

timescales requiring the dominant scattering media to be within at most 0.4 AU of the source, and potentially within $\sim 10^4$ km (Ocker et al., 2022b). In this scenario, scattering serves as an important probe of the circum-burst region which would inform our understanding of FRB progenitors, favouring formation channels where the central engine evolves in a dense turbulent magnetised medium, such as a magnetar embedded within a nebula (Margalit & Metzger, 2018).

Another region of interest is the circum-galactic media (CGM) of foreground galaxies. To date, observations of FRBs passing through the CGM/halos of intervening galaxies have shown very little scattering, with only as much as $\sim 80\,\mu$s recorded at 1.4 GHz (Prochaska et al., 2019a; Connor et al., 2020, 2023). The possible presence, however, of cloudlets of cold gas in the CGM, inferred from quasar absorption spectra (McCourt et al., 2018), has the potential to cause scattering consistent with that observed in the FRB population (Vedantham & Phinney, 2019, see Prochaska et al. (2019a) for a corrected description). If this model is correct then FRBs could serve as an important probe of the CGM. As discussed by Vedantham & Phinney (2019), distinguishing between scattering in the CGM and circum-burst media will be crucial.

For scattering that is well approximated by a thin screen model, the degeneracy between the angular broadening and screen distance makes it difficult to directly constrain where the scattering is occurring based only on the pulse-broadening time. For repeating FRBs, a direct constraint can be made by observing the variation of decorrelation bandwidth ($\nu_{\rm DC}$) or temporal broadening over time ($t_{\rm scatt}$) (Ocker et al., 2022b; Main et al., 2022). For FRBs that are not seen to repeat, a variability study cannot be conducted; however, in cases where scattering and scintillation have been contributed by separate screens, the scattering geometry can be constrained using the observation of only a single burst (Masui et al., 2015; Farah et al., 2018; Ocker et al., 2022c). This can allow not only for the distinction between host and intervening scattering screens, but also constrain the level of scatter-broadening in the Milky Way, for independent com-

parison with electron distribution models such as NE2001 and YMW16 (Cordes & Lazio, 2003; Yang & Zhang, 2017, respectively).

Where previously Day et al. (2020) relied on lower time resolutions and image-plane-based techniques, it is now routinely possible to conduct detailed burst morphology analysis, of the type undertaken by Cho et al. (2020), for all CRAFT FRBs with the advent of the CELEBI post-processing pipeline (Scott et al., 2023). This allows for the high-precision estimates of $\nu_{\rm DC}$ and $t_{\rm scatt}$, required to robustly identify scintillation and scattering. We are therefore motivated to search for evidence of two-screen scattering within CRAFT FRBs.

In this work we greatly expand the sample of FRBs analysed for two-screen scattering. We measure the level of scattering and scintillation in 10 CRAFT FRBs with high spectro-temporal resolution and apply the two-screen model developed by Masui et al. (2015) and Ocker et al. (2022c) to place constraints on the distances to their respective scattering screens. In §7.3 we detail the data and our methodology. In §7.4 we present the results, and in §7.5 we discuss their implications.

7.3 Method

The scattering and scintillation resulting from multi-path propagation through the same medium will be related via a Fourier uncertainty relationship,

$$2\pi\nu_{\rm DC}t_{\rm scatt} = C. \tag{7.1}$$

The precise value of C depends on the geometry and the density fluctuations in the scattering media, however, it typically ranges between 0.5 and 2 (Lambert & Rickett, 1999). As observed previously by Masui et al. (2015) and Ocker et al. (2022c), this is not always the case for FRBs, with discrepancies indicating that a single scattering medium is a poor model for propagation along the line of sight.

In these cases, a two-screen model can provide a natural explanation for the

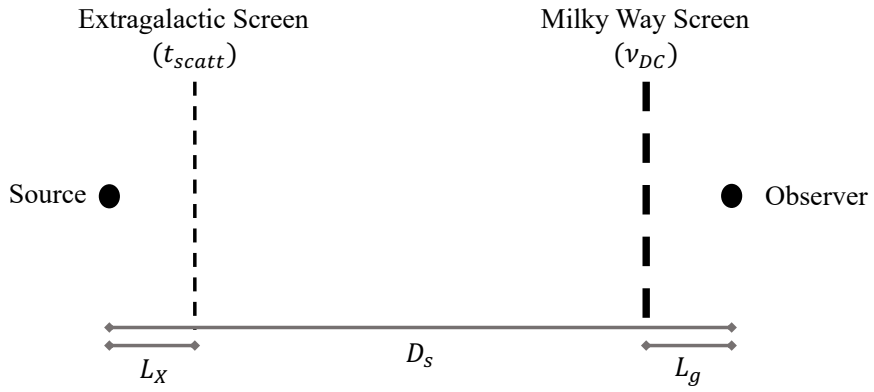

Figure 7.1: Diagram of the two screen scattering geometry.

differences. Under this model, a relatively large $t_{\rm scatt}$ and $\nu_{\rm DC}$ are contributed by separate screens, allowing them to be observed simultaneously for a given line of sight without violating the uncertainty relationship within a single screen. The geometry is often described as shown in Fig. 7.1, using L_x, the distance between the source and the first screen, and L_g, the distance between the observer and the second screen, labeled according to the expectation that the first screen is extragalactic and the second Galactic. In order for both screens to cause diffractive scintillation, the scattered image formed by the first screen must be unresolved by the second. Assuming that the distance between the scattering screens is much larger than either L_x or L_g (i.e. $(L_x + L_g)/D_s \ll 1$), this leads to the following constraint on the geometry (Ocker et al., 2022c)

$$L_x L_g \lesssim \frac{D_s^2}{2\pi\nu^2(1+z_s)} \frac{\nu_{\rm DC}}{t_{\rm scatt}}. \tag{7.2}$$

The factor of $(1+z)$, where z_s is the redshift of the source, results from estimating $\theta_{\rm scatt}$ from the observed $t_{\rm scatt}$, as derived in Macquart & Koay (2013). This allows the position of scattering media to be constrained directly using once-off FRBs, allowing mediums such as a diffuse IGM to be ruled out as the dominant source of scattering (Masui et al., 2015). In the case of FRB 201905020b, a reasonable assumption of L_g places the extragalactic screen within 100 pc of the FRB progenitor, suggesting that the scattering could be occurring in the circum-

burst environment (Ocker et al., 2022c).

Our data comprise 10 localised FRBs which had been processed through the CELEBI post-processing pipeline (Scott et al., 2023) at the time of writing. These bursts were detected in real-time searches of the incoherent sum of intensities of each antenna in each of the 36 beams formed digitally using ASKAP's phased-array receivers (Bannister et al., 2017, 2019b). Each detection triggered the download of the 3.1 s voltage buffers channelised using an oversampled polyphase filterbank (PFB). To localise the FRB, the voltage data are correlated, calibrated and imaged as detailed by Day et al. (2021) and exemplified in Ryder et al. (2022). To study the burst morphology, as we shall here, the PFB is inverted to recover the full ~ 3 ns time resolution of the voltage data, which are then beamformed and dedispersed as outlined in Scott et al. (2023), with the dispersion measure (DM) chosen to optimise the sharpness of temporal structures within the bursts as detailed in Sutinjo et al. (2023). We identify the bursts within the ~ 3 s of voltage data sampled at ~ 3 ns resolution and form dynamic spectra using a Fast Fourier Transform of the four Stokes parameters. By default the resolution is chosen to be 0.1 MHz and 10 μs. However, when temporal or spectral structures were found to be unresolved, respective scales as small as 1 μs or 10 kHz were explored independently[1]. Here we analyse only the Stokes I data associated with each burst; a more complete polarimetric study of each burst is reserved for a future work.

From the dynamic spectra formed, we select on and off-pulse (pre-burst) regions to account for the shape of the bandpass and to mitigate any radio frequency interference (RFI). To do this, the time-averaged spectrum in the off-pulse region is subtracted from the burst and each spectral channel in the burst is divided by the standard deviation of the corresponding off-pulse channel. The resulting burst dynamic spectrum has a noise that is normally distributed with a mean of zero and a standard deviation of unity. Furthermore, the burst intensity is now

[1]In these cases where greater resolution was required the spectral and temporal analyses were performed on separate data sets formed from the same voltages at independent resolutions.

represented in units of per-channel signal-to-noise ratio (S/N).

The level of spectral modulation in a burst is calculated from the lowest, non-zero frequency lag in the mean normalised spectral auto-covariance, as per Macquart et al. (2019). Bursts with a high modulation index (m) or obvious scintillation in their dynamic spectra are then investigated further. Following other studies (Nimmo et al., 2022a; Ocker et al., 2022c), we fit a Lorentzian to the auto-correlation of the mean-subtracted, time-integrated, normalised burst spectra and we measure the $\nu_{\rm DC}$ to be the half-width-half-maximum (HWHM) of the best-fit case.

In cases where significant RFI is present in the unnormalised burst dynamic spectrum, we investigate the impact of RFI subtraction on the auto-correlation function (ACF) of normalised bursts. To do so, a fake FRB with a uniform spectral profile is injected into the off-pulse noise and then normalised via the same method. If a significant excess is found in the ACF of this normalised fake FRB then the RFI is deemed too significant to compensate for, and the FRB in question (or at least the section of bandwidth containing the RFI) are discarded from the sample. To avoid large Poisson noise associated with measuring only a small number of scintles (the finite scintle effect) (Cordes et al., 1990), we require the retained bandwidth to be much larger than $\nu_{\rm DC}$.

To distinguish scintillation from frequency structures intrinsic to the burst such as self-noise[2], we split the normalised FRB into four even sub-bands and fit a Lorentzian to the ACF of each band's spectra. Due to the large number of scintles in each sub-band we expect the effect of re-binning on the results will be minimal. If $\nu_{\rm DC}$ is observed to increase with frequency, as expected for multi-path propagation through a cold plasma, we assume the spectral structures are caused by scintillation. We characterise the minimum scintillation bandwidth we are sensitive to ($\nu_{\rm min}$) using simulations as described in Appendix C.4, we highlight that this quantity is distinct from the spectral resolution of the data set.

[2]Following Ocker et al. (2022b), we refer to frequency structures on the reciprocal scale of FRB temporal sub-structures as self-noise.

We also fitted for $t_{\rm scatt}$ in each burst's frequency-integrated pulse profile. By default we assume a scattered Gaussian pulse profile, however, we allow intrinsic burst profiles to comprise multiple Gaussians when necessary. All burst morphology and auto-correlation fitting are performed using a nested sampling technique outlined in Qiu et al. (2020). The frequency evolution of scattering is measured using independent fits to burst sub-bands as done for $\nu_{\rm DC}$, with $t_{\rm scatt}$ expected to decrease at higher frequencies. We expect that $t_{\rm scatt}$ and $\nu_{\rm DC}$ will evolve in frequency following a power law with indices $\alpha_t \approx -4$ and $\alpha_\nu = 4$ for scattering and scintillation respectively. These indices correspond to the expectation for very strong scattering in a Kolmogorov turbulence with an inner scale (Cordes & Lazio, 1991; Cordes & Rickett, 1998). We fit for these spectral indices in every burst where data permits. In cases where only two sub-bands are used these spectral indices have no measured uncertainty.

We compare our measurements of scintillation or lack thereof with the expected Galactic scintillation ($\nu_{\rm NE2001}$) using the NE2001 electron density model (Cordes & Lazio, 2003). We note that there can be order of magnitude differences in scatter broadening and scintillation bandwidths for Galactic lines of sight with the same DM (Bhat et al., 2004). Moreover, we use the best fit $\nu_{\rm DC}$ and $t_{\rm scatt}$ to compute C as per Eq. 7.1. Finally, when $C \gg 1$ we derive the two-screen distance product $L_x L_g$ as expressed in Eq. 7.2.

7.4 Results

The properties of each burst in our sample can be found in Table C.1, where a '–' denotes parameters that could not be measured or derived. Within our sample, we find three FRBs with convincing evidence of spectral scintillation, from which two-screen constraints can be formed. Of the remaining FRBs, four FRBs were found to contain no spectral scintillation, two contained evidence of spectral structure that could not be confirmed as scintillation and one, FRB 20191228A, contained instrumental effects for which we could not adequately compensate. In

the following sub-sections, we will describe each of these cases in greater detail, with the exception of FRB 20191228A, which is not analysed further.

7.4.1 FRB 20190608B

The dynamic spectrum of FRB 20190608B is shown in Fig. 7.2 at a reduced time and frequency resolution of 0.2 ms and 2 MHz to improve visual distinction. The burst has the lowest integrated S/N in our sample, however, obvious bands of intensity can still be seen in the dynamic spectrum of the burst. The unnormalised spectrum contains negligible RFI effects and therefore we use all 336 MHz of the observed bandwidth centred at 1271.5 MHz. Analysing the time-integrated spectra at 0.1 MHz resolution, we measure a high modulation index of $m = 0.78$ and $\nu_{\rm DC} = 1.4 \pm 0.1$ MHz for the whole band as shown in Fig. 7.3. Integrating over frequency, we find a scattering time of $t_{\rm scatt} = 4.0 \pm 0.4$ ms, as shown in Fig. 7.4.

Dividing the observation into four subbands we measure the spectral indices of $\nu_{\rm dc}$ and $t_{\rm scatt}$ to be $\alpha_\nu = 5.8 \pm 0.5$ and $\alpha_t = -3 \pm 1$, as shown in Fig. 7.5 top and bottom, respectively. The frequency evolution of the $t_{\rm scatt}$ is consistent within 1σ with $t_{\rm scatt} \propto \nu^{-4}$ as expected. Conversely, the evolution of $\nu_{\rm DC}$ is steeper than the Kolmogorov expectation at a marginal significance of 3.6σ.

Given the high modulation index and the positive slope of $\nu_{\rm DC}$ evolution in frequency, we assume the spectral modulation in this burst is the result of diffractive scintillation of a point-like source. Similarly, the negatively sloped frequency evolution of $t_{\rm scatt}$ is consistent with multi-path scattering. Combining the measurements of each over the full bandwidth we find $2\pi\nu_{\rm DC}t_{\rm scatt} = C \approx 35000$, indicating that a single thin screen is insufficient to describe the scattering medium along the line of sight to FRB 20190608B. Using Eq. 7.2 we find an upper limit on the two-screen distance product of $L_x L_g \lesssim 6 \pm 1\,{\rm kpc}^2$.

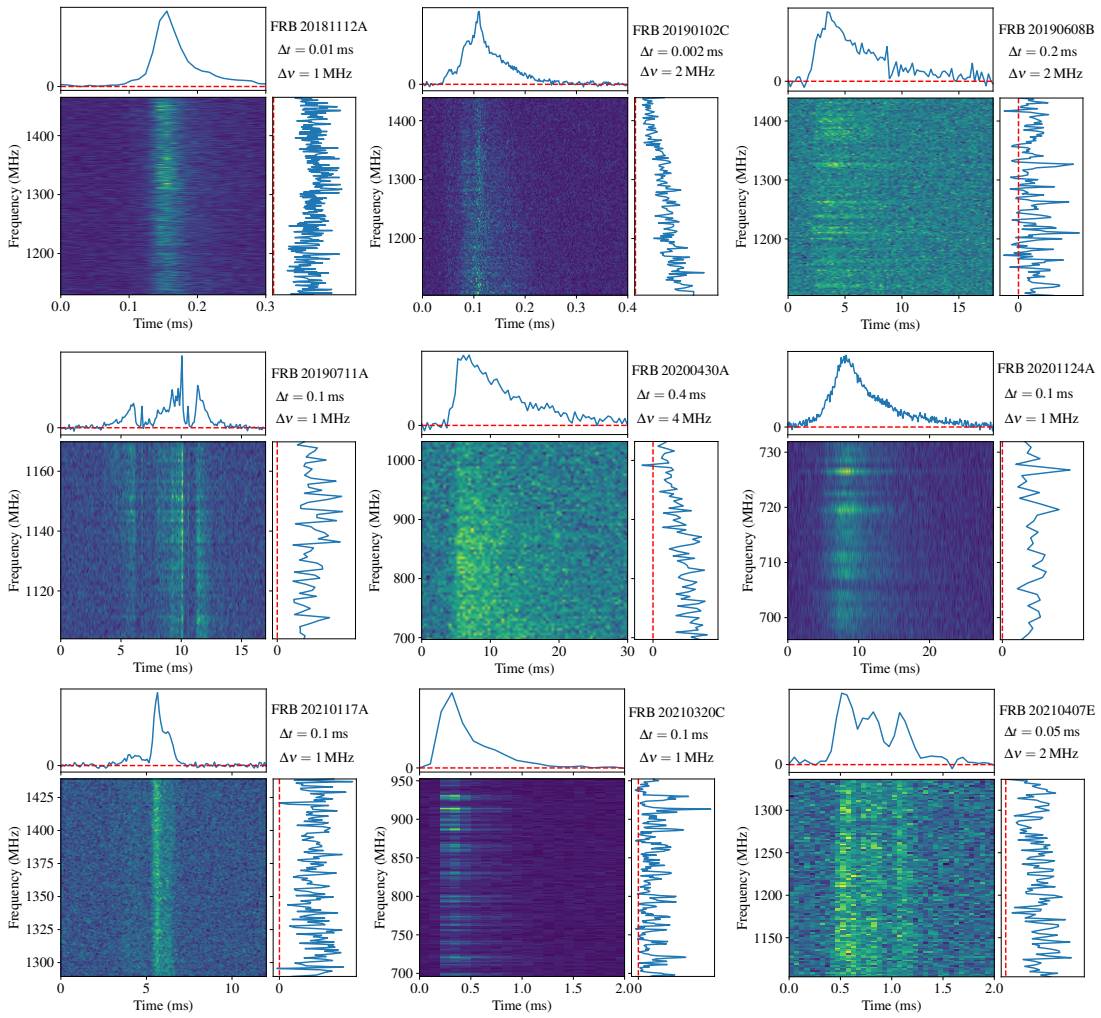

Figure 7.2: Dedispersed dynamic spectrum of all analysed FRBs. FRB names and spectral and temporal resolutions corresponding to the shown dynamic spectra are labelled in the top right corner of each plot. The top panels of each dynamic spectra show the burst profiles integrated over frequency, and the right-hand panels are integrated over time.

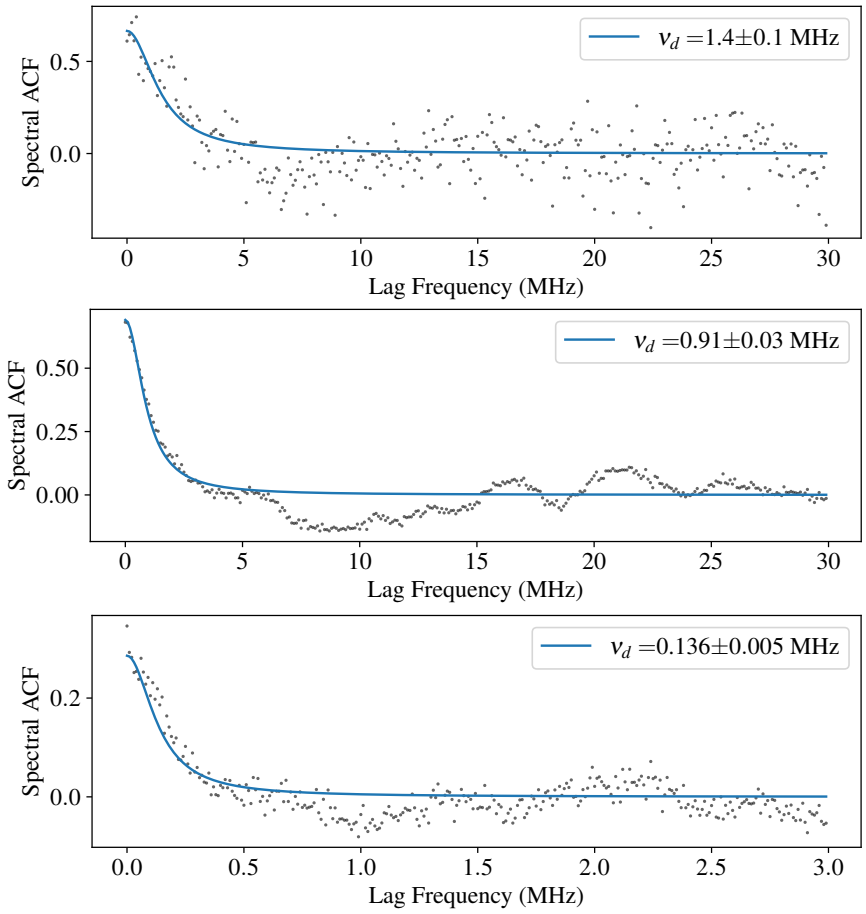

Figure 7.3: Scintillation fits of FRBs 20190608B, 20210320C and 20201124A from *top* to *bottom*. Black points show the ACF of the time-integrated burst spectra at 0.1 MHz, 0.1 MHz and 0.01 MHz resolution respectively. Blue lines show the best-fit model Lorentzians. The maximum amplitude of the ACF represents the square of the modulation index m^2.

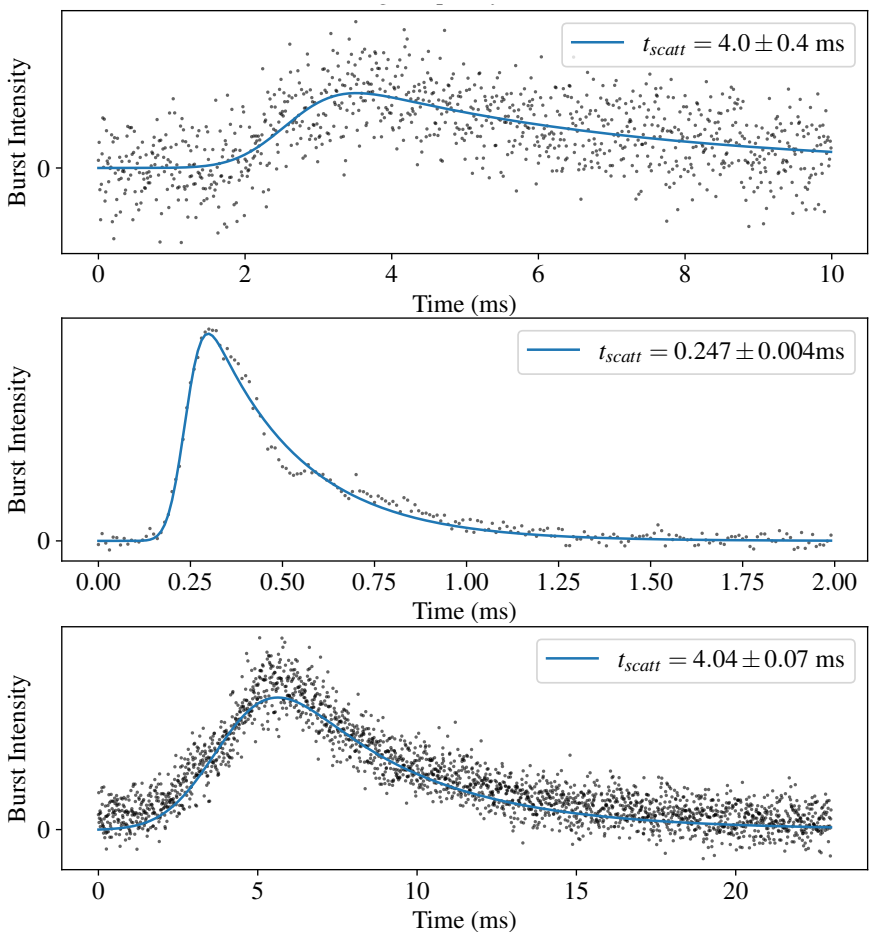

Figure 7.4: Scattering fits of FRBs 20190608B, 20210320C and 20201124A from *top* to *bottom*. Black points show the frequency-integrated pulse profiles at 10 μs resolution. The blue lines show the best-fit scattered Gaussian models.

7.4.2 FRB 20210320C

The dynamic spectrum of FRB 20210320C is shown in Fig. 7.2. The burst has $S/N = 113$ and a high modulation index of $m = 0.83$, consistent with the obvious intensity bands in the burst spectra. The de-dispersion and localisation analysis of this burst will be presented in Shannon et al. (in preparation). Due to the dispersive sweep of ~ 1.8s across the 336 MHz ASKAP bandwidth and the ~ 1.6 s latency of the detection system, some of the FRB was lost from the voltage buffer before it was downloaded. As a result the burst emission is only found in 257 MHz of bandwidth around a central frequency 824.2 MHz. The spectral ACF is particularly well fit by a Lorentzian profile with $\nu_{\rm DC} = 0.91 \pm 0.03$ MHz, as seen in Fig. 7.3. Fig. 7.4 shows the best-fit model of the pulse profile, with $t_{\rm scatt} = 0.247 \pm 0.004$ ms.

Fitting to four sub-bands, we find $\alpha_\nu = 2 \pm 1$ and $\alpha_t = -3.30 \pm 0.01$, as per Fig. 7.5, top and bottom respectively. Each of these parameters evolves with the sign expected for multi-path propagation and are within the ranges observed for pulsars (Bhat et al., 2004). Hence we assume they are caused by scintillation and scattering respectively. Measurements over the whole band yield $C = 1410$ with an upper limit on the two-screen distance product of $L_x L_g \lesssim 550 \pm 30\,{\rm kpc}^2$.

7.4.3 FRB 20201124A

The dynamic spectrum of FRB 20201124A is shown in Fig. 7.2. The burst appears as a bright narrow-bandwidth pulse, with a $S/N = 172$.

The measured modulation index of the burst is somewhat low at only $m = 0.59$, however, the intensity banding in its spectrum motivates us to search for scintillation. To probe the fine spectral structure observed in the burst we analyse the spectrum at 0.01 MHz resolution. The Lorentzian structure expected for scintillation provides a good fit to the spectral ACF as plotted in Fig. 7.3, with a best fit $\nu_{\rm DC} = 0.136 \pm 0.005$ MHz.

Despite the narrow bandwidth the burst occupies, its high S/N allows us to

measure $\alpha_\nu = 10 \pm 3$ across four sub-bands as shown in the top of Fig. 7.5. This spectral index is consistent with expectations at the 2σ level. The value of the decorrelation bandwidth is also consistent with the average of other measurements made for FRB 20201124A (Main et al., 2021, 2022) assuming $\alpha_\nu = 4$. We, therefore, assume that the frequency structures are caused by scintillation.

We measure the scattering time to be 4.03 ± 0.09 ms over the whole band, with a $\alpha_t = -7.3 \pm 0.9$ measured over four sub-bands as shown in Figs. 7.4 and 7.5. This measurement is steeper than the expectation at 3.7σ, however, we note that for this FRB the dynamic range in frequency is extremely limited. Assuming $\alpha_t = -4$, this measurement is consistent with previously measured upper limits on the scattering time for this source (Marthi et al., 2022).

Combined $\nu_{\rm DC}$ and $t_{\rm scatt}$ over the used bandwidth yields $C \approx 3450$, indicating that a single screen is a poor model for the scattering media along the line of sight. If we assume that the initial scattering screen is unresolved by the first we constrain $L_x L_g \lesssim 1.43 \pm 0.08\,{\rm kpc}^2$, however, we note that in this case, we would expect the observed FRB spectrum to be fully modulated. In §7.5 we consider the case of a partially resolved initial scattering screen which could explain the low modulation index.

7.4.4 No Observed Scintillation

For four FRBs within our sample, we observe no spectral scintillation. These are FRBs 20181112A, 20200430A, 20210117A, and 20210407E. As shown in Fig. 7.2, the dynamic spectra of these bursts appear spectrally smooth corresponding to relatively constant ACFs, as shown in Fig. C.6 contained in the Appendix. As a result, each of these FRBs has a low modulation index, with the exception of FRB 20200430A which has a modulation index of $m = 0.45$, presumably caused by the broad spectral structure in its time-integrated spectrum which we do not attribute to scintillation. Moreover, no significant excess was seen in the spectral ACFs of these bursts at lower resolutions. We are therefore confident in the

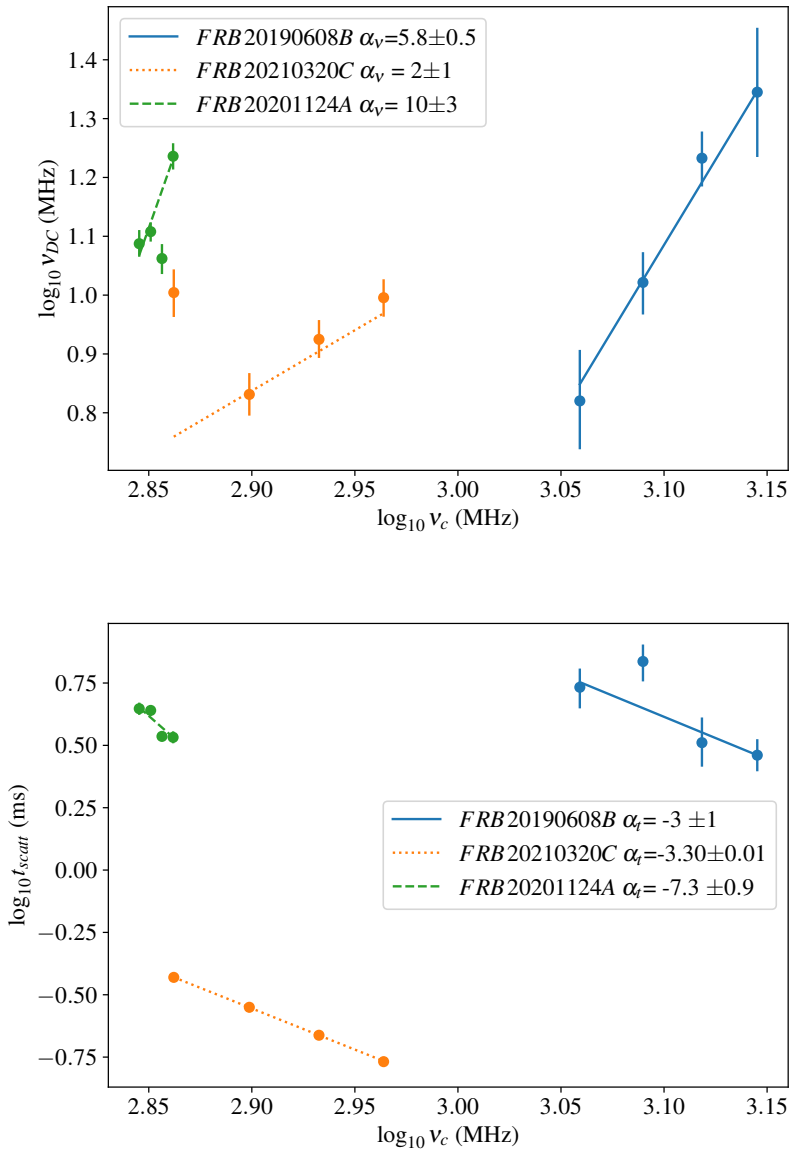

Figure 7.5: Frequency evolution of $\nu_{\rm DC}$ (*top*) and $t_{\rm scatt}$ (*bottom*) modelled from sub-band analysis of each scintillating FRB. The lines show the best-fit power-law models for each case.

absence of spectral scintillation on frequency scales above $\nu_{\rm min}$ for each of these FRBs, as reported in Table C.1.

7.4.5 Anomalous

We characterise two FRBs within our sample as anomalous. These FRBs, 20190102C and 20190711A, show low spectral modulation indices associated with small excesses in their spectral ACFs. In the case of FRB 20190102C the ACF of the whole band shows a broad spectral structure which we do not associate with scintillation, and a sharper ACF peak at low spectral lags (< 5 MHz), as shown in Fig. C.8, which is potentially consistent with scintillation. We fail to find an ACF excess when we decompose the burst into four sub-bands, however, reducing the division to two sub-bands yields a reasonable fit as shown in Fig. C.8. Derived $\nu_{\rm DC}$ values evolve in the expected direction for scintillation, however, given the low number of sub-bands we are unable to estimate the error on the spectral index of $\alpha_\nu = 10$.

In the case of FRB 20190711A the ACF is well fit by the expected lorentzian form of scintillation, as shown in Fig. C.7. Analysis of the sub-bands measures $\alpha_\nu = -10 \pm 5$, contrary to the expectation for scintillation decorrelation bandwidths to increase in size with frequency. We highlight however the low fractional bandwidth (≈ 0.06) over which these data are measured.

Both FRBs show complex pulse profiles, with multiple components. Owing to the computational load associated with multi-component fitting we only model the temporal properties of each of these bursts with two sub-bands. In each case the short timescale structure of each of these bursts could also cause intrinsic spectral structure on the reciprocal scale (Nimmo et al., 2022a). Given the uncertainty associated with their measurements and the low C values, which can indicate the consistency of spectral structures with self-noise, we conclude that there is insufficient evidence to prove scintillation in these cases.

7.5 Discussion

For the cases where we find convincing evidence for scintillation and pulse broadening, i.e. FRBs 20190608B, 20201124A, and 20210320C, the scattering geometry is constrained by the $L_x L_g$ product upper limit. FRBs 20190608B and 20201124A provide particularly tight constraints.

7.5.1 FRB 20190608B

Due to limitations in spectral resolution, the presence of diffractive scintillation was unable to be confirmed in a previous analysis of FRB 20190608B (Day et al., 2020). Without the presence of this scintillation the position of the screen causing temporal scattering in the burst had to be inferred indirectly from estimates of the host galaxy properties (Chittidi et al., 2021) and the properties of the cosmic web along the FRB line of sight (Simha et al., 2020). The joint conclusion of these studies is that the temporal scattering in FRB 20190608B is likely contributed by a region within the host galaxy as there are no cosmic web structures or foreground galaxies intersecting the line of sight sufficiently to explain the large scattering time.

By confirming scintillation and placing an upper limit of $L_x L_g \lesssim 6 \pm 1\,\mathrm{kpc}^2$ our results provide a direct constraint on the scattering geometry. For similar values $L_x \simeq L_g$, the screens must be contained within the host and Milky Way galaxies respectively.

By measuring the angular broadening extent of an FRB using VLBI the effective distance to the relevant scattering screen can be determined (Ocker et al., 2021). This has been done for FRB 20121102 using the European VLBI network (Marcote et al., 2017), the effective distance to its Galactic scattering screen is constrained to be consistent with a peak in differential scattering measure associated with a sharp change in electron density predicted by the NE2001 model Ocker et al. (2021). Fig. 7.6 shows the C_n^2 and differential DM estimated for each of our scintillating FRB lines of sight. Using the peak in C_n^2, corresponding to

a sharp change in differential DM, we estimate $L_g \approx 0.36\,\mathrm{kpc}$, corresponding to $L_x \lesssim 16.7\,\mathrm{kpc}$. This region corresponds to the host galaxy of FRB 20190608B and therefore our direct constraints support the conclusions of Simha et al. (2020); Chittidi et al. (2021). Additionally, by assuming $L_g \approx 0.36\,\mathrm{kpc}$, ν_{DC} and the fully modulate version of Eq. C.30 can be used to constrain the product

$$t_{\mathrm{scatt}}(1+z_d)\frac{D_{ds,x}}{D_{d,x}} \lesssim \frac{\nu_{\mathrm{DC}} D_s}{2\pi\nu^2 L_g} \tag{7.3}$$

where $D_{d,x}$ is the distance to the extragalactic scattering screen at redshift z_d, and $D_{ds,x}$ is the distance between the screen and the host. From this constraint, we place an upper limit on the amount of scattering caused by the IGM. In the case of FRB 20190608B, we find $t_{\mathrm{scatt}}(1+z_d)D_{ds,x}/D_{d,x} \lesssim 1.7\times10^{-7}\,\mathrm{s}$, corresponding to less than $0.43\,\mu\mathrm{s}$ of scattering at 1 GHz (assuming a ν^{-4} scaling), for a screen at redshift $z \approx 0.056$, where $D_{ds,x}/D_{d,s} \approx 1$ and the scattering time associated with a given scattering measure is maximised (Macquart & Koay, 2013).

7.5.2 FRB 20210320C

FRB 20210320C provides perhaps our sample's best example of scattering and scintillation, with the burst morphologies presented in Fig. 7.3 and Fig. 7.4 showing good agreement with the expected shapes and frequency evolutions for diffractive scintillation and pulse broadening. The small amount of observed scattering in this case, however, results in only a loose constraint on the scattering geometry of $L_x L_g \lesssim 550 \pm 30\,\mathrm{kpc}^2$. From Fig. 7.6 the peak in turbulence strength is close to the observer at a distance of 0.18 kpc, which corresponds to $L_x \lesssim 3000\,\mathrm{kpc}$. As such, the scattering cannot be definitively constrained to the host galaxy. We note however, that the observed scattering must still be occurring within the first $\approx 0.3\%$ of the total path length from the host and so cannot be due to some diffuse component of the IGM as its contribution to the scattering would characteristically peak halfway between the source and the observer. For

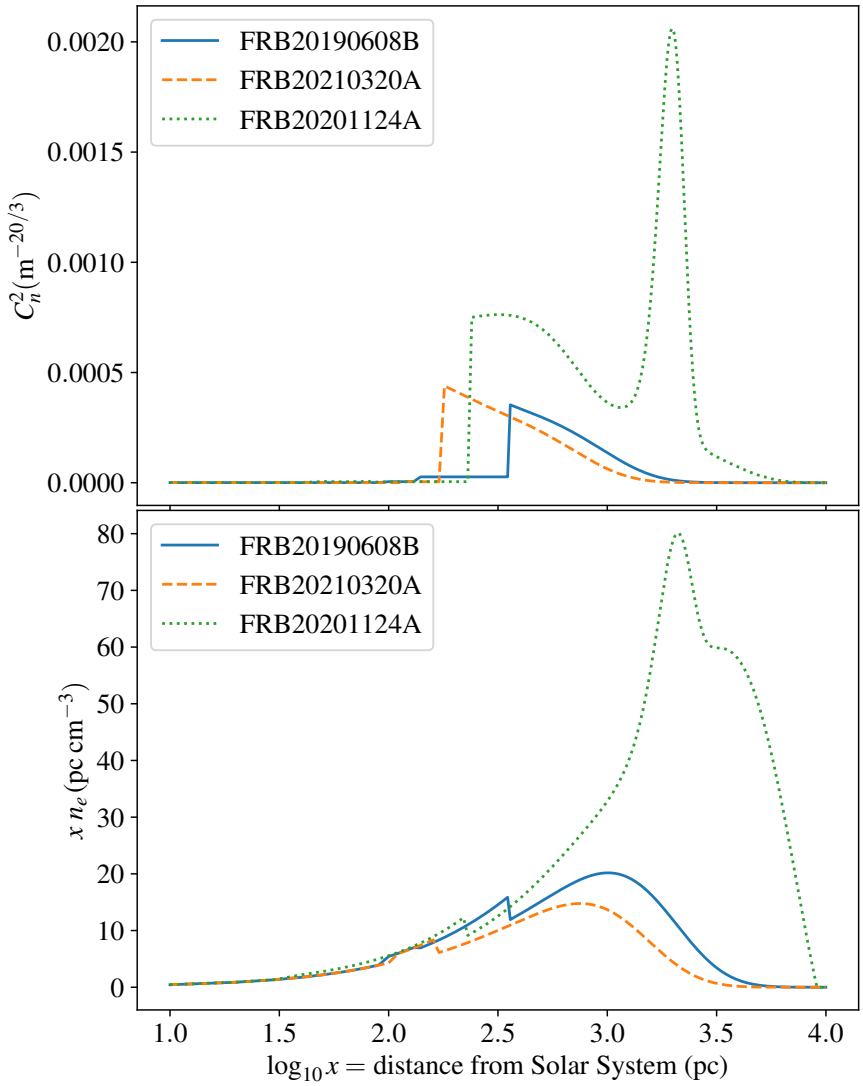

Figure 7.6: *Top*: The expected differential scattering measure contributed by the Milky Way for scintillating FRB lines of sight as calculated from the NE2001 model (Cordes & Lazio, 2003). *Bottom*: For the same lines of sight, the expected contribution to DM as a function of $\log_{10} x$ where x is the distance from the Solar system. For each FRB line of sight the maximum of C_n^2 occurs at 0.36 kpc, 0.18 kpc, and 1.98 kpc respectively, corresponding to sharp changes in DM contribution.

IGM scattering in general, by assuming $L_g \approx 0.18\,\mathrm{kpc}$, we find $t_{\mathrm{scatt}} D_{ds,x}/D_{d,x} \lesssim 1.1 \times 10^{-6}\,\mathrm{s}$, using Eq. 7.3. This corresponds to less than $0.44\,\mu\mathrm{s}$ of scattering at 1 GHz (assuming a ν^{-4} scaling), for a screen at redshift $z \approx 0.126$, where $D_{ds,x}/D_{d,s} \approx 1$.

The host galaxy localisation image of FRB 20210320C, shows a faint object nearby to the line of sight. The redshift of this object has yet to be determined, however, if it lies foreground to the host galaxy at a similar redshift it may be the source of the observed scatter broadening.

7.5.3 FRB 20201124A

Conversely to the other scintillating FRBs in our sample, FRB 20201124A is a closely studied repeating FRB with existing measurements for its scattering time and decorrelation bandwidth. Analysis by Main et al. (2021) measured $\nu_{\mathrm{DC}} \approx 0.1\,\mathrm{MHz}$ and $t_{\mathrm{scatt}} \approx 11\,\mathrm{ms}$ at a central frequency of 575 MHz. Substituting these values into Eq. 7.2 yields $L_x L_g \lesssim 0.6\,\mathrm{kpc}^2$, which is tighter than the limit we derive, $L_x L_g \lesssim 1.43 \pm 0.08\,\mathrm{kpc}^2$, consistent with the expected steep frequency dependence of the constraints (Main et al., 2021).

Despite the evidence for scintillation, the observed modulation index of FRB 20201124A remains too low to be consistent with the full modulation expected for diffractive scintillation of a point-like source. In this context, a source will be considered point-like if it satisfies Eq. C.33. If the equation is violated, we enter the regime of diffractive scintillation of an extended source. Here, the modulation index of the spectral scintillation will begin to decrease as the angular extent of the scattering disk of the first screen increases (Narayan, 1992). Within the temporal profile of scattered bursts, later times are associated with larger angular extents in the scattering disk. Similarly to the analysis of Masui et al. (2015), we can analyse the modulation index of the burst as a function of time to identify whether the entire angular extent of the scattered image undergoes the same scintillation. If the scattered image associated with the observed temporal broadening is respon-

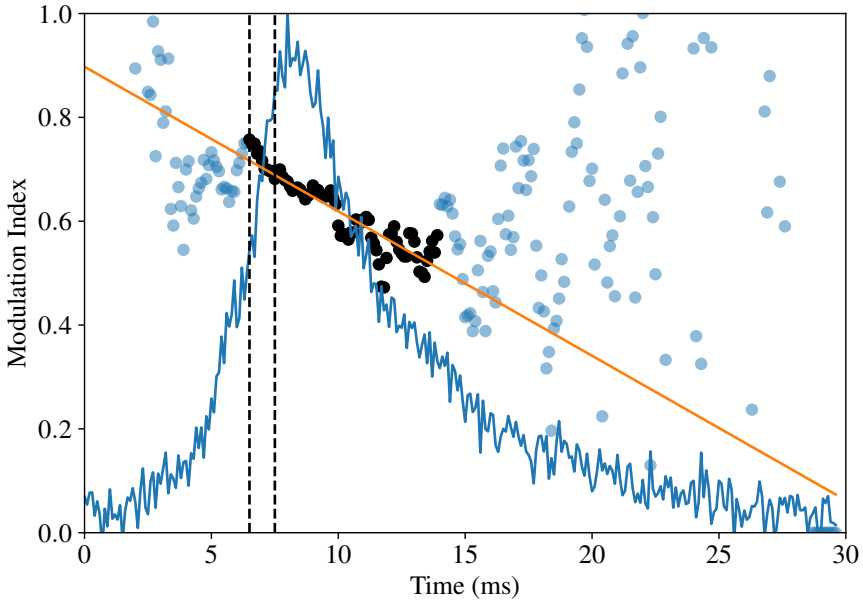

Figure 7.7: Modulation index of FRB 20201124A as a function of time. Scatter points show the modulation index calculated for the burst spectrum at a resolution of 0.01 MHz integrated over 1 ms of the bursts time profile (shown by the blue line) beginning at the time marked by the point. The dotted black lines depict the area of integration in time. The linear model of modulation index decay is shown by the orange line. The points used in the fit are shown in black.

sible for the suppression of Galactic scintillation, we expect that the later parts of the burst, with larger angular extents, will show lower modulation indices. Fig. 7.7 shows the evolution of the modulation index over the duration of the burst in increments of 0.1 ms. At each increment a 1 ms wide boxcar of the burst's dynamic spectrum is used to calculate the modulation index, effectively smoothing the result to boost S/N. As seen in Fig. 7.7 the modulation index shows a small decrease of ~ 0.2 over the main component of the burst profile with a large variance in m_g displayed on either side of the burst as S/N decreases. A linear model shows reasonable agreement with the data, as would be expected for a circularly symmetric scattered image, where separation in time is linearly proportional to angular offset. The low modulation index of spectral scintillation in FRB 20201124A may, therefore, indicate that the scattering screen at the host is partially resolved by the Milky Way scattering screen.

For the fully modulated case, the coherence length of a wave incident on the second screen can only be constrained to be larger than the projected scattering angle length. In the partially resolved case, however, it can be solved for exactly using the modulation index. This, in turn, allows the two-screen distance product to be specified exactly, as, (see C.5 for derivation)

$$L_x L_g \approx \frac{D_s^2}{2\pi\nu^2(1+z)\,m^2}\frac{\nu_{DC}}{t_{\rm scatt}}, \tag{7.4}$$

where m is the modulation index. Solving this for the case of FRB 20201124A indicates that the two-screen distance product should be equal to $L_x L_g \approx 4\,\mathrm{kpc}^2$.

A recent study of the annual variation of scintillation in FRB 20201124A has revealed that the scattering screen contributing the observed Galactic scintillation is much closer than the peak in C_n^2 at $\sim 2\,\mathrm{kpc}$ suggests, located at around $L_g = 0.40 - 0.46\,\mathrm{kpc}$, depending on the isotropy of the screen (Main et al., 2022). We discuss the potential impact of screen anisotropy in appendix C.6. Taking the case of the uniform two-dimensional screen, $L_g = 0.46\,\mathrm{kpc}$, we can approximate the distance between the source and host screen to be $L_x \approx 9\,\mathrm{kpc}$, which is greater than the optical extent of the host galaxy (Xu et al., 2022). This indicates that, if the angular broadening associated with the measured scattering tail is suppressing the observed Galactic scintillation, that scattering is likely occurring in the halo of the galaxy, rather than in the circum-burst environment or the host ISM.

The low modulation index of the burst could also be caused by angular broadening from a third screen along the line of sight which contributes negligibly to the observed scattering and scintillation of the burst. This is precisely the inverse of the case discussed in §7.5.1 regarding limits on IGM scattering. The two possible locations for this potential third screen are within the Milky Way or the IGM. The case where the third screen is also within the host galaxy is captured implicitly by the above discussion. Already, some motivation for a third screen within the Milky Way exists, in the form of the peak in C_n^2 at $\approx 2\,\mathrm{kpc}$ shown in Fig. 7.6, which we know is not associated with the observed scintillation. The

scattering time required from the third screen to reduce the modulation index of the Galactic scintillation is given by

$$t_{\rm scatt} \approx \frac{\nu_{\rm DC} D_{d,x}}{2\pi\nu^2 m_g^2 L_g}, \tag{7.5}$$

adapted from Eq. 7.3. Solving for $m_g = 0.59$ yields $t_{\rm scatt} \approx 1.3 \times 10^{-7}\,\mu$s at 1 GHz (assuming a ν^{-4} scaling), showing that the foreground Galactic scintillation can be suppressed with very little additional scattering from a third screen in the Milky Way. From this result, we conclude that while it is possible for such a scenario to be true, it is more likely that any third screen in the Milky Way would completely suppress the scintillation from the foreground screen at 0.46 kpc and is therefore inconsistent with our observations.

If the third screen is instead placed within the IGM, we can use the inverse of Eq. 7.3, dividing the right-hand side by m_g^2 to take the partial modulation into account. This yields $t_{\rm scatt}(1+z_d)D_{ds,x}/D_{d,x} \approx 0.027\,\mu$s at 1 GHz (assuming a ν^{-4} scaling). We plot this result as a function of $D_{d,x}$ in Fig. C.9. The scattering times required to cause $m_g = 0.59$ are reasonable expectations for scattering from the IGM (Macquart & Koay, 2013) and would be invisible in the temporal profile of the burst. The range of decorrelation bandwidths corresponding to the spectral scintillation also imposed by an IGM screen, however, falls mostly within our detectable range and therefore should appear in our observations. As a result we find it unlikely that angular broadening from a third screen in the IGM can adequately explain the observed scintillation modulation. We note however that for IGM screens closer than 50 Mpc the decorrelation bandwidth would be greater than our observed bandwidth, and therefore undetectable.

Given the issues outlined above with a third screen interpretation, coupled with the observed evolution of the modulation index over the burst, we tentatively conclude that the most likely scenario is that the Galactic scintillation observed in the burst is suppressed by the angular broadening corresponding to the observed temporal broadening. As such FRB 20201124A is a potential candidate of interest

for probing the CGM, and we recommend its modulation index and scattering times be studied in detail in future statistical studies of its repeating bursts.

7.5.4 Circum-burst Scattering

Given the localisation of the scattering to within 0.4 AU of the source for FRB 20190520B (Ocker et al., 2022b), it is prudent to consider the ramifications if this were typical for all FRBs. The extremely low value of L_x in each case would leave $L_g \lesssim D_s$, and hence the position of the screen responsible for the spectral scintillation would be unbounded. While the diffuse IGM is not expected to cause sufficient scattering to account for FRB temporal broadening, it is expected to be able to cause the microsecond level scattering required to see scintillation on megahertz scales (Macquart & Koay, 2013). It is, therefore, possible, if the screen causing the observed temporal broadening of FRBs is associated with the circum-burst environment, that the observed spectral scintillation could come from the IGM, invalidating the previous IGM scattering constraints in §7.5.1 and 7.5.2. However, in order for no additional scintillation from the Milky Way to be observed, consistent with our observations, which show only one scale of frequency modulation, the angular broadening from the IGM must be such that any subsequent Milky Way scintillation is suppressed.

The two-screen interaction between the IGM and the Milky Way, can be considered using Eq. 7.3 where $t_{\rm scatt} = 1/2\pi\nu_{\rm DC}$ and $D_{ds,x} = D_{d,x}$, and assuming that the Milky Way scintillates as expected by NE2001, Galactic scintillation will be suppressed for all

$$L_g \gtrsim \frac{D_s}{\nu^2(1+z_d)}\nu_{\rm DC}\nu_{\rm NE2001}, \tag{7.6}$$

where z_d is the redshift of the IGM screen. For FRBs 20190608B and 20210320C, Eq. 7.6 yields $L_g \gtrsim 1\,$kpc. Fig. 7.6 shows that for both FRBs, the Galactic scattering screens are expected to be closer than 1 kpc, and therefore would still cause visible scintillation in each, in addition to the IGM scintillation. This is inconsistent with our observations, and therefore we find it unlikely that the ob-

served scintillation comes from the IGM. This agrees with the observed correlation between FRB scintillation and expectations from Galactic electron distribution models (Schoen et al., 2021). We highlight, however, that scintillation from the IGM is a reasonable possibility for FRBs that appear sufficiently point-like. To investigate this possibility further we recommend a statistical study that measures the correlation between FRB redshift and $\nu_{\rm DC}$. The use of redshift is preferable to dispersion measure as the host contribution to dispersion is difficult to separate from the IGM contribution. If a significant fraction of FRBs contain scintillation from the IGM, we expect that an anti-correlation between redshift and $\nu_{\rm DC}$ will be present.

7.5.5 Galactic Scintillation

Galactic electron distribution models such as NE2001 and YMW16 are widely used to determine the expected Galactic scintillation along a given line of sight. While a correlation between observed scintillation and model expectations has been established (Schoen et al., 2021), it has also been shown that Galactic scintillation can be dominated by extremely small scale features (Stinebring, 2006; Trang & Rickett, 2007; Brisken et al., 2010). Existing models are therefore not expected to satisfactorily map the distribution of Galactic scintillation, due to their limited number of components (Yang & Zhang, 2017). FRB 20201124A is a prime example of this, demonstrating significantly less scattering than expected for its line of sight (Main et al., 2022, 2021). Motivated by this we compare our measured Galactic scintillation to expectations.

We plot the scintillation measured for FRBs in our sample against the expected Galactic scattering from these models in Fig. 7.8, scaling all measures to 1 GHz using a ν^4 scaling relation. While our observations of FRB 20201124A also show anomalously low scattering ($\sim 1/20$ NE2001 and $\sim 1/1000$ YMW16), consistent with previous observations (Main et al., 2021), scintillation in FRBs 20190608B and 20210320C agrees with estimates from both YMW16 and NE2001

FRB Positions on NE2001

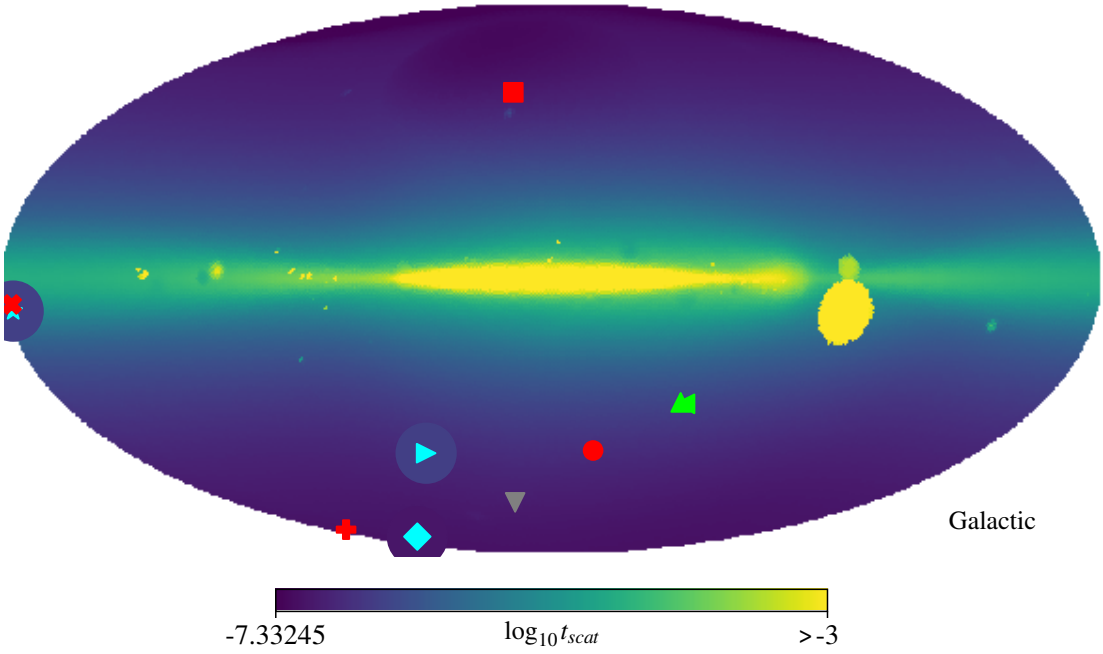

FRB Positions on YMW16

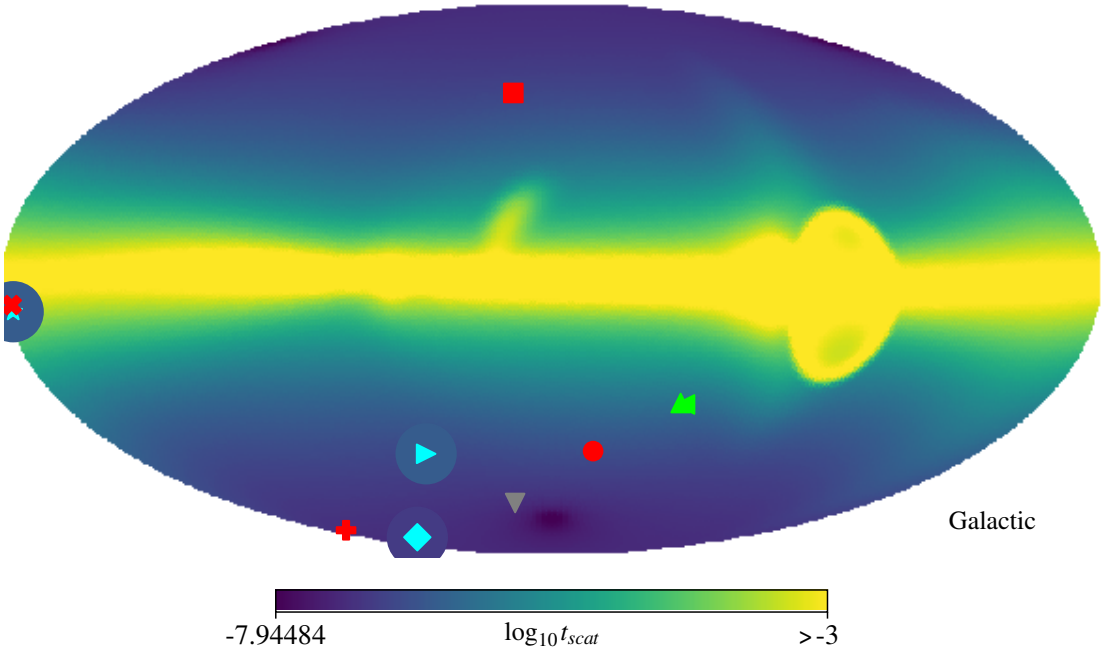

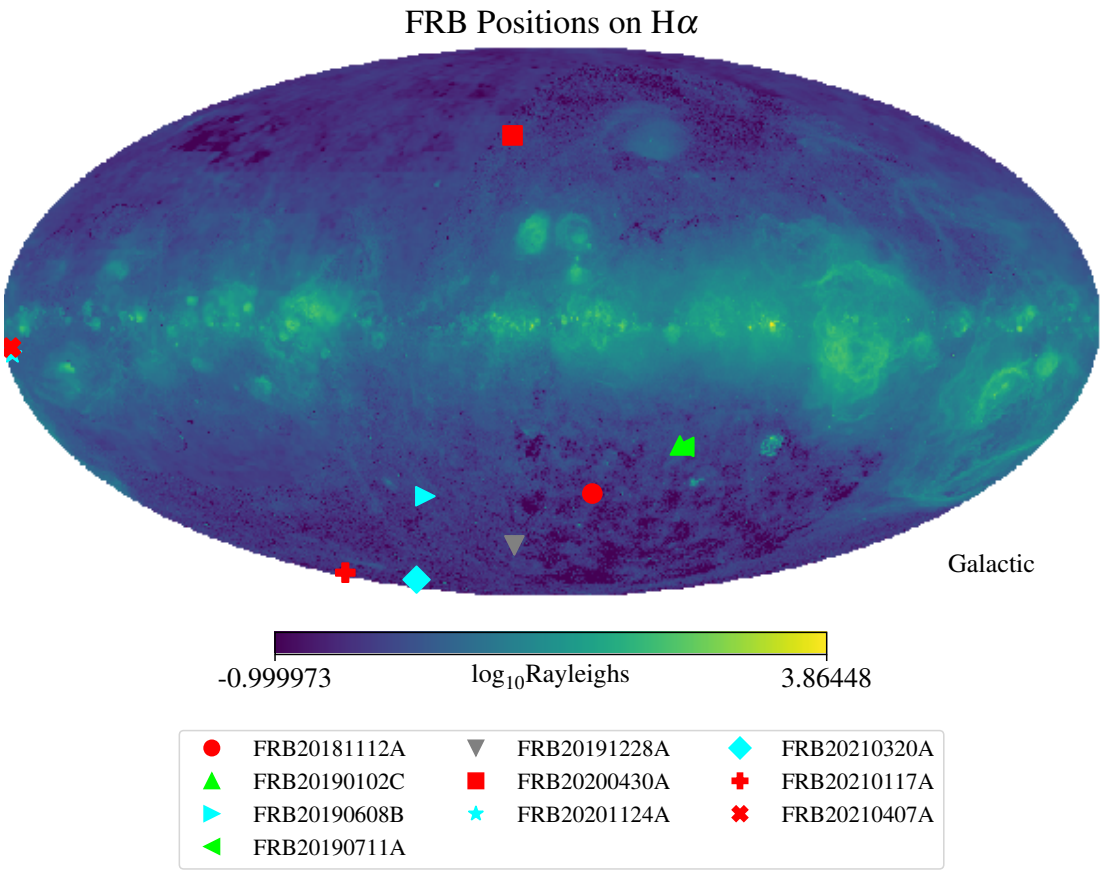

Figure 7.8: FRB localisations superimposed on Galactic electron distribution models and measured Hα intensities. Cyan points represent FRBs confirmed to scintillate. Red points represent FRBs confirmed to not scintillate. Green points represent FRBs where evidence of scintillation was inconclusive. The grey point represents FRB 20191228A, where data was corrupted. Around each cyan point on the Galactic electron density maps (*top* and *middle*) we change the region colour to represent the FRBs measured Galactic scintillation time for comparison with the model estimates. To aid visual distinction scattering times greater than or equal to 10^{-3} s are shown as the same colour. *Top*: Ne2001 model (Cordes & Lazio, 2003). *Middle*: YMW16 model, which uses DM and the Bhat relationship to predict scattering (Bhat et al., 2004; Yang & Zhang, 2017). *Bottom*: The Finkbeiner (2003) Hα all-sky intensity map.

to within a factor of ≈ 2. FRBs 20190608B and 20201124A show very similar levels, however, FRB 20210320C has a much lower Galactic scattering time as expected for higher Galactic latitudes.

The four non-scintillating FRBs within our sample are distributed over a range of Galactic latitudes where we have observed FRB scintillation, as shown in Fig. 7.8. Given the smoothness of the expected Galactic electron distributions, we expect to observe similar Galactic scintillation in each of these cases. The lack of apparent scintillation could suggest that either the Galactic electron distribution models fail to capture coarse variations in the expected scattering or that angular broadening from another screen is suppressing Galactic scintillation. For the three non-scintillating FRBs with confirmed redshifts, we can use Eq. 7.2 to calculate the distance an extragalactic scattering screen would need to be from the host, in order to suppress the expected Galactic scintillation. Using NE2001 we find that, in each case, the screen causing the temporal broadening of these FRBs would need to be greater than ~ 10 kpc away from the source (in some cases several Mpc further) in order to suppress the expected Galactic scintillation.

Scintillation could also be suppressed by a third scattering screen contained within the IGM. In this case Eq. 7.3 can be inverted to determine the minimum value of $t_{\rm scatt}(1+z_d)D_{ds,x}/D_{d,x}$ for an IGM screen to begin suppressing the expected Galactic scintillation. For FRBs 20181112A, 20200430A and 20210117A, respectively, we find that the IGM would need to cause scattering well in excess[3] of 3.3 μs, 0.11 μs and 5.0 μs at 1 GHz (assuming a ν^{-4} scaling) for screens at redshifts 0.198, 0.076 and 0.099 (where $D_{ds,x}/D_{d,x} \approx 1$, resulting in the maximum scattering time for a given scattering measure).

From Macquart & Koay (2013), observed scattering times are related to the effective scattering measure ($\rm SM_{eff}$) via

$$t_{\rm scatt}(1+z_d) \propto \nu^{-4} \left(\frac{D_{d,x}D_{ds,x}}{D_s}\right) \rm SM_{eff}, \tag{7.7}$$

[3]For scattering times, exactly equal to the limit the modulation index will be one, and will decrease as $\sqrt{t_{\rm scatt}/t_{\rm limit}}$.

for scattering dominated by diffractive scales below a constant inner turbulence scale. Using the redshifts associated with each source and midpoint, the limits on the IGM scattering times derived for both scintillating and non-scintillating FRBs can then be converted to limits proportional to SM_{eff}. For the case of a diffuse IGM, Macquart & Koay (2013) show that SM_{eff} should be a monotonically increasing function of redshift, which is inconsistent with the limits we derive, as shown in Fig. C.10. As a result, a diffuse IGM component cannot be responsible for suppressing Galactic scintillation expected from NE2001 in our non-scintillating bursts given our observations of scintillation in others. We, therefore, suggest that it is unlikely that angular broadening associated with scattering from the diffuse IGM, or regions within the host galaxy of each burst is suppressing the Galactic scintillation of the non-scintillating FRBs in our sample. Rather, it is more likely that either 1) the true scintillation bandwidths are different from that predicted under the NE2001 and YMW16 models, similar to the case of FRB 20201124A, or 2) significant structures in the IGM, such as a galaxy halo, are intervening between the source and the observer, resulting in significant angular broadening. In the case of FRB 20181112A such a structure exists in the form of a foreground galaxy intervening at $z = 0.36738$ (Prochaska et al., 2019a). However, at this redshift a screen contributing the maximum amount of scattering allowed for this burst (0.0278 ,ms, as per Table C.1) results in a modulation index of $m_g = 0.46$ and should be visible in its ACF (see Fig. C.6).

As demonstrated in Morgan et al. (2022), there exists a strong correlation between the angular broadening of extragalactic point sources and the intensity of Galactic Hα emissions. Angular broadening of extragalactic sources is weighted approximately uniformly with distance for Galactic scattering screens (Cordes & Lazio, 2003), and therefore, ionised regions, shown by Galactic Hα observations, are expected to contribute significantly to angular broadening by the ISM. Conversely, the scintillation bandwidths and scattering times associated with the ISM are weighted more heavily towards the middle of the path length (Cordes &

Lazio, 2003), allowing background regions of lower Hα intensity to cause greater scattering times than more intense foreground regions, confusing any correlation. Moreover, close to the Galactic plane the ionised region responsible for the observed scattering may not be visible in Hα, due to extinction (Finkbeiner, 2003). As such, we do not necessarily expect to observe a strong correlation between FRB $\nu_{\rm DC}$ and Hα. The association of scintillation in FRB 20201124A to a more local screen, however, does provide some motivation to search for scintillation screens locally, where extinction should be relatively low. Thus, we also compare scintillation in our sample to a Galactic map of Hα intensity (Finkbeiner, 2003) as shown in Fig. 7.8. We find no obvious relation between scintillating and non-scintillating FRBs and Hα intensity or variance in $2.5^\circ \times 2.5^\circ$ area surrounding each FRB line of sight. We note, however, that the size of a reasonable scattering disk lies well below the resolution of data used to compose this map and therefore may show correlation with smaller scale Hα structures.

7.6 Conclusion

The location of the dominant scattering screens contributing to the temporal broadening and spectral scintillation of FRBs has important ramifications for many areas of astrophysics. Scattering near the host galaxy or circum-burst environments, such as FRB 20190520B affects our understanding of progenitor evolution; scattering in intervening galaxies could constrain the presence of cold cloudlets in the CGM; finally, scattering in our own Galaxy could inform models of the Galactic electron distribution. For apparently non-repeating FRBs scattering can be difficult to localise, but if bursts are observed to scatter and scintillate independently then a two-screen model can be used to make direct constraints.

In this work, we have measured the level of scattering and scintillation in 10 CRAFT FRBs with high spectro-temporal resolution and applied the two-screen model developed by Masui et al. (2015) and Ocker et al. (2022c) to place constraints on the distances to their respective scattering screens. We find strong

evidence for scattering and scintillation in three FRBs, and strong evidence for no spectral modulation in four FRBs. The remaining are indeterminate. Of the scintillating FRBs the scattering in FRB 20190608B is robustly associated with the host galaxy in agreement with previous estimates; the scattering in FRB 20210320C must occur within 3 Mpc of the host; finally, we find that the scattering in FRB 20201124A is likely associated with its host galaxy environment, however, the low modulation index of its Galactic scintillation suggests the dominant scattering region may be in the halo rather than the host ISM. The Galactic scintillation of FRBs 20190608B and 20210320C are in general agreement with the scintillation expected from Galactic models YMW16 (Yang & Zhang, 2017) and NE2001 (Cordes & Lazio, 2003). However, the anomalously low scattering of FRB 20201124A and the definitive lack of scintillation in four FRBs indicates that, if the observed pulse broadening is contributed by host galaxy ISMs or circum-burst environments, existing models may be poor estimators of the scattering times associated with the Milky Way's ISM, as has been noted already by Ocker et al. (2021) in the case of YMW16. Additionally, we find no obvious relationship with the large-scale mean and variance of surrounding Galactic Hα emission. We leave a statistical comparison of scintillation quantities with other burst and host galaxy properties to a future study, once the sample of high-resolution bursts has been expanded.

With the automated CELEBI post-processing pipeline now operational and the CRAFT Coherent upgrade expected soon we expect that the number of observed scintillating FRBs will grow, allowing for a statistical study of their Galactic and extragalactic screen properties. Furthermore, we highlight that targeting low Galactic latitudes for FRB searches may further increase the number of observed, strongly scintillating FRBs, allowing for the stronger constraint of their extragalactic counterparts and Galactic electron distribution models.

Acknowledgements

We would like to acknowledge A/Prof. Kiyoshi Masui for refereeing this manuscript and providing helpful insights related to the evolution of spectral modulation indices in bursts undergoing multi-path scattering. CMT is supported by an Australian Research Council Future Fellowship under project grant FT180100321. ATD acknowledges support from the Australian Government through the Australian Research Council's Discovery Projects funding scheme (project ID DP220102305). KG acknowledges support through Australian Research Council Discovery Project DP200102243. CWJ and MG acknowledge support by the Australian Government through the Australian Research Council's Discovery Projects funding scheme (DP210102103). RMS acknowledges support through Australian Research Council Future Fellowship FT190100155 and Discovery Project DP220102305.

Data Availability

The data underlying this article are available in the article and in its online supplementary material.

Chapter 8

Summary and Conclusion

The study of cosmological transients lies at the frontier of modern astrophysics. In particular, the burgeoning field of FRB research has already contributed to long-standing issues, such as the missing baryon problem, and may hold the key to unravelling other cosmological mysteries such as the H_0 tension. The methods in each of these cases rely upon understanding the phenomena which affect FRB propagation, e.g. dispersion, which can be measured to quantify the baryonic content of the IGM. By understanding how FRBs propagate through various distributions of matter we can infer properties about those distributions. Furthermore, because FRBs are the most angularly compact sources known, we can infer properties on scales that are inaccessible via other methods. Over the cosmological scales FRBs propagate, there are many media of interest, however, in this thesis, I have primarily investigated how gravitational lensing can allow FRBs to constrain the fraction of dark matter in compact objects. Secondarily, I have investigated how to constrain the position of turbulent plasmas along an FRBs path, by measuring the scattering and scintillation which result from their intervention.

8.1 First Constraints on Compact Dark Matter From Fast Radio Burst Microstructure

In §5 I investigated how FRBs observed by CRAFT could be used to inform forecasts of FRB constraints on compact dark matter. The identity of dark matter is one of the biggest unsolved problems in modern cosmology, with many forms proposed, from beyond-the-standard-model particles such as axions, to PBHs formed in the early Universe. PBHs are a candidate of particular interest as a population of black holes in the poorly constrained stellar mass ($10-100\,M_{\odot}$) region could also explain the merger event rates inferred from gravitational waves observed by LIGO.

Strong gravitational lensing results in multiple images in the spatial domain, corresponding to multiple temporal echoes in the time domain. By searching for echoes of transient signals, the population of gravitational lenses between the observer and the transient source can be constrained. As FRBs have extremely short durations they make ideal probes of the stellar mass range of interest. Previous treatments assumed minimum temporal separations of 0.1 ms and magnification ratios $\lesssim 5$. More recent observations of FRBs at high time resolution, however, have shown FRB temporal structures on the scale of tens of microseconds, at much higher S/N ratios than previously achieved. This allows for the consideration of temporal separations an order of magnitude lower, and magnification ratios an order of magnitude higher than in previous cases. Using the previously established formalism, I modelled the optical depth to strong lensing probed by two high-time resolution FRBs and found that ~ 130 FRBs would be required to improve upon current constraints if lenses were distributed homogeneously throughout the cosmic web. Furthermore, FRB 20181112A had been observed to pass within 20 kpc of a foreground galaxy, allowing it to directly probe the dense dark matter halo surrounding that galaxy. Motivated by this I derived similar constraints for the more physically accurate case where dark matter is concen-

trated within galaxy halos. I predicted that ~ 170 FRBs, that similarly probe foreground halos, could improve upon existing limits that assume dark matter to be homogeneous throughout the Universe. Finally, I derive limits that could be placed on non-compact dark matter following a power-law distribution. By measuring the size of the gravitational scattering tail that would result from propagating through such a distribution, FRBs provide a way to potentially constrain the mass of exotic dark matter particles as well as the compact PBHs.

8.2 Effect of Gravitational Lensing on Fast Transient Event Rates

The constraints formed in §5 require the temporal echoes associated with each gravitationally lensed image to be distinguishable within an observation. Naturally, this places a lower limit on the time delays that can be observed, corresponding to a lower limit on the lens masses that FRBs can probe. In §5 the minimum temporal delays were given by the smallest temporal substructures that could be resolved within a burst's profile, $\approx 10\,\mu$s. This corresponds to a minimum detectable lens mass of $0.1\,M_\odot$. In more recent works (Kader et al., 2022; Leung et al., 2022), that search the electric field data for coherent gravitational lensing, the minimum time delay is much smaller at 1.25 ns, allowing strong lensing from lens masses $\gtrsim 10^{-4}\,M_\odot$ to be detected in FRB temporal profiles. Below these scales, the temporal echoes from the lensing will not be distinguishable and therefore lensing will not be detectable. However, gravitational lensing can still occur below these detection thresholds, potentially affecting our inferences of intrinsic FRB properties. In §6 I derived the minimum lens masses which could cause a significant magnification of FRBs using a wave optics treatment. Furthermore, I derived the effect that lenses above this mass would have the observed differential event rate of FRBs over all fluences. By considering the cumulative effects of lensing on the observed population of FRBs, I demonstrated how the en-

tire population of compact objects capable of lensing FRBs could be constrained, regardless of whether lensing can be detected in individual FRBs using the aforementioned methods. I find that 8000 unlocalised, high fluence FRBs at 1.4 GHz would be required to rule out a Universe comprised entirely of FRB lenses, with 3.5×10^5 required to exclude more than 6% of dark matter being comprised of PBHs $\gtrsim 10^{-5}\,M_\odot$. Additionally, I also rule out the prospect of all FRBs being highly magnified, intrinsically low-energy phenomena for static lensing geometries, which had been a scenario of interest within the FRB community.

8.3 Two-Screen Scattering in CRAFT FRBs

Where gravitational lensing can be used to investigate the properties of dark matter along the line of sight, plasma propagation effects such as scattering and scintillation can be used to constrain the density and turbulence of baryonic matter. Of particular interest are the circum-galactic and circum-burst regions, as little is known about these media and their properties have important implications for the evolution of galaxies and FRB sources respectively. In general, the position of the baryonic media responsible for such multi-path propagation effects is difficult to ascertain. However, in cases where both Galactic and extragalactic scattering are observed, previous works have shown that the positions of the relevant scattering screens can be constrained. In §7 I applied these methods to a greatly expanded sample of high-resolution FRB dynamic spectra rendered by the CRAFT's CELEBI pipeline, and found three FRBs where such limits can be placed. For FRBs 20190608B and 20210320C I found that the extragalactic scattering media are likely within 16.7 kpc and 3000 kpc of their sources, respectively. In the case of FRB 20201124A I derived a new method and used the scintillation's low modulation index to infer an exact extragalactic scattering media position of ≈ 9 kpc. Each of these results are consistent with scattering occurring within the FRB's host galaxy ISM or CGM. If this holds true for all FRBs then the definitive lack of Milky Way scintillation for four other FRBs in my sample suggests

that models of the Galactic electron distribution may be poor estimators of the scattering times associated with the Milky Way's ISM, similar to the well-known case of FRB 20201124A, which I also confirm here. Such discrepancies could have important implications for many fields of FRB and pulsar research which regularly make use of these models. Furthermore, I found no correlation between the measured Galactic scintillation decorrelation bandwidths and the mean or variance of large-scale $H\alpha$ intensities surrounding each burst line of sight, which have been shown to be correlated with Galactic angular broadening.

8.4 Conclusion and Outlook

The gravitational and plasma lensing of FRBs provides a way to constrain both the baryonic and non-baryonic matter distributions in our Universe over cosmological scales. By constraining these distributions we gain insight not only into the long-standing question of the nature of dark matter, but also into the nature of FRB progenitors, by constraining the properties of the media in which they are embedded.

The methods demonstrated within this thesis allow for these constraints to be formed, provided that a statistical sample of FRBs can be observed. Specifically, I have shown that FRBs can probe a wider range of the PBH parameter space than any previously established limit and that the presence of turbulent, ionic media along the line of sight to an FRB source may be localised precisely with respect to the total length of its propagation path.

A caveat common to all the methods derived in this thesis is that currently, the samples of localised and unlocalised FRBs are not large enough to support a meaningful improvement upon existing limits. In the coming years, the number of localised and unlocalised FRBs is expected to increase drastically with the advent of new instruments such as BURSTT (Lin et al., 2022) and DSA-2000 (Hallinan et al., 2021), and upcoming upgrades to existing FRB detectors, such as CHIME's outriggers (Sanghavi et al., 2023) or the coherent upgrade to CRAFT.

As the number of localised FRBs grows, so will the number that are confirmed to intersect foreground halos, allowing the current constraints on compact dark matter to be improved and potentially non-compact dark matter distributions to be constrained. As the total number of observed FRBs grows, the fraction of observed FRBs with measured host galaxy redshifts may actually decline, owing to the resource-intensive nature of spectroscopic follow-up observations. Through measurements of the differential event rates of FRBs, the remaining sample of unlocalised FRBs can also be used to form constraints on the population of PBHs, allowing for an additional consistency check on the limits derived from the localised bursts.

As CRAFT and other surveys continue to render more high-resolution dynamic spectra from captured voltage data, scattering and scintillation analysis similar to that outlined in this thesis will be possible on a statistical scale. This will allow stronger constraints on the IGM and host galaxy ISMs and CGMs to be formed. In turn, this may potentially allow for better estimates of host DM contributions, which currently inhibit FRB constraints on other cosmological parameters such as H_0 (James et al., 2022). Comparing scattering properties between repeating and apparently non-repeating bursts may also provide evidence for or against a single population of bursts.

The treatments contained within this thesis could be improved by expanding the complexity of some models to capture more realistic propagation behaviours. In estimating the optical depth of high magnification transients a wave optics treatment could be deployed to better estimate the cross sections involved. When determining the effect of lensing on the observed differential event rate of FRBs, the magnification probability distribution for lensing in dynamic geometries could be considered. In considering the interference between separate FRB images in a wave optics treatment I make no attempt to include boundary wave diffraction effects that emerge when the time delay between signals is comparable to the signal length. Such a description would provide a more complete wave optics

treatment. Finally, throughout this thesis, I have neglected the effect of lensing (gravitational or plasma) on the observed polarisation properties of a burst, which provides an additional dimension of information that should be considered in the future. These additional complexities provide a way forward to improving existing models of FRB propagation. At present however, the methods to place sweeping constraints on the baryonic and non-baryonic matter distributions in our Universe have been established, what remains is to simply measure more bursts.

8.5 Closing Remarks

FRBs have demonstrated that they are extremely powerful probes of our Universe, and 16 years after their discovery, there remains no shortage of compelling new applications propounded for them. With the flood of proposed FRB detectors promising a drastic increase in the sample size, it is doubtless that there are exciting discoveries in the future of transient science and cosmology. It is my hope that fuelled by these future detections, the works contained within this thesis will provide a strong foundation upon which future constraints on dark matter and FRB progenitors can be made.

Appendices

Appendix A

Cosmological Populations

A.1 Derivations

A.1.1 Bolometric General Luminosity-Function Source Counts for Constant Flux Sources in a Flat Universe

The luminosity function yields a number density per unit luminosity. A small number of sources dN can be expressed as (Carroll et al., 1992):

$$dN = \phi(L, z) dL \; dV \tag{A.1}$$

The volume associated with the density from the luminosity function is the co-moving volume, expressed generally as

$$dV_c = R_0^3 \frac{r^2}{(1 - kr^2)^{1/2}} dr d\Omega \tag{A.2}$$

$$= \frac{d_M^2}{(1 + \Omega_K H_0^2 d_M^2)^{1/2}} d(d_M) d\Omega \tag{A.3}$$

These forms are analytically integrable, giving (Hogg, 2000)

$$V_c = \begin{cases} \left(\frac{4\pi D_H^3}{2\Omega_k}\right)\left[\frac{D_M}{D_H}\sqrt{1+\Omega_k\frac{D_M^2}{D_H^2}} - \frac{1}{\sqrt{|\Omega_k|}}\text{arcsinh}\left(\sqrt{|\Omega_k|}\frac{D_M}{D_H}\right)\right] & \Omega_k > 0 \\ \frac{4\pi}{3}D_M^3 & \Omega_k = 0 \\ \left(\frac{4\pi D_H^3}{2\Omega_k}\right)\left[\frac{D_M}{D_H}\sqrt{1+\Omega_k\frac{D_M^2}{D_H^2}} - \frac{1}{\sqrt{|\Omega_k|}}\text{arcsin}\left(\sqrt{|\Omega_k|}\frac{D_M}{D_H}\right)\right] & \Omega_k < 0 \end{cases} \quad \text{(A.4)}$$

where D_M is the transverse comoving distance, given by (Hogg, 2000):

$$D_M = \begin{cases} D_H\frac{1}{\sqrt{|\Omega_k|}}\sinh\left[\sqrt{\Omega_k}\frac{D_c}{D_H}\right] & \Omega_k > 0 \\ D_c & \Omega_k = 0 \\ D_H\frac{1}{\sqrt{|\Omega_k|}}\sin\left[\sqrt{\Omega_k}\frac{D_c}{D_H}\right] & \Omega_k < 0 \end{cases} \quad \text{(A.5)}$$

For the case of $\Omega_k = 0$

A.1.1.1 Replacing dV with dz and dL with dS

$$V_c = \frac{4}{3}\pi D_c^3 \quad \text{(A.6)}$$

differentiating with respect to redshift

$$\frac{dV_c}{dz} = 4\pi D_c(z)^2\frac{dD_c(z)}{dz} \quad \text{(A.7)}$$

$$dV_c = 4\pi D_c(z)^2\frac{dD_c(z)}{dz}dz \quad \text{(A.8)}$$

Considering the bolometric relation between flux and luminosity

$$L = 4\pi D_L^2 S \quad \text{(A.9)}$$

$$dL = 4\pi D_L^2 dS \quad \text{(A.10)}$$

where D_L is the luminosity distance and is given by: (D_A *is the angular diameter distance*)

$$D_L = (1+z)D_M \tag{A.11}$$

Therefore, in our case of $\Omega_k = 0$

$$dL = 4\pi D_M^2 (1+z)^2 dS \tag{A.12}$$

$$dL = 4\pi D_c^2 (1+z)^2 dS \tag{A.13}$$

Substituting these expression into A.1 yields

$$dN = 16\pi^2 D_c^4 (1+z)^2 \ \phi(L,z) \frac{dD_c}{dz} dz \ dS \tag{A.14}$$

Therefore, the differential source counts are

$$\frac{dN}{dS} = \int 16\pi^2 D_c^4 (1+z)^2 \ \phi(L,z) \frac{dD_c}{dz} dz \tag{A.15}$$

A.1.1.2 δ-Luminosity-Function

This is the desired result for a generic luminosity function, however if we assume the luminosity function is a delta function in luminosity, then additional simplification is possible. A delta function is defined as

$$\int_{-\infty}^{\infty} \delta(x) dx = 1 \tag{A.16}$$

generalising x to a monotonically increasing 1-1 function $u = f(x)$ we can derive the effect of composition of a delta function with another function $g(x)$

$$\int \delta(f(x)) g(x) dx \tag{A.17}$$

the delta function has non-zero value at the roots of f(x), i.e. when f(x)=0. Because we are considering a monotonic function f(x), we need only integrate a negligible ε amount around its single root

$$\int \delta(f(x))g(x)dx = \int_{x_0-\varepsilon}^{x_0+\varepsilon} \delta(f(x))g(x)dx \tag{A.18}$$

As our function is also 1-1 we can express x as the inverse function f^{-1} of u

$$= \int_{x_0-\varepsilon}^{x_0+\varepsilon} \delta(u)g(f^{-1}(u))df^{-1}(u) \tag{A.19}$$

under the chain rule

$$df^{-1}(u) = \frac{df^{-1}(u)}{df(f^{-1}(u))}df(f^{-1}(u)) \tag{A.20}$$

substituting in

$$= \int_{f(x_0-\varepsilon)}^{f(x_0+\varepsilon)} \delta(u)g(f^{-1}(u))\frac{df^{-1}(u)}{df(f^{-1}(u))}df(f^{-1}(u)) \tag{A.21}$$

$$= \int_{f(x_0-\varepsilon)}^{f(x_0+\varepsilon)} \delta(u)\frac{g(f^{-1}(u))}{f'(f^{-1}(u))}du \tag{A.22}$$

the delta function has non-zero value at $u = f(x_0)$ so the RHS integral evaluates as

$$= \frac{g(f^{-1}(f(x_0)))}{f'(f^{-1}(f(x_0)))} \tag{A.23}$$

simplifying to

$$\int \delta(f(x))g(x)dx = \frac{g(x_0)}{f'(x_0)} \tag{A.24}$$

$$g(f(x)) = \frac{g(x_0)}{f'(x_0)} \tag{A.25}$$

from which we can infer

$$\delta(f(x)) = \frac{\delta(x)}{f'(x_0)} \tag{A.26}$$

This allows the delta function in our luminosity to be converted to a delta function in redshift as follows

$$\delta(L(z)) = \delta(z)\frac{dz}{dL(z)} \tag{A.27}$$

$$L(z) = 4\pi D_c^2(z)(1+z)^2 S \tag{A.28}$$

$$\frac{dL(z)}{dz} = 8\pi D_c(z)\frac{dD_c(z)}{dz}(1+z)^2 S + 8\pi D_c^2(1+z)S \tag{A.29}$$

$$= 8\pi D_c(1+z)S\left((1+z)\frac{dD_c(z)}{dz} + D_c(z)\right) \tag{A.30}$$

where, using Eq. 3.5, $dD_c(z)/dz$ is given by

$$\frac{dD_c(z)}{dz} = \frac{d_H}{E(z)} \tag{A.31}$$

$$\frac{dD_c(z)}{dz} = \frac{c}{H_0}\frac{H_0}{H(z)} = \frac{c}{H(z)} \tag{A.32}$$

removing the delta function in luminosity in the luminosity function ϕ converts the remainder into a number density function that takes in only redshift

$$\frac{dN}{dS} = \int 16\pi^2 D_c^4(z)(1+z)^2 n(z)\frac{c}{H(z)}\frac{\delta(z)}{dL(z)/dz}dz \tag{A.33}$$

evaluating at the non-zero value of the delta function z_0

$$\frac{dN}{dS} = 16\pi^2 D_c^4(z_0)(1+z_0)^2 n(z_0)\frac{c}{H(z_0)}\frac{1}{dL(z_0)/dz} \tag{A.34}$$

where z_0 is determined by the observed flux and considered luminosity. Furthermore, for a non-evolving population, the z_0 dependence of the number density can be dropped to yield

$$\frac{dN}{dS} = 16\pi^2 D_c^4(z_0)(1+z_0)^2 N_0\frac{c}{H(z_0)}\frac{1}{dL(z_0)/dz}, \tag{A.35}$$

where N_0 is the local number density of sources.

A.2 Tables

Table 1: Determinations of the cosmic star formation rate density from UV data (top group) and IR data (bottom group) used in this review.

Reference	Redshift range	$A_{\rm FUV}^{\rm a}$ [mag]	$\log \psi^{\rm a}$ [$M_\odot$ year^{-1} Mpc^{-3}]	Symbols used in Figure 9
Wyder et al. (2005)	0.01-0.1	1.80	$-1.82^{+0.09}_{-0.02}$	blue-gray hexagon
Schiminovich et al. (2005)	0.2-0.4	1.80	$-1.50^{+0.05}_{-0.05}$	blue triangles
	0.4-0.6	1.80	$-1.39^{+0.15}_{-0.08}$	
	0.6-0.8	1.80	$-1.20^{+0.31}_{-0.13}$	
	0.8-1.2	1.80	$-1.25^{+0.31}_{-0.13}$	
Robotham & Driver (2011)	0.05	1.57	$-1.77^{+0.08}_{-0.09}$	dark green pentagon
Cucciati et al. (2012)	0.05-0.2	1.11	$-1.75^{+0.18}_{-0.18}$	green squares
	0.2-0.4	1.35	$-1.55^{+0.12}_{-0.12}$	
	0.4-0.6	1.64	$-1.44^{+0.10}_{-0.10}$	
	0.6-0.8	1.92	$-1.24^{+0.10}_{-0.10}$	
	0.8-1.0	2.22	$-0.99^{+0.09}_{-0.08}$	
	1.0-1.2	2.21	$-0.94^{+0.09}_{-0.09}$	
	1.2-1.7	2.17	$-0.95^{+0.15}_{-0.08}$	
	1.7-2.5	1.94	$-0.75^{+0.49}_{-0.09}$	
	2.5-3.5	1.47	$-1.04^{+0.26}_{-0.15}$	
	3.5-4.5	0.97	$-1.69^{+0.22}_{-0.32}$	
Dahlen et al. (2007)	0.92-1.33	2.03	$-1.02^{+0.08}_{-0.08}$	turquoise pentagons
	1.62-1.88	2.03	$-0.75^{+0.12}_{-0.12}$	
	2.08-2.37	2.03	$-0.87^{+0.09}_{-0.09}$	
Reddy & Steidel (2009)	1.9-2.7	1.36	$-0.75^{+0.09}_{-0.11}$	dark green triangles
	2.7-3.4	1.07	$-0.97^{+0.11}_{-0.15}$	
Bouwens et al. (2012a),(2012b)	3.8	0.58	$-1.29^{+0.05}_{-0.05}$	magenta pentagons
	4.9	0.44	$-1.42^{+0.06}_{-0.06}$	
	5.9	0.20	$-1.65^{+0.08}_{-0.08}$	
	7.0	0.10	$-1.79^{+0.10}_{-0.10}$	
	7.9	0.0	$-2.09^{+0.11}_{-0.11}$	
Schenker et al. (2013)	7.0	0.10	$-2.00^{+0.10}_{-0.11}$	black crosses
	8.0	0.0	$-2.21^{+0.14}_{-0.14}$	
Sanders et al. (2003)	0.03	—	$-1.72^{+0.02}_{-0.03}$	brown circle
Takeuchi et al. (2003)	0.03	—	$-1.95^{+0.20}_{-0.20}$	dark orange square
Magnelli et al. (2011)	0.40-0.70	—	$-1.34^{+0.22}_{-0.11}$	red open hexagons
	0.70-1.00	—	$-0.96^{+0.15}_{-0.19}$	
	1.00-1.30	—	$-0.89^{+0.27}_{-0.21}$	
	1.30-1.80	—	$-0.91^{+0.17}_{-0.21}$	
	1.80-2.30	—	$-0.89^{+0.21}_{-0.25}$	
Magnelli et al. (2013)	0.40-0.70	—	$-1.22^{+0.08}_{-0.11}$	red filled hexagons
	0.70-1.00	—	$-1.10^{+0.10}_{-0.13}$	
	1.00-1.30	—	$-0.96^{+0.13}_{-0.20}$	
	1.30-1.80	—	$-0.94^{+0.13}_{-0.18}$	
	1.80-2.30	—	$-0.80^{+0.18}_{-0.15}$	
Gruppioni et al. (2013)	0.00-0.30	—	$-1.64^{+0.09}_{-0.11}$	dark red filled hexagons
	0.30-0.45	—	$-1.42^{+0.03}_{-0.04}$	
	0.45-0.60	—	$-1.32^{+0.05}_{-0.05}$	
	0.60-0.80	—	$-1.14^{+0.06}_{-0.06}$	
	0.80-1.00	—	$-0.94^{+0.05}_{-0.06}$	
	1.00-1.20	—	$-0.81^{+0.04}_{-0.05}$	
	1.20-1.70	—	$-0.84^{+0.04}_{-0.04}$	
	1.70-2.00	—	$-0.86^{+0.02}_{-0.03}$	
	2.00-2.50	—	$-0.91^{+0.09}_{-0.12}$	
	2.50-3.00	—	$-0.86^{+0.15}_{-0.23}$	
	3.00-4.20	—	$-1.36^{+0.23}_{-0.50}$	

[a] In our notation, $A_{\rm FUV} = -2.5 \log_{10}\langle k_d \rangle$.
[b] All our star-formation rate densities are based on the integration of the best-fit luminosity function parameters down to the same *relative* limiting luminosity, in units of the characteristic luminosity L^*, of $L_{\rm min} = 0.03\,L^*$. A Salpeter initial mass function has been assumed.
[c] Madau & Dickinson

Figure A.1: Tabular legend corresponding to Fig. 4.1 reproduced from Madau & Dickinson (2014).

Appendix B

Methods

B.1 Derivations

As discussed in §3.3, the optical depth for a cosmological population is given by

$$\tau = \int_0^{z_s} d\chi(z_d)(1+z_d)^2 n\sigma(\mu), \tag{B.1}$$

where n is the number density of lenses with cross-section σ, z_d is the redshift of the lens plane, z_s is the redshift of the source and χ is the comoving distance. As discussed §3.1, comoving distance can be expressed as an integral over redshift (Hogg, 2000)

$$\chi = d_H \int_0^z \frac{dz'}{E(z')} \tag{B.2}$$

where $d_H = c/H_0$ is the Hubble distance and

$$E(z) = \frac{H(z)}{H_0}. \tag{B.3}$$

Therefore the element $d\chi$ is given by

$$d\chi = \frac{d\chi}{dz}dz = \frac{d_H}{E(z)}dz \tag{B.4}$$

$$d\chi = \frac{c}{H_0}\frac{H_0}{H(z)}dz \tag{B.5}$$

$$d\chi = \frac{c}{H(z)} \tag{B.6}$$

Substituting into Eq. B.1 converts the optical depth into an integral over lens redshift

$$\tau = \int_0^{z_s} dz_d \frac{c}{H(z_d)}(1+z_d)^2 n\,\sigma \tag{B.7}$$

to relate the number density of lensing objects to the Universe's density of matter the number density can be expressed in terms of critical density ($\rho_{\rm cr}$

$$\tau = \int_0^{z_s} dz_d \frac{\Omega_L \rho_{\rm cr}}{M_L}\frac{c}{H(z_d)}(1+z_d)^2\sigma \tag{B.8}$$

where M_L is the mass of an individual lens.

The cross-section to lensing above a magnification of μ is given by

$$\sigma = \pi y(\mu)^2 \theta_E^2 D_d^2 \tag{B.9}$$

where D_d is the angular diameter distance of the lens from the observer and y is the angular impact parameter of the source with respect to the lens in units of the Einstein radius (θ_E), given by

$$y(\mu) = \sqrt{2\left(\frac{\mu}{\sqrt{\mu^2-1}} - 1\right)}. \tag{B.10}$$

The differential cross section as a function of the magnification is given by

$$\frac{d\sigma}{d\mu} = 2\pi y \frac{dy}{d\mu} \theta_E^2 D_d^2, \tag{B.11}$$

where the gradient of y with respect to μ is given by

$$\frac{dy}{d\mu} = \left(\frac{2\mu}{\sqrt{\mu^2 - 1}} - 2 \right)^{-1/2} \frac{-1}{(\mu^2 - 1)^{3/2}}, \tag{B.12}$$

which yields

$$\frac{d\sigma}{d\mu} = \frac{-2\pi}{(\mu^2 - 1)^{3/2}} \left(\theta_E D_d\right)^2 . \tag{B.13}$$

An infinitesimal area $\frac{d\sigma}{d\mu} d\mu$ corresponds to an infinitesimal optical depth $\mathrm{d}\tau$ to lensing at a magnification between μ and $\mu + d\mu$ given by

$$d\tau = \int_0^{z_s} dz_d \frac{\Omega_{\mathrm{L}} \rho_{\mathrm{cr}}}{M_L} \frac{c}{H(z_d)} (1 + z_d)^2 \frac{d\sigma}{d\mu} d\mu \tag{B.14}$$

$$d\tau = \int_0^{z_s} dz_d \frac{\Omega_{\mathrm{L}} \rho_{\mathrm{cr}}}{M_L} \frac{c}{H(z_d)} (1 + z_d)^2 \frac{2\pi}{(\mu^2 - 1)^{3/2}} \left(\theta_E D_d\right)^2 d\mu \tag{B.15}$$

This form can be simplified by recognising that θ_E^2 has a linear dependence on the mass of the lensing object that can be cancelled with the M_L term in the wider expression, yielding

$$d\tau = \int_0^{z_s} dz_d \frac{\Omega_{\mathrm{L}} \rho_{\mathrm{cr}}}{\Sigma_{\mathrm{cr}}} \frac{c}{H(z_d)} (1 + z_d)^2 \frac{2}{(\mu^2 - 1)^{3/2}} \mu \tag{B.16}$$

where

$$\Sigma_{\rm cr} = \frac{c^2 D_s}{4\pi G D_{ds} D_d} \tag{B.17}$$

which when integrated over μ yields Eq. 3.20

Appendix C

The Effect of Gravitational Lensing on Fast Transient Event Rates

C.1 D_η

There are many models available for calculating cosmological distances in an inhomogeneous universe. We have opted here to use the ZKDR distance equation (Zel'dovich, Kantowski, Dyer/Dashevskii, Roeder, also known as the Dyer-Roeder distance), principally for its simplicity as an effective model rather than a full space-time description. More complicated models such as Swiss-cheese space-times are computationally limited to treating galaxy scale inhomogeneities (Fleury et al., 2013) and so are inadequate for addressing the scales we wish to consider here. Despite questions of the ZKDR distance's validity (e.g. Clarkson et al., 2012) the model has been shown analytically to be consistent with certain Swiss-cheese models (Fleury, 2014) which are exact solutions to Einstein's field equations and achieves good agreement with more generalised models such as Holz & Wald (1998) and Bergström et al. (2000).

The ZKDR distance equation calculates the value of D_A for propagation

through a void in an inhomogeneous, but on-average Friedmann-Lemaitre dust universe (dust refers to cold/non-relativistic matter) which we refer to as D_η. The equation, its derivation and the relevant boundary conditions can be found in Kayser et al. (1997). The authors also present a general numerical method to solve for the ZKDR angular diameter distance (D_η) in an arbitrary cosmology. Their treatment makes three key assumptions.

1. The distribution of matter in the Universe can be divided into clumpy (inhomogeneous) and smooth categories, described by η, the fraction of the mass which is smooth.

2. The beam subtended by the source contains no clumps.

3. The light propagates far from all clumps, i.e. there is vanishing shear on the beam.

Following their method we provide a simple numerical implementation for calculating the D_η in the Python programming language (Rossum & Drake, 2011). D_η can be solved for by considering the following system of coupled ordinary differential equations (Kayser et al., 1997):

$$D'_\eta(z) = \frac{1}{(1+z)\sqrt{Q(z)}} \tag{C.1}$$

$$D''_\eta(z) = \frac{-\left(\frac{2Q(z)}{(1+z)+\frac{Q'(z)}{2}}\right) D' - \frac{3}{2}\eta\Omega_{M,0}(1+z)D}{Q(z)} \tag{C.2}$$

$$Q(z) = \Omega_{M,0}(1+z)^3 - (\Omega_{M,0} + \Lambda_0 - 1)(1+z)^2 + \Lambda_0 \tag{C.3}$$

$$Q'(z) = 3\Omega_{M,0}(1+z)^2 - 2(\Omega_{M,0} + \Lambda_0 - 1), \tag{C.4}$$

where primes denote derivatives with respect to redshift and $\Omega_{M,0}$ & Λ_0 are the matter density parameter and cosmological constant respectively at $z = 0$.

To solve the system we implement a numerical routine using SOLVE_IVP (Virtanen et al., 2020). The source code for our implmentation can be found here : https://github.com/MWSammons/ZKDRDistance.

Also implemented in our function set is the generalised Dyer-Roeder model of Linder (1988). This solution includes a treatment of relativistic matter and radiation densities in the universe. However, we note that results of this method achieve a worse agreement with the analytic solutions for a smooth universe in the case of a Planck cosmology compared to the forced-flat Kayser model.

The results of our numerical approach are presented in Fig. C.1, which compares D_η in a completely inhomogeneous universe ($\eta = 0$) and D_1, for a Planck cosmology (Planck Collaboration et al., 2018). For the remainder of this work D_η will be calculated assuming this cosmology. To demonstrate the fidelity of our numeric method we also plot the residuals of D_1 with its analytic solution in the bottom panel of Fig. C.1. Our results show good agreement with the analytic solution. Moreover, we reproduce the large difference between D_1 and D_η for $\eta = 0$ at high redshift seen in Fig. 1 of Kayser et al. (1997). One short-coming of the Kayser model is that any density not in cold matter Ω_M or dark energy Λ implicitly contributes to the universe's curvature. Considering this, relativistic and radiation density in the Planck cosmology have been amalgamated into $\Omega_{M,0}$ to force a flat universe within the boundaries of the Kayser model.

C.2 The Effect of Wave Optics

Formally, geometric optics describes the behaviour of emission with an infinite frequency. In reality however, geometric optics provides an adequate description of gravitational lensing for all emission wavelengths much shorter than the gravitational radius of the lens. For the case of point mass lenses, Oguri (2019) defines a dimensionless parameter w from this condition,

$$w = 2\pi f \frac{4GM(1+z_d)}{c^3}, \tag{C.5}$$

where z_d is the redshift of the lens.

The magnification for a point mass lens as a function of the source's angular

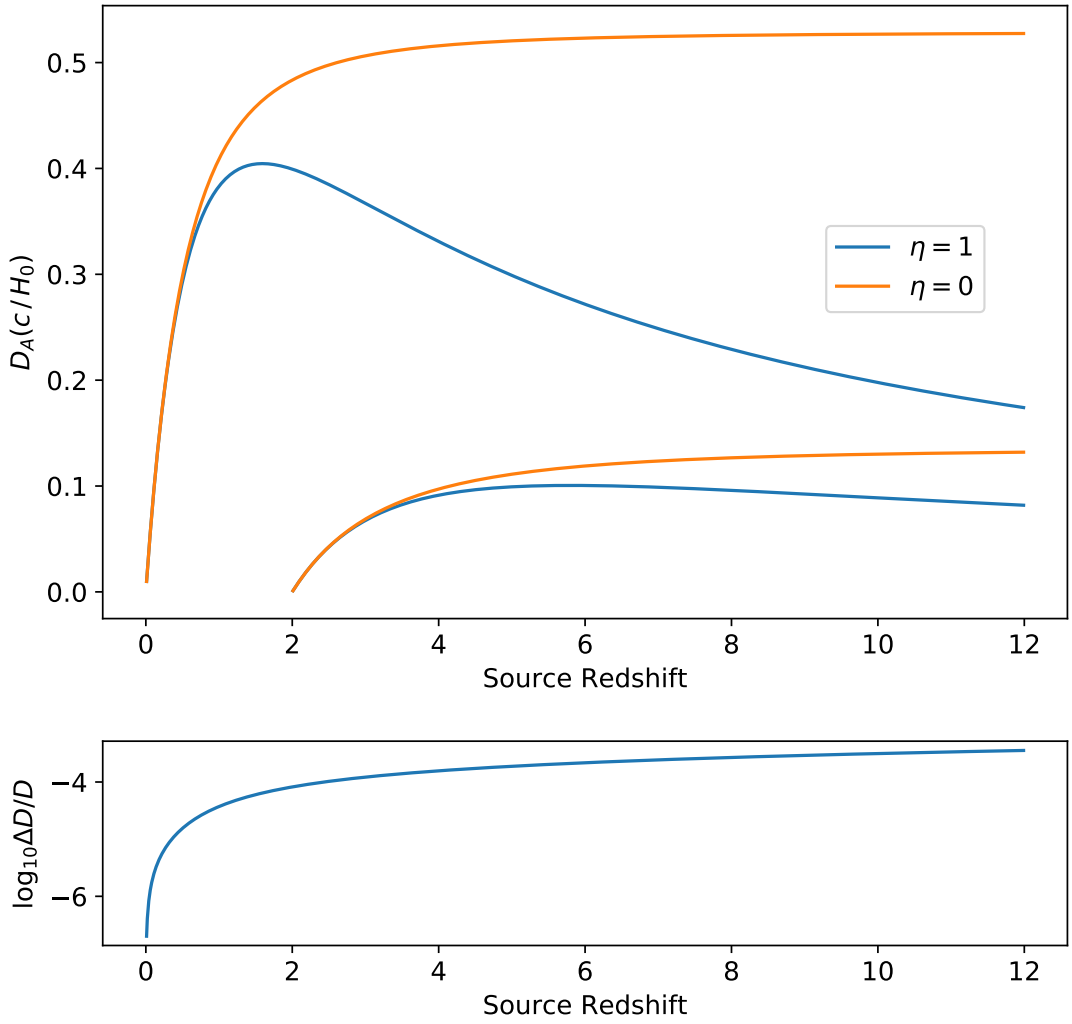

Figure C.1: (Top panel) Comparison of D_1 and D_η for a completely inhomogeneous universe ($\eta = 0$) in a Planck cosmology. Upper plots are for an observer at $z = 0$, lower plots are for an observer at $z = 2$. (Bottom panel) The log residuals between the analytic solution to D_1 (Hogg, 2000) and our numerical result for a Planck cosmology.

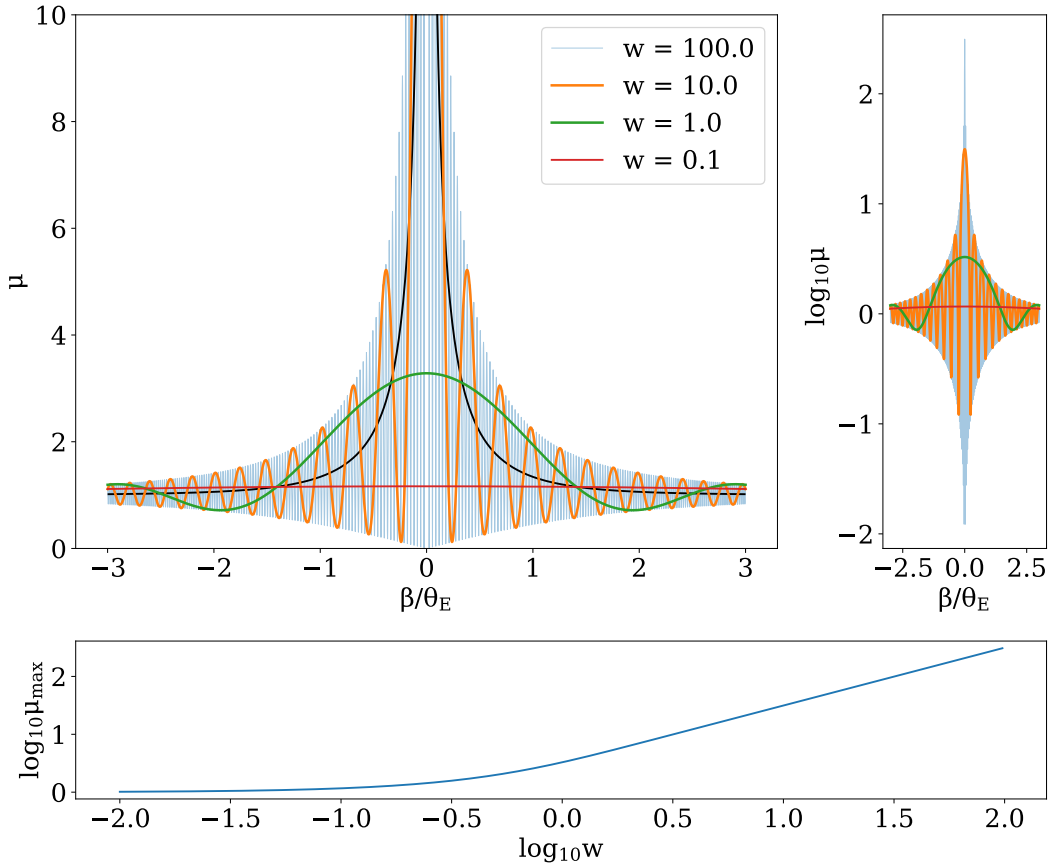

Figure C.2: Behaviour of magnification in wave optics. *(Top left/right)* magnification/log magnification of the source as a function of the source's angular impact parameter with respect to the optic axis centred on the lens, normalised by the einstein radius of the lens θ_E, plotted for various dimensionless w parameter choices. *(Bottom)* Maximum magnification as a function of dimensionless parameter w, calculated using Eq. (45) in (Oguri, 2019).

impact parameter β can then be defined for a wave optics regime as [1].

$$\mu = \frac{\pi w}{1 - e^{-\pi w}} \left| {}_1F_1\left(\frac{i}{2}w, 1; \frac{i}{2}w\left(\frac{\beta}{\theta_E}\right)^2\right)\right|^2, \tag{C.6}$$

where ${}_1F_1$ is the confluent hypergeometric function.

Fig. C.2 shows this for a variety of w values as well as the geometric case. For

[1] We note this treatment is only valid when the geometric time delay along paths contributing to the interference pattern are much less than the pulses duration. Otherwise the boundary diffraction wave should be modelled explicitly (Born & Wolf, 2013).

a w value approaching infinity the wave and geometric optics results will agree, with a finite extent source smoothing over the infinitely compressed oscillations. As w decreases so does the maximum possible magnification. Additionally, fringe spacing increases allowing sources of greater extent to exhibit an oscillatory magnification with β.

If the optical depth to lensing is low, the magnification cumulative probability distribution function (CDF; $P(>\mu)$) will be proportional to the cross section of normalised angular impact (β/θ_E) greater than a magnification μ (Turner et al., 1984). In the case of geometric optics, evaluating the cross section becomes simply

$$\sigma = \pi \left(\frac{\beta_\mu}{\theta_E}\right)^2 \tag{C.7}$$

where β_μ is the angular impact parameter of the source at a magnification μ. β_μ can be determined from the black line on Fig. C.2, which is governed by Eq. (2.5) in Turner et al. (1984). Ultimately this yields the conventional $dP/d\mu \equiv p(\mu) \propto \mu^{-3}$ behaviour.

As can be intuited from Fig. C.2, the cross section to lensing above μ for lower values of w is significantly more complicated. By integrating the ring element $2\pi\beta d\beta$ for all magnifications above μ we can determine the cross section corresponding to $P(>\mu)$ for any w. We plot this cross section in Fig. C.3, normalised by its geometric counterpart to provide a comparison between the results of geometric and wave optics.

Fig. C.3 shows that the normalised cross section over the range of μ and w values plotted is often significantly above 1. This means that $P(>\mu)$ is often greater in the wave optics regime than the geometric regime. This is in agreement with wave optics results derived by Jow et al. (2020).

For high values of w, the low magnifications behave very similarly to the geometric case (i.e. the normalised cross section is flat with μ). As the magnification increases however, the scale of cross section oscillation increases and subsections of the magnification space begin to deviate significantly from the flat geometric

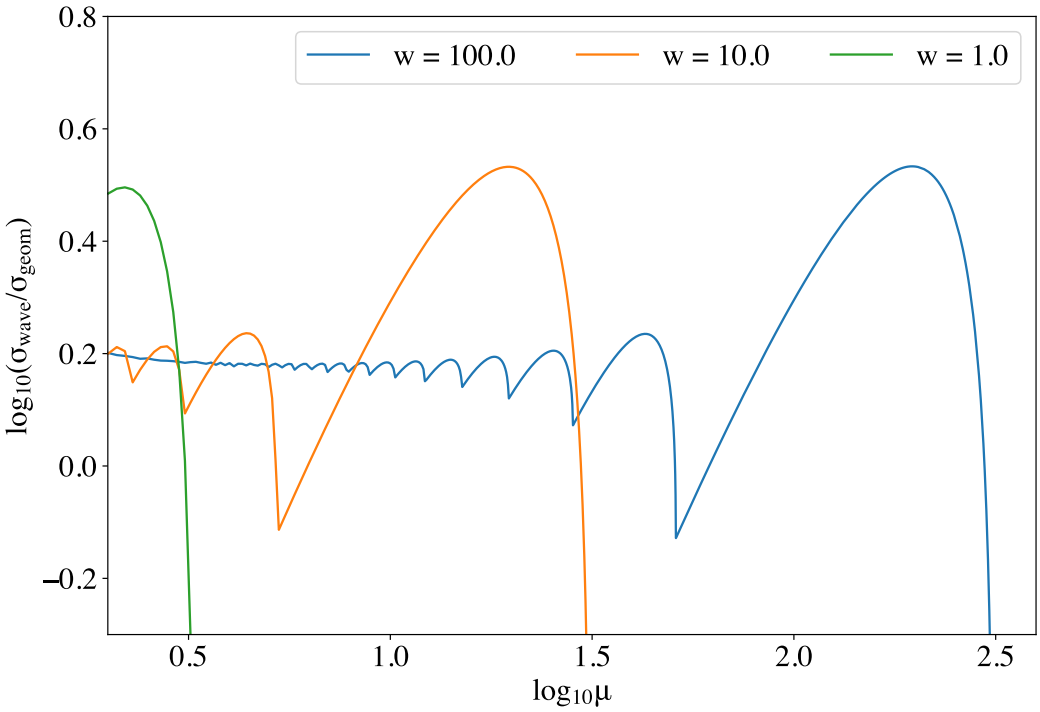

Figure C.3: Cross section to lensing above a magnification μ calculated from the wave optics magnifications shown in Fig. C.2, normalised by the corresponding cross section derived using geometric optics (Eq. (C.7)). w values are calculated from Eq. (C.5). Cross sections are directly proportional to the magnification CDF.

behaviour until the maximum magnification is reached. Decreasing w, either by decreasing the emission frequency or decreasing lens mass then effectively translates the normalised cross section to lower magnification.

If the frequency of emission or lens mass is low enough such that regions of significant oscillation in normalised cross section are present at observed magnifications, then geometric optics should not be applied to calculate the expected effects of lensing. For an FRB emitted at 1 GHz, at redshift 0.1, lensed by a 0.01 $M_\odot$ point mass, $w \sim 10^3$ and the maximum magnification will be $\approx 10^{3.5}$. From Fig. C.3 we can see that for the $w = 100$ case, magnifications a factor of $10^{1.5}$ below the maximum (at around $\log_{10}\mu = 1.0$) have geometric like behaviour. Applying this same condition to our canonical FRB case, it is reasonable to assume that magnifications below $\sim 10^2(10^{3.5}/10^{1.5})$ will have $p(\mu) \propto \mu^{-3}$. Taking the results of our lensed dR/df calculation shown in Fig. 6.11 and decomposing it into its components in magnification space we get Fig. 6.12. From this figure we can see that the fractional change in dR/df due to lensing is dominated by low magnifications. Specifically, more than 98% of the total comes from magnifications less than 100 at all fluences. This suggests that the fraction of observed sources at magnifications above 10^2 will be negligible and therefore that our results for FRB lensing, using the geometric $p(\mu) \propto \mu^{-3}$ should apply for lens masses greater than $0.01 M_\odot$[2].

If observed bursts are dominated by lensing at magnifications where the cross section to lensing shows prominent fringes, e.g. $\mu = [10 - 300]$ for $w = 100$, the true lensing PDF could have behaviour significantly different from $p(\mu) \propto \mu^{-3}$. In this context, counter to the discussion in §6.6, all observed bursts could be highly magnified, despite an observed $\gamma \neq -3$. The associated decrease in $\mu_{\rm max}$ however restricts the parameter space where this could occur. Using $w = 100$, a potential example could be FRBs at an emission frequency of 1 GHz requiring a magnification above ~ 10 but below ~ 300 to be observed in a universe populated

[2]We have not accounted for the increased cross section size in the case of a wave optics and so our results will underestimate the effect of lensing.

by $\sim 10^{-3} M_{\odot}$ mass lenses ($w \approx 100$). In such a scenario all observed FRBs would be lensed but the energy index γ could differ from the expected -3 value. These FRBs would also only be observable above ~ 30 MHz, at which point $\mu_{\rm max} \approx 10$.

C.3 Derivations

C.3.1 Differential Rates in a Smooth Universe

A small observed rate can be expressed using the event rate energy function of the fast transient population Θ_E as,

$$dR = \Theta_E(E_{\nu_e}, z, \nu_e) dE \; dV_c \tag{C.8}$$

the comoving volume element is given by

$$V_c = \frac{4}{3}\pi D_c^3(z) \tag{C.9}$$

differentiating with respect to redshift gives

$$\frac{dV_c}{dz} = 4\pi D_c^2(z) \frac{dD_c}{dz} \tag{C.10}$$

Intrinsic spectral energy (E_{ν_e}) is given by

$$E_{\nu_e} = 4\pi D_L^2(z) \frac{F_\nu}{(1+z)^2} \tag{C.11}$$

where F_ν is the observed fluence of the transient at observation frequency ν, the factor of $1/(1+z)^2$ accounts for bandwidth compression by cosmological redshift as well as the dilation of the bursts duration in time, differentiating with respect to observed fluence and holding redshift constant gives us

$$\frac{\partial E_{\nu_e}}{\partial F_\nu} = 4\pi D_L^2(z)\frac{1}{(1+z)^2} \tag{C.12}$$

putting these components into a integration over redshift transforms our partial differential equation into a full differential equation, yielding

$$\frac{dR}{dF_\nu} = \int dz\ 16\pi^2 D_L^2(z) D_c^2(z)\frac{1}{(1+z)^3}\frac{dD_c}{dz}\Theta_E(E_{\nu_e}, z, \nu_e) \tag{C.13}$$

where ν_e can be expressed as $\nu_e = (1+z)\nu$, sampling from the emission frequency region of the energy function as opposed to the observation frequency implicitly handles the required k-correction. The additional factor of $1/(1+z)$ accounts for the redshift of the burst rate itself.

$$\frac{dR}{dF_\nu} = \int dz\ 16\pi^2 D_L^2(z) D_c^2(z)\frac{1}{(1+z)^3}\frac{dD_c}{dz}\Theta_E(E_{\nu_e}, z, (1+z)\nu) \tag{C.14}$$

C.3.2 Differential Rates in a Clumpy Universe

Similarly to above, a small observed rate of fast trasnients can be expressed for an inhomogeneous universe using the event rate energy function of the transient population and the probability of magnification by a factor μ from gravitational lensing as,

$$dR = p(\mu, z)\Theta_E(E_{\nu_e}, z, \nu_e) dE\ dV_c \tag{C.15}$$

the comoving volume element is given by

$$V_c = \frac{4}{3}\pi D_c^3(z) \tag{C.16}$$

differentiating with respect to redshift gives

$$\frac{dV_c}{dz} = 4\pi D_c^2(z)\frac{dD_c}{dz} \tag{C.17}$$

Intrinsic spectral energy (E_{ν_e}) is given by

$$E_{\nu_e} = 4\pi(D_\eta(1+z)^2)^2\frac{F_\nu}{\mu(1+z)^2} \tag{C.18}$$

where F_ν is the observed fluence of the transient at observation frequency ν, $D_\eta(1+z)^2$ is the luminosity distance in an inhomogeneous universe with a smooth matter fraction η and the factor of $1/(1+z)^2$ accounts for bandwidth compression by cosmological redshift as well as the dilation of the bursts duration in time. Differentiating with respect to observed fluence and holding redshift constant gives us

$$\frac{\partial E_{\nu_e}}{\partial F_\nu} = 4\pi(D_\eta(1+z)^2)^2\frac{1}{\mu(1+z)^2} \tag{C.19}$$

putting these components into a integration over redshift transforms our partial differential equation into a full differential equation, yielding

$$\frac{dR}{dF_\nu} = \int dz 16\pi^2(D_\eta(1+z)^2)^2 D_c^2(z)\frac{1}{(1+z)^3}\frac{dD_c}{dz} \tag{C.20}$$

$$\times \int d\mu\ \frac{1}{\mu}p(\mu,z)\Theta_E(E_{\nu_e},z,\nu_e) \tag{C.21}$$

where ν_e can be expressed as $\nu_e = (1+z)\nu$, sampling from the emission frequency region of the energy function as opposed to the observation frequency implicitly handles the required k-correction. The additional factor of $1/(1+z)$ accounts for the redshift of the burst rate itself.

$$\frac{dR}{dF_\nu} = \int dz 16\pi^2 (D_\eta (1+z)^2)^2) D_c^2(z) \frac{1}{(1+z)^3} \frac{dD_c}{dz} \tag{C.22}$$

$$\times \int d\mu \, \frac{1}{\mu} p(\mu, z) \Theta_E(E_{\nu_e}, z, (1+z)\nu) \tag{C.23}$$

FRB	S/N	m	ν_c (MHz)	ν_{DC} (MHz)	$t_{\rm scatt}$ (ms)	C	α_ν	α_t	$\nu_{\rm Ne2001}$ (MHz)	$\nu_{\rm min}$ (MHz)	$L_x L_g$ (kpc^2)
20181112A	143	0.1	1297.5	-	$.0278 \pm 0.0008$	-	-	-0.8 ± 0.6	2.82	0.001	-
20190102C	124	0.41	1271.5	0.6 ± 0.3	0.046 ± 0.001	170	10	-4	1.26	0.001	-
20190608B	32.9	0.78	1271.5	1.4 ± 0.1	4.0 ± 0.4	35000	5.8 ± 0.5	-4 ± 1	3.08	1	6 ± 1
20190711A	89.3	0.64	1136.9	0.11 ± 0.01	0.008 ± 0.003	6	-10 ± 5	-10	0.837	0.0001	
20191228A	51.1	0.77	1340.3	-	5.5 ± 0.2	-	-	-	5.47	0.1	-
20200430A	56.7	0.45	864.5	-	7.7 ± 0.5	-	-	-3.0 ± 0.3	0.973	0.1	-
20201124A	172	0.59	713.9	$.136 \pm 0.005$	4.04 ± 0.07	3450	10 ± 3	-7.3 ± 0.9	0.00721	1×10^{-4}	1.43 ± 0.08
20210117A	43.9	0.0	1364.2	-	0.14 ± 0.6	-	-	1 ± 4	5.82	0.1	-
20210320C	113	0.83	824.2	0.91 ± 0.03	0.247 ± 0.006	1410	2 ± 1	-3.30 ± 0.01	1.03	0.1	550 ± 30
20210407E	49.7	0.0	1220.2	-	0.090 ± 0.010	-	-		3.01	1	-

Table C.1: Measured scintillation parameters for a sample of localised CRAFT FRBs.

C.4 Simulating spectral scintillation detection threshold

We create blank spectra with 336 MHz of bandwidth around a central frequency of 1271.5 MHz at 0.1 MHz resolution. We then populate it with $N = f \times 336/\nu_{\mathrm{DC},0}$ scintles, where the filling fraction f is 0.5, a typical assumption for pulsar scintillation (Bhat et al., 1999; Nicastro et al., 2001) and $\nu_{\mathrm{DC},0}$ is the decorrelation bandwidth of the simulated burst at 1 GHz. The amplitude of the scintles is set such that the sum of the noiseless spectra is equal to the simulated burst's S/N and their positions in frequency (ν_p) are drawn randomly from a uniform distribution. The scintles are Lorentzian in shape with a HWHM of $2\nu_{\mathrm{DC}}$ (Bartel et al., 2022), corresponding to a decorrelation bandwidth of $\nu_{\mathrm{DC}} = (\nu_{\mathrm{DC},0}(\nu_p)/1000)^4$. These arrays represent the noise-free signal (S) of a burst. We also construct noise arrays (N) filled with white noise following a $N(0, 1/\sqrt{3360})$ distribution.

We simulate 1000 signal and noise arrays for each of a range of combinations of S/N and ν_{DC} values. For each, we calculate the ACF signal and noise as

$$\mathrm{ACF}_S(j) = \sum_{i=0}^{3360} S(i)S(i+j) \tag{C.24}$$

$$\mathrm{ACF}_N(j) = \sum_{i=0}^{3360} S(i)N(i+j) + S(i+j)N(i) + N(i)N(i+j). \tag{C.25}$$

The χ^2 value for the significance of the burst ACF at a given S/N and ν_{DC} is then calculated as

$$\chi^2 = \sum_{j=0}^{3360} \frac{\overline{\mathrm{ACF}_S(j)} - \overline{\mathrm{ACF}_N(j)}}{\sigma(j)}, \tag{C.26}$$

where the bar represents the mean over the 1000 simulated instances and $\sigma(j)$ is the standard deviation of $\mathrm{ACF}_N(j)$. Due to the high degree of freedom of the χ^2 distribution (roughly equal to the number of channels, 3360) the probability of chance significance ($p = 1 - \mathrm{CDF}(\chi^2)$) also transitions sharply from ≈ 1 to ≈ 0 and hence we set the detection threshold at this transition at χ^2 value of

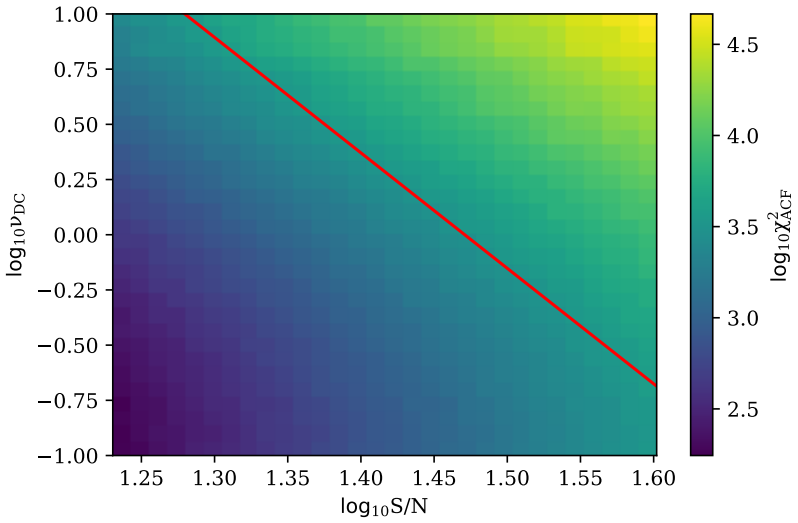

Figure C.4: $\log_{10}\chi^2$ values for the significance of scintillation structure in the burst ACF as a function of burst S/N and $\nu_{\rm DC}$. Red line represents the detection threshold, fit to χ^2 values of ≈ 3360, where the CDF of the χ^2 distribution is ≈ 0.5.

≈ 3360. Fig. C.4 depicts the simulated χ^2 values and over-plots the detection threshold from linear fit in log space to the $\chi^2 \approx 3360$ values in red. For values of $\nu_{\rm DC}$ greater than the threshold at a given S/N the scintillation should be detectable. By extrapolating the threshold relationship we calculate the minimum detectable scintillation bandwidths $\nu_{\rm min}$ using the observed burst S/N. Given the assumptions used in this model we round $\nu_{\rm min}$ to the nearest order of magnitude.

C.5 Derivation of Eq. 3

As per Narayan (1992) the modulation index of an extended source is given by

$$m = \frac{\theta_{\rm diff}}{\theta_S} \tag{C.27}$$

where $\theta_{\rm diff}$ is the angle subtended by the diffractive scale $r_{\rm diff}/D_d$, and θ_S is the apparent angle of the source. In the case where light scattered by an extragalactic screen into an angle $\theta_{{\rm scatt},x}$ is incident upon a Galactic screen characterised by $r_{{\rm diff},g}$, the modulation index of scintillation from the Galactic screen (m_g) will be given by

$$m_g = \frac{r_{{\rm diff},g}}{D_{d,g}\theta_{{\rm scatt},x}} \tag{C.28}$$

where $D_{d,g}$ is the distance to the Galactic screen from the observer. The diffractive scale the Galactic screen may also be approximated as $r_{{\rm diff},g} \sim \lambda/2\pi\theta_{{\rm scatt},g}$ (Narayan, 1992), yielding

$$m_g = \frac{\lambda}{2\pi\theta_{{\rm scatt},g}\theta_{{\rm scatt},x}D_{d,g}} \tag{C.29}$$

where λ is the observed wavelength. As per Macquart & Koay (2013) scattering angles can be expressed as scattering times following $t_{\rm scatt} = D_d D_s \theta^2_{\rm scatt}/[cD_{ds}(1+z_d)]$, where z_d is the redshift at the screen. Substituting the scattering angles for scattering times gives

$$t_{{\rm scatt},g}t_{{\rm scatt},x} = \frac{1}{(2\pi\nu)^2 m_g^2(1+z_x)}\frac{D_{s,x}D_{d,x}}{D_{ds,x}}\frac{D_{s,g}}{D_{ds,g}D_{d,g}} \tag{C.30}$$

When $m_g = 1$, the left hand side becomes $\lesssim$ the right hand side, and the general form of Eq. 7.2 is recovered. By assuming that the screens are close to their respective ends of the path length (i.e. they are associated with the Milky Way and host galaxies), we can approximate $D_{d,x} \approx D_{ds,g}$, and $D_{s,x} \approx D_{s,g} \approx D_s$, reducing the above expression to

$$t_{{\rm scatt},g}t_{{\rm scatt},x} \approx \frac{D_s^2}{(2\pi\nu)^2 m_g^2}\frac{1}{D_{d,g}D_{ds,x}} \tag{C.31}$$

Exchanging $t_{\rm scatt,g}$ for $1/2\pi\nu_{\rm DC}$ via Eq. 7.1 and recognising that $D_{d,g}$ and $D_{ds,x}$ are L_g and L_x respectively yields Eq. 7.4

$$L_x L_g \approx \frac{D_s^2}{2\pi\nu^2(1+z_x)}\frac{\nu_{\rm DC}}{t_{\rm scatt}} \tag{C.32}$$

C.6 Anisotropic Scattering Screens

The constraints on the $L_x L_g$ product are derived from the condition, that to have fully modulated diffractive scintillation at the second screen, the coherence length set by the diffractive scale of the first scattering screen ($r_{\rm diff,1}$) must be greater than the scattering angle of the second screen projected back onto that screen (Ocker et al., 2022c), i.e.

$$r_{\rm diff,1} \geq \theta_{\rm scatt,2} D_d. \tag{C.33}$$

The implicit assumption within this condition is that the thin screens are two-dimensional and isotropic. Under this assumption the extent of angular broadening caused by the first screen is equivalent to the extent of the source as seen by the second screen. If however, the screens were anisotropic, the direction of angular broadening will also be important. In the extreme case where each screen is one dimensional, e.g. scattering by a filament or tidal stream similar to that observed by Wang et al. (2021), then the angular extent of the source seen by the second screen will be given by the projection of the image scattered by the first screen onto the second. The condition to observe fully modulated diffractive scintillation at the second screen then becomes

$$r_{\rm diff,1} \geq \theta_{\rm scatt,2} D_d \cos\phi, \tag{C.34}$$

where ϕ would be the angle between the one-dimensional screens if they were projected onto a plane perpendicular to the optic axis, as depicted in Fig. C.5.

For parallel, one-dimensional screens the constraints will remain unchanged. Conversely, for perfectly orthogonal screens, the second screen will always observe

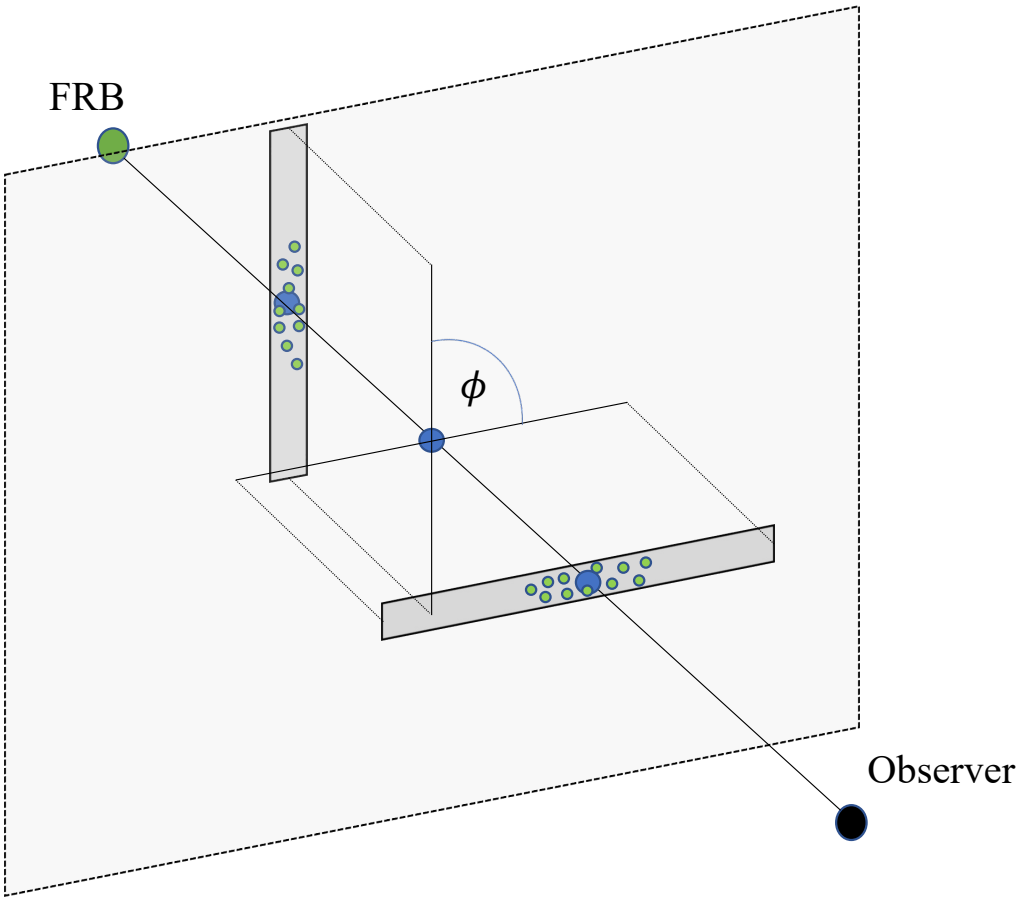

Figure C.5: Depiction of two-screen scattering for two anisotropic screens. The observer is shown as a black dot and the FRB source as a large green dot. The smaller green dots on each screen represent the images comprising the angularly broadened image seen by an observer. Blue dots show the interception point of the optic axis for each screen. By projecting each screen onto a plane perpendicular to the optic axis the angle between the dominant directions of each screens anisotropy can be described by the angle ϕ.

the source to be point-like, regardless of the extent of angular broadening from the first screen. In this case, the scattering in each dimension will be completely independent and we will be unable to constrain the scattering geometry. Constraints on the two-screen distance product are therefore completely degenerate with the anisotropy of the scattering screens.

We highlight, however, that in the case of anisotropic scattering screens, it is expected that the shapes of both the temporal impulse response function (i.e. the temporal broadening profile) and the spectral auto-correlation function of the scattered pulse will differ from those used here. Specifically, in the case of the temporal impulse response function, anisotropic screens are expected to show a greater fraction of intensity at larger time delays (Cordes & Lazio, 2001; Rickett, 2006). The more one-dimensional these screens become, the greater the difference in expected pulse morphology will be. Within our sample, the observed pulses are well described by the pulse morphology expected for scattering through an isotropic, two-dimensional thin screen, particularly FRB 20210320C. We, therefore, conclude that significant anisotropy in the scattering screens associated with our observations is unlikely, and we leave a rigorous treatment of the expected FRB morphology for scattering through anisotropic screens to a future work.

C.7 Additional Figures

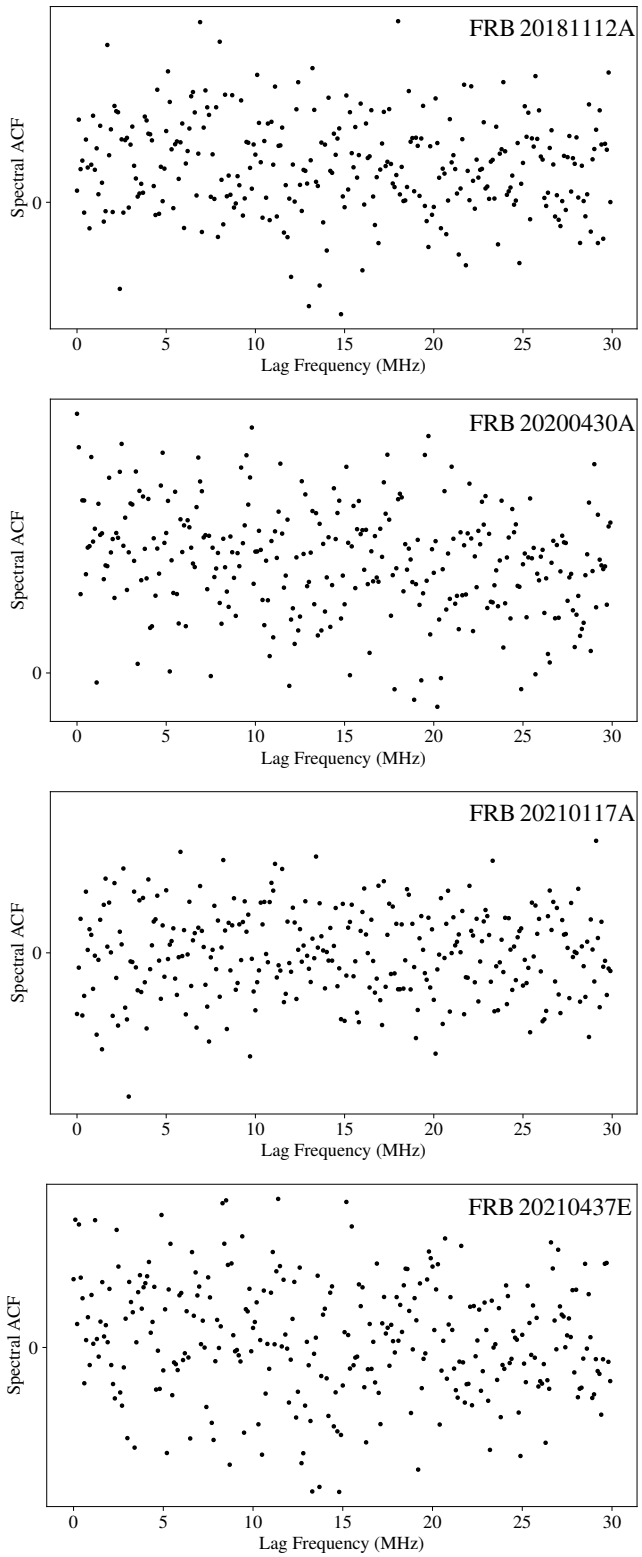

Figure C.6: Time-integrated spectral ACFs for FRBs within the sample confirmed not to scintillate. Each panel is labelled with the relevant FRB name.

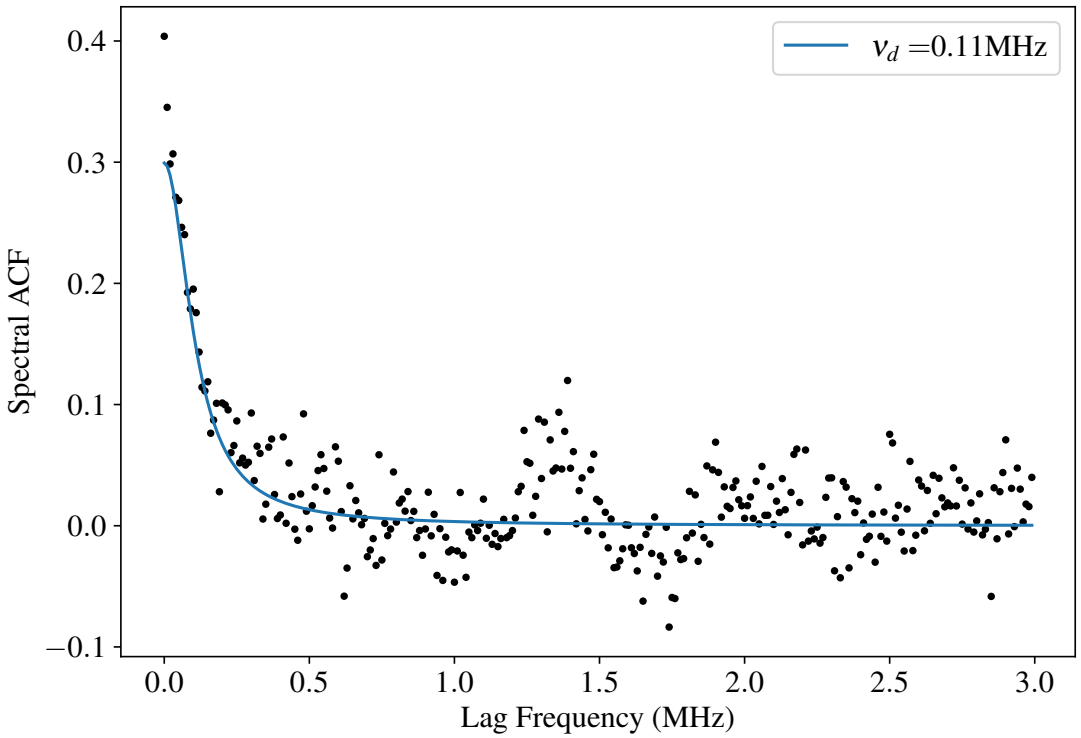

Figure C.7: Time-integrated spectral ACF for FRB 20190711A, for which we found insufficient evidence to prove scintillation.

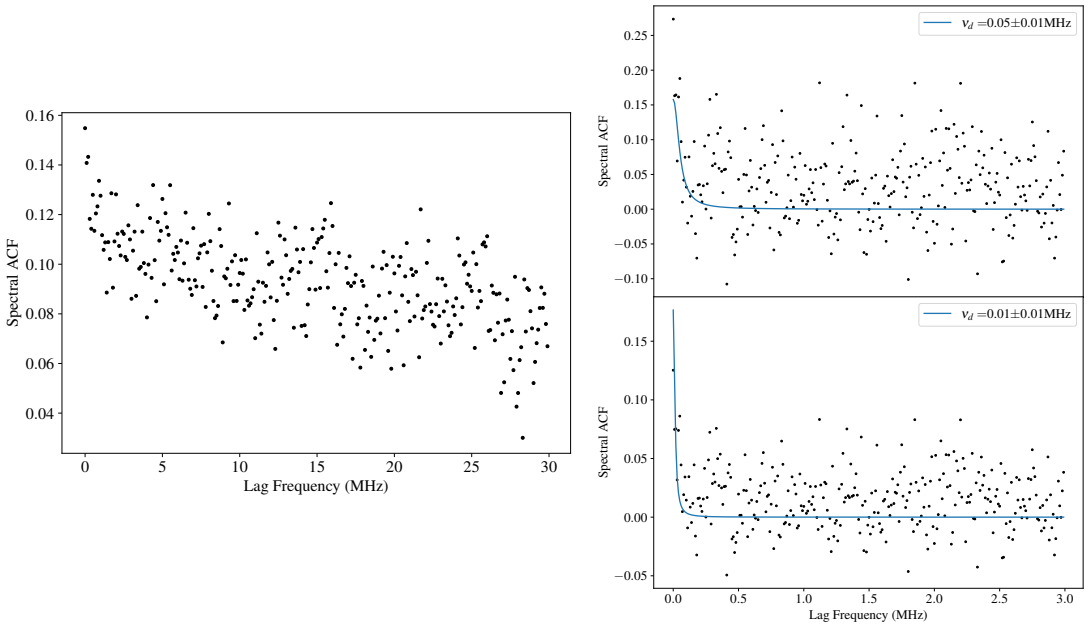

Figure C.8: Time-integrated spectral ACFs for FRB 20190102C, for which we found insufficient evidence to prove scintillation. *Left*: ACF over the full used bandwidth. *Right*: ACFs for the *top* and *bottom* sub-bands respectively.

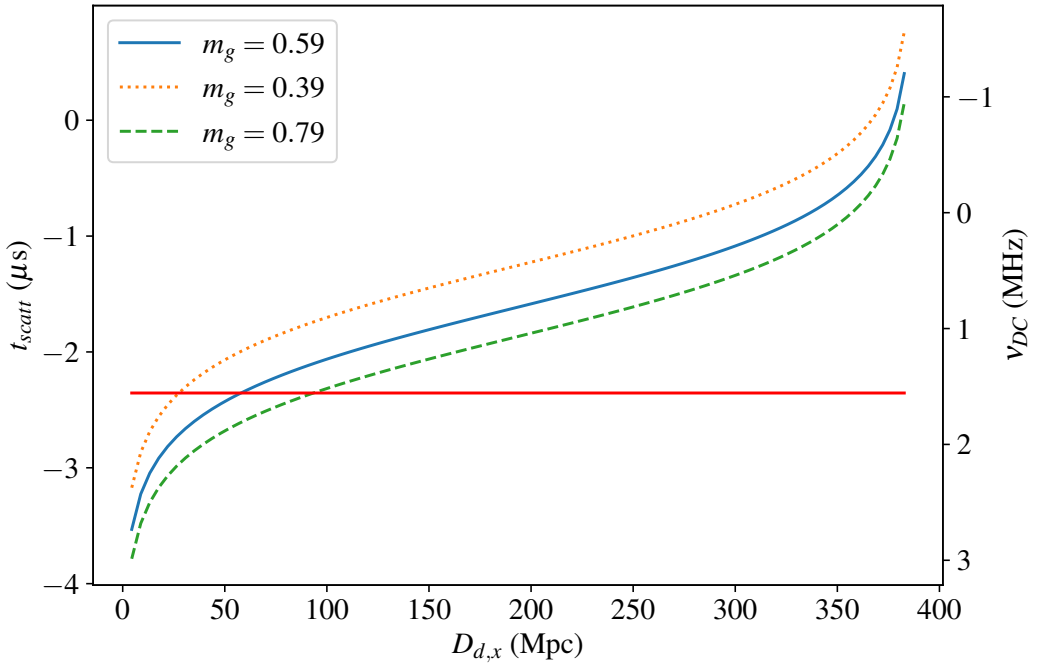

Figure C.9: Scattering timescale and corresponding decorrelation bandwidths (assuming $2\pi\nu_{DC}t_{\rm scatt} = 1$) contributed by a potential third IGM screen which would be responsible for suppressing the modulation of spectral scintillation in FRB 20201124A through angular broadening. The blue line corresponds to the calculation for the measured modulation index of $m_g = 0.59$, additional dotted and dashed lines display how the required scattering time changes with the modulation index. The red line displays the observed bandwidth of FRB 20201124A.

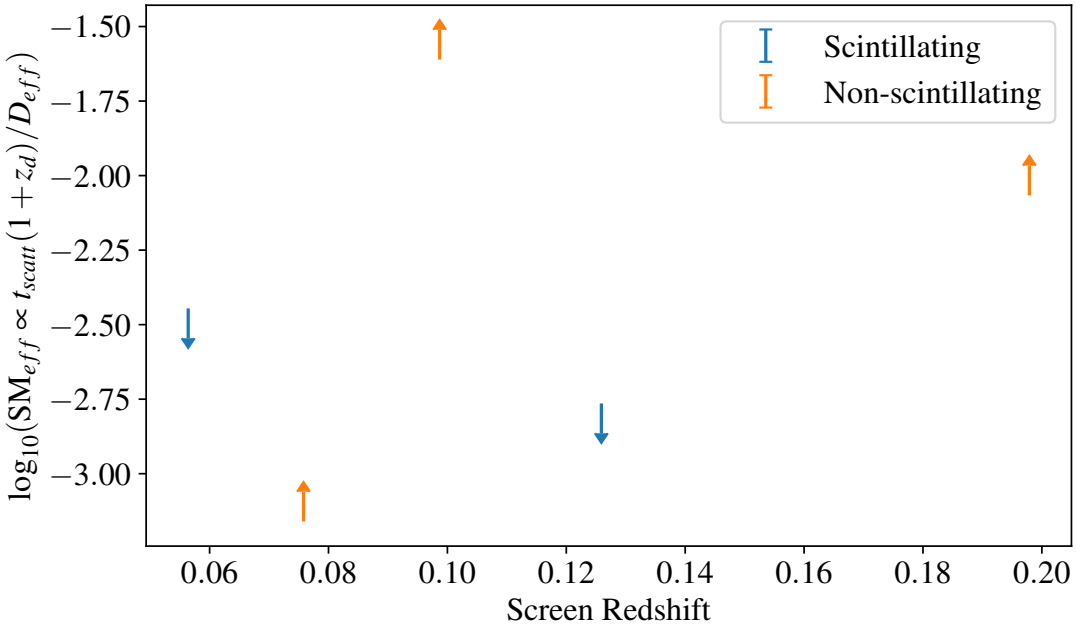

Figure C.10: Limits on values proportional to the effective scattering measure defined in Macquart & Koay (2013) from scintillating and non-scintillating FRBs as discussed in §7.5.1 and 7.5.2 and §7.5.5 respectively.

Appendix D

Copyright Information

AMERICAN ASTRONOMICAL SOCIETY

This agreement must be electronically signed before the American Astronomical Society (AAS) can publish your paper. In the event the article is not judged acceptable for publication in the journal you will be notified in writing and the copyright and all rights conferred by this agreement shall revert to you.

PUBLICATION AND TRANSFER OF COPYRIGHT AGREEMENT Manuscript number: AAS23144

Article title: First Constraints on Compact Dark Matter from Fast Radio Burst Microstructure

Names of authors: Mawson Sammons Jean-Pierre Macquart Ron Ekers Ryan Shannon Hyerin Cho Jason Prochaska Adam Deller Cherie Day

Author Rights: AAS grants to the author(s) (or their below-named employers, in the case of works made for hire) the following rights. All copies of the Article made under any of these rights shall include notice of the AAS copyright.

(1) All proprietary and statutory rights other than copyright, such as patent rights.

(2) The right after publication by the AAS to grant or refuse permission to third parties to republish all or part of the Article or a translation thereof. In the case of whole articles only, third parties must first obtain permission from the AAS before any right of further publication is granted. The AAS may choose to publish an abstract or portions of the Article before the AAS publishes it in a journal.

(3) The right to use all or part of the Article in future works and derivative works of their own of any type, and to make copies of all or part of the Article for the authors' use for educational or research purposes.

(4) In the case of a work made for hire, the right of the employer to make copies of the Article for the employer's internal use, but not for resale.

Copyright Assignment: Copyright in the Article is hereby transferred to the AAS for the full term of copyright throughout the world, effective as of date of acceptance of the Article for publication in a journal of the AAS. The copyright consists of all rights protected by copyright laws of the United States and of all foreign countries, in all languages and forms of communication, and includes all material to be published as part of the Article in any format or medium. The AAS shall have the right to register copyright to the Article in its name as claimant, whether separately or as part of the journal issue or other medium in which the Article is included and the right to sue, counterclaim, and recover for past, present and future infringement of the rights assigned under this agreement.

This Agreement shall be controlled, construed and enforced in accordance with the laws of the District of Columbia without reference to the conflict of laws provisions thereof. The Parties consent to jurisdiction of the state and federal courts located in the District of Columbia in connection with any proceeding related to this Agreement or its enforcement.

Authorized Signature: Mawson Sammons Date: 29/02/2020

Certification of Government Employment: An article prepared by a government officer or employee as part of his or her official duties may not be eligible for copyright, if the authors are all employed by one of the governments of Australia, Canada, New Zealand, the UK, or the US. If all the authors of the article are such government employees, one of the authors should sign here. If any of the authors is not such a government employee, do not sign in this box.

Authorized Signature:
Date:

RAS Journals - Author self-archiving policy

Author's original version

The author's original version is defined here as the un-refereed author version of an article that is considered by the author to be of sufficient quality to be submitted for formal peer review by a second party. The author accepts full responsibility for the article, which may have a version number or date stamp and the content and layout is set out by the author.

Prior to acceptance for publication in the journal, authors retain the right to make their original version of the article available on their own personal website and/or that of their employer and/or in free public servers of original version articles in their subject area, provided that, upon acceptance, they acknowledge that the article has been accepted for publication as follows:

This article has been accepted for publication in [Journal Title] *Published by Oxford University Press on behalf of the Royal Astronomical Society*.

Authors may replace their author's original version with the accepted manuscript or the version of record when their article is accepted for publication or upon publication in the journal (respectively). However, there is no obligation to do so and authors may continue to post their original version.

Accepted manuscript

The accepted manuscript is defined here as the final draft author manuscript, as accepted for publication by a journal, including modifications based on referees' suggestions, before it has undergone copyediting and proof correction.

Authors may upload a PDF of the accepted manuscript to institutional and/or centrally organized repositories and/or in

free public servers, upon acceptance for publication in the journal.

When uploading an accepted manuscript, authors should include the following acknowledgment with complete citation information as well as a link to the version of record once these are available. This will guarantee that the version of record is readily available to those accessing the article from public repositories, and means that the article is more likely to be cited correctly.

This is a pre-copyedited, author-produced PDF of an article accepted for publication in [insert journal title] *following peer review. The version of record* [insert complete citation information here] *is available online at: xxxxxxx* [insert URL that the author will receive upon publication here].

Version of record

The version of record is defined here as a fixed version of the journal article that has been made available by OUP by formally and exclusively declaring the article "published".

Authors may upload the version of record to institutional and/or centrally organized repositories and/or in free public servers, upon publication in the journal.

When uploading the version of record, authors should include a credit line and a link to the article on the OUP website. This will guarantee that the definitive version is readily available to those accessing your article from public repositories, and means that your article is more likely to be cited correctly.

Authors should include the following credit line when depositing the version of record.

This article has been accepted for publication in [Journal Title] ©: [year] [owner as specified on the article] *Published by Oxford University Press on behalf of the Royal Astronomical Society. All rights reserved.*

Appendix E

Co-Authorship Agreements

Below are the co-author responses to the originality statements included at the beginning of each chapter comprised of an accepted of submitted publication. The originality statements are also repeated here.

Chapter 5 is comprised of a pre-copyedited, author-produced version of an article accepted for publication in *The Astrophysical Journal* following peer review. The version of record: Mawson W. Sammons, Jean-Pierre Macquart, Ron D. Ekers, Ryan M. Shannon, Hyerin Cho, J. Xavier Prochaska, Adam T. Deller and Cherie K. Day, First Constraints on Compact Dark Matter from Fast Radio Burst Microstructure, *The Astrophysical Journal*, Volume 900, Issue 2, id. 122, December 2022, is available online at: https://doi.org/10.3847/1538-4357/aba7bb. This work was motivated and supervised by A/Prof. Jean-Pierre Macquart. Initial calibration and pre-processing of data, including PFB inversion and dedispersion, was performed by Prof. Adam Deller, Dr Cherie Day and Ms. Hyerin Cho. I performed all analyses of the processed data, making use of code written by Prof. J. Xavier Prochaska to evaluate Galactic intersection probabilities. Prof. Ron Ekers and A/Prof. Ryan Shannon motivated sections on clumpy dark matter. Apart from Figure 3, which was generated for publication by Ms. Hyerin Cho, the draft manuscript was written by me and distributed to co-authors for critique. All co-authors provided input over several iterations of feedback until

the manuscript was complete.

Chapter 6 is comprised of a pre-copyedited, author-produced version of an article accepted for publication in *Monthly Notices of the Royal Astronomical Society* following peer review. The version of record: Mawson W Sammons, C W James, C M Trott, M Walker, The effect of gravitational lensing on fast transient event rates, *Monthly Notices of the Royal Astronomical Society*, Volume 517, Issue 4, December 2022, Pages 5216–5231 is available online at: https://doi.org/10.1093/mnras/stac3013. Its contents are my own work, except for the input and supervision from Prof. Cathryn Trott, Dr. Clancy James and Dr. Mark Walker during the modelling of lensing probabilities and implementation of numerical integration routines. I wrote the draft of the paper and distributed copies to all co-authors for critique. All co-authors provided input over several iterations of feedback until the manuscript was complete.

Chapter 7 is comprised of a pre-copyedited, author-produced version of an article accepted for publication in *Monthly Notices of the Royal Astronomical Society* following peer review. The version of record: Mawson W Sammons, Adam T. Deller, Marcin Glowacki, Kelly Gourdji, C. W. James, J. Xavier Prochaska, Hao Qiu, Danica R. Scott, R. M. Shannon and C. M. Trott, Two-Screen Scattering in CRAFT FRBs, *Monthly Notices of the Royal Astronomical Society*, is available online at: https://doi.org/10.1093/mnras/stad2631. I motivated this work, which was supervised by Prof. Cathryn Trott and Dr Clancy James. A/Prof. Ryan Shannon contributed to the initial discovery of the FRBs used in the analysis. Initial calibration and pre-processing of data was performed by Ms. Danica R. Scott, Prof. Adam Deller, Dr Kelly Gourdji and Dr Marcin Glowacki. I performed all analyses of the processed data, making use of code written by Dr Hao Qiu to characterise burst morphology. Prof. J. Xavier Prochaska motivated additional extragalactic scattering constraints. The draft manuscript was written by me and distributed to co-authors for critique. All co-authors provided input over several iterations of feedback until the manuscript was complete.

Below are the signed statements from co-authors, acknowledging that they concur with the above statements.

International Centre for
Radio Astronomy Research

May 9, 2023

Mawson William Sammons
Email: mawson.sammons@postgrad.curtin.edu.au
1 Turner Ave
Bentley, WA, 6102, Australia

To whom it may concern,

I, Mawson William Sammons, have outlined my contributions and the contributions of co-authors to the chapters in this thesis that have been adapted from published or submitted papers (Chapter 5, "First Constraints on Compact Dark Matter from Fast Radio Burst Microstructure"; Chapter 6, "The effect of gravitational lensing on fast transient event rates"; and Chapter 7, "Two-Screen Scattering in CRAFT FRBs")

[redacted]

(Signature of candidate)

Cathryn Margaret Trott

(Full name of co-author)

[redacted]

(Signature of co-author)

International Centre for
Radio Astronomy Research

May 9, 2023

Mawson William Sammons
Email: mawson.sammons@postgrad.curtin.edu.au
1 Turner Ave
Bentley, WA, 6102, Australia

To whom it may concern,

I, Mawson William Sammons, have outlined my contributions and the contributions of co-authors to the chapters in this thesis that have been adapted from published or submitted papers (Chapter 5, "First Constraints on Compact Dark Matter from Fast Radio Burst Microstructure"; Chapter 6, "The effect of gravitational lensing on fast transient event rates"; and Chapter 7, "Two-Screen Scattering in CRAFT FRBs")

[redacted]

(Signature of candidate)

Clancy William James

(Full name of co-author)

[redacted]

(Signature of co-author)

International Centre for
Radio Astronomy Research

May 11, 2023

Mawson William Sammons
Email: mawson.sammons@postgrad.curtin.edu.au
1 Turner Ave
Bentley, WA, 6102, Australia

To whom it may concern,

I, Mawson William Sammons, have outlined my contributions and the contributions of co-authors to the chapters in this thesis that have been adapted from published or submitted papers (Chapter 5, "First Constraints on Compact Dark Matter from Fast Radio Burst Microstructure"; Chapter 6, "The effect of gravitational lensing on fast transient event rates"; and Chapter 7, "Two-Screen Scattering in CRAFT FRBs")

[redacted]

(Signature of candidate)

Hyerin Cho

(Full name of co-author)

[redacted]

(Signature of co-author)

International Centre for
Radio Astronomy Research

May 11, 2023

Mawson William Sammons
Email: mawson.sammons@postgrad.curtin.edu.au
1 Turner Ave
Bentley, WA, 6102, Australia

To whom it may concern,

I, Mawson William Sammons, have outlined my contributions and the contributions of co-authors to the chapters in this thesis that have been adapted from published or submitted papers (Chapter 5, "First Constraints on Compact Dark Matter from Fast Radio Burst Microstructure"; Chapter 6, "The effect of gravitational lensing on fast transient event rates"; and Chapter 7, "Two-Screen Scattering in CRAFT FRBs")

[redacted]

(Signature of candidate)

Danica Scott

(Full name of co-author)

[redacted]

(Signature of co-author)

International Centre for
Radio Astronomy Research

May 11, 2023

Mawson William Sammons
Email: mawson.sammons@postgrad.curtin.edu.au
1 Turner Ave
Bentley, WA, 6102, Australia

To whom it may concern,

I, Mawson William Sammons, have outlined my contributions and the contributions of co-authors to the chapters in this thesis that have been adapted from published or submitted papers (Chapter 5, "First Constraints on Compact Dark Matter from Fast Radio Burst Microstructure"; Chapter 6, "The effect of gravitational lensing on fast transient event rates"; and Chapter 7, "Two-Screen Scattering in CRAFT FRBs")

[redacted]

(Signature of candidate)

Kelly Gourdji

(Full name of co-author)

[redacted]

(Signature of co-author)

International Centre for
Radio Astronomy Research

May 11, 2023

Mawson William Sammons
Email: mawson.sammons@postgrad.curtin.edu.au
1 Turner Ave
Bentley, WA, 6102, Australia

To whom it may concern,

I, Mawson William Sammons, have outlined my contributions and the contributions of co-authors to the chapters in this thesis that have been adapted from published or submitted papers (Chapter 5, "First Constraints on Compact Dark Matter from Fast Radio Burst Microstructure"; Chapter 6, "The effect of gravitational lensing on fast transient event rates"; and Chapter 7, "Two-Screen Scattering in CRAFT FRBs")

[redacted]

(Signature of candidate)

Cherie Day

(Full name of co-author)

[redacted]

(Signature of co-author)

International Centre for
Radio Astronomy Research

May 11, 2023

Mawson William Sammons
Email: mawson.sammons@postgrad.curtin.edu.au
1 Turner Ave
Bentley, WA, 6102, Australia

To whom it may concern,

I, Mawson William Sammons, have outlined my contributions and the contributions of co-authors to the chapters in this thesis that have been adapted from published or submitted papers (Chapter 5, "First Constraints on Compact Dark Matter from Fast Radio Burst Microstructure"; Chapter 6, "The effect of gravitational lensing on fast transient event rates"; and Chapter 7, "Two-Screen Scattering in CRAFT FRBs")

[redacted]

(Signature of candidate)

MARK ANDREW WALKER

(Full name of co-author)

[redacted]

(Signature of co-author)

International Centre for
Radio Astronomy Research

May 11, 2023

Mawson William Sammons
Email: mawson.sammons@postgrad.curtin.edu.au
1 Turner Ave
Bentley, WA, 6102, Australia

To whom it may concern,

I, Mawson William Sammons, have outlined my contributions and the contributions of co-authors to the chapters in this thesis that have been adapted from published or submitted papers (Chapter 5, "First Constraints on Compact Dark Matter from Fast Radio Burst Microstructure"; Chapter 6, "The effect of gravitational lensing on fast transient event rates"; and Chapter 7, "Two-Screen Scattering in CRAFT FRBs")

[redacted]

(Signature of candidate)

Marcin Glowacki

(Full name of co-author)

[redacted]

(Signature of co-author)

International Centre for
Radio Astronomy Research

May 11, 2023

Mawson William Sammons
Email: mawson.sammons@postgrad.curtin.edu.au
1 Turner Ave
Bentley, WA, 6102, Australia

To whom it may concern,

I, Mawson William Sammons, have outlined my contributions and the contributions of co-authors to the chapters in this thesis that have been adapted from published or submitted papers (Chapter 5, "First Constraints on Compact Dark Matter from Fast Radio Burst Microstructure"; Chapter 6, "The effect of gravitational lensing on fast transient event rates"; and Chapter 7, "Two-Screen Scattering in CRAFT FRBs")

[redacted]

(Signature of candidate)

Prof. Adam Deller

(Full name of co-author)

[redacted]

(Signature of co-author)

International Centre for
Radio Astronomy Research

May 11, 2023

Mawson William Sammons
Email: mawson.sammons@postgrad.curtin.edu.au
1 Turner Ave
Bentley, WA, 6102, Australia

To whom it may concern,

I, Mawson William Sammons, have outlined my contributions and the contributions of co-authors to the chapters in this thesis that have been adapted from published or submitted papers (Chapter 5, "First Constraints on Compact Dark Matter from Fast Radio Burst Microstructure"; Chapter 6, "The effect of gravitational lensing on fast transient event rates"; and Chapter 7, "Two-Screen Scattering in CRAFT FRBs")

[redacted]

(Signature of candidate)

Hao Qiu

(Full name of co-author)

[redacted]

(Signature of co-author)

International Centre for
Radio Astronomy Research

May 11, 2023

Mawson William Sammons
Email: mawson.sammons@postgrad.curtin.edu.au
1 Turner Ave
Bentley, WA, 6102, Australia

To whom it may concern,

I, Mawson William Sammons, have outlined my contributions and the contributions of co-authors to the chapters in this thesis that have been adapted from published or submitted papers (Chapter 5, "First Constraints on Compact Dark Matter from Fast Radio Burst Microstructure"; Chapter 6, "The effect of gravitational lensing on fast transient event rates"; and Chapter 7, "Two-Screen Scattering in CRAFT FRBs")

[redacted]

(Signature of candidate)

Ronald D Ekers

(Full name of co-author)

[redacted]

(Signature of co-author)

International Centre for
Radio Astronomy Research

May 11, 2023

Mawson William Sammons
Email: mawson.sammons@postgrad.curtin.edu.au
1 Turner Ave
Bentley, WA, 6102, Australia

To whom it may concern,

I, Mawson William Sammons, have outlined my contributions and the contributions of co-authors to the chapters in this thesis that have been adapted from published or submitted papers (Chapter 5, "First Constraints on Compact Dark Matter from Fast Radio Burst Microstructure"; Chapter 6, "The effect of gravitational lensing on fast transient event rates"; and Chapter 7, "Two-Screen Scattering in CRAFT FRBs")

[redacted]

(Signature of candidate)

Ryan M. Shannon

(Full name of co-author)

[redacted]

(Signature of co-author)

International Centre for
Radio Astronomy Research

May 11, 2023

Mawson William Sammons
Email: mawson.sammons@postgrad.curtin.edu.au
1 Turner Ave
Bentley, WA, 6102, Australia

To whom it may concern,

I, Mawson William Sammons, have outlined my contributions and the contributions of co-authors to the chapters in this thesis that have been adapted from published or submitted papers (Chapter 5, "First Constraints on Compact Dark Matter from Fast Radio Burst Microstructure"; Chapter 6, "The effect of gravitational lensing on fast transient event rates"; and Chapter 7, "Two-Screen Scattering in CRAFT FRBs")

(Signature of candidate)

J. Xavier Prochaska

(Full name of co-author) (Signature of co-author)

Bibliography

B. P. Abbott, et al. (2017). 'Gravitational Waves and Gamma-Rays from a Binary Neutron Star Merger: GW170817 and GRB 170817A'. *The Astrophysical Journal* **848**(2):L13. Publisher: American Astronomical Society.

T. M. C. Abbott, et al. (2019). 'First Cosmology Results using Type Ia Supernovae from the Dark Energy Survey: Constraints on Cosmological Parameters'. *The Astrophysical Journal Letters* **872**(2):L30. Publisher: The American Astronomical Society.

N. J. Adams, et al. (2023). 'Discovery and properties of ultra-high redshift galaxies ($9 < z < 12$) in the JWST ERO SMACS 0723 Field'. *Monthly Notices of the Royal Astronomical Society* **518**:4755–4766. ADS Bibcode: 2023MNRAS.518.4755A.

P. a. R. Ade, et al. (2014). 'Planck 2013 results. I. Overview of products and scientific results'. *Astronomy & Astrophysics* **571**:A1. Publisher: EDP Sciences.

C. Alcock, et al. (1997). 'The Macho Project: 45 Candidate Microlensing Events from the First Year Galactic Bulge Data'. *The Astrophysical Journal* **479**(1):119.

R. A. Alpher, et al. (1948). 'The Origin of Chemical Elements'. *Physical Review* **73**(7):803–804. Publisher: American Physical Society.

P. K. Aluri, et al. (2023). 'Is the observable Universe consistent with the cosmo-

logical principle?'. *Classical and Quantum Gravity* **40**(9):094001. Publisher: IOP Publishing.

R. Anna-Thomas, et al. (2022). 'A Highly Variable Magnetized Environment in a Fast Radio Burst Source'. Number: arXiv:2202.11112 arXiv:2202.11112 [astro-ph].

J. W. Armstrong, et al. (1981). 'Density power spectrum in the local interstellar medium'. *Nature* **291**(5816):561–564. Number: 5816 Publisher: Nature Publishing Group.

J. W. Armstrong, et al. (1995). 'Electron density power spectrum in the local interstellar medium'. *The Astrophysical Journal* **443**:209–221.

P. Atri, et al. (2019). 'Potential Kick Velocity distribution of black hole X-ray binaries and implications for natal kicks'. *arXiv:1908.07199 [astro-ph]* arXiv: 1908.07199.

D. Band, et al. (1993). 'BATSE Observations of Gamma-Ray Burst Spectra. I. Spectral Diversity'. *The Astrophysical Journal* **413**:281. ADS Bibcode: 1993ApJ...413..281B.

S. Banerjee, et al. (2021). 'Differential Source Count for Gamma-Ray Bursts'. *The Astrophysical Journal* **921**(1):79. Publisher: IOP Publishing.

K. Bannister, et al. (2017). 'The detection of an extremely bright fast radio burst in a phased array feed survey'. *The Astrophysical Journal* **841**(1):L12. arXiv: 1705.07581.

K. Bannister, et al. (2019a). 'FREDDA: A fast, real-time engine for de-dispersing amplitudes'. *Astrophysics Source Code Library* p. ascl:1906.003. ADS Bibcode: 2019ascl.soft06003B.

K. W. Bannister (2018). 'Australia's game-changing fast radio burst hunter'. *Nature Astronomy* **2**(11):922–922. Number: 11 Publisher: Nature Publishing Group.

K. W. Bannister, et al. (2019b). 'A single fast radio burst localized to a massive galaxy at cosmological distance'. *Science* **365**(6453):565–570.

N. Bartel, et al. (2022). 'Electron Density Variations in the Interstellar Medium and the Average Frequency Profile of a Scintle from Pulsar Scintillation Spectra'. *The Astrophysical Journal* **941**(2):112. Publisher: The American Astronomical Society.

M. Bartelmann (1996). 'Arcs from a Universal Dark-Matter Halo Profile'. *arXiv:astro-ph/9602053* arXiv: astro-ph/9602053.

M. Bartelmann & P. Schneider (2001). 'Weak gravitational lensing'. *Physics Reports* **340**(4):291–472.

S. D. Barthelmy, et al. (2005). 'The Burst Alert Telescope (BAT) on the SWIFT Midex Mission'. *Space Science Reviews* **120**(3):143–164.

G. Battaglia, et al. (2005). 'The radial velocity dispersion profile of the Galactic halo: constraining the density profile of the dark halo of the Milky Way'. *Monthly Notices of the Royal Astronomical Society* **364**(2):433–442.

P. M. Bellan (2006). 'Cold plasma waves in a magnetized plasma'. In *Fundamentals of Plasma Physics*, pp. 206–241. Cambridge University Press, Cambridge.

A. M. Beloborodov (2017). 'A Flaring Magnetar in FRB 121102?'. *The Astrophysical Journal Letters* **843**(2):L26. Publisher: The American Astronomical Society.

C. L. Bennett, et al. (2013). 'Nine-year Wilkinson Microwave Anisotropy Probe (WMAP) Observations: Final Maps and Results'. *The Astrophysical Journal Supplement Series* **208**(2):20.

D. P. Bennett (1993). 'The First Data from the MACHO Experiment'. *Annals of the New York Academy of Sciences* **688**(1):612–618. arXiv: astro-ph/9304014.

L. Bergström, et al. (2000). 'Lensing effects in an inhomogeneous universe'. *Astronomy and Astrophysics* **358**:13–29.

G. Bertone, et al. (2005). 'Particle Dark Matter: Evidence, Candidates and Constraints'. *Physics Reports* **405**(5-6):279–390. arXiv: hep-ph/0404175.

S. Bhandari, et al. (2018). 'The SUrvey for Pulsars and Extragalactic Radio Bursts – II. New FRB discoveries and their follow-up'. *Monthly Notices of the Royal Astronomical Society* **475**(2):1427–1446.

S. Bhandari, et al. (2020). 'The host galaxies and progenitors of Fast Radio Bursts localized with the Australian Square Kilometre Array Pathfinder'. *The Astrophysical Journal* **895**(2):L37. arXiv: 2005.13160.

N. D. R. Bhat, et al. (2004). 'Multifrequency Observations of Radio Pulse Broadening and Constraints on Interstellar Electron Density Microstructure'. *The Astrophysical Journal* **605**(2):759. Publisher: IOP Publishing.

N. D. R. Bhat, et al. (1999). 'Long-Term Scintillation Studies of Pulsars. I. Observations and Basic Results'. *The Astrophysical Journal Supplement Series* **121**(2):483. Publisher: IOP Publishing.

S. Bird, et al. (2016). 'Did LIGO Detect Dark Matter?'. *Physical Review Letters* **116**(20):201301.

C. D. Bochenek, et al. (2020). 'A fast radio burst associated with a Galactic magnetar'. *arXiv e-prints* **2005**:arXiv:2005.10828.

P. Bode, et al. (2001). 'Halo Formation in Warm Dark Matter Models'. *The Astrophysical Journal* **556**:93–107. ADS Bibcode: 2001ApJ...556...93B.

M. Born & E. Wolf (2013). *Principles of Optics: Electromagnetic Theory of Propagation, Interference and Diffraction of Light*. Elsevier.

A. Bosma (1981). '21-cm line studies of spiral galaxies. II. The distribution and kinematics of neutral hydrogen in spiral galaxies of various morphological types.'. *The Astronomical Journal* **86**:1825–1846. ADS Bibcode: 1981AJ.....86.1825B.

M. Boudaud & M. Cirelli (2019). 'Voyager 1 ${e}ˆ{\ifmmode\pm\else\textpm\fi{}}$ Further Constrain Primordial Black Holes as Dark Matter'. *Physical Review Letters* **122**(4):041104. Publisher: American Physical Society.

T. D. Brandt (2016). 'Constraints on MACHO Dark Matter in Compact Stellar Systems in Ultra-Faint Dwarf Galaxies'. *The Astrophysical Journal* **824**(2):L31.

M.-A. Breton & P. Fleury (2020). 'Theoretical and numerical perspectives on cosmic distance averages'. *arXiv:2012.07802 [astro-ph, physics:gr-qc]* arXiv: 2012.07802.

W. F. Brisken, et al. (2010). '100 uas resolution VLBI imaging of Anisotropic Interstellar Scattering Toward Pulsar B0834+06'. *The Astrophysical Journal* **708**(1):232. Publisher: The American Astronomical Society.

J. S. Bullock & M. Boylan-Kolchin (2017). 'Small-Scale Challenges to the ΛCDM Paradigm'. *Annual Review of Astronomy and Astrophysics* **55**(1):343–387. arXiv: 1707.04256.

B. Carr & F. Kühnel (2020). 'Primordial Black Holes as Dark Matter: Recent Developments'. *Annual Review of Nuclear and Particle Science* **70**:355–394.

B. Carr, et al. (2016). 'Primordial black holes as dark matter'. *Physical Review D* **94**:083504.

B. J. Carr & S. W. Hawking (1974). 'Black Holes in the Early Universe'. *Monthly Notices of the Royal Astronomical Society* **168**(2):399–415.

B. J. Carr, et al. (2010). 'New cosmological constraints on primordial black holes'. *Physical Review D* **81**(10):104019. Publisher: American Physical Society.

S. M. Carroll, et al. (1992). 'The cosmological constant'. *Annual Review of Astronomy and Astrophysics* **30**:499–542.

S. Chatterjee (2021). 'Fast radio bursts'. *Astronomy & Geophysics* **62**(1):1.29–1.35.

S. Chatterjee, et al. (2017). 'A direct localization of a fast radio burst and its host'. *Nature* **541**:58–61. ADS Bibcode: 2017Natur.541...58C.

P. Chawla, et al. (2022). 'Modeling Fast Radio Burst Dispersion and Scattering Properties in the First CHIME/FRB Catalog'. *The Astrophysical Journal* **927**(1):35. Publisher: The American Astronomical Society.

A. Chepurnov & A. Lazarian (2010). 'Extending the Big Power in the Sky With Turbulence Spectra From Wisconsin Halpha Mapper Data'. *The Astrophysical Journal* **710**(1):853. Publisher: The American Astronomical Society.

J. S. Chittidi, et al. (2021). 'Dissecting the Local Environment of FRB 190608 in the Spiral Arm of its Host Galaxy'. *The Astrophysical Journal* **922**(2):173. Publisher: American Astronomical Society.

H. Cho, et al. (2020). 'Spectropolarimetric Analysis of FRB 181112 at Microsecond Resolution: Implications for Fast Radio Burst Emission Mechanism'. *The Astrophysical Journal* **891**(2):L38. Publisher: American Astronomical Society.

C. Clarkson, et al. (2012). '(Mis)interpreting supernovae observations in a lumpy universe'. *Monthly Notices of the Royal Astronomical Society* **426**:1121–1136.

A. W. Clegg, et al. (1998). 'The Gaussian Plasma Lens in Astrophysics: Refraction'. *The Astrophysical Journal* **496**(1):253–266.

S. Clesse & J. García-Bellido (2017). 'The clustering of massive Primordial Black Holes as Dark Matter: measuring their mass distribution with Advanced LIGO'. *Physics of the Dark Universe* **15**:142–147. arXiv: 1603.05234.

D. Clowe, et al. (2004). 'Weak-Lensing Mass Reconstruction of the Interacting Cluster 1E 0657–558: Direct Evidence for the Existence of Dark Matter*'. *The Astrophysical Journal* **604**(2):596. Publisher: IOP Publishing.

J. Colin, et al. (2017). 'High-redshift radio galaxies and divergence from the CMB dipole'. *Monthly Notices of the Royal Astronomical Society* **471**(1):1045–1055.

M. Colpi, et al. (1999). 'Period Clustering of the Anomalous X-Ray Pulsars and Magnetic Field Decay in Magnetars'. *The Astrophysical Journal* **529**(1):L29. Publisher: IOP Publishing.

J. J. Condon (1988). 'Radio Sources and Cosmology'. In G. L. Verschuur & K. I. Kellermann (eds.), *Galactic and Extragalactic Radio Astronomy*, Astronomy and Astrophysics Library, pp. 641–678. Springer, New York, NY.

L. Connor (2019). 'Interpreting the distributions of FRB observables'. *Monthly Notices of the Royal Astronomical Society* **487**(4):5753–5763.

L. Connor & V. Ravi (2022). 'Stellar prospects for FRB gravitational lensing'. arXiv:2206.14310 [astro-ph].

L. Connor, et al. (2023). 'Deep Synoptic Array science: Two fast radio burst sources in massive galaxy clusters'. arXiv:2302.14788 [astro-ph].

L. Connor, et al. (2020). 'A bright, high rotation-measure FRB that skewers the M33 halo'. *Monthly Notices of the Royal Astronomical Society* **499**(4):4716–4724.

R. J. Cooke, et al. (2018). 'One Percent Determination of the Primordial Deuterium Abundance*'. *The Astrophysical Journal* **855**(2):102. Publisher: The American Astronomical Society.

J. Cordes & T. Lazio (1991). 'Interstellar Scattering Effects on the Detection of Narrow-Band Signals'. *ApJ* **376**:123.

J. M. Cordes & S. Chatterjee (2019). 'Fast Radio Bursts: An Extragalactic Enigma'. *Annual Review of Astronomy and Astrophysics* **57**(1):417–465. _eprint: https://doi.org/10.1146/annurev-astro-091918-104501.

J. M. Cordes & T. J. W. Lazio (2001). 'Anomalous Radio-Wave Scattering from Interstellar Plasma Structures'. *The Astrophysical Journal* **549**(2):997. Publisher: IOP Publishing.

J. M. Cordes & T. J. W. Lazio (2003). 'NE2001.I. A New Model for the Galactic Distribution of Free Electrons and its Fluctuations'. arXiv:astro-ph/0207156.

J. M. Cordes, et al. (2022). 'Redshift Estimation and Constraints on Intergalactic and Interstellar Media from Dispersion and Scattering of Fast Radio Bursts'. *The Astrophysical Journal* **931**:88. ADS Bibcode: 2022ApJ...931...88C.

J. M. Cordes & B. J. Rickett (1998). 'Diffractive Interstellar Scintillation Timescales and Velocities'. *The Astrophysical Journal* **507**:846–860. ADS Bibcode: 1998ApJ...507..846C.

J. M. Cordes, et al. (2017). 'Lensing of Fast Radio Bursts by Plasma Structures in Host Galaxies'. *The Astrophysical Journal* **842**(1):35. Publisher: The American Astronomical Society.

J. M. Cordes, et al. (1990). 'Timing and Scintillations of the Millisecond Pulsar 1937+214'. *The Astrophysical Journal* **349**:245. ADS Bibcode: 1990ApJ...349..245C.

R. Courant, et al. (1924). *Methoden der mathematischen Physik*. Springer, Berlin Heidelberg, 4. aufl. 1993. softcover reprint of the original 4th ed. 1993 edition edn.

D. Coward, et al. (2013). 'The Swift Gamma-Ray Burst redshift distribution: selection biases and optical brightness evolution at high-z?'. *Monthly Notices of the Royal Astronomical Society* **432**(3):2141–2149. arXiv: 1210.2488.

D. F. Crawford, et al. (1970). 'Maximum-Likelihood Estimation of the Slope from Number-Flux Counts of Radio Sources'. *The Astrophysical Journal* **162**:405. ADS Bibcode: 1970ApJ...162..405C.

H. T. Cromartie, et al. (2020). 'Relativistic Shapiro delay measurements of an extremely massive millisecond pulsar'. *Nature Astronomy* **4**(1):72–76. arXiv: 1904.06759.

D. Croon, et al. (2020). 'Subaru-HSC through a different lens: Microlensing by extended dark matter structures'. *Physical Review D* **102**(8):083021. Publisher: American Physical Society.

A. Cucchiara, et al. (2011). 'A Photometric Redshift of z ˜ 9.4 for GRB 090429B'. *The Astrophysical Journal* **736**(1):7. Publisher: The American Astronomical Society.

T. Dahlén & C. Fransson (1999). 'Rates and redshift distributions of high-z supernovae'. *Astronomy and Astrophysics* **350**:349–367. ADS Bibcode: 1999A&A...350..349D.

L. Dam, et al. (2023). 'Testing the cosmological principle with CatWISE quasars: a bayesian analysis of the number-count dipole'. *Monthly Notices of the Royal Astronomical Society* **525**(1):231–245.

Dark Energy Survey Collaboration 1, et al. (2018). 'Dark Energy Survey year 1 results: Cosmological constraints from galaxy clustering and weak lensing'. *Physical Review D* **98**(4):043526. Publisher: American Physical Society.

P. D'Avanzo (2015). 'Short gamma-ray bursts: A review'. *Journal of High Energy Astrophysics* **7**:73–80.

K. Davidson & Y. Terzian (1969). 'Dispersion Measures of Pulsars'. *The Astronomical Journal* **74**:849. ADS Bibcode: 1969AJ.....74..849D.

M. Davis, et al. (1985). 'The evolution of large-scale structure in a universe dominated by cold dark matter'. *The Astrophysical Journal* **292**:371–394. ADS Bibcode: 1985ApJ...292..371D.

C. K. Day, et al. (2021). 'Astrometric accuracy of snapshot fast radio burst localisations with ASKAP'. *Publications of the Astronomical Society of Australia* **38**:e050. Publisher: Cambridge University Press.

C. K. Day, et al. (2020). 'High time resolution and polarisation properties of ASKAP-localised fast radio bursts'. *arXiv:2005.13162 [astro-ph]* arXiv: 2005.13162.

A. Dekel (1983). 'Superclusters as nondissipative pancakes : flattening'. *The Astrophysical Journal* **264**:373–391. ADS Bibcode: 1983ApJ...264..373D.

A. Dekel, et al. (1984). 'Alignments of clusters of galaxies as a probe for superclusters.'. *The Astrophysical Journal* **279**:1–12. ADS Bibcode: 1984ApJ...279....1D.

A. Del Popolo & M. Le Delliou (2021). 'Review of Solutions to the Cusp-Core Problem of the ΛCDM Model'. *Galaxies* **9**(4):123. Number: 4 Publisher: Multidisciplinary Digital Publishing Institute.

J. M. Dickey, et al. (2001). 'Southern Galactic Plane Survey Measurements of the Spatial Power Spectrum of Interstellar H I in the Inner Galaxy'. *The Astrophysical Journal* **561**(1):264. Publisher: IOP Publishing.

J. M. Diego, et al. (2018). 'Dark Matter under the Microscope: Constraining Compact Dark Matter with Caustic Crossing Events'. *The Astrophysical Journal* **857**(1):25. Publisher: The American Astronomical Society.

F. W. Dyson, et al. (1920). 'IX. A determination of the deflection of light by the sun's gravitational field, from observations made at the total eclipse of May 29,

1919'. *Philosophical Transactions of the Royal Society of London. Series A, Containing Papers of a Mathematical or Physical Character* **220**(571-581):291–333. Publisher: Royal Society.

J. Ehlers & P. Schneider (1986). 'Self-consistent probabilities for gravitational lensing in inhomogeneous universes'. *Astronomy and Astrophysics* **168**:57–61.

D. Eichler (2017). 'Nanolensed Fast Radio Bursts'. *The Astrophysical Journal* **850**(2):159.

A. Einstein (1916). 'Die Grundlage der allgemeinen Relativitätstheorie'. *Annalen der Physik* **354**:769–822. ADS Bibcode: 1916AnP...354..769E.

D. J. Eisenstein, et al. (2005). 'Detection of the Baryon Acoustic Peak in the Large-Scale Correlation Function of SDSS Luminous Red Galaxies'. *The Astrophysical Journal* **633**(2):560. Publisher: IOP Publishing.

G. F. R. Ellis & J. E. Baldwin (1984). 'On the expected anisotropy of radio source counts'. *Monthly Notices of the Royal Astronomical Society* **206**(2):377–381.

G. F. R. Ellis & M. Bruni (1989). 'Covariant and gauge-invariant approach to cosmological density fluctuations'. *Physical Review D* **40**(6):1804–1818. Publisher: American Physical Society.

X. Er & S. Mao (2014). 'Effects of plasma on gravitational lensing'. *Monthly Notices of the Royal Astronomical Society* **437**(3):2180–2186.

X. Er & S. Mao (2022). 'The effects of plasma on the magnification and time delay of strongly lensed fast radio bursts'. *Monthly Notices of the Royal Astronomical Society* p. stac2323. arXiv:2208.08208 [astro-ph].

I. M. H. Etherington (1933). 'LX. On the definition of distance in general relativity'. *The London, Edinburgh, and Dublin Philosophical Magazine and Journal of Science* **15**(100):761–773. Publisher: Taylor & Francis _eprint: https://doi.org/10.1080/14786443309462220.

Event Horizon Telescope Collaboration, et al. (2019). 'First M87 Event Horizon Telescope Results. I. The Shadow of the Supermassive Black Hole'. *The Astrophysical Journal* **875**:L1. ADS Bibcode: 2019ApJ...875L...1E.

W. Farah (2020). 'private communication'.

W. Farah, et al. (2018). 'FRB microstructure revealed by the real-time detection of FRB170827'. *Monthly Notices of the Royal Astronomical Society* **478**(1):1209–1217.

J. Feldbrugge, et al. (2019). 'Oscillatory path integrals for radio astronomy'. arXiv:1909.04632 [astro-ph, physics:gr-qc, physics:hep-th, physics:quant-ph].

D. P. Finkbeiner (2003). 'A Full-Sky Ha Template for Microwave Foreground Prediction'. *The Astrophysical Journal Supplement Series* **146**(2):407. Publisher: IOP Publishing.

R. E. Firth, et al. (2015). 'The Rising Light Curves of Type Ia Supernovae'. *Monthly Notices of the Royal Astronomical Society* **446**(4):3895–3910. arXiv: 1411.1064.

M. Fishbach, et al. (2018). 'Does the Black Hole Merger Rate Evolve with Redshift?'. *The Astrophysical Journal Letters* **863**(2):L41. Publisher: The American Astronomical Society.

D. J. Fixsen, et al. (1996). 'The Cosmic Microwave Background Spectrum from the Full COBE* FIRAS Data Set'. *The Astrophysical Journal* **473**(2):576.

P. Fleury (2014). 'Swiss-cheese models and the Dyer-Roeder approximation'. *Journal of Cosmology and Astroparticle Physics* **2014**(06):054–054. arXiv: 1402.3123.

P. Fleury, et al. (2013). 'Interpretation of the Hubble diagram in a nonhomogeneous universe'. *Physical Review D* **87**(12):123526. arXiv: 1302.5308.

P. Fleury & J. García-Bellido (2020). 'On simple analytic models of microlensing amplification statistics'. *Physics of the Dark Universe* **29**:100567. arXiv: 1907.05163.

P. Fleury, et al. (2015). 'The theory of stochastic cosmological lensing'. *Journal of Cosmology and Astroparticle Physics* **2015**(11):022.

P. Fleury, et al. (2017). 'Weak Gravitational Lensing of Finite Beams'. *Physical Review Letters* **119**(19):191101. Publisher: American Physical Society.

P. Fleury, et al. (2019). 'Cosmic convergence and shear with extended sources'. *Physical Review D* **99**(2):023525. Publisher: American Physical Society.

R. A. Flores & J. R. Primack (1994). 'Observational and Theoretical Constraints on Singular Dark Matter Halos'. *The Astrophysical Journal* **427**:L1. ADS Bibcode: 1994ApJ...427L...1F.

D. D. Frederiks, et al. (2013). 'The ultraluminous GRB 110918A'. *The Astrophysical Journal* **779**(2):151. arXiv: 1311.5734.

C. S. Frenk, et al. (1983). 'Nonlinear evolution of large-scale structure in the universe'. *The Astrophysical Journal* **271**:417–430. ADS Bibcode: 1983ApJ...271..417F.

F. Frontera, et al. (2000). 'Prompt and Delayed Emission Properties of Gamma-Ray Bursts Observed with BeppoSAX'. *The Astrophysical Journal Supplement Series* **127**:59–78. ADS Bibcode: 2000ApJS..127...59F.

M. Fukugita & P. J. E. Peebles (2004). 'The Cosmic Energy Inventory'. *The Astrophysical Journal* **616**(2):643–668.

J. Garcia-Bellido, et al. (2017). 'LIGO Lo(g)Normal MACHO: Primordial Black Holes survive SN lensing constraints'. *arXiv:1712.06574 [astro-ph, physics:gr-qc, physics:hep-ph]* arXiv: 1712.06574.

J. Garriga, et al. (2016). 'Black holes and the multiverse'. *Journal of Cosmology and Astroparticle Physics* **2016**:064–064. ADS Bibcode: 2016JCAP...02..064G.

N. Gehrels, et al. (2009). 'Gamma-Ray Bursts in the Swift Era'. *Annual Review of Astronomy and Astrophysics* **47**:567–617.

E. S. Giesel, et al. (2023). 'Etherington duality breaking: gravitational lensing in non-metric space–times versus intrinsic alignments'. *Monthly Notices of the Royal Astronomical Society* **518**(4):5490–5499.

G. Grillo & J. Cordes (2018). 'Wave asymptotics and their application to astrophysical plasma lensing'. arXiv:1810.09058 [astro-ph].

V. Gupta, et al. (2022). 'The ultranarrow FRB20191107B, and the origins of FRB scattering'. *Monthly Notices of the Royal Astronomical Society* **514**(4):5866–5878.

S. Hagstotz, et al. (2022). 'A new measurement of the Hubble constant using fast radio bursts'. *Monthly Notices of the Royal Astronomical Society* **511**(1):662–667.

M. Hallbäck, et al. (1996). 'The Basics of Turbulence Modelling'. In M. Hallbäck, D. S. Henningson, A. V. Johansson, & P. H. Alfredsson (eds.), *Turbulence and Transition Modelling: Lecture Notes from the ERCOFTAC/IUTAM Summerschool held in Stockholm, 12–20 June, 1995*, Series, pp. 81–154. Springer Netherlands, Dordrecht.

G. Hallinan, et al. (2021). 'The DSA-2000: A Radio Survey Camera'. *Bulletin of the AAS* **53**(1).

E. Harrison (1993). 'The Redshift-Distance and Velocity-Distance Laws'. *The Astrophysical Journal* **403**:28. ADS Bibcode: 1993ApJ...403...28H.

S. Hawking (1971). 'Gravitationally Collapsed Objects of Very Low Mass'. *Monthly Notices of the Royal Astronomical Society* **152**(1):75–78.

S. W. Hawking (1974). 'Black hole explosions?'. *Nature* **248**(5443):30–31. Number: 5443 Publisher: Nature Publishing Group.

S. W. Hawking (1989). 'Black holes from cosmic strings'. *Physics Letters B* **231**:237–239. ADS Bibcode: 1989PhLB..231..237H.

P. Helbig (2015). 'The m-z relation for type Ia supernovae, locally inhomogeneous cosmological models, and the nature of dark matter'. *Monthly Notices of the Royal Astronomical Society* **451**(2):2097–2107. arXiv: 1505.02917.

P. Helbig (2020). 'Calculation of distances in cosmological models with small-scale inhomogeneities and their use in observational cosmology: a review'. *The Open Journal of Astrophysics* **3**:1.

D. M. Hewitt, et al. (2021). 'Arecibo observations of a burst storm from FRB 20121102A in 2016' p. 28.

G. H. Hilmarsson, et al. (2021). 'Rotation Measure Evolution of the Repeating Fast Radio Burst Source FRB 121102'. *The Astrophysical Journal Letters* **908**(1):L10. Publisher: The American Astronomical Society.

D. W. Hogg (2000). 'Distance measures in cosmology'. *arXiv:astro-ph/9905116* arXiv: astro-ph/9905116 version: 4.

D. E. Holz & R. M. Wald (1998). 'New method for determining cumulative gravitational lensing effects in inhomogeneous universes'. *Physical Review D* **58**:063501.

A. W. Hotan, et al. (2021). 'Australian square kilometre array pathfinder: I. system description'. *Publications of the Astronomical Society of Australia* **38**:e009. Publisher: Cambridge University Press.

E. Hubble (1929). 'A relation between distance and radial velocity among extra-galactic nebulae'. *Proceedings of the National Academy of Sciences* **15**(3):168–173. Publisher: Proceedings of the National Academy of Sciences.

C. W. James, et al. (2022). 'A measurement of Hubble's Constant using Fast Radio Bursts'. Tech. rep. Publication Title: arXiv e-prints ADS Bibcode: 2022arXiv220800819J Type: article.

C. W. James, et al. (2021a). 'The z–DM distribution of fast radio bursts'. *arXiv:2101.08005 [astro-ph]* arXiv: 2101.08005.

C. W. James, et al. (2021b). 'The fast radio burst population evolves, consistent with the star-formation rate'. *Monthly Notices of the Royal Astronomical Society* ADS Bibcode: 2021MNRAS.tmpL.103J.

O. James, et al. (2015). 'Gravitational lensing by spinning black holes in astrophysics, and in the movie Interstellar'. *Classical and Quantum Gravity* **32**(6):065001. Publisher: IOP Publishing.

D. L. Jauncey (1975). 'Radio surveys and source counts.'. *In: Annual review of astronomy and astrophysics. Volume 13. (A76-10076 01-88) Palo Alto, Calif., Annual Reviews, Inc., 1975, p. 23-44.* **13**:23.

L. Ji, et al. (2018). 'Strong Lensing of Gamma Ray Bursts as a Probe of Compact Dark Matter'. *Physical Review D* **98**(12):123523. arXiv: 1809.09627.

D. L. Jow, et al. (2020). 'Wave effects in the microlensing of pulsars and FRBs by point masses'. *Monthly Notices of the Royal Astronomical Society* **497**(4):4956–4969.

J. Jönsson, et al. (2010). 'Constraining dark matter halo properties using lensed Supernova Legacy Survey supernovae'. *Monthly Notices of the Royal Astronomical Society* **405**(1):535–544.

Z. Kader, et al. (2022). 'High-time resolution search for compact objects using fast radio burst gravitational lens interferometry with CHIME/FRB'. *Physical Review D* **106**(4):043016. Publisher: American Physical Society.

N. Kaiser (1983). 'Constraints on neutrino-dominated cosmologies from large-scale streaming motion'. *The Astrophysical Journal* **273**:L17–L20. ADS Bibcode: 1983ApJ...273L..17K.

N. Kaiser & J. A. Peacock (2016). 'On the bias of the distance-redshift relation from gravitational lensing'. *Monthly Notices of the Royal Astronomical Society* **455**:4518–4547.

B. J. Kavanagh (2019). 'bradkav/PBHbounds: Release version'.

B. J. Kavanagh, et al. (2018). 'Merger rate of a subdominant population of primordial black holes'. *Physical Review D* **98**(2):023536. Publisher: American Physical Society.

R. Kayser, et al. (1997). 'A general and practical method for calculating cosmological distances.'. *Astronomy and Astrophysics* **318**:680–686.

K. I. Kellermann & J. V. Wall (1987). 'Radio Source Counts and their Interpretation'. In A. Hewitt, G. Burbidge, & L. Z. Fang (eds.), *Observational Cosmology*, International Astronomical Union/ Union Astronomique Internationale, pp. 545–564, Dordrecht. Springer Netherlands.

P. L. Kelly, et al. (2015). 'Multiple images of a highly magnified supernova formed by an early-type cluster galaxy lens'. *Science* **347**(6226):1123–1126. Publisher: American Association for the Advancement of Science.

W. T. Kelvin (1904). *Baltimore lectures on molecular dynamics and the wave theory of light*. C.J. Clay and Sons; Publication agency of the Johns Hopkins University, London, Baltimore.

I. R. Kenyon (1990). *General relativity*. Oxford University Press, Oxford [England] ; New York.

U. Keshet, et al. (2021). 'Protruding bullet heads indicating dark matter pull'. *Monthly Notices of the Royal Astronomical Society* **508**(3):3455–3462.

A. Klypin, et al. (2016). 'MultiDark simulations: the story of dark matter halo concentrations and density profiles'. *Monthly Notices of the Royal Astronomical Society* **457**(4):4340–4359.

A. A. Klypin, et al. (1999). 'Where are the missing galactic satellites?'. *The Astrophysical Journal* **522**(1):82–92. arXiv: astro-ph/9901240.

A. Kogut, et al. (2003). 'First-Year Wilkinson Microwave Anisotropy Probe (WMAP)* Observations: Temperature-Polarization Correlation'. *The Astrophysical Journal Supplement Series* **148**(1):161. Publisher: IOP Publishing.

R. Laha (2020). 'Lensing of fast radio bursts: Future constraints on primordial black hole density with an extended mass function and a new probe of exotic compact fermion and boson stars'. *Physical Review D* **102**(2):023016. Publisher: American Physical Society.

R. Laha, et al. (2020). '$INTEGRAL$ constraints on primordial black holes and particle dark matter'. *Physical Review D* **101**(12):123514. Publisher: American Physical Society.

H. C. Lambert & B. J. Rickett (1999). 'On the Theory of Pulse Propagation and Two-Frequency Field Statistics in Irregular Interstellar Plasmas'. *The Astrophysical Journal* **517**:299–317. ADS Bibcode: 1999ApJ...517..299L.

G. Lemaître (1927). 'Un Univers homogène de masse constante et de rayon croissant rendant compte de la vitesse radiale des nébuleuses extra-galactiques'. *Annales de la Société Scientifique de Bruxelles* **47**:49–59. ADS Bibcode: 1927ASSB...47...49L.

G. Lemaître (1931). 'The Beginning of the World from the Point of View of Quantum Theory'. *Nature* **127**(3210):706–706. Number: 3210 Publisher: Nature Publishing Group.

C. Leung, et al. (2022). 'Constraining primordial black holes using fast radio burst gravitational-lens interferometry with CHIME/FRB'. *Physical Review D* **106**(4):043017. Publisher: American Physical Society.

G. F. Lewis (2020). 'Gravitational Microlensing Time Delays at High Optical Depth: Image Parities and the Temporal Properties of Fast Radio Bursts'. *arXiv:2007.03919 [astro-ph]* arXiv: 2007.03919.

LIGO Scientific Collaboration and Virgo Collaboration, et al. (2016). 'Observation of Gravitational Waves from a Binary Black Hole Merger'. *Physical Review Letters* **116**(6):061102.

LIGO Scientific Collaboration and Virgo Collaboration, et al. (2019). 'GWTC-1: A Gravitational-Wave Transient Catalog of Compact Binary Mergers Observed by LIGO and Virgo during the First and Second Observing Runs'. *Physical Review X* **9**(3):031040.

H.-H. Lin, et al. (2022). 'BURSTT: Bustling Universe Radio Survey Telescope for Taiwan'. arXiv:2206.08983 [astro-ph].

E. V. Linder (1988). 'Cosmological tests of generalized Friedmann models'. *Astronomy and Astrophysics* **206**:175–189.

M. S. Longair & P. A. G. Scheuer (1966). 'On the Interpretation of Radio Source Counts'. *Monthly Notices of the Royal Astronomical Society* **133**(4):421–436.

D. R. Lorimer (1998). 'Binary and Millisecond Pulsars'. *Living Reviews in Relativity* **1**(1):10.

D. R. Lorimer (2005). *Handbook of pulsar astronomy / D.R. Lorimer, M. Kramer.* Cambridge observing handbooks for research astronomers ; 4. Cambridge University Press, New York.

D. R. Lorimer, et al. (2007). 'A bright millisecond radio burst of extragalactic origin'. *Science (New York, N.Y.)* **318**(5851):777–780.

R. Luo, et al. (2020). 'On the FRB luminosity function - - II. Event rate density'. *Monthly Notices of the Royal Astronomical Society* **494**:665–679. ADS Bibcode: 2020MNRAS.494..665L.

A. Lyne & F. Graham-Smith (2012). *Pulsar Astronomy*. Cambridge Astrophysics. Cambridge University Press, Cambridge, 4 edn.

Y. Lyubarsky (2014). 'A model for fast extragalactic radio bursts'. *Monthly Notices of the Royal Astronomical Society: Letters* **442**(1):L9–L13.

J.-P. Macquart (2004). 'Scattering of gravitational radiation: second order moments of the wave amplitude'. *Astronomy & Astrophysics* **422**(3):761–775. arXiv: astro-ph/0402661.

J.-P. Macquart, et al. (2010). 'The Commensal Real-Time ASKAP Fast-Transients (CRAFT) Survey'. *Publications of the Astronomical Society of Australia* **27**(3):272–282. Publisher: Cambridge University Press.

J.-P. Macquart & A. G. d. Bruyn (2006). 'Diffractive interstellar scintillation of the quasar J1819+3845 at 21 cm'. *Astronomy & Astrophysics* **446**(1):185–200. Number: 1 Publisher: EDP Sciences.

J.-P. Macquart & R. Ekers (2018a). 'FRB event rate counts II — fluence, redshift and dispersion measure distributions'. *Monthly Notices of the Royal Astronomical Society* **480**(3):4211–4230. arXiv: 1808.00908.

J.-P. Macquart & R. D. Ekers (2018b). 'Fast radio burst event rate counts – I. Interpreting the observations'. *Monthly Notices of the Royal Astronomical Society* **474**(2):1900–1908.

J.-P. Macquart & J. Y. Koay (2013). 'Temporal Smearing of Transient Radio Sources by the Intergalactic Medium'. *The Astrophysical Journal* **776**(2):125. Publisher: The American Astronomical Society.

J.-P. Macquart, et al. (2020). 'A census of baryons in the Universe from localized fast radio bursts'. *Nature* **581**(7809):391–395. arXiv: 2005.13161.

J.-P. Macquart, et al. (2019). 'The Spectral Properties of the Bright Fast Radio Burst Population'. *The Astrophysical Journal* **872**(2):L19. Publisher: American Astronomical Society.

P. Madau & M. Dickinson (2014). 'Cosmic Star Formation History'. *Annual Review of Astronomy and Astrophysics* **52**(1):415–486. arXiv: 1403.0007.

R. A. Main, et al. (2022). 'Modelling Annual Scintillation Velocity Variations of FRB 20201124A'. arXiv:2212.04839 [astro-ph].

R. A. Main, et al. (2021). 'Scintillation time-scale measurement of the highly active FRB20201124A'. *Monthly Notices of the Royal Astronomical Society* **509**(3):3172–3180.

D. Maoz (2016). *Astrophysics in a nutshell*. Princeton University Press, Princeton, NJ, 2nd edition edn.

D. Maoz, et al. (2014). 'Observational Clues to the Progenitors of Type Ia Supernovae'. *Annual Review of Astronomy and Astrophysics* **52**:107–170.

B. Marcote, et al. (2020). 'A repeating fast radio burst source localized to a nearby spiral galaxy'. *Nature* **577**(7789):190–194. Number: 7789 Publisher: Nature Publishing Group.

B. Marcote, et al. (2017). 'The Repeating Fast Radio Burst FRB 121102 as Seen on Milliarcsecond Angular Scales'. *The Astrophysical Journal Letters* **834**(2):L8. Publisher: The American Astronomical Society.

B. Margalit & B. D. Metzger (2018). 'A Concordance Picture of FRB 121102 as a Flaring Magnetar Embedded in a Magnetized Ion–Electron Wind Nebula'. *The Astrophysical Journal Letters* **868**(1):L4. Publisher: The American Astronomical Society.

M. Markevitch, et al. (2004). 'Direct Constraints on the Dark Matter Self-Interaction Cross Section from the Merging Galaxy Cluster 1E 0657–56'. *The Astrophysical Journal* **606**(2):819. Publisher: IOP Publishing.

V. R. Marthi, et al. (2022). 'Burst properties of the highly active FRB20201124A using uGMRT'. *Monthly Notices of the Royal Astronomical Society* **509**:2209–2219. ADS Bibcode: 2022MNRAS.509.2209M.

K. Masui, et al. (2015). 'Dense magnetized plasma associated with a fast radio burst'. *Nature* **528**(7583):523–525. arXiv: 1512.00529.

M. McCourt, et al. (2018). 'A characteristic scale for cold gas'. *Monthly Notices of the Royal Astronomical Society* **473**(4):5407–5431.

R. B. Metcalf & J. Silk (1999). 'A Fundamental Test of the Nature of Dark Matter'. *The Astrophysical Journal* **519**(1):L1–L4. arXiv: astro-ph/9901358.

B. D. Metzger, et al. (2019). 'Fast radio bursts as synchrotron maser emission from decelerating relativistic blast waves'. *Monthly Notices of the Royal Astronomical Society* **485**(3):4091–4106.

D. Michilli, et al. (2018). 'An extreme magneto-ionic environment associated with the fast radio burst source FRB 121102'. *Nature* **553**(7687):182–185. Number: 7687 Publisher: Nature Publishing Group.

C. W. Misner, et al. (2018). *Gravitation*. Publication Title: Gravitation. Charles W. Misner ADS Bibcode: 2018grav.book.....M.

B. Moore, et al. (1999). 'Dark Matter Substructure within Galactic Halos'. *The Astrophysical Journal Letters* **524**:L19–L22.

J. S. Morgan, et al. (2022). 'A census of compact sources at 162 MHz: First data release from the MWA Phase II IPS Survey'. *Publications of the Astronomical Society of Australia* **39**:e063. Publisher: Cambridge University Press.

J. B. Muñoz, et al. (2016). 'Lensing of Fast Radio Bursts as a Probe of Compact Dark Matter'. *Physical Review Letters* **117**(9):091301. arXiv: 1605.00008.

T. T. Nakamura (1997). 'Effect of Shear on the Cosmological Distance and Image Amplification: Power Spectrum Approach'. *Publications of the Astronomical Society of Japan* **49**:151–157.

R. Narayan (1992). 'The Physics of Pulsar Scintillation'. *Philosophical Transactions of the Royal Society of London Series A* **341**:151–165.

J. F. Navarro, et al. (1996). 'The Structure of Cold Dark Matter Halos'. *The Astrophysical Journal* **462**:563.

J. F. Navarro, et al. (2010). 'The diversity and similarity of simulated cold dark matter haloes'. *Monthly Notices of the Royal Astronomical Society* **402**(1):21–34.

L. Nicastro, et al. (2001). 'Scintillation measurements of the millisecond pulsar PSR J0030+0451 and pulsar space velocities'. *Astronomy & Astrophysics* **368**(3):1055–1062. Number: 3 Publisher: EDP Sciences.

H. Niikura, et al. (2019). 'Constraints on Earth-mass primordial black holes from OGLE 5-year microlensing events'. *Physical Review D* **99**(8):083503. Publisher: American Physical Society.

K. Nimmo & S. Chatterjee (2023). 'Fast Radio Burst Community Newsletter - Volume 4, Issue 03' Accepted: 2023-04-03T16:32:44Z.

K. Nimmo, et al. (2022a). 'Burst timescales and luminosities as links between young pulsars and fast radio bursts'. *Nature Astronomy* **6**(3):393–401. Number: 3 Publisher: Nature Publishing Group.

K. Nimmo, et al. (2022b). 'Milliarcsecond Localization of the Repeating FRB 20201124A'. *The Astrophysical Journal Letters* **927**(1):L3. Publisher: The American Astronomical Society.

A. H. Nitz & Y.-F. Wang (2022). 'Broad search for gravitational waves from subsolar-mass binaries through LIGO and Virgo's third observing run'. *Physical Review D* **106**(2):023024. Publisher: American Physical Society.

S. K. Ocker, et al. (2021). 'Constraining Galaxy Halos from the Dispersion and Scattering of Fast Radio Bursts and Pulsars'. *The Astrophysical Journal* **911**(2):102. Publisher: The American Astronomical Society.

S. K. Ocker, et al. (2022a). 'Radio Scattering Horizons for Galactic and Extragalactic Transients'. *The Astrophysical Journal* **934**(1):71. arXiv:2203.16716 [astro-ph].

S. K. Ocker, et al. (2022b). 'Scattering variability detected from the circumsource medium of FRB 20190520B'. arXiv:2210.01975 [astro-ph].

S. K. Ocker, et al. (2022c). 'The Large Dispersion and Scattering of FRB 20190520B Are Dominated by the Host Galaxy'. *The Astrophysical Journal* **931**(2):87. Publisher: The American Astronomical Society.

M. Oguri (2019). 'Strong gravitational lensing of explosive transients'. *Reports on Progress in Physics* **82**(12):126901. Publisher: IOP Publishing.

T. A. Oosterloo, et al. (2020). 'Extreme intra-hour variability of the radio source J1402+5347 discovered with Apertif'. *Astronomy & Astrophysics* **641**:L4. Publisher: EDP Sciences.

F. Pacucci & A. Loeb (2019). 'Most Lensed Quasars at z $\greater$ 6 are Missed by Current Surveys'. *The Astrophysical Journal* **870**(2):L12. Publisher: American Astronomical Society.

T. Padmanabhan (2000). *Theoretical Astrophysics: Volume 1: Astrophysical Processes*, vol. 1. Cambridge University Press, Cambridge.

J. Paynter, et al. (2021). 'Evidence for an intermediate-mass black hole from a gravitationally lensed gamma-ray burst'. *Nature Astronomy* **5**(6):560–568. Number: 6 Publisher: Nature Publishing Group.

J. A. Peacock (1985). 'The high-redshift evolution of radio galaxies and quasars'. *Monthly Notices of the Royal Astronomical Society* **217**(3):601–631.

P. J. E. Peebles (1980). *The large-scale structure of the universe*. Publication Title: Large-Scale Structure of the Universe by Phillip James Edwin Peebles. Princeton University Press ADS Bibcode: 1980lssu.book.....P.

P. J. E. Peebles (1993). *Principles of Physical Cosmology*. Publication Title: Principles of physical cosmology ADS Bibcode: 1993ppc..book.....P.

P. J. E. Peebles & J. T. Yu (1970). 'Primeval Adiabatic Perturbation in an Expanding Universe'. *The Astrophysical Journal* **162**:815. ADS Bibcode: 1970ApJ...162..815P.

L. Perivolaropoulos & F. Skara (2022). 'Challenges for ΛCDM: An update'. *New Astronomy Reviews* **95**:101659.

S. Perlmutter, et al. (1999). 'Measurements of Ω and Λ from 42 High-Redshift Supernovae'. *The Astrophysical Journal* **517**(2):565. Publisher: IOP Publishing.

E. Petroff, et al. (2022). 'Fast radio bursts at the dawn of the 2020s'. *The Astronomy and Astrophysics Review* **30**(1):2.

Planck Collaboration, et al. (2018). 'Planck 2018 results. VI. Cosmological parameters'. *arXiv:1807.06209 [astro-ph]* arXiv: 1807.06209.

E. Platts, et al. (2019). 'A living theory catalogue for fast radio bursts'. *Physics Reports* **821**:1–27.

S. B. Popov & K. A. Postnov (2010). *Hyperflares of SGRs as an engine for millisecond extragalactic radio bursts*. eprint: arXiv:0710.2006. Conference Name: Evolution of Cosmic Objects through their Physical Activity Pages: 129-132 ADS Bibcode: 2010vaoa.conf..129P.

C. Porciani & P. Madau (2000). 'Gravitational Lensing of Distant Supernovae in Cold Dark Matter Universes'. *The Astrophysical Journal* **532**:679–693. ADS Bibcode: 2000ApJ...532..679P.

J. X. Prochaska, et al. (2019a). 'The low density and magnetization of a massive galaxy halo exposed by a fast radio burst'. *arXiv:1909.11681 [astro-ph]* arXiv: 1909.11681.

J. X. Prochaska & M. Neeleman (2018). 'The astrophysical consequences of intervening galaxy gas on fast radio bursts'. *Monthly Notices of the Royal Astronomical Society* **474**(1):318–325.

J. X. Prochaska, et al. (2019b). 'FRBs/FRB: First DOI release of this repository'. *zndo* .

H. Qiu, et al. (2020). 'A population analysis of pulse broadening in ASKAP fast radio bursts'. *Monthly Notices of the Royal Astronomical Society* **497**(2):1382–1390.

D. P. Quinn, et al. (2009). 'On the Reported Death of the MACHO Era'. *Monthly Notices of the Royal Astronomical Society: Letters* **396**(1):L11–L15. arXiv: 0903.1644.

K. P. Rauch (1991). 'Gravitational Microlensing of High-Redshift Supernovae by Compact Objects'. *The Astrophysical Journal* **374**:83. ADS Bibcode: 1991ApJ...374...83R.

S. Refsdal (1964). 'On the Possibility of Determining Hubble's Parameter and

the Masses of Galaxies from the Gravitational Lens Effect'. *Monthly Notices of the Royal Astronomical Society* **128**(4):307–310.

S. Refsdal (1970). 'On the Propagation of Light in Universes with Inhomogeneous Mass Distribution'. *The Astrophysical Journal* **159**:357.

L. F. Richardson (1922). *Weather prediction by numerical process*. Cambridge, The University press.

B. Rickett (2006). 'Anisotropy in Pulsar Interstellar Scattering'. *Chinese Journal of Astronomy and Astrophysics* **6**(S2):197.

B. J. Rickett, et al. (1997). 'Interstellar fringes from pulsar B0834+06'. *Monthly Notices of the Royal Astronomical Society* **287**(4):739–752.

M. Ricotti, et al. (2008). 'Effect of Primordial Black Holes on the Cosmic Microwave Background and Cosmological Parameter Estimates'. *The Astrophysical Journal* **680**(2):829. Publisher: IOP Publishing.

A. Ridnaia, et al. (2021). 'A peculiar hard X-ray counterpart of a Galactic fast radio burst'. *Nature Astronomy* **5**(4):372–377. Number: 4 Publisher: Nature Publishing Group.

A. G. Riess, et al. (1998). 'Observational Evidence from Supernovae for an Accelerating Universe and a Cosmological Constant'. *The Astronomical Journal* **116**(3):1009. Publisher: IOP Publishing.

A. G. Riess, et al. (1999). 'The Rise Time of Nearby Type IA Supernovae'. *The Astronomical Journal* **118**:2675–2688.

W. Rindler (1956). 'Visual Horizons in World Models'. *Monthly Notices of the Royal Astronomical Society* **116**(6):662–677.

G. V. Rossum & F. L. J. Drake (2011). *The Python Language Reference Manual*. Network Theory Ltd., Bristol.

V. C. Rubin (1983). 'The Rotation of Spiral Galaxies'. *Science* **220**(4604):1339–1344. Publisher: American Association for the Advancement of Science Section: Articles.

V. C. Rubin, et al. (1980). 'Rotational properties of 21 SC galaxies with a large range of luminosities and radii, from NGC 4605 (R=4kpc) to UGC 2885 (R=122kpc).'. *The Astrophysical Journal* **238**:471–487. ADS Bibcode: 1980ApJ...238..471R.

S. D. Ryder, et al. (2022). 'Probing the distant universe with a very luminous fast radio burst at redshift 1'. arXiv:2210.04680 [astro-ph].

R. K. Sachs & A. M. Wolfe (1967). 'Perturbations of a Cosmological Model and Angular Variations of the Microwave Background'. *The Astrophysical Journal* **147**:73. ADS Bibcode: 1967ApJ...147...73S.

M. W. Sammons, et al. (2020). 'First Constraints on Compact Dark Matter from Fast Radio Burst Microstructure'. *The Astrophysical Journal* **900**(2):122. Publisher: IOP Publishing.

P. Sanghavi, et al. (2023). 'TONE: A CHIME/FRB Outrigger Pathfinder for localizations of Fast Radio Bursts using Very Long Baseline Interferometry'. arXiv:2304.10534 [astro-ph].

M. Sasaki, et al. (2016). 'Primordial Black Hole Scenario for the Gravitational-Wave Event GW150914'. *Physical Review Letters* **117**(6):061101. Publisher: American Physical Society.

T. Sawala, et al. (2016). 'The APOSTLE simulations: solutions to the Local Group's cosmic puzzles'. *Monthly Notices of the Royal Astronomical Society* **457**(2):1931–1943.

P. Schneider (1987). 'An analytically soluble problem in fully nonlinear statistical gravitational lensing'. *The Astrophysical Journal* **319**:9–13.

P. Schneider (2019). 'Generalized multi-plane gravitational lensing: time delays, recursive lens equation, and the mass-sheet transformation'. *Astronomy & Astrophysics* **624**:A54. Publisher: EDP Sciences.

P. Schneider, et al. (1992). *Gravitational Lenses*. Astronomy and Astrophysics Library. Springer, Berlin, Heidelberg.

P. Schneider & A. Weiss (1988). 'Light propagation in inhomogeneous universes'. *The Astrophysical Journal* **327**:526–543.

E. Schoen, et al. (2021). 'Scintillation Timescales of Bright FRBs Detected by CHIME/FRB'. *Research Notes of the AAS* **5**(11):271. Publisher: The American Astronomical Society.

D. R. Scott, et al. (2023). 'CELEBI: The CRAFT Effortless Localisation and Enhanced Burst Inspection Pipeline' .

P. D. Serpico, et al. (2020). 'Cosmic microwave background bounds on primordial black holes including dark matter halo accretion'. *Physical Review Research* **2**(2):023204. Publisher: American Physical Society.

R. M. Shannon, et al. (2018). 'The dispersion–brightness relation for fast radio bursts from a wide-field survey'. *Nature* **562**(7727):386–390.

K. Shin, et al. (2022). 'Inferring the Energy and Distance Distributions of Fast Radio Bursts using the First CHIME/FRB Catalog'. arXiv:2207.14316 [astro-ph].

T. M. Siewert, et al. (2021). 'Cosmic radio dipole: Estimators and frequency dependence'. *Astronomy & Astrophysics* **653**:A9. Publisher: EDP Sciences.

S. Simha, et al. (2020). 'Disentangling the Cosmic Web toward FRB 190608'. *The Astrophysical Journal* **901**(2):134. Publisher: The American Astronomical Society.

V. M. Slipher (1917). 'Nebulae'. *Proceedings of the American Philosophical Society* **56**:403–409. ADS Bibcode: 1917PAPhS..56..403S.

G. F. Smoot, et al. (1992). 'Structure in the COBE Differential Microwave Radiometer First-Year Maps'. *The Astrophysical Journal* **396**:L1. ADS Bibcode: 1992ApJ...396L...1S.

J. G. v. Soldner (1804). 'Ueber die Ablenkung eines Lichtstrals von seiner geradlinigen Bewegung'. *Berliner Astronomisches Jahrbuch* pp. 161–172.

L. G. Spitler, et al. (2014). 'Fast Radio Burst Discovered in the Arecibo Pulsar ALFA Survey'. *The Astrophysical Journal* **790**(2):101.

L. G. Spitler, et al. (2016). 'A repeating fast radio burst'. *Nature* **531**(7593):202–205.

V. Springel, et al. (2006). 'The large-scale structure of the Universe'. *Nature* **440**(7088):1137–1144. Number: 7088 Publisher: Nature Publishing Group.

V. Springel, et al. (2005). 'Simulations of the formation, evolution and clustering of galaxies and quasars'. *Nature* **435**(7042):629–636. Number: 7042 Publisher: Nature Publishing Group.

S. Stanimirović & A. Lazarian (2001). 'Velocity and density spectra of the Small Magellanic Cloud'. *The Astrophysical Journal* **551**(1):L53–L56. arXiv: astro-ph/0102191.

D. Stinebring (2007). 'Pulsar Scintillation Arcs and the Ionized ISM' **365**:254. Conference Name: SINS - Small Ionized and Neutral Structures in the Diffuse Interstellar Medium ADS Bibcode: 2007ASPC..365..254S.

D. R. Stinebring (2006). 'Scintillation Arcs: Probing Turbulence and Structure in the ISM'. *Chinese Journal of Astronomy and Astrophysics* **6**(S2):204.

L.-G. Strolger, et al. (2015). 'The Rate of Core Collapse Supernovae to Redshift 2.5 From The Candels and Clash Supernova Surveys'. *The Astrophysical Journal* **813**(2):93. Publisher: The American Astronomical Society.

H. Sun, et al. (2015). 'Extragalactic High-Energy Transients: Event Rate Densities and Luminosity Functions'. *The Astrophysical Journal* **812**(1):33. Publisher: IOP Publishing.

R. A. Sunyaev & Y. B. Zeldovich (1970). 'Small-Scale Fluctuations of Relic Radiation'. *Astrophysics and Space Science, Volume 7, Issue 1, pp.3-19* **7**(1):3.

A. T. Sutinjo, et al. (2023). 'Calculation and Uncertainty of Fast Radio Burst Structure Based on Smoothed Data'. arXiv:2302.06220 [astro-ph].

S. P. Tendulkar, et al. (2017). 'The Host Galaxy and Redshift of the Repeating Fast Radio Burst FRB 121102'. *The Astrophysical Journal* **834**(2):L7.

The CHIME/FRB Collaboration (2020). 'A bright millisecond-duration radio burst from a Galactic magnetar'. *Nature* **587**(7832):54–58. Number: 7832 Publisher: Nature Publishing Group.

The CHIME/FRB Collaboration, et al. (2021). 'The First CHIME/FRB Fast Radio Burst Catalog'. *The Astrophysical Journal Supplement Series* **257**(2):59. Publisher: IOP Publishing.

The Event Horizon Telescope Collaboration (2022). 'First Sagittarius A* Event Horizon Telescope Results. I. The Shadow of the Supermassive Black Hole in the Center of the Milky Way'. *The Astrophysical Journal Letters* **930**(L12).

K. S. Thorne (1980). 'Multipole expansions of gravitational radiation'. *Reviews of Modern Physics* **52**(2):299–339. Publisher: American Physical Society.

D. Thornton, et al. (2013). 'A Population of Fast Radio Bursts at Cosmological Distances'. *Science* **341**(6141):53–56.

P. Tisserand, et al. (2007). 'Limits on the Macho content of the Galactic Halo from the EROS-2 Survey of the Magellanic Clouds'. *Astronomy & Astrophysics* **469**(2):387–404. Number: 2 Publisher: EDP Sciences.

F. S. Trang & B. J. Rickett (2007). 'Modeling of Interstellar Scintillation Arcs from Pulsar B1133+16'. *The Astrophysical Journal* **661**(2):1064. Publisher: IOP Publishing.

E. L. Turner, et al. (1984). 'The statistics of gravitational lenses - The distributions of image angular separations and lens redshifts'. *The Astrophysical Journal* **284**:1–22.

K. Umetsu (2010). 'Cluster Weak Gravitational Lensing' .

H. K. Vedantham & E. S. Phinney (2019). 'Radio wave scattering by circumgalactic cool gas clumps'. *Monthly Notices of the Royal Astronomical Society* **483**(1):971–984. arXiv: 1811.10876.

M. Viel, et al. (2013). 'Warm dark matter as a solution to the small scale crisis: New constraints from high redshift Lyman-alpha forest data'. *Physical Review D* **88**:043502. ADS Bibcode: 2013PhRvD..88d3502V.

P. Virtanen, et al. (2020). 'SciPy 1.0: fundamental algorithms for scientific computing in Python'. *Nature Methods* **17**(3):261–272. Number: 3 Publisher: Nature Publishing Group.

S. von Hoerner (1973). 'Radio Source Counts and Cosmology'. *The Astrophysical Journal* **186**:741–766. ADS Bibcode: 1973ApJ...186..741V.

J. Wagner (2018). 'Generalised model-independent characterisation of strong gravitational lenses - IV. Formalism-intrinsic degeneracies'. *Astronomy & Astrophysics* **620**:A86. Publisher: EDP Sciences.

J. Wagner, et al. (2019). 'Multiply imaged time-varying sources behind galaxy clusters - Comparing fast radio bursts to QSOs, SNe, and GRBs'. *Astronomy & Astrophysics* **621**:A91. Publisher: EDP Sciences.

J. V. Wall & J. A. Peacock (1985). 'Bright extragalactic radio sources at 2.7 GHz – III. The all-sky catalogue'. *Monthly Notices of the Royal Astronomical Society* **216**(2):173–192.

D. Walsh, et al. (1979). '0957 + 561 A, B - Twin quasistellar objects or gravitational lens'. *Nature* **279**:381–384.

Y. Wang, et al. (2021). 'ASKAP observations of multiple rapid scintillators reveal a degrees-long plasma filament'. *Monthly Notices of the Royal Astronomical Society* **502**(3):3294–3311.

S. Weinberg (1972). 'Gravitation and Cosmology: Principles and Applications of the General Theory of Relativity'. *Gravitation and Cosmology: Principles and Applications of the General Theory of Relativity, by Steven Weinberg, pp. 688. ISBN 0-471-92567-5. Wiley-VCH , July 1972.* ISBN: 9780471925675 Num Pages: 688.

S. Weinberg (1976). 'Apparent luminosities in a locally inhomogeneous universe.'. *The Astrophysical Journal* **208**:L1–L3.

K. C. Wong, et al. (2019). 'H0LiCOW XIII. A 2.4% measurement of H_{0} from lensed quasars: 5.3σ tension between early and late-Universe probes'. *arXiv:1907.04869 [astro-ph]* arXiv: 1907.04869.

S. E. Woosley & J. S. Bloom (2006). 'The Supernova Gamma-Ray Burst Connection'. *Annual Review of Astronomy & Astrophysics, vol. 44, Issue 1, pp.507-556* **44**(1):507.

Q. Wu, et al. (2022). 'An 8 percent determination of the Hubble constant from

localized fast radio bursts'. *Monthly Notices of the Royal Astronomical Society: Letters* **515**(1):L1–L5.

L. Wyrzykowski, et al. (2011). 'The OGLE View of Microlensing towards the Magellanic Clouds. IV. OGLE-III SMC Data and Final Conclusions on MACHOs'. *Monthly Notices of the Royal Astronomical Society* **416**(4):2949–2961. arXiv: 1106.2925.

H. Xu, et al. (2022). 'A fast radio burst source at a complex magnetized site in a barred galaxy'. *Nature* **609**(7928):685–688. Number: 7928 Publisher: Nature Publishing Group.

Y.-P. Yang & B. Zhang (2017). 'Dispersion Measure Variation of Repeating Fast Radio Burst Sources'. *The Astrophysical Journal* **847**(1):22. arXiv: 1707.02923.

J. M. Yao, et al. (2017). 'A New Electron-Density Model For Estimation of Pulsar and FRB Distances'. *The Astrophysical Journal* **835**(1):29. Publisher: The American Astronomical Society.

M. Yue, et al. (2022). 'Revisiting the Lensed Fraction of High-Redshift Quasars'. *The Astrophysical Journal* **925**(2):169. arXiv: 2112.02821.

B. Zackay & E. O. Ofek (2017). 'An Accurate and Efficient Algorithm for Detection of Radio Bursts With Unknown Dispersion Measure, for Single-Dish Telescopes and Interferometers'. *The Astrophysical Journal* **835**(1):11.

Y. B. Zel'dovich & I. D. Novikov (1966). 'The Hypothesis of Cores Retarded during Expansion and the Hot Cosmological Model'. *Astronomicheskii Zhurnal* **43**:758.

B. Zhang (2022). 'The Physics of Fast Radio Bursts'. Tech. rep. Publication Title: arXiv e-prints ADS Bibcode: 2022arXiv221203972Z Type: article.

R. C. Zhang, et al. (2021). 'On the energy and redshift distributions of fast radio bursts'. *Monthly Notices of the Royal Astronomical Society* **501**(1):157–167.

M. Zumalacárregui & U. Seljak (2018). 'Limits on Stellar-Mass Compact Objects as Dark Matter from Gravitational Lensing of Type Ia Supernovae'. *Physical Review Letters* **121**(14):141101. Publisher: American Physical Society.

F. Zwicky (1933). 'Die Rotverschiebung von extragalaktischen Nebeln'. *Helvetica Physica Acta* **6**:110–127. ADS Bibcode: 1933AcHPh...6..110Z.